TROPOSPHERIC ULTRAVIOLET RADIATION, PHOTOLYSIS AND CLOUDS

by

Kirsten Margaret Hilla Mitchell

A thesis submitted in fulfilment of
the requirements for the degree
of

Doctor of Philosophy

Imperial College, University of
London

January 2001

IMPL. COLL. LOND. UNIV.

Abstract

Solar ultraviolet radiation initiates photolysis in the troposphere. Accurate knowledge of the rate of photolysis, j, is vital in modelling atmospheric chemistry. It is widely accepted that the most important photolysis frequencies are jNO_2 and $jO(^1D)$. In agreement with previous authors, the effect of cloud optical depth on these photolysis frequencies is shown to be large. In the past, photolysis frequencies have been calculated using average cloud optical depths. Here, a more representative approach is adopted and the relationship between cloud optical depth and photolysis frequency investigated.

To this end, a novel method for obtaining cloud optical depths from jNO_2 data is developed. The cloud optical depths obtained in this way are higher than satellite observed optical depths but are consistent with previous ground-based methods. A lognormal probability density function describes the distribution of cloud optical depth obtained from the data very well. Analysis of the cloud optical depth distribution shows that the average cloud optical depth can lead to errors in calculation of photolysis frequencies in atmospheric models.

The question of the relative responses of jNO_2 and $jO(^1D)$ to cloud is then addressed. jNO_2 is shown to decrease more than $jO(^1D)$, on average, under cloudy conditions. This response is qualitatively reproduced by simple use of the model, although the magnitude of the model response differs from that in the data. A theoretical explanation for the observed and modelled responses is proposed. Use of the lognormal cloud optical depth distribution improves the agreement between the model and observations. Various refinements are included. The inclusion of a clear sky probability and a cloud optical depth distribution is found to provide good agreement with the data and this is proposed as the best method of simulating the observed data.

I dedicate this thesis to my parents.

Acknowledgements

There are many people I would like to thank for helping me in this thesis.

I would like to thank my supervisor, Ralf Toumi, for his patience, numerous ideas and time, particularly during the final two years of this work. In the last six months, his support and enthusiasm were inspirational. I would also like to thank: Vic Williams, Jacqui Russell, Richard Bantges, Catherine Naud, Ashley Tomsett, Laila Gohar, Adam Hadley, Guiseppe Pettatino, Justin Ashmall, Diana Humphries, Sandy Gray, Alice Larkin and the rest of the Space and Atmospheric group, past and present. Each person, and the group as a whole, has helped me towards submitting this thesis. My parents also deserve extra-special thanks, not just for moral, but also, financial support, especially in the last year. I would never have been able to continue without their help. Finally, I would like to thank my boyfriend, Richard, for helping to keep me sane!

I would also like to thank NERC for providing the research grant and Gordon McFayden and Paul Monks for the use of their data.

Contents

Abstract 2

Acknowledgements 4

Contents 5

Figures 8

Tables 13

1. **Introduction** 15

1.1 What is photolysis? 16

1.1.1 Quantum yield of ozone 18

1.1.2 Ultraviolet 20

1.2 Significance of photolysis in the Earth-atmosphere system 22

1.3 Nitrogen dioxide and Ozone photolysis 23

1.3.1 Nitrogen dioxide photolysis 24

1.3.2 Ozone photolysis 25

1.3.3 Factors affecting photolysis rate 28

1.4 Measurements 28

1.5 Measurements at Mace Head 32

1.6 Summary 36

2. Radiative transfer and the model **44**

2.1 Introduction to radiative transfer 44

2.1.1 Definitions 44

2.2 Radiative processes 45

2.2.1 Absorption 45

2.2.2 Scattering 46

2.2.2.1 A note on optical depth 49

2.2.3 Emission 50

2.3	The Equation of Radiative Transfer	50
2.3.1	Plane parallel approximation	51
2.4	A solution for the equation of radiative transfer	52
2.4.1	Two stream approximation	53
2.5	A note on actinic flux and flux	55
2.6	The atmosphere and its description by the Tropospheric Ultraviolet Visible Model	57
2.6.1	Incident solar radiation	58
2.6.2	Oxygen	58
2.6.3	Ozone	59
2.6.4	Nitrogen dioxide	61
2.6.5	Sulphur dioxide and other absorbing gases	61
2.6.6	Rayleigh scattering	62
2.6.7	Surface Albedo	63
2.6.8	Aerosol	63
2.6.9	Cloud	64
2.6.9.1	Anomalous absorption in a cloudy atmosphere	66
2.7	Summary	68
3.	**Sensitivity of the model and measurements at Mace Head**	**73**
3.1	Introduction	73
3.2	Two stream method	74
3.3	Resolution	75
3.4	Ozone Quantum Yield	75
3.5	Absorbing gasses	76
3.5.1	Column Ozone	76
3.5.2	Nitrogen Dioxide	78
3.6	Aerosol	79
3.7	Surface Albedo	82
3.8	Cloud	85

3.8.1	Cloud Optical Thickness	87
3.8.2	Cloud Base Height	87
3.8.3	Asymmetry Factor	88
3.8.4	Single Scattering Albedo	88
3.9	Summary	89
4.	**Cloud optical depth distribution from photolysis frequency measurements**	**101**
4.1	Introduction	102
4.2	Method	104
4.2.1	Clear sky parameterisation	105
4.3	Cloud optical depth from photolysis frequency	108
4.3.1	Method: Parameterisation of model response	108
4.4	Results	110
4.4.1	Diurnal cycle of 'thick' cloud	111
4.4.2	Frequency distributions and derivation of a probability density function	111
4.4.3	Support for the lognormal distribution	117
4.4.4	Comparison with ISCCP satellite data	119
4.5	Impact of lognormal distribution of cloud optical depths and photolysis rates	120
4.6	Summary	123
5.	**Response of photolysis rates to cloud**	**136**
5.1	Introduction	137
5.2	Method	140
5.3	Data Analysis	142
5.3.1	What causes attenuation of $jO(^1D)$ to dominate in the case of small changes?	144
5.3.2	Anti-correlations	146
5.3.3	How do the relative responses compare to previous work?	148

5.4	Model Analysis	150
5.4.1	Can the model explain the observed ratio?	150
5.4.1.1	Control Run	151
5.4.1.2	NO_2 column	152
5.4.1.3	Wavelength dependent albedo	152
5.4.1.4	Ozone	152
5.4.1.5	Summary	153
5.5	Model predictions of the effect of increased cloud optical depth on jNO_2 and $jO(^1D)$	153
5.6	Towards a theoretical explanation for the responses of jNO_2 and $jO(^1D)$ to cloud	156
5.6.1	$\Delta jNO_2 > \Delta jO(^1D)$	156
5.6.2	$\Delta jO(^1D) > \Delta jNO_2$	158
5.7	Mechanisms for obtaining a more realistic ratio	159
5.7.1	Introducing a realistic cloud field into the model	161
5.7.1.1	Possible evidence for anomalous absorption?	164
5.7.1.2	Clear sky and cloud optical depth distributions	165
5.8	Summary	167
6.	**Conclusions and further work**	**182**
6.1	Introduction	182
6.2	Summary	182
6.3	Further Work	184
References		**186**
Appendix A		**207**

Figures

Chapter 1

1.1 Spectral dependence of the product of absorption cross-sections and quantum yields and actinic flux for the photodissociation of NO_2 and the photodissociation of $O_3 \rightarrow O(^1D)$. Data are normalised to the largest value and shown at a temperature of 298K, from Pfister (2000) 38

1.2 Exploded view of the $jO(^1D)$ photoelectric detector (from Junkermann *et al.*,1989). 39

1.3 Position of radiometers during EASE96 and EASE97. (a) Top view (b) side view 40

1.4 jNO_2 (2π sr) as a function of solar zenith angle for cloud-free conditions (from Kraus and Hofzumahaus, 1998). 41

1.5 Measured $jO(^1D)$ photolysis frequencies (2π sr) as a function of slant ozone column for cloud-free conditions. 42

1.6 Photolysis data from Mace Head (a) jNO_2 as a function of zenith angle in 1996 (b) $jO(^1D)$ as a function of slant ozone column in 1996 (c) jNO_2 as a function of zenith angle in 1997 (d) $jO(^1D)$ as a function of slant ozone column in 1997 43

Chapter 2

2.1 A schematic showing spherical co-ordinates used to describe a pencil of radiation. 69

2.2 The Planck function at atmospheric temperatures and photolysis wavelengths 69

2.3 Absorption cross section as a function of wavelength for molecular oxygen, from Salby, 1996 (after Brasseur and Soloman, 1986) 70

2.4 Absorption cross section as a function of wavelength for ozone, from Salby 1996 (after Andrews, 1987 and WMO, 1996) 70

2.5 Absorption cross section of NO_2 as a function of wavelength 71

Chapter 3

3.1 i) Sensitivity of jNO_2 and $jO(^1D)$ to two stream method (a) jNO_2, (b) $jO(^1D)$ 90

ii) Sensitivity of jNO_2 and $jO(^1D)$ to two stream method (c) percentage change in jNO_2 compared to delta-Eddington, (d) percentage change in $jO(^1D)$ compared to delta-Eddington 91

3.2 Sensitivity of $jO(^1D)$ to O_3 quantum yield 92

3.3 Sensitivity of jNO_2 and $jO(^1D)$ to ozone column (a) jNO_2 (b) $jO(^1D)$ jNO_2 (b) $jO(^1D)$ (c) percentage change in jNO_2 relative to jNO_2 at 324 DU (d) percentage change in $jO(^1D)$ relative to $jO(^1D)$ 93

3.4 Sensitivity of jNO_2 and $jO(^1D)$ to nitrogen dioxide column (a) jNO_2 (b) percentage change in jNO_2 relative to no column (c) $jO(^1D)$ (d) $jO(^1D)$ compared to no column 94

3.5 Sensitivity of jNO_2 and $jO(^1D)$ to surface albedo (a) jNO_2 (b) percentage change in jNO_2 relative to a surface albedo of 0.05, (c) $jO(^1D)$ (d) percentage change in $jO(^1D)$ relative to a surface albedo of 0.05 95

3.6 i) Sensitivity of jNO_2 and $jO(^1D)$ to cloud optical thickness (a) jNO_2 (b) jNO_2 relative to clear sky 96

ii) (c) $jO(^1D)$ (d) $jO(^1D)$ relative to clear sky 97

3.7 Sensitivity of jNO_2 and $jO(^1D)$ to cloud base height 98

3.8 Sensitivity of jNO_2 and $jO(^1D)$ to asymmetry factor (a) jNO_2 (b) jNO_2 relative g=0.85 (c) $jO(^1D)$ (d) $jO(^1D)$ relative to g=0.85 99

3.9 Sensitivity of jNO_2 and $jO(^1D)$ to single scattering albedo (a) jNO_2 (b) jNO_2 relative ω=0.9999 (c) $jO(^1D)$ (d) $jO(^1D)$ relative to ω=0.9999 100

Chapter 4

4.1 Clear sky parameterisation of jNO_2 (a) polynomial in terms of cos(solar zenith angle) (b) exponential in terms of sec(solar zenith angle) 125

4.2 Optical depth as a function of $\ln(j_{clear}/j_{cloudy})$ for different zenith angles (a) for low optical depths (b) for high optical depths 126

4.3 Percentage difference between parameterisation and exact values (a) for low optical depth (b) for high optical depth 127

4.4 Derived cloud optical depths as a function of local time for 1996 (a) optical depth (b) truncated average optical depth 128

4.5 Derived cloud optical depths as a function of local time for 1997 (a) optical depth (b) truncated average optical depth 129

4.6 Frequency distributions of cloud optical depth for different bin sizes (a) (b) (c) (d) and (ii) on a double logarithmic plot 130

4.7 Frequency distributions of cloud optical depth for different cloud base heights (i)(a) 1 km (b) 2 km (c) 3 km (d) 4 km (ii) on a double logarithmic plot 131

4.8 Fit of stretched exponential for different values of c 132

4.9 Best fit to lognormal using a simple estimation technique 133

4.10 Best fit to lognormal using curve fitting technique (a) cloud base of 1km (b) average from data cloud base 1-4 km. 134

4.11 jNO_2 as a function of cloud optical depth 135

Chapter 5

5.1 $\Delta jO(^1D)$ as a function of ΔjNO_2 for solar zenith angles less than 75° (a) All data (b) All data without anti-correlations (c) Absolute values of all data without anticorrelations (d) As (c) but only including values >10% (e) Positive-positive changes only (f) Negative-negative changes only 170

5.2 Model predicted clear to cloudy changes (a) control run (b) Including NO_2 column (c) Decreased O_3 column (d) Increased O_3 column (e) Wavelength dependent albedo 171

5.3 $jO(^1D)$ and jNO_2 normalised to their clear sky values as a function of cloud optical depth 172

5.4 $jO(^1D)/jNO_2$ as a function of optical depth, normalised to unity at clear sky. Smallest zenith angles are at bottom of plot, largest at the top 173

5.5 Diffuse fraction of $jO(^1D)$ and jNO_2 as a fraction of their clear sky values 174

for (a) 33.9° and (b) 70°

5.6 Direct and diffuse downwards portions of photolysis frequency flux, each normalised to unity at clear sky (a)jNO_2 (b)j$O(^1D)$ 175

5.7 (i) Simulation including cloud probability density function for zenith angle of 35° (a) All data (b) Absolute values of all data without anticorrelations (c) As (b) but only including values >10% (d) Positive-positive changes only (e) Negative-negative changes only 176

(ii) Simulation including cloud probability density function for zenith angle of 55° (a) All data (b) Absolute values of all data without anticorrelations (c) As (b) but only including values >10% (d) Positive-positive changes only (e) Negative-negative changes only 177

5.8 Data for solar zenith angle bin centred on 35° (a) All data (b) All data without anti-correlations (c) Absolute values of all data without anticorrelations (d) As (c) but only including values >10% (e) Positive-positive changes only (f) Negative-negative changes only 178

5.9 Data for solar zenith angle bin centred on 55° (a) All data (b) All data without anti-correlations (c) Absolute values of all data without anticorrelations (d) As (c) but only including values >10% (e) Positive-positive changes only (f) Negative-negative changes only 179

5.10 Results of model simulation including wavelength dependent single scattering albedo (a) All data (b) Absolute values of all data without anticorrelations (c) As (b) but only including values >10% (d) Positive-positive changes only (e) Negative-negative changes only 180

5.11 Results of model simulation including clear sky probability, solar zenith angle=55° a) All data (b) Absolute values of all data without anticorrelations (c) As (b) but only including values >10% (d) Positive-positive changes only (e) Negative-negative changes only 181

Tables

Chapter 1

1-1 Wavelength distribution of solar irradiance prior to attenuation by Earth's atmosphere (from Fredrick *et al.*, 1989). 21

1-2 Primary dissociative processes for certain atmospheric species (from Wayne & Wayne, 1997) 23

1-3 Components of the radiometers used in this study (from Junkermann *et al.*, 1989) 31

Chapter 2

2-1 Examples of gamma coefficients used in different 2 stream approximations (adapted from Toon *et al.*, 1989 and Meador and Weaver, 1980) 54

2-2 Absorption cross sections, typical volume mixing ratios and optical depths of various atmospheric gases from Forster (1994), adapted from Wayne (1990) 61

2-3 Reports of the Most Common Cloud types over Oceans (from Heymsfield, 1996) 64

2-4 Reports of the most common cloud types over land (from Heymsfield, 1996) 64

2-5 A summary of some papers on anomalous absorption published since 1995 (from Wendisch, *et al.*, 1999) 67

Chapter 3

3-1 Relative optical depth of aerosol, ozone and Rayleigh molecules at 300 and 400nm respectively (from Liao *et al.*, 1999) 79

Chapter 4

4-1 Comparison of parameterisations for clear sky jNO_2 107

4-2 Properties of the lognormal distribution, $\Lambda(\mu, \sigma^2)$ (adapted from Aitchison and Brown (1956)) 116

4-3 Monthly ISCCP derived (D1) data for the Mace Head site 119

4-4 Comparison of the mean of the photolysis frequencies obtained from the distribution and the photolysis frequencies obtained using the mean of the distribution 121

Chapter 5

5-1 Changes in photolysis rates due to aerosol from Reuder and Schwander (1999) 145

5-2 Response of jNO_2 and $jO(^1D)$ to clouds from Crawford *et al.* (1999) 148

5-3 A summary of the results of the model simulation with varying atmospheric parameters 153

1. Introduction

The interaction of sunlight with the atmosphere underlies atmospheric science, driving everything from dynamics to chemistry. This work focuses on solar radiation in the lower atmosphere, two of the most important photochemical reactions it initiates and what the rates of these photochemical reactions can tell us about cloud.

The reactions of interest are photodissociation reactions caused by shortwave radiation in the troposphere. Since the sun can be characterised approximately as a black body emitting at 5770 K, the portion of sunlight in the ultraviolet is small compared with the visible and infra-red wavelength regions; only 7.5 % of solar radiation is in the ultraviolet (Meier *et al.*, 1997). Despite its relatively small contribution, this radiation is critical to the development and maintenance of the biosphere (e.g. Wayne, 1991). Ultraviolet radiation causes those reactions that initiate and maintain atmospheric chemistry: tropospheric and stratospheric photolysis.

This chapter begins with an introduction to photolysis and its relationship with ultraviolet. A discussion of the importance of photolysis follows, with special emphasis on nitrogen dioxide and ozone photolysis. Methods of measuring photolysis rates are then outlined and previous studies commented on. A short comparison between the photolysis frequencies measured at Mace Head and other studies follows.

Chapter 2 contains the fundamentals of radiative transfer theory, including the approximations required for calculation of radiation quantities in a real atmosphere and their application in the model used in this study. Following this, chapter 3 presents a short sensitivity study and briefly compares the results to previous studies. The problems of simulating the radiation field at Mace Head accurately are discussed. Combined with an outline of the importance of cloud for radiation modelling, this provides a background for

the exciting new method for the derivation of cloud optical depths from photolysis rates presented in chapter 4. Here a new parameterisation of the nitrogen dioxide photolysis rate under clear skies is presented and compared with those of Parrish (1983) and Dickerson (1982). The new parameterisation compares well and with these extends the altitude range of previous parameterisations. The response of the model calculated photolysis rates to cloud optical depth is parameterised, enabling cloud optical depths to be derived from photodissociation rate data. The diurnal variation of these cloud optical depths is discussed. A lognormal cloud optical depth distribution is obtained from Mace Head data and its significance for modelling is discussed.

In the final chapter, the question of the relative responses of nitrogen dioxide and ozone photolysis rates to cloud is investigated. Mace Head data are analysed using a method based on that of Crawford *et al.* (1999). Results of the data analysis are very similar to those of Crawford *et al.* (1999) and show no significant evidence of tropospheric path length enhancement (e.g. Pfeilsticker *et al.*, 1998). The model is used to find a theoretical explanation for the responses. The zenith angle dependence of the responses is explained. Modelling studies show that clear to cloudy changes can never explain the observed data, whatever the atmospheric conditions. Use of the lognormal cloud distribution derived in chapter 4 improves the agreement between the data and the model. Finally, two mechanisms are proposed which allow good agreement between the data and the model. The favoured mechanism uses the lognormal distribution, so validating previous results.

1.1 What is photolysis?

Photolysis is one result of the reaction of photons with molecules or atoms. A photochemical reaction causes transitions between the electronic levels of an atom or molecule, leading to electronic excitation. The excited state of a species can be radically different from that of its ground state; it can have more energy or a different electronic arrangement. One possible result of the electronic excitation is splitting, or photolysis, of a molecular species. If X-Y is a molecule, photolysis can be represented as follows:

$$X\text{-}Y + h\nu \rightarrow X + Y \qquad (1.1)$$

As with all chemical reactions, it is essential to know how quickly the reaction takes place. For atmospheric photolysis, the kinetics of the reaction determine the atmospheric lifetime of the constituent, X-Y, and are described by the photolysis rate coefficient, j. The photolysis rate coefficient is defined as the first order rate of reaction:

$$-d[X\text{-}Y]/dt = jX\text{-}Y \qquad (1.2)$$

where *j* is the photolysis rate coefficient or photolysis frequency of species X-Y (s^{-1})

j is often simply called the 'photolysis rate', although strictly speaking, the photolysis rate refers to the product of the photolysis rate coefficient and the concentration of the species, [X-Y]. In this text, the terms photolysis rate, photolysis frequency and photolysis rate coefficient will be used interchangeably.

Although equation 1.2 furnishes us with the definition of the photolysis frequency, it is not predictive. Equation 1.3 allows us to find the photolysis rate given certain variables.

$$j_i = \int_{\lambda min}^{\lambda max} F_{act}(\lambda, Z)\sigma_i(\lambda, T(Z))\phi_i(\lambda, T(z))d\lambda \qquad (1.3)$$

where F_{act} = solar actinic flux (4 pi times the mean ultraviolet intensity), dependent on wavelength and solar zenith angle (see section 2.6)

σ_i = absorption cross section of species i, dependent on wavelength and temperature

ϕ_i =wavelength and temperature dependent photodissociation quantum yield of the particular photolysis channel

The quantum yield gives an indication of the number of molecules undergoing the process divided by the number of photons absorbed.

1.1.1 Quantum yield of ozone

The quantum yield of ozone has been a subject of much debate, particularly in the 'tail' region (λ> 310 nm) where the quantum yield of $O(^1D)$ falls off rapidly. The literature can be divided into 2 groups: those who propose that the quantum yield to drops to zero in this spectral region and others who advocate a non-zero quantum yield. The quantum yield at these 'tail' wavelengths is of great consequence in the troposphere. Ozone absorption in the stratosphere removes much of the radiation below 300nm. Thus, any increase in the quantum yield in the spectral region above 300 nm combines with the correspondingly increased actinic flux intensity to give very significantly increased photolysis frequency (see equation 1.3).

The presence of a 'tail' on the quantum yield values was contentious over 20 years ago. Brock and Watson (1980) observed a small tail in the region, and checked carefully to ascertain it was not an experimental artefact, despite the fact that it had been observed by previous authors (e.g. Martin *et al.*, 1974). Their results were only reported to wavelengths of 325 nm and the magnitude of the tail was given as 0.12 ± 0.05 at 320nm. Silvente *et al.* (1992) used laser induced fluorescence and also found a significant tail at wavelengths of longer then 320 nm. The tail was variously explained as an experimental artefact (De More, 1992), a result of photodissociation of vibrationally excited O_3 (Brock and Watson, 1980), or a spin forbidden process (Ball *et al.,* 1992).

Despite the experimental evidence for a tail, the subsequent, often-used JPL recommended values allowed for a negligible quantum yield, <0.1 at wavelengths longer than 315 nm. It was believed that the tail was, indeed, simply an artefact (DeMore *et al.*, 1992). because it was believed that the contributions to $O(^1D)$ production from internally excited ozone and the spin-forbidden pathway could not be important at the tail wavelengths. This apparent contradiction prompted a flurry of research activity, and Ball and Hancock (1995) measured the quantum yield at 227 K and found it to be as much as 0.1 at 320nm. Further to this, Michelsen *et al.* (1994) found that the quantum yield at 298 K was between 0.2 and 0.3 in the 312-320 nm region. Shetter *et al.*(1996) presented a further set of quantum yield

data based on a critical evaluation of previous studies. Their chosen quantum yield had tail values in agreement with those of previous authors (Armerding *et al.*, 1995; Brock and Watson, 1980). The wavelength dependence, normalisation and temperature dependence of this quantum yield were all carefully considered.

During the second Mauna Loa Observatory Photochemistry Experiment (MLOPEX 2), Shetter *et al.*(1996) compared two quantum yields including tails: their newly calculated quantum yield and that that of Michelsen *et al.* (1994), with the tail-less quantum yield recommended by De More *et al.*(1994). They found that $jO(^1D)$ had a different diurnal profile depending on the quantum yield chosen. The tail region is most important at low sun when the optical path increases; the shorter wavelength photons are more likely to be absorbed. The photolysis rates containing the tail data were about 10 % and 90% greater than those without, for overhead sun and zenith angle of 78° respectively.

Absorption by ozone can be approximated by the ratio of the overhead ozone column and the cosine of the zenith angle, the 'slant ozone column'. A high slant ozone column corresponds to low sun and/or a large ozone column. Since a high slant ozone column corresponds to increased absorption of the shorter wavelength photons (by ozone), the effect of the longer wavelength tail increasing the photolysis rates would be most obvious under these conditions. The authors used their measured photolysis rates, which were independent of quantum yield, and compared those to photolysis rates calculated using the three different quantum yields. If the spectral dependence of the quantum yield is correct, the ratio of measured to modelled quantum yield against slant ozone column should be approximately constant. The quantum yields with a longer wavelength tails fulfilled this criterion and thus shown to be more appropriate for atmospheric modelling.

Ball *et al.* (1997) have further confirmed the existence of this tail using resonance-enhanced multiple photon ionisation of the fragment between 300 and 328 nm at 298 K. Further to the disagreement over its wavelength dependence, the temperature dependence of this quantum yield has also seen recent controversy with Talkudar *et al.* (1997)

suggesting that current recommendations over estimate the effect of temperature on $O(^1D)$ yields in O_3 photolysis at 308 nm.

Takahashi *et al.* (1998) use photofragment excitation spectra of $O(^1D)$ and $O(^3P)$ to determine the wavelength and temperature dependence of the $O(^1D)$ quantum yield. They confirmed that both Brock and Watson (1980) and Ball *et al.*(1992) had proposed correct mechanisms for longer wavelength production of $O(^1D)$. It was found that the photodissociation of vibrationally excited O_3 was mostly responsible for the quantum yield from 310-320 nm. Longwave of that ($\lambda > 329$ nm), the non-zero yield was caused by the spin forbidden photodissociation of ozone to $O(^1D) + O_2(X^3\Sigma_g^-)$

$$O_3 + h\nu(\lambda<411 \text{ nm}) \rightarrow O(^1D) + O_2(X^3\Sigma_g^-) \quad (1.4)$$

Bauer *et al.* (2000) have found a non-zero quantum yield as far as 375 nm, so although the presence of a tail is now firmly established, the extent and significance of this for atmospheric chemistry still must be determined. The tail, however, does not have a marked effect at low zenith angles at mid-latitudes (Monks, 1998). The quantum yield used in the $jO(^1D)$ measurements, is, therefore, that of Brock and Watson (1980).

Short wavelength (high frequency) radiation is required to induce the relatively energetic transitions required for photolysis. To facilitate further discussion, a short description of the ultraviolet region follows.

1.1.2 Ultraviolet

Ultraviolet (UV) is the portion of the electromagnetic spectrum between the X-ray and the visible. The ultraviolet makes up a small portion of the radiation incident on the Earth's atmosphere (see Table 1.1). The total contribution from the ultraviolet to the top of atmosphere flux (Wm^{-2}) is less than a sixth of that that from the largest contributor, the longer infrared wavelengths. However, its relatively high energy makes this small fraction radiation extremely important since it can induce electronic transitions in atmospheric molecules.

The UV is divided into three sub-regions. The UV-C is the shortest wavelength region and does not penetrate into the troposphere since it is absorbed by molecular oxygen (see chapter 2 for details). Radiation much shorter than 290 nm does not penetrate into the troposphere (Wayne, 1991) and so in the troposphere, only the longer UV-B wavelengths require consideration.

Table 1-1:Wavelength distribution of solar irradiance prior to attenuation by Earth's atmosphere (from Frederick *et al.*, 1989).

Wavelength region	Irradiance (W/m^2)	Percentage of total
UV-C (< 280 nm)	6.4	0.5
UV-B (280-320 nm)	21.1	1.5
UV-A (320-400 nm)	85.7	6.3
Visible(400-700 nm)	532	38.9
Infrared (>700 nm)	722	52.8

Figure 1.1 shows the significant wavelengths for the photolysis of nitrogen dioxide and ozone. The spectra are normalised by their maximum value and are representative for sea level and a temperature of 298 K. It can be seen that nitrogen dioxide photolysis occurs at longer wavelengths (UV-A and visible) than ozone photolysis. The greater area under the curve indicates the much larger values of jNO_2 ($\sim 10^{-3}$ s^{-1}) compared to $jO(^1D)$ ($\sim 10^{-6}$ s^{-1}). It should be noted that the data for ozone include a tail on the quantum yield, that of Shetter *et al.* (1996). The temperature dependence is that of Molina and Molina (1986). In the case of a smaller tail quantum yield such as that of Brock and Watson (1980), the ozone photolysis will be confined to shorter wavelengths. The nitrogen dioxide quantum yield shown here is that used in this study from Gardner (1987).

1.2 Significance of photolysis in the Earth-atmosphere system

Photolysis plays a fundamental role in atmospheric chemistry and indeed, the maintenance of life on this planet. In the stratosphere, one of the most important reactions is the photolysis of ozone which prevents harmful ultraviolet radiation reaching the Earth's surface. Stratospheric ozone, its depletion and the consequences have been a topic of much interest in the last fifteen years or so (e.g. WMO, 1985). Table 1-2 gives some examples of species that are photolysed in the atmosphere.

This study is concerned with tropospheric photolysis. About 90% of the mass of the atmosphere is found in the troposphere (Wayne & Wayne, 1999). Most of the trace gases are also found there and produced at the Earth's surface. In addition to that, the troposphere is the atmosphere that surrounds our daily lives and comprises the air we breathe.

Photolysis decomposes trace gases (e.g. ozone, HCHO, HONO) in the atmosphere and contributes to their removal from the troposphere. It also produces highly reactive species e.g. the hydroxyl radical. The hydroxyl radical is important to many areas of atmospheric chemistry: it removes trace-gases like CO, CH_4, and hydrochlorofluorocarbons (HCFCs), which influence tropospheric photochemistry, global climate change and stratospheric ozone respectively (Mueller *et al.*, 1995). Photochemistry can also be important in the tropospheric urban environment (e.g. Jacobson, 1999). Reactive organic gases, such as aldehydes and ketones, are photolysed to give radicals which contribute to the production of photochemical smog. In the troposphere, the photolysis of ozone also plays a vital role since it can produce an excited oxygen atom that reacts with OH radicals to form water vapour. This is one of the most important reactions in atmospheric chemistry.

Table 1-2: Primary dissociative processes for certain atmospheric species (from Wayne & Wayne, 1999)

Species	Products	Wavelength λ(nm)	Quantum yield
O_2	$O(^3P) + O(^3P)$	~ 245.4	
	$O(^3P) + O(^1D)$	<175.9	~1
	$O(^3P) + O(^1S)$	<134.2	
O_3	$O(^1D) + O_2(^1\Delta_g)$	<310 *	~1
	$O(^1D) + O_2(^1\Sigma_g^+)$	<266	-
	$O(^3P) + O_2(^1\Sigma_g^+)$	~600	~1
NO_2	$NO + O(^3P)$	< 400	
	$NO + O(^3P)$	228.8	
SO_2	SO + O	< 218	

The term symbol is not normally given if a species is formed in its ground electronic state; if, however, ground & electronically excited states of both product appear, then the states are specified

* indicates that this wavelength is under debate; the controversy over the spectral dependence of O_3 quantum yield is discussed in 1.1.1

Photolysis frequencies for ozone, nitrogen dioxide, HONO, formaldehyde (CH_2O), peroxy (H_2O_2), CH_3COOH, HNO_3, peroxyacetylnitrate ($CH_3CO.O_2NO_2$), CH_3NO_3, $CH_3CH_2NO_3$ and acetone can be measured during atmospheric chemistry campaigns (e.g. Kraus and Hofzumahaus, 1998).

1.3 Nitrogen dioxide and Ozone photolysis

Chemical models represent the transport and the chemical responses of atmospheric gases to perturbations in the atmosphere's composition. These models are used for tracing the transfer and evolution of pollutants, the effects of anthropogenic sulphur and NO_x, sulphur chemistry and the changing concentrations of radiatively active gases (e.g. methane). These models provide a fundamental tool in assessing man's impact on the climate.

There are two main methods of including photolysis frequencies in these models: the off-line and the on-line. In the off-line approach, look-up tables of photolysis rates under

different conditions are available. These are calculated before the model is run and contain parameterisations for different atmospheric conditions: cloud, ozone column and albedo are all considered (e.g. Krol and Van Weele, 1997). In the on-line approach, photolysis rates are calculated each time the atmospheric conditions change: for global atmospheric models this is computationally expensive. It is therefore important to have a comprehensive understanding of the response of photolysis rates to different conditions so that realistic parameterisations that reflect real atmospheric changes can be obtained.

The PhotoComp intercomparison carried out as part of the IPCC (Intergovernmental Panel on Climate Change) report found that variations in the modelled ozone concentration were primarily due to different calculated values of $jO(^1D)$ (Olson, 1997). Thomson and Stewart (1991) showed that the photodissociation rates of O_3 and NO_2 are the most critical parameters in tropospheric chemistry (Krol and Van Weele, 1997). The reasons for this will be discussed below.

1.3.1 Nitrogen dioxide photolysis

Atmospheric photodissociation of NO_2 determines the partitioning of NO_x components (NO and NO_2), the photostationary states of O_3, NO_2 and NO and the photochemical generation of tropospheric ozone. It is therefore an important quantity in photochemical air quality and atmospheric chemistry models. The photolysis of NO_2 provides the only known mechanism for the generation of ozone in the troposphere.

$$NO_2 + h\nu(\lambda=290\text{-}430\ nm) \rightarrow NO + O(^3P) \qquad (1.5)$$

Oxidation of carbon monoxide can complete this cycle:

$$O + O_2 + M \rightarrow O_3 + M \qquad (1.6)$$

$$OH + CO \rightarrow H + CO_2 \qquad (1.7)$$

$$H + O_2 + M \rightarrow HO_2 + M \qquad (1.8)$$

$$HO_2 + NO \rightarrow OH + NO_2 \qquad (1.9)$$

NET $$CO + 2O_2 + h\nu \rightarrow CO_2 + O_3 \quad (1.10)$$

This sequence only occurs in a polluted environment where NO_x is present. In a clean environment, where the mixing ratio of NO_X is small ($<3x10^{-11}$) (Wayne, 1996) ozone loss replaces ozone production.

$$HO_2 + O_3 \rightarrow OH + 2O_2 \quad (1.11)$$

$$CO + OH \rightarrow H + CO_2 \quad (1.12)$$

$$H + O_2 + M \rightarrow HO_2 + M \quad (1.13)$$

NET $$CO + O_3 \rightarrow CO_2 + O_2 \quad (1.14)$$

$j(NO_2)$ is very weakly temperature dependent between 227 and 401K (Dickerson *et al.*, 1992). Shetter *et al.* (1988) give an empirical relationship connecting the nitrogen dioxide photolysis rate to the ambient temperature.

1.3.2 Ozone photolysis

It is only in the last quarter of a century that ozone has been recognised as a reactive tropospheric constituent (Crutzen, 1999). It is now known that it is widely formed within the troposphere and not, as previously believed, simply transported from the ozone-rich stratosphere.

Although a very small portion, only ~10%, of the total atmospheric ozone is found in the troposphere, all primary initiation of oxidation chains in the natural atmosphere depends on that ozone.

The photolysis of ozone is:

$$O_3 + h\nu\ (\lambda < 330\ nm) \rightarrow O(^1D) + O_2(a^1\Delta_g) \quad (1.15)$$

$$(\lambda < 410\ nm) \rightarrow O(^3P) + O_2(X^3\Sigma^-_g) \quad (1.16)$$

Reaction 1.15 dominates with a quantum yield of approximately 0.9, compared to only 0.1 for reaction 1.16 (e.g. Ball *et al.*, 1997). This first channel is of particular interest as the resulting oxygen atom is in an excited state. After photolysis, most of the excited oxygen atoms are collisionally deactivated to ground state oxygen atoms which reform ozone via the third body recombination shown in equation 1.6. The remaining $O(^1D)$ atoms have enough energy to react with water vapour to produce OH radicals (equation 1.17). Since the water vapour is relatively scarce, a small portion of $O(^1D)$ atoms will follow this path. At Mace Head, this is about 10% of the atoms (Carslaw *et al.*, 1999). Quenching (equation 1.18) is much more likely.

$$O(^1D) + H_2O \rightarrow 2OH \qquad (1.17)$$

$$O(^1D) + M \rightarrow O + M \qquad (1.18)$$

These hydroxyl radicals are responsible for the initiation of oxidation chains. Although they are very few in number, approximately 4×10^{13} cm^{-3} at midday in mid-latitude summer, they have a huge effect, dominating the daytime chemistry of the troposphere. Their capacity to remove other trace gases by reaction means that they are sometimes referred to as "atmospheric detergents". The lifetimes of these trace gases therefore depend on the efficiency of their reaction with OH. This can range from very short lifetimes e.g. isoprene (C_5H_8) with a lifetime of only a few hours, to methane with a lifetime of about 8 years. The concentration and distribution lifetime of anthropogenic gases like methylchloroform (CH_3CCl_3) can be used to infer the global average hydroxyl concentration (e.g. Krol *et al.*, 1998).

[OH] has a linear dependence on $j(O^1D)$ in all environments studied so far (Ehhalt, 2000) Determination of the concentration of hydroxyl radicals can require exact knowledge of the photolysis frequency of ozone (e.g. Monks *et al.*, 2000). Further to this, studies of peroxy radicals have found direct correlations between the hydroxyl concentration and $jO(^1D)$ in clear air or $\sqrt{jO(^1D)}$ in polluted air (Penkett *et al.*, 1997). The first relationship is characteristic of a photochemical ozone destruction scheme and the second, net ozone production. These peroxy radical concentrations can be used to calculate instantaneous

hydroxyl radical concentrations. OH, RO_2 and HO_2 typically peak around solar noon when photolysis occurs most rapidly.

OH concentrations can also be determined directly from aircraft (e.g. Mauldin *et al.*, 1998). This method had been used with some success and extended to investigate the [OH] in and around clouds. DOAS and Laser Induced Fluorescence have also been used successfully (e.g. Hofzumahaus *et al.*, 1998). However, the concentration of OH is so highly spatially variable that these methods reveal nothing about the global picture.

The main sinks for hydroxyl radicals in the clean troposphere are CO and CH_4. Approximately 70% of the OH reacts with carbon monoxide (1.19), and remaining 30% reacts with methane (1.20). Hydroxyl reacts with other non-methane hydrocarbons (NMHCs), although this process is much more complex and can involve thousands of reactions.

$$OH + CO\ (+ O_2) \rightarrow HO_2 + CO_2 \qquad (1.19)$$

$$OH + CH_4\ (+O_2) \rightarrow CH_3O_2 + H_2O \qquad (1.20)$$

These peroxy radicals are removed from the clean atmosphere by reaction with HO_2 to form hydrogen peroxide and methylhydroperoxide respectively. This leads to their elimination from the system as they can be dissolved in cloud droplets and hence, be washed out as rain. However, if nitrogen oxides are present, these peroxy radicals suffer quite a different fate. In this case, NO is converted to NO_2, the essential ingredient for tropospheric ozone production. Further, radicals are produced that are capable of oxidising more CO and CH_4 (1.19 & 1.20) or more NO to NO_2, enabling the oxidation to continue.

$$HO_2 + NO \rightarrow OH + NO_2 \qquad (1.21)$$

$$CH_3O_2 + NO \rightarrow CH_3O + NO_2 \qquad (1.22)$$

In this way, OH is reformed and a methoxyl radical that will react with oxygen is generated.

$$CH_3O + O_2 \rightarrow HCHO + HO_2 \qquad (1.23)$$

The formaldehyde is photolysed to form two radical fragments, H and HCO. These radicals return to the HO_x chain.

Krol and van Weele (1997) show that the global OH distribution is directly coupled with the ozone photodissociation rate, reiterating that global photodissociation rates and their variations play a crucial role in the chemical feedbacks in the climate system.

1.3.3 Factors affecting photolysis rate

Any factor that influences the actinic flux, F_{act}, at photolysis wavelengths (see equation (1.3)) will, by definition, affect the photolysis rate. Solar zenith angle, surface albedo, altitude, aerosol, molecular absorption and cloud all modify the actinic flux. Factors that modulate the radiation field will be discussed in chapter 2.

The value of a photolysis rate coefficient also depends on the particular absorption cross-section and quantum yield used in its determination. These quantities are derived from laboratory measurements and are subject to significant uncertainties (see section 1.1.1 for the most striking example).

1.4 Measurements

Many measurements of photolysis rates have been reported in the literature. The observed photolysis rate is dependent on the radiation field at the site and the instrumentation used. Measurements of photolysis rates can be made on the ground or in the air on meteorological research aircraft, balloons, or even hanggliders. Photolysis rates generally increase with height (e.g. Kelley *et al.*, 1995) and it is of special interest to know their values in and above clouds (e.g. Junkermann, 1994).

Three instruments are used to measure photolysis frequencies. These are the chemical actinometer (e.g. Bahe, 1980), filterradiometer (e.g. Junkermann, 1989), and, more recently the spectroradiometer (e.g. Shetter *et al.*, 1999). Although measurements can also be made using an Eppley radiometer, its geometry makes it less suitable (see Madronich, 1987a and section 2.4). The first measurements of photodissociation constants were made with chemical actinometers (e.g. Dickerson, 1979). Chemical actinometers are complicated and delicate pieces of instrumentation that provide a direct measurement of the ambient actinic flux. A chemical actinometer consists of three main components: 1) an apparatus generating a known flow, concentration and pressure of the gas of interest, 2) a photolysis cell of known volume for exposing the gas to ambient actinic flux and 3) a method of detecting the photolysis products. This final aspect is different for the two photolysis rates of interest in this study: NO_2 can be measured directly, but $O(^1D)$ cannot. $O(^1D)$ can be measured indirectly by introducing N_2O and measuring the concentration of one of the products from its reaction from N_2O. This product could be: N_2 (e.g. Bahe *et al.*, 1979), NO_2 (e.g. Bairai *et al.*, 1992) or N_2O_5 (e.g. Blackburn *et al.*, 1992, Shetter *et al.*, 1992).

Filterradiometers (see Figure 1.2) are simpler and more robust than chemical actinometers. This makes them the instrument of choice for many field campaigns, including ACSOE at Mace Head. As will be seen, they are particularly popular on moving platforms where chemical actinometers might be difficult to operate.

Brauers *et al.* (1992) used a ship-board filterradiometer to measure the latitudinal variation of jNO_2 over the Atlantic Ocean. They estimated the error associated with these measurements to be $\pm 10\%(1\sigma)$. They checked its calibration against global irradiance and in turn the calibration of chemical actinometer with global irradiance and found good agreement. A radiometer was also used by Shetter *et al.* (1992) to measure $jO(^1D)$ at Mauna Loa. Results from this radiometer were compared to a chemical actinometer and showed that the radiometer gave lower readings for overhead sun, but higher readings

elsewhere. For the period between 1000 and 1400, the ratio of actinometer to radiometer readings was 1.1 ± 0.03. The uncertainty at the 1σ level was given as ± 15%.

Volz-Thomas *et al.* (1996) described a new design of filterradiometer to measure jNO_2 on aircraft. This modified filterradiometer design was used to measure jNO2 in this study. The main improvement, as compared to Junkermann's original instrument, is an additional downward-facing hemisphere designed to capture the larger portion of upwelling actinic flux found at the longer jNO_2 wavelengths. Uncertainties using these filterradiometers was recorded as ±8 % (Volz-Thomas *et al.*, 1996). Kraus *et al.* (1998) again measured jNO2 and $jO(^1D)$ using radiometers during the POPCORN campaign. The same filterradiometer was used recently by Frueh *et al.* (2000) in their comparison between models and measurements in a cloudy atmosphere. Once again, the filterradiometer had been calibrated using a chemical actinometer. Crawford *et al.* (1999) find a large discrepancy between their filterrradiometer and spectroradiometer data for jNO_2 of about 30%. One suggestion for this is that the radiometer was employed without a shadow ring, possibly leading to overlap of view between the two hemispheres. However, the authors state that they would expect this to only influence the result by 5-7% and the persistence of this effect with altitude leads them to doubt this overlap is the cause.

The radiometer consists of three main parts: a photosensitive device, an optical filter and an input system designed to so that there is no bias towards received light from any direction.

The photolysis frequency equation, (1.3), must be integrated over a finite wavelength interval determined by the incoming solar spectrum and the product of the quantum yield and absorption cross-section of each species.

$$J_p = f_c(T).\int_0^{\infty} S_d(\lambda).F_s(\lambda).d\lambda \qquad (1.24)$$

where f_c is the wavelength independent calibration factor (s^{-1}/V)

$S_d(\lambda)$ is the spectral sensitivity of the detector ($V/photon.cm^{-2}$)

It should be noted that f_c depends on temperature due to the temperature dependence of the quantum yield for $jO(^1D)$. This is less important for calculation of jNO_2 where the quantum yield is only weakly temperature dependent.

$$J_p = f_c(T).U_d \qquad (1.25)$$

where U_d is the electrical output of the detector

The spectral sensitivity function, $S_d(\lambda)$, must reflect the spectral behaviour of the product of the quantum yield and absorption cross-section as closely as possibly, so that the calibration factor is independent of the spectral shape of the actinic flux. Obviously, the spectral sensitivity function is unimportant in regions where there is no actinic flux since the integral will be zero. The spectral sensitivity function of the detector is matched to the product of quantum yield and absorption cross-section by using optical filters and sensors appropriate to the wavelength region of interest (Table 1.3).

Table 1-3:Components of the radiometers used in this study (from Junkermann *et al.*, 1989)

J	Wavelength (nm)	Filter	Photosensitive device
$jO(^1D)$	290-320	Interference filter	Solar blind photomultiplier
JNO_2	300-380	Coloured glass filter	UV-photodiode

In addition to correct wavelength sensitivity, it is important that the detector response is independent of the angle of incidence of the radiation since, even under clear skies, a large portion of actinic flux in the ultraviolet is diffuse scattered radiation and can reach the detector from any direction. This geometric problem is prevalent when Eppley radiometers are used to measure photolysis rates. Flat plates imply a cosine response but under cloudy conditions or at large zenith angles (Madronich, 1987), the angular distribution is not known.

Unfortunately, filterradiometers must be calibrated against an absolute reference technique (e.g. chemical actinometers). Thus, each photolysis frequency requires its own instrument. The absolute accuracy for $jO(^1D)$ is estimated at ±20% and for jNO_2 ± 15% (Reuder *et al.*, 1996, Mueller, 1994). It should also be noted that whilst both radiometers calibrated against chemical actinometers, the $jO(^1D)$ is less accurate because of a systematic error introduced by differences between the current and calibration ozone columns.

The spectroradiometer is the most recent innovation in photolysis rates measurement. Spectroradiometry was first used by Mueller *et al.*(1995) to measure $jO(^1D)$. Spectroradiometers measure actinic flux spectra thus enabling the measurement of many different photolysis rates e.g. O_3, NO_2, HCHO, CH_3CHO, H_2O_2 and HONO with just one instrument (e.g. Kraus, *et al*, 1998). The spectra are recorded with an accuracy of ± 5%, but the photolysis frequencies are still limited by the accuracy of the molecular data. Kraus *et al.* (2000) presented an intercomparison between nitrogen dioxide photolysis frequencies measured with a chemical actinometer and a spectroradiometer. They reported an excellent overall agreement, with the chemical actinometer measurements 6% above those of the spectroradiometer. Shetter *et al.* (1999) used this technique during the PEM Tropic Missions. Although the accuracy of the actinic flux measurements was only ±11.5% in the UV-B and ±8% in the UV-A, the uncertainties of the photolysis frequencies were still between ±15 and ±20% because of the uncertainties in the molecular cross-section and quantum yield data. Swartz *et al.*(1999) also used a spectroradiometer to study altitude and solar zenith profiles of $jO(^1D)$ and jNO_2 and to compare them with modelled values.

1.5 Measurements at Mace Head

Data were collected as part of the Eastern Atlantic Summer Experiment in 1996 and Eastern Atlantic Spring Experiment in 1997 (EASE96 and EASE97). The campaign formed part of the Oxidative Capacity of the Oceanic Atmosphere (OXICOA) component of the Natural Environmental Research Council (NERC) funded Atmospheric Chemistry Studies of the Oceanic Environment (ACSOE). The Mace Head Atmospheric

Observatory (53°19'35"N, 9°54'14"W) is situated on the west coast of Ireland, 60km away from Galway. In this remote location, little fresh anthropogenic pollution is experienced.

jNO_2 and $jO(^1D)$ were measured using filterradiometers situated on a 12'x12', 10m high tower near a cottage. Figure 1.3 shows their relative location. During EASE96, the jNO_2 radiometer was approximately 2.6 m from the $jO(^1D)$ radiometer. The jNO_2 radiometer was moved closer to the jO^1D radiometer in 1997. The vertical heights of the radiometers also changed slightly between the campaigns, with the jNO_2 radiometer slightly higher in 1997. Data were only considered where measurements existed for both jNO_2 and $jO(^1D)$, leading to 13 days of data in 1996 and 32 days in 1997.

The filterradiometers conformed to the description given above: the $jO(^1D)$ filterradiometer had one face and the jNO_2 filterradiometer two faces, the improvement suggested by Volz-Thomas (1996). The jNO_2 radiometer had about 40% of the downward face view including the cottage roof or scaffolding (G. McFayden, pers comm, 1997). Data were taken at a frequency of 1 Hz and using Campbell 21x loggers and averaged over 1 minute. The NO_2 cross-sections and quantum yield emulated by the radiometer were those of Davidson *et al.* (1988) and Gardener *et al.* (1987). Those emulated in the case of ozone were those of and Brock and Watson (1980).

Figure 1.4 shows some results from previous jNO_2 measurement studies. It should be noted that these were all taken with an upward-facing hemisphere (2 π steradian). The jNO_2 data from Mace Head will therefore be slightly increased compared to this, analysis shows that the bottom hemisphere (see chapter 3) contributes about 17% of the value of the top hemisphere. These clear sky data will compare approximately to the upper limit of the Mace Head data, all of which is presented here (Figure 1.6(a) and (c)). A great many of the photolysis rates are significantly lower than the (smooth) upper limit. Generally, these decreases in photolysis frequency can be attributed to cloud. Examination of Figure 1.6(a)-(d) shows that there are many of these departures and this is in keeping with the wet and cloudy weather often experienced at Mace Head. It can also be seen that there is a strong dependence of jNO_2 on solar zenith angle for all the data shown.

In Figure 1.4, at 40°, the measurements range from approximately 5 - 12 x10^{-3} s^{-1}. The lower and upper bounds are filterradiometer data from Kraus and Hofzumahaus (1998) and data from Lantz *et al.* (1996). The first set of data was taken at a continental site at sea level. Other ground based measurements shown are those of Muller and Schurath (1980), Brauers and Hofzumamhaus (1992) and Madronich *et al.* (1983). Those of Dickerson *et al.* (1982), Parrish *et al.* (1983) and Shetter *et al.* (1992) are at elevations of 1.8, 3 and 3.5 km respectively. These photolysis rates are expected to be larger than those at Mace Head because of the increase in actinic flux with altitude (see e.g. Finlayson and Finlayson-Pitts, 1986). However, those of Lantz *et al.* (1996) are much larger and the authors provided no adequate explanation for this difference.

Comparison of the EASE96, Figure 1.6(a), with these previous studies shows that the present data fall within the range of previous studies. The upper limit of jNO_2 at 40° is about 9.5 x10^{-3} s^{-1}. Considering the EASE96 data are from a 4π radiometer, it can be estimated that the data are in the range of the measurements of Muller and Schurath (1986), Brauers and Hofzumamhaus (1982) and Kraus and Hofzumahaus (1998) and are less than the parameterisations for higher altitudes, as expected. The EASE97 data, Figure 1.6 (c), follow a similar upper limit to the EASE96 data, except at low zenith angles. Here, a large number of obvious enhancements of the photolysis frequency data above clear sky are seen.

Many examples exist of flux enhancements below clouds. The magnitude and timescale of these events is not precisely known. Schafer (1996) found increases of up to 11% in the UV-B for some fractional cloud cover cases. Estupiñán (1996) found localised increases in UV-B of up to 27% over timescales less than 1 hour. Laird and Harshvardan (1997) carried out an analysis of what they called CSIR (cumulus solar irradiance reflectance) events and found that these could increase the UV irradiance below clouds and persist for up to 30 minutes. The enhancement above clear sky was larger in the UV-A than in the UV-B (10.1 and 7.8% respectively). Similar enhancements have also been observed in photolysis rates (e.g. Shetter *et al.*, 1996, Dickerson *et al.*, 1982 for $jO(^1D)$, Lantz *et al.*,

1996, Volz Thomas *et al.*, 1996 for jNO_2) Lantz *et al.*(1996) proposed a simple model for this enhancement. Their mechanism is valid for situations of optically thin cloud where the sun is not obscured by the cloud. Radiation is transmitted through the optically thin cloud and so the resulting total actinic flux is greater than under clear skies. However, this mechanism does not include scattering and reflection from the sides of clouds, which is commonly given as the cause of these enhancements.

Figure 1.5 shows the ozone photolysis rate as a function of slant ozone column, the ratio of overhead ozone column and cosine of the zenith angle. Since the ozone photolysis rate is so heavily influenced by atmospheric ozone absorption, it is necessary to use the slant ozone column rather than just the solar zenith angle to describe its shape. It can be seen that the $O(^1D)$ photolysis frequency is a largest when the sun is overhead and/or the ozone column is low. Previous measurements have values of ~ 1.7-2.2 x 10^{-5} s^{-1} for a slant ozone column of 400 DU. Kraus and Hofzumahaus (1998) used a spectroradiometer at sea level, Blackburn (1992) and Barai and Stedman (1992) used chemical actinometers at sea level. Hofzumahaus (1992) used a filterradiometer at sea level. Shetter *et al.* (1996) measurements are for 3.5 km.

Figure 1.6 (b) and (d) shows the Mace Head measurements during EASE96 and EASE97 as a function of slant ozone column. At Mace Head, at a slant ozone column of 400 DU, the values for 1996 are higher than previous measurements ~$2.7x10^{-5}$ s^{-1} (~ 14% increase). This could be a problem in the data processing – the slant ozone column is calculated using TOMS (Total Ozone Mapping Spectrometer) data. It is possible that diurnal variations in the ozone column could cause such a problem. Ozone column variations are frequently observed at mid-latitudes. This is due the variation tropopause height associated with mid-latitude weather systems.. A change in column ozone of 1% changes the ozone photolysis rate by 2% in the opposite sense (see chapter 3). A 7% decrease in the column ozone could therefore lead to a 14% increase in the photolysis rate. These high photolysis rates are observed across the range of slant ozone, but could just be caused by an incorrect ozone column used for one day.

The disagreement between previous measurements and those of this study could conceivably be caused by lower aerosol loadings than are observed at any of the other sites. However, in this case, it would also be expected that the EASE96 jNO_2 would also be increased compared to the values of Kraus and Hofzumahaus (1998), albeit less (see chapter 3). This is not seen and therefore, the most likely cause is variation from the column ozone. Additionally, the effects of aerosol are unlikely to be large enough to account for this change (see chapter 3).

During EASE97, the same cloud induced enhancements are seen as in the jNO_2 data. However, the overall agreement between the values of $jO(^1D)$ as a function of slant ozone are much better than in EASE96.

It should be noted that the jNO2 radiometer response increases more rapidly than the $jO(^1D)$ radiometer at dawn because of the very low content of near UV in the early morning red light (Penkett *et al.*, 1997). This effect is also mirrored at dusk. NO_2 photolysis, with a cut-off near 420 nm, can therefore take place soon after dawn whereas ozone photolysis with a cut-off near 320 nm increases about 2 hours later.

1.6 Summary

Photolysis is a key process in atmospheric chemistry. Accurate values of photolysis rates are required to derive the concentrations and distributions of atmospheric gases. Measurements of photolysis frequencies are a routine part of experimental campaigns like ACSOE. There are many existing measurements for different ambient conditions. In particular, due to their influence on tropospheric chemistry, nitrogen dioxide and ozone photolysis rates are very important.

Unfortunately, all methods of photolysis rate determination have their drawbacks: the chemical actinometer is large and delicate with a slow response time and the

spectroradiometer depends on inexact molecular data. For a simple and relatively method of photolysis rate determination, filterrradiometers using band pass filters are used.

Mace Head data compares reasonably with other photolysis rate data. An initial survey of the data has shown the large impact of cloud on photolysis rates measured at this location. Cloud has a very marked effect on photolysis rates and so its effect merits further investigation.

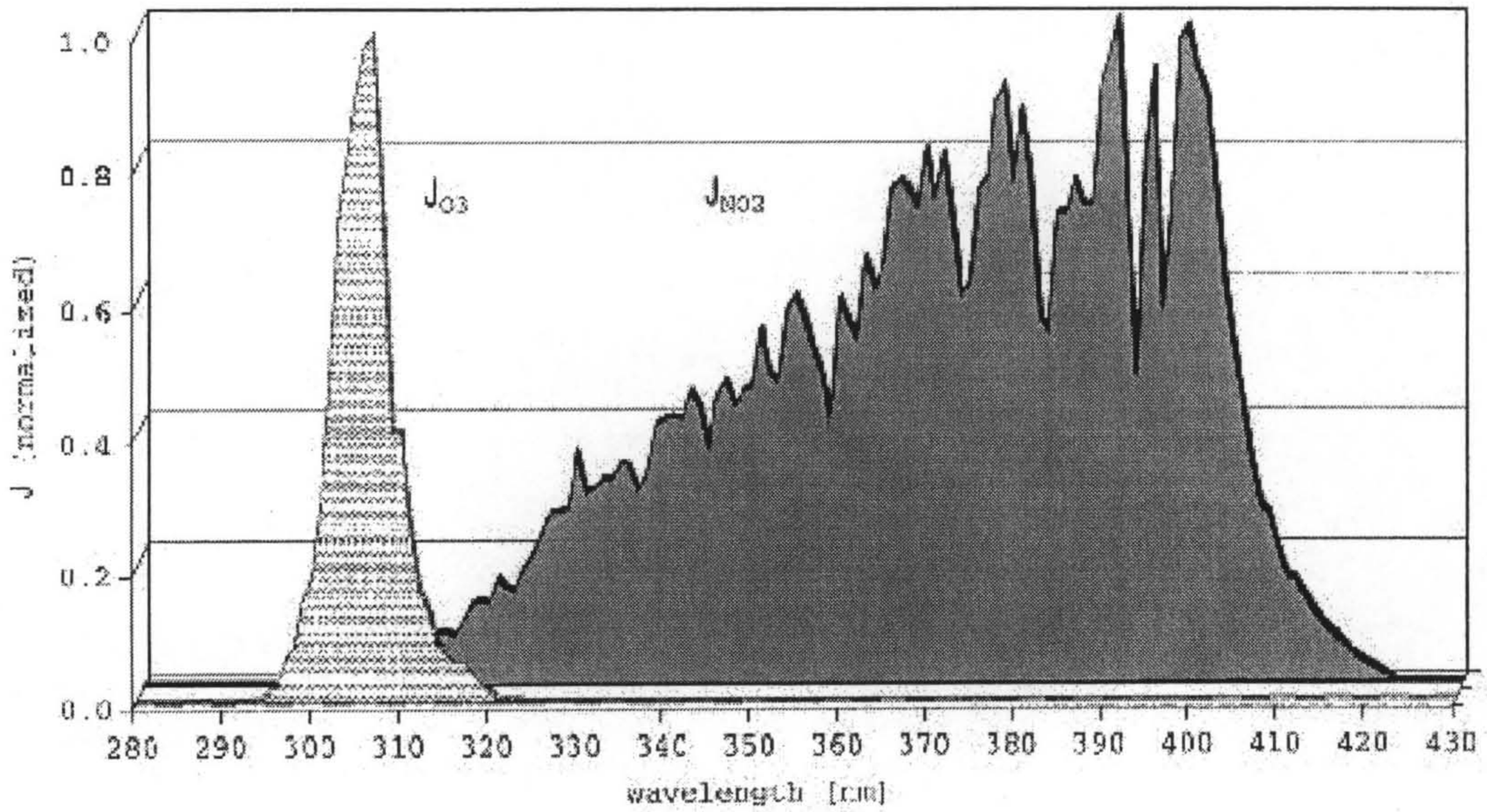
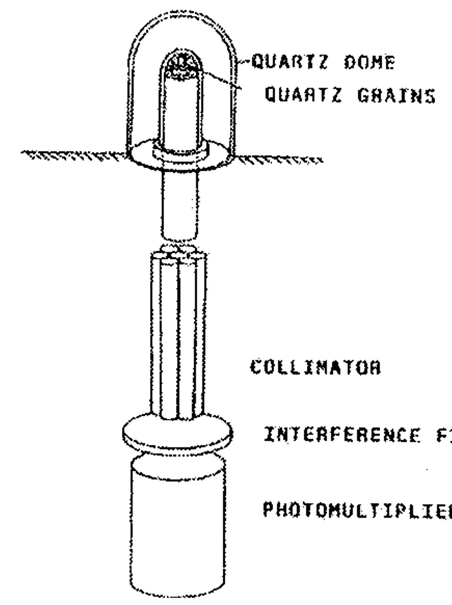


Figure 1.1: Spectral dependence of the product of absorption cross-section, quantum yield and actinic flux for the photodissociation of NO_2 and the photodissociation of $O_3 \rightarrow O(^1D)$. Data are normalised to the largest value and presented for a temperature of 298K, from Pfister (2000)



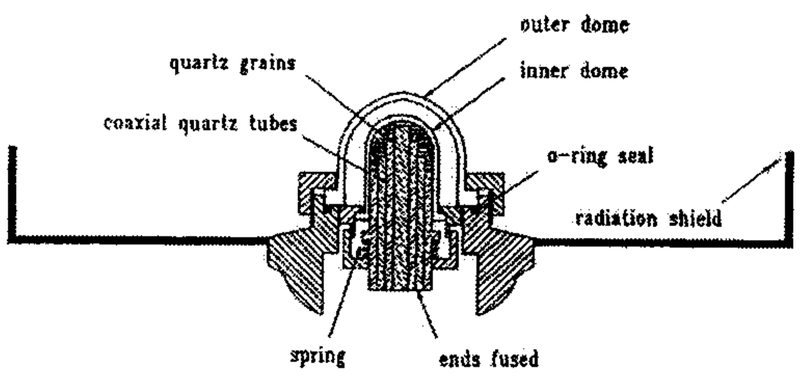


Figure 1.2: Exploded view of the jO(^{1}D) photoelectric detector (from Junkermann *et al.*,1989) Light sampling head (scattering dome) of the detector. The field of view is limited to 2π by a black radiation shield.

Figure 1.3: Position of radiometers during EASE96 and EASE97.

EASE96 ran from the 8th July until 8th August and EASE97 from the 24th April until 29th May.

(a) Top view (b) side view

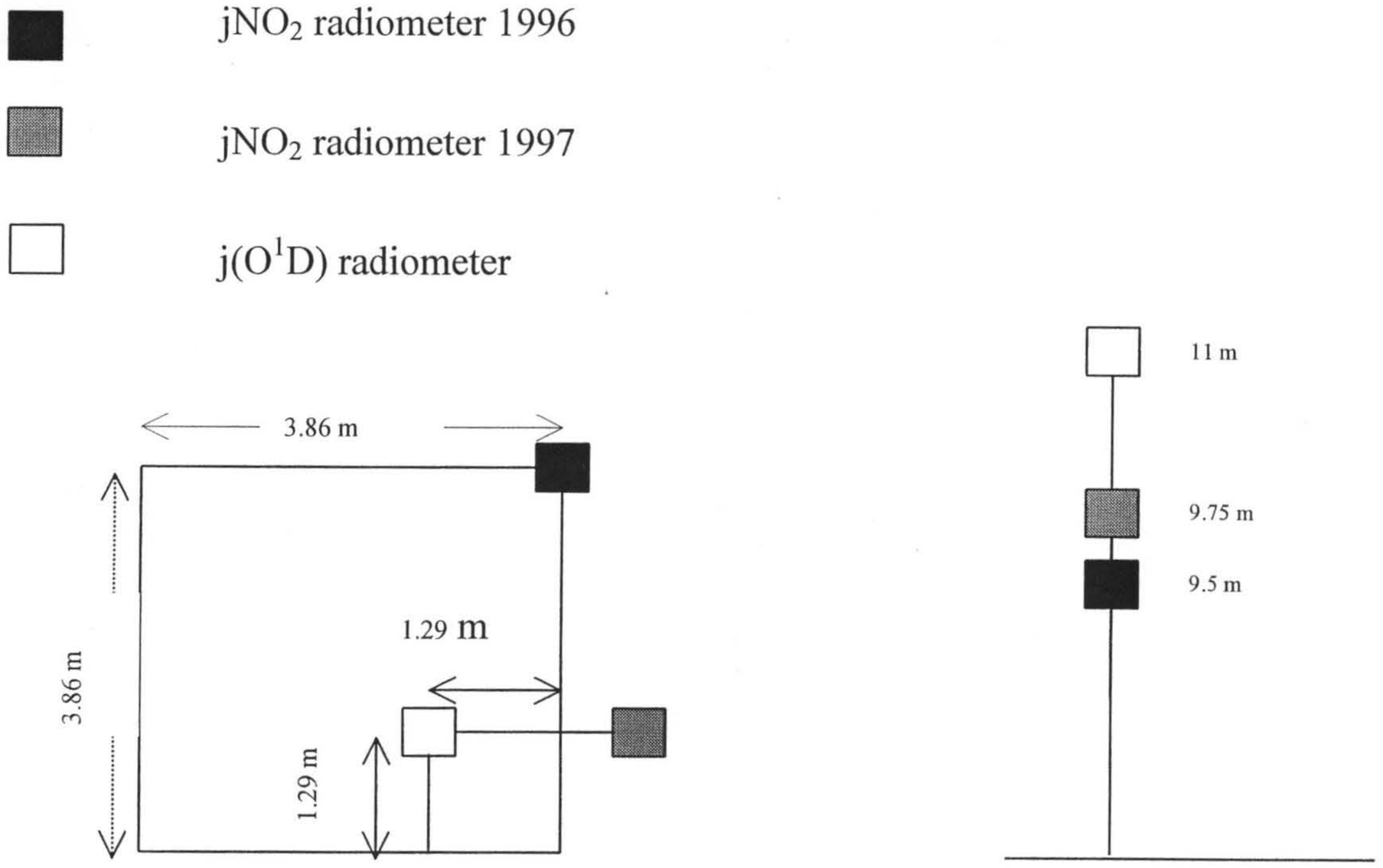
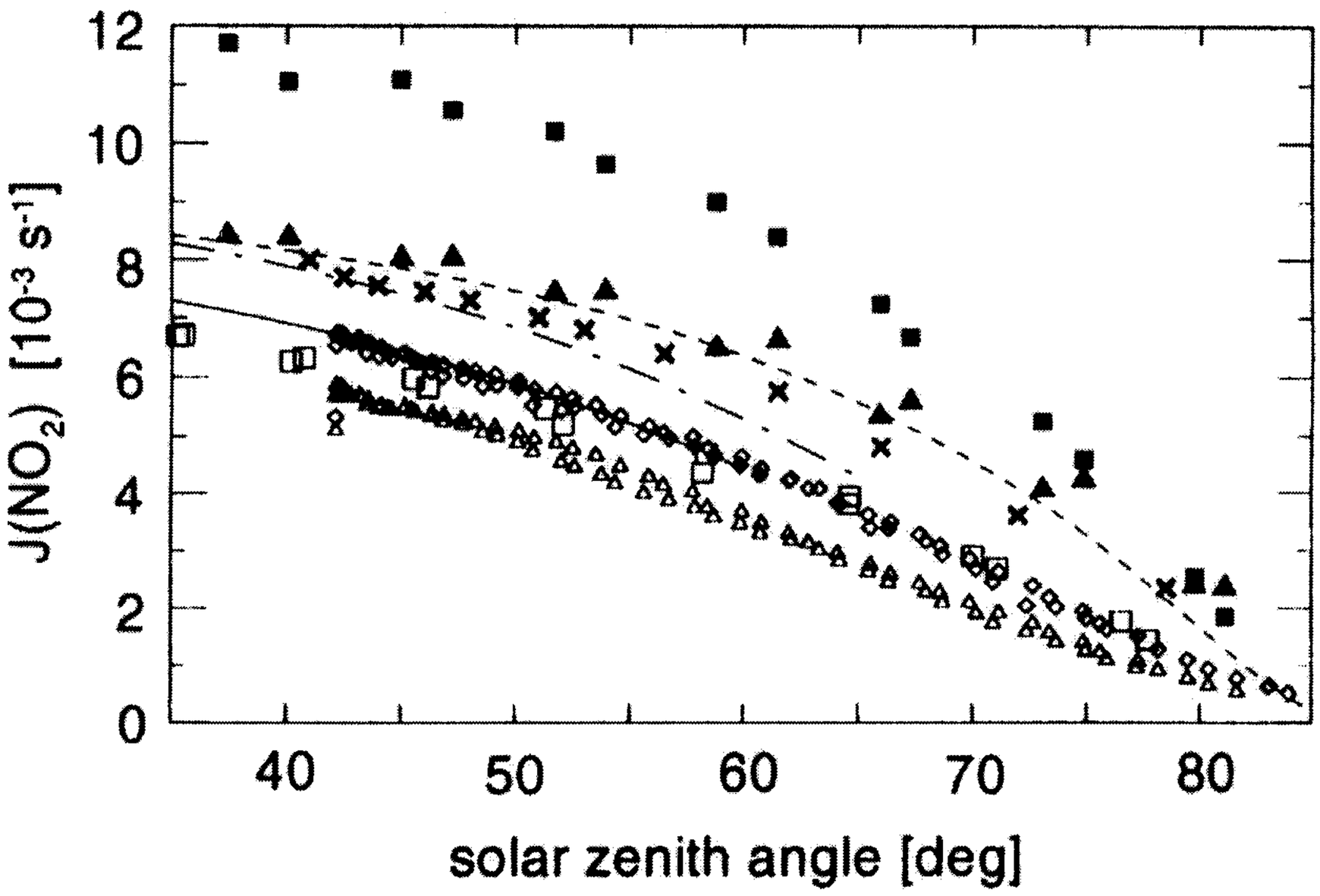


Figure 1.4: jNO_2 (2π sr) as a function of solar zenith angle for cloud-free conditions (from Kraus and Hofzumahaus, 1998). Actinic flux spectroradiometer (open diamonds), filerradiometer (open triangles) Dickerson *et al.*,1983, (long dashed line), Madronich *et al.*,1983 (crosses), Parrish *et al.*, 1983 (short dashed line), Mueller and Schurath, 1986 (solid line), Brauers and Hofzumahaus, 1992 (open squares), Shetter *et al.*, 1992 (solid triangles), Lantz *et al.*,1996 (solid squares). Lines are empirical paramterisations



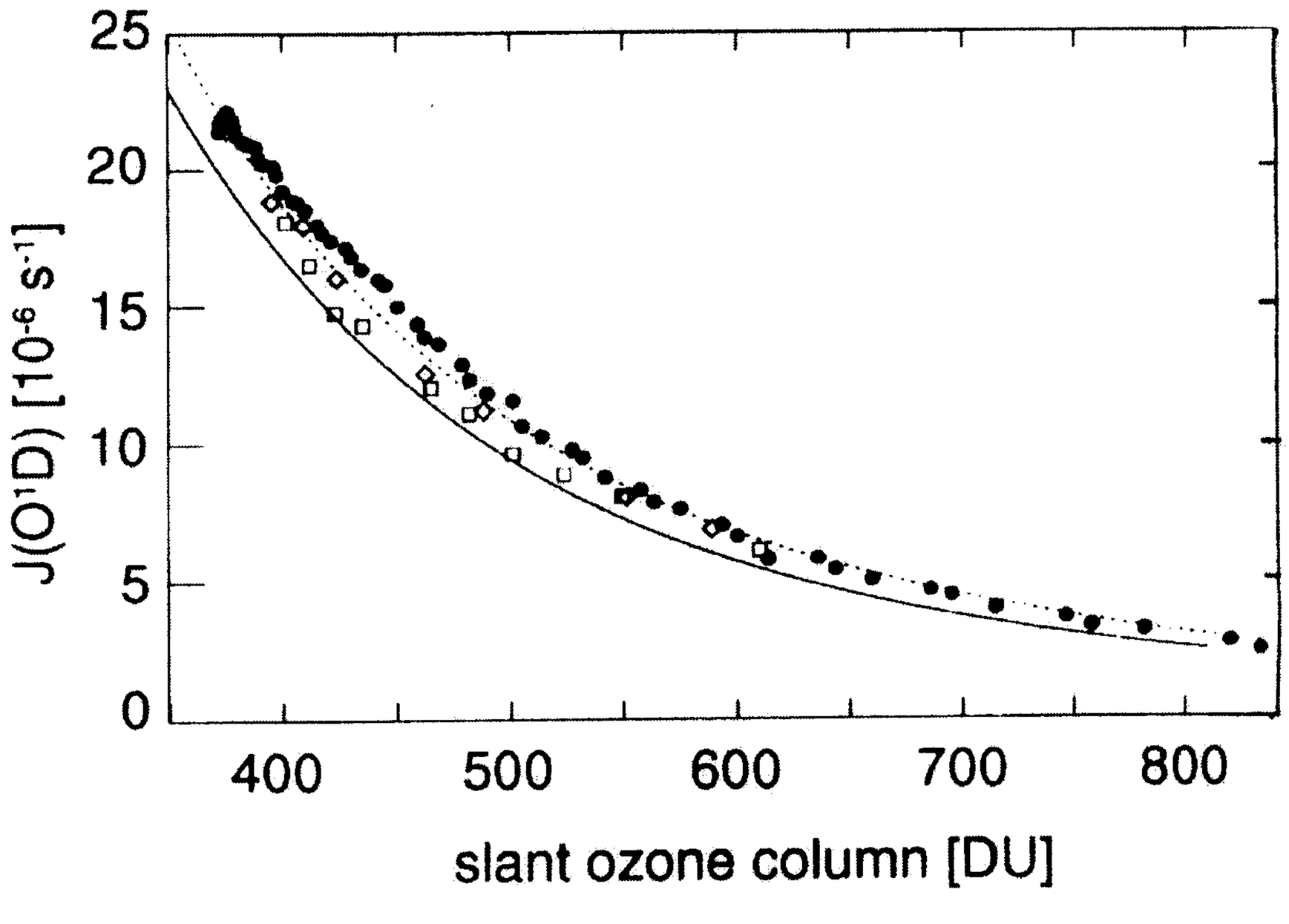


Figure 1.5: Measured jO^1D photolysis frequencies (2π sr) as a function of slant ozone column for cloud-free conditions (from Kraus and Hofzumahaus, 1998). Kraus and Hofzumahaus, 1998 (solid circles), Blackburn *et al.*, 1992 (open diamonds), Bairai and Stedman, 1992 (open squares), Hofzmahaus *et al.*, 1992 (solid line). Lines are empirical parameterisations

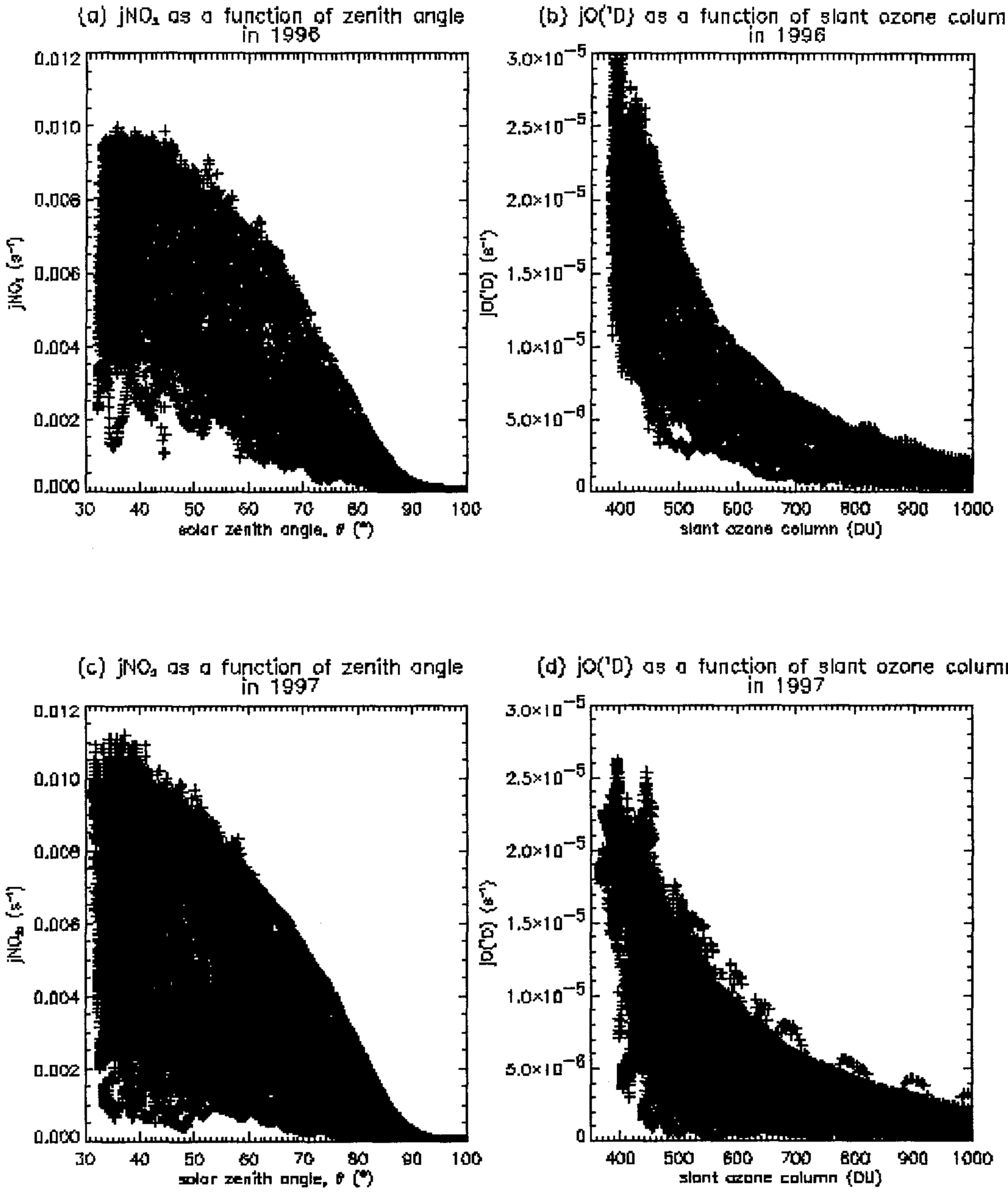


Figure 1.6 Photolysis data from Mace Head (a) jNO_2 as a function of zenith angle in 1996 (b) j $O(^1D)$ as a function of slant ozone column in 1996 (c) jNO_2 as a function of zenith angle in 1997 (d) $jO(^1D)$ as a function of slant ozone column in 1997

2. Radiative transfer and the model

This chapter outlines the processes that govern the interaction of shortwave radiation with the atmosphere. Basic radiative transfer theory is introduced and the relative importance of absorption, scattering and emission in the shortwave explained. The equation of radiative transfer is then presented and the approximations required for its solution discussed. The plane parallel approximation is defined and a pseudo-spherical correction, used in this work, described. Following this, two stream approximations are discussed. A note on the difference between actinic flux, flux and irradiance follows, stressing the importance of the former for photolysis frequency calculations.

After this introduction to the theory, the chapter continues with a discussion of the atmosphere's physical components and their description in the model used in this study. Extra-terrestrial irradiance, and oxygen, ozone and nitrogen dioxide absorption are discussed. A brief description of the representation and description of surface albedo, aerosol and cloud are given. This provides a background for chapter 3.

2.1 Introduction to radiative transfer

2.1.1 Definitions

Radiance is the flux of energy per unit time per square metre (Wm^{-2}) coming from a solid angle, Ω (steradian) where:

$$d\Omega = \frac{dA}{r^2} \tag{2.1}$$

where A is the area of the segment

and r is the distance from the origin point

Radiance is the fundamental quantity used in radiative transfer. Since the Earth is very nearly spherical, it is useful to use a spherical co-ordinate system when considering

problems involving radiances. From Figure 2.1, it can be seen that, in spherical co-ordinates:

$$d\Omega = \sin\theta d\theta d\phi \tag{2.2}$$

where θ is the zenith angle

and ϕ is the azimuthal angle.

The processes that change the intensity within this solid angle 'pencil' of radiation are the processes that must be considered in radiative transfer. In the atmosphere, there are three such processes: absorption, scattering and emission. Absorption and single scattering out of the pencil will decrease the radiation. Scattering, either from the direct solar beam or from another direction into the solid angle will increase the radiation in the pencil. Emission would also increase the radiation in the pencil.

2.2 Radiative processes

2.2.1 Absorption

Absorption is described by the Beer-Lambert[1] Law (Equation 2.3). This states that the absorption from a pencil of radiation is proportional to the mass of gas transversed by the beam in the pencil. If I_λ is the intensity in the pencil of radiation at a wavelength λ, then the change in intensity of the radiation, dI_λ is given by:

$$\frac{dI_\lambda}{I_\lambda} = -\rho\sigma_{a\lambda} ds \tag{2.3}$$

where ρ is the density of the absorbing material

$\sigma_{a\lambda}$ is the wavelength and material dependent absorption cross-section

and s is the path through the absorbing material

The absorption cross-section is the effective absorbing area of the mass of material. Integrating this equation along the path of the radiation we obtain (2.4)

[1] Also known as Beer's Law or the Beer-Lambert-Bouger Law

$$I_{\lambda s}(s) = I_{\lambda}(0)\exp\left(-\int_0^s \rho\sigma_{a\lambda}\,ds\right) \qquad (2.4)$$

The integral relates to the attenuation of the initial radiation intensity after it has traversed a distance, s. This quantity is known as the (absorption) optical depth, τ.

$$\tau = \int_0^s \rho\sigma_{a\lambda}\,ds \qquad (2.5)$$

In the atmosphere, where vertical co-ordinates are those of interest, this relationship can be rewritten in terms of the height, z.

$$I_{\lambda}(z) = I_{\lambda}(\infty)\exp\left(-\int_{\infty}^s \rho\sigma_{a\lambda}\sec\theta\,dz\right) \qquad (2.6)$$

where $I_\lambda(\infty)$ is the intensity at the top of the atmosphere

and θ is the solar zenith angle

It can be seen that the absorption optical depth depends on the height, the density of the medium, its absorption cross-section and the solar zenith angle.

2.2.2 Scattering

Scattering refers to the extraction and subsequent reemission of radiation by matter, that is, the redirection of radiance without the loss of energy. This occurs when the oscillating electric field interacts with scattering particles. In the terrestrial atmosphere, scattering particles cover a large range of sizes, from molecules (4×10^{-10}m) to cloud droplets ($\sim 10^{-4}$m) (e.g. Liou, 1992)

In the atmosphere, there are two important elastic scattering regimes, in which the wavelength of the scattered light is the same as the incident beam. These are: Rayleigh scattering and Mie scattering. The scattering regime is determined by the ratio of the size

of the scattering particle and the wavelength of the incident radiation, the 'size parameter', x^2. If the wavelength is much larger than the particle size ($x << 1$), we can approximate the scattering of the radiation as Rayleigh scattering. If the size of the particle is approximately equal to the wavelength of the radiation, the radiation will be Mie scattered. At even greater particle sizes ($x > 100$), the radiation will be geometrically scattered - this is the phenomenon responsible for rainbows in the visible region of the spectrum.

Rayleigh scattering occurs when solar radiation interacts with the molecules in the atmosphere. The magnitude of the scattering is very heavily dependent on the wavelength of the radiation (2.7) and indeed, this is why the sky is blue when the sun is high in the sky. (Shorter wavelength blue light is scattered approximately five times more than red light).

Analagous to the absorption cross-section, $\sigma_{a\lambda}$, the scattering cross-section, $\sigma_{s\lambda}$ describes the fractional area removed from a pencil of radiation through scattering.

The Rayleigh scattering cross-section for the molecules in the air, σ_R is given by:

$$\sigma_R = \frac{32\pi^3}{3N_0\lambda^4\rho_0}(n-1)^2 \qquad (2.7)$$

where N_0 is the number of molecules per unit volume

ρ_0 is the density of the air

and n the real part of the refractive index of air

The inverse relationship with the fourth power of wavelength means that Rayleigh scattering is important at the short wavelengths of the ultraviolet and is, therefore, a very important process when considering the high energy photons that cause photodissociation.

For larger particles (e.g. cloud droplets and aerosol), the much more complex Mie theory is used to describe the scattering (for a discussion, see Liou, 1992). In fact, because of the short wavelength in the ultraviolet, geometrical scattering approximations are sometimes

---

[2] $x = 2\pi r/\lambda$

used to describe the interaction between cloud particles and radiation in this spectral region.

As discussed above, although scattering causes radiation to leave the pencil in one direction (single scattering), it can also cause it to be reintroduced to the beam from a different direction (multiple scattering). Scattering, therefore, causes an angular redistribution, rather than a simple decrease or increase in the intensity of the radiation.

To describe scattering, two terms are required: (1) a term to describe how much radiation is removed at a single scattering event and (2) a term to describe the directionality of the scattering. The first term is the single scattering albedo, ω. This represents the scattering fraction of the total extinction.

$$\omega_\lambda = \frac{\sigma_{s\lambda}}{\sigma_\lambda} \tag{2.8}$$

where $\sigma_{s\lambda}$ is the scattering absorption cross-section, as defined above

and σ_λ is the extinction cross-section (the sum of the scattering and absorption cross-sections)

The single scattering albedo depends on the absorbing properties of the medium and the wavelength considered e.g. for water droplets at 550 nm, scattering is almost conservative, with ω=0.9999, whereas for ice crystals in the IR at 10 μm ω is about 0.44.

The angular redistribution of scattered radiation is described by the phase function, which gives the fraction of radiation scattered by an individual particle from direction ϕ to direction ϕ'. The angle between ϕ and ϕ' is defined as the scattering angle, Θ. The phase function is normalised so that its integral over all solid angles is unity.

$$\frac{1}{4\pi}\int_{4\pi} P(\Theta)d\Omega = 1 \tag{2.9}$$

In two stream models (see 2.4.2), the phase function is characterised by the asymmetry parameter, g. The asymmetry parameter gives the fraction of forward scattered radiation. The asymmetry parameter is the sum of the cosines of the scattering angles (the angle between the direct incoming and outgoing radiant fluxes, ϕ and ϕ') weighted by the phase function:

$$g = \frac{1}{4\pi}\int_{4\pi} P(\Theta)\cos\Theta d\Omega \qquad (2.10)$$

The asymmetry parameter increases as the forward scatter increases, $\Theta < 90°$. Values for g for different scattering regimes are given below:

g > 0.5 Mie scattering

=0 isotropic or Rayleigh scattering

<0.5 backward scattering

Multiple scattering occurs when scattered photon undergoes further scattering. The significance of atmospheric multiple scattering can be illustrated by the high albedos of cloud in the visible - although the probability of backscatter from a single scattering event is low, after many scattering events it is increasingly probable that the photon will leave the cloud in the backward direction.

2.2.2.1 A note on optical depth

It should be noted that the use of the term 'optical depth' can lead to ambiguity. In this work, the term optical depth refers to the extinction optical depth. This relates to the total radiation extinguished from the beam, whether absorbed or scattered.

$$\tau = k_{ext}\Delta z \qquad (2.11)$$

where k_{ext} is the extinction coefficient, which is obtained by integrating the absorption and scattering cross-sections for all interacting particles over the size distribution

and Δz is the layer thickness

The different effects of absorption and scattering can be illustrated by considering two clouds of equal optical depth, but composed of material with different absorption

properties. The first cloud is made of an absorbing material e.g. soot. The second cloud is made of a non-absorbing material e.g. water at a visible or ultraviolet wavelength. Although the extinction optical depth of each cloud is the same, the number of photons underneath the clouds will be very different. Very few photons will escape from the base of the soot cloud. However, a substantial number of the photons that are multiply scattered by the cloud droplets will still emerge from the cloud base. Optical depth, therefore, quantifies both scattering and absorption.

2.2.3 Emission

Emission of radiation by matter is described by the Planck function. Since atmospheric temperatures are unlikely to exceed 320 K, the emission at the ultraviolet wavelengths considered here is negligible. This is illustrated in Figure 2.2, which shows the Planck function calculated for some different atmospheric temperatures. Atmospheric emission does not, therefore need to be considered as a contribution to radiance in the shortwave.

2.3 The Equation of Radiative Transfer

The change in intensity, dI, of radiation for a beam traversing a distance, ds, can be written:

$$\frac{dI}{\sigma_{ext}\rho ds} = -I + J \qquad (2.12)$$

where σ_{ext} is the mass extinction cross section

ρ is the material density

I is the intensity of radiation

and J is the radiation source function

The properties of the material are described by the mass extinction cross-section: the sum of the mass scattering cross-section and the mass absorption cross-section.

The radiation at a point in the atmosphere will be the sum of processes that increase the radiation intensity minus the sum of processes that decrease the radiation intensity. In the atmosphere, the height, z, is used as a measure of distance. The radiative transfer equation can be re-written in terms of optical depth as:

$$\mu \frac{\partial I_\lambda}{\partial \tau_\lambda} = I_\lambda(\tau_\lambda, \mu) - J_\lambda(\tau_\lambda, \mu) \qquad (2.13)$$

where I the cosine of the zenith angle (see Figure 2.1)

and τ_λ is the atmospheric extinction optical depth

At solar wavelengths, the source is purely external (i.e. the Sun) and the source function consists of a contribution from the attenuated direct solar beam and a contribution from scattered radiation.

$$J(\tau, \mu, \phi) = \frac{\omega}{4\pi} \int_0^{2\pi} \int_{-1}^{1} I(\tau, \mu, '\phi') P(\mu, \phi; \mu', \phi') d\mu' d\phi' \qquad + \frac{\omega}{4\pi} F_s P(\mu, \phi; -\mu_0, \phi_0) \exp(-\frac{\tau}{\mu_o}) \quad (2.14)$$

where P is the scattering phase function

ω is the single scattering albedo

F_s is the solar source function (top of atmosphere flux)

μ_0 is the cosine of the zenith angle of the solar beam

2.3.1 Plane parallel approximation

The atmospheric composition changes much more rapidly in the vertical direction than it does in the horizontal direction. The vertical changes are, therefore, those of primary importance to the modeller. With this in mind, radiative transfer calculations are often simplified by invoking the plane-parallel approximation. The plane parallel approximation ignores the curvature of the Earth. The atmosphere is regarded as horizontally homogeneous and the radiation field horizontally isotropic (Salby, 1996).

Although widely used and accepted in the atmospheric community, it is becoming clear that there are problems with this approximation, particularly when it is used to model clouds. Clouds and are not usually spatially horizontally homogeneous so result in

inhomogenities in the horizontal radiation field. A particular example of this is 'photon leakage' from the sides of 3-D clouds (e.g. Titov, 1997)

Another problem occurs at low sun angles, where the curvature of the Earth becomes important. In this model, a pseudo-spherical correction is included to increase accuracy in these cases (Dahlback and Stamnes, 1991). The radiative transfer equation is solved for a spherical shell, and the so-called 'Chapman' function replaces the simple attenuation factor for a plane parallel beam. The Chapman function is the sum over the layers of product of the optical depth and relative path through the layer, which is the ratio of the slant path through the layer to the height of the layer. The relative path can then be evaluated using simple geometric considerations as described by Dahlback and Stamnes (1991).

Dahlback and Stamnes (1991) compared a model containing this correction to one assuming a plane-parallel atmosphere in a Rayleigh scattering atmosphere at wavelengths of 300nm and 400 nm. At solar zenith angles of less than 83°, the diffuse component of the surface irradiances differed by less than 2% between the models. However, at higher zenith angles, the plane-parallel approximation led to large errors. At a zenith angle of 87°, the error had amplified to 40%.

2.4 A solution for the equation of radiative transfer

Radiant flux is the integral of the radiance, or intensity, weighted by the cosine of the zenith angle over a hemisphere of 2π steradian:

$$F = \int_{2\pi} I \cos\theta d\Omega \tag{2.15}$$

The radiant flux, F, can then be separated into two components, the upward and downward components. The monochromatic upward(+) and downward(-) fluxes at each optical depth level, τ, are given by:

$$F_{dif}^{\pm}(\tau) = 2\pi \int_{0}^{\pm 1} I(\tau,\mu)\mu d\mu \tag{2.16}$$

The direct downward solar flux is given by:

$$F_{dir}^{-}(\tau) = \mu_o F_s \exp\left(-\frac{\tau}{\mu_0}\right) \tag{2.17}$$

The upward and downward radiant fluxes may be written in terms of the height co-ordinate:

$$F^{+}(z) = \int_0^{\infty} F_{dif}^{+}(\tau)d\lambda \tag{2.18}$$

$$F^{-}(z) = \int_0^{\infty} (F_{dif}^{-} + F_{dir}^{-})d\lambda \tag{2.19}$$

The net radiant flux is therefore:

$$F = F^{-}(z) - F^{+}(z) \tag{2.20}$$

2.4.1 Two stream approximation

The two stream approximation simply considers the radiant flux in two directions, upward and downward. This differs from more complex models where the radiant flux can be considered over a number of different directions. Using the radiative transfer equation and the expressions for upward and downward diffuse fluxes, the solution to the radiative transfer equation can be rewritten:

$$\frac{1}{2\pi}\frac{dF^{+}}{d\tau} = \int_0^1 I(\tau,\mu)d\mu - \frac{\omega}{2}\int_0^1\int_{-1}^1 I(\tau,\mu')P(\mu,\mu')d\mu' d\mu - \frac{\omega}{4\pi}F_s \exp(-\frac{\tau}{\mu})\int_0^1 P(\mu,-\mu_0)d\mu \tag{2.21}$$

$$\frac{1}{2\pi}\frac{dF^{-}}{d\tau} = -\int_0^1 I(\tau,-\mu)d\mu + \frac{\omega}{2}\int_0^1\int_{-1}^1 I(\tau,\mu')P(-\mu,\mu')d\mu' d\mu + \frac{\omega}{4\pi}F_s \exp(-\frac{\tau}{\mu})\int_0^1 P(-\mu,-\mu_0)d\mu \tag{2.22}$$

The solution consists of approximating the flux so that it is related to the solar flux.

The two stream equation is solved for each layer, n. The generalised two stream equation in the shortwave can be expressed as:

$$\frac{\partial F_n^{+}}{\partial \tau_n} = \gamma_{1n}F_n^{+} - \gamma_{2n}F_n^{-} - \gamma_3\omega\ F_s \exp(-\frac{\tau}{\mu_0}) \tag{2.23}$$

$$\frac{\partial F_n^{-}}{\partial \tau_n} = \gamma_{2n}F_n^{+} - \gamma_{1n}F_n^{-} + (1-\gamma_3)\omega\ F_s \exp(-\frac{\tau}{\mu_0}) \tag{2.24}$$

where $\gamma_{1,2,3}$ are coefficients specific to the two stream approximation and the subscript n refers to the layer

The two stream approximation does not refer to one single approximation, but rather to a family of numerical methods used to solve the equation of radiative transfer. These include the delta-Eddington approximation, quadrature, hemispheric mean and discrete ordinates methods. The prefix 'delta' refers to the inclusion of a delta-Dirac function in the radiative transfer method. This is used to improve the representation of scattering and is particularly important in the shortwave where the wavelength of light is small compared to the size of atmospheric particulates e.g. aerosols and cloud water droplets. This results in much more forward than backward scattering – scattering anisotropy. In this case the scattering is taken as proportional to the square of the asymmetry parameter (Zeng *et al.*, 1996).

Table 2.1 shows some examples of the different gamma coefficients used in the solution of two stream approximations. The significance of μ_1 term will be discussed in the next section.

Table 2-1: Examples of gamma coefficients used in different 2 stream approximations (adapted from Toon *et al.*, 1989 and Meador and Weaver, 1980)

Method	γ_1	γ_2	γ_3	μ_1
Eddington[1]	$[7-\omega(4+3g)]/4$	$-[1-\omega(4+3g)]/4$	$(2-3g\mu_0)/4$	½
Quadrature[2]	$(3)^{1/2}[2-\omega(1+g)]/2$	$\omega(3)^{1/2}-\omega(1-g)]/2$	$[1-(3)^{1/2}g\mu_0]/4$	$1/(3)^{1/2}$
Hemispheric mean[3]	$2-\omega(1+g)$	$\omega(1-g)$	…	½
Delta function[6]	$[(1-\omega(1-\beta_0]/\mu_0$	$[\omega\beta_0]/\mu$	β_0	μ_o
PIFM[4]	$[8-\omega(5+3g)]/4$	$3\omega(1-g)/4$	$(2-3g\mu_0)/4$	½
Delta Discrete Ordinate[5]	$[(3)^{1/2}(2-\omega(1+g))]/2$	$[(3)^{1/2}(\omega(1+g))]/2$	$[1-(3)^{1/2}g\mu_0]/2$	$1/(3)^{1/2}$

[1]Joseph *et al.*(1976),[2]Liou (1973),[3] Toon (1989),[4] Zdunvonski (1980),[5] Schaller (1979).[6]Meador, and Weaver (1980)

2.5 A note on actinic flux and flux

During the discussion of radiative transfer, the solution has been discussed in terms of the flux, F. However, this is not the quantity required in photolysis frequency calculations.

In this case, the actinic flux, F_{act}, is required, where

$$F_{act} = \int_{\Omega} I d\Omega \tag{2.25}$$

Great care must be taken when calculating photolysis rates. Actinic flux is not equal to flux (Madronich, 1987), despite the quantities having the same units. Flux is the energy flow through a flat, usually horizontal surface where the radiance (photon $cm^{-2}s^{-1}nm^{-1}$) is weighted by the cosine of the angle of incidence to the surface. To cause a photochemical reaction, a photon can approach a molecule from any direction so the relevant radiative quantity is therefore the 'actinic' or 'spherical' flux, which is the integral of the radiance over all directions (4π steradian) without a cosine factor. The appropriate factor for the calculation of photolysis is the mean diffusive intensity, since the actinic flux is simply 4π times the mean diffusive intensity.

$$J = \frac{1}{4\pi}\int I d\Omega = \frac{(F^{+} - F^{-})}{4\pi\mu_1} \tag{2.26}$$

so

$$F_{act} = \frac{F^{+} - F^{-}}{\mu_1} \tag{2.27}$$

Approximating the angular dependence of the intensity so that this integral can be approximated is central to the derivation of the two stream approximation. The parameter, μ_1 is a constant, such as 0.5, or $(3)^{-1/2}$ (see Table 2.1), depending on the chosen two stream approximation (e.g. Meador and Weaver, 1980, Toon *et al.*, 1989). μ_1 is sometimes called a 'diffusivity factor' as will be seen below.

A slightly different aspect of the same problem is described below. When the radiant flux is incident on a surface it is called 'irradiance'. Irradiance measurements are sometimes used to calculate actinic flux, although this is not altogether satisfactory (e.g. Cotte *et al.*, 1997). There is a problem transforming irradiance measurements into actinic flux

measurements. Like the irradiance, the actinic flux, F_{act}, consists of a direct and diffuse component:

$$F_{act}(\lambda,z) = F_{act,dir}(\lambda,z) + F_{act,diff}(\lambda,z) \quad (2.28)$$

The direct term, F_{dir}, refers to the direct actinic flux from the solar beam and is essential unidirectional. The integration of this term is trivial; this term is the attenuated solar radiance. The direct irradiance is simply converted to the direct part of the actinic flux by dividing by the cosine of the solar zenith angle.

The second term, F_{diff}, is the diffuse component of the actinic flux. The diffuse radiance is caused by atmospheric and surface scattering and becomes the dominant component when cloud is present. In the presence of cloud, the contribution of the direct flux becomes negligible, so the problem of obtaining the actinic flux is especially important in cloudy atmospheres. The problem in converting diffuse irradiance to diffuse actinic flux is non-trivial (e.g. Ruggaber *et al.*, 1993). The ratio of diffuse spectral irradiance to diffuse spectral actinic flux is called the diffusivity ratio, r_d. This quantity depends on height and atmospheric conditions. There are a number of different values, usually ranging from 0.5 to 1.0. The diffuse ratio represents the distribution of the diffuse ratio over the angle of incidence: a diffuse ratio of 0.5 describes an isotropic distribution of the diffuse radiance and a diffuse ratio of 1.0 describes collimated light from a solar zenith angle of 0. It can be seen that the approximation of the integral by a constant factor is the same as using a diffusivity ratio to transform the diffuse irradiance into diffuse actinic flux since it assumes a distribution of the flux over the angle of incidence.

Two stream methods are not especially suitable for vertical studies of actinic flux e.g. the delta-Eddington approximation is known to underestimate the actinic flux in the mid-troposphere with errors of 5-20% (Lantz *et al.*, 1996). This is because the distribution of the flux changes with height, so approximation of the integral in (2.21) is no longer suitable (e.g. Volz Thomas *et al.*, 1996). However, the estimation of the actinic flux at the surface is reasonably accurate (e.g. Volz Thomas *et al.*, 1996).

The consequent increase in computational time for an n-stream model (e.g. DISORT, Stamnes (1988)) justifies using a two-stream model for studies such as this. This is particularly true when the inaccurate spectral data of the molecules means that the error associated with calculation of photolysis rates is already potentially large.

2.6 The atmosphere and its description by the Tropospheric Ultraviolet Visible Model

This section outlines important atmospheric mechanisms and processes that influence shortwave radiation and their treatment the model. TUV (Tropospheric Ultraviolet and Visible Radiation model) is a one-dimensional radiative transfer model specifically designed to calculate photolysis rate coefficients. The structure of TUV is given is Appendix A. Calculations are for a plane parallel atmosphere with a pseudo-spherical approximation. It offers a choice of two stream methods and calculates the actinic flux by approximating the integral of the radiant flux over the solid angle (see 2.26). To approximate a real, vertically changing atmosphere, the atmosphere is split into multiple horizontal layers and the radiative transfer equation is solved for these layers. Using the approximations described above, the radiative transfer equation can be solved for a single homogeneous layer. The necessary quantities, g, ω and τ, are provided for each layer. The application of boundary conditions to these layers gives a matrix, later converted to a tridiagonal matrix and finally inverted to provide the radiant fluxes through the atmosphere (see Toon *et al.* (1989) for details).

These radiant fluxes are transformed into actinic fluxes. Photolysis rates are calculated by multiplying the actinic fluxes over the appropriate spectral range by the reaction-specific spectrally dependent weighting function (the product of the absorption cross-section and the quantum yield). These weighting functions are also altitude dependent due to their dependence on temperature and pressure.

For realistic flux calculations, the model must adequately describe atmospheric conditions. The atmospheric flux at the top of the atmosphere and the complex absorption spectra of

atmospherically significant gases must be suitably parameterised. In our context, the value of incident solar radiation and absorption by oxygen, ozone and nitrogen dioxide are relevant. The concentrations of some other atmospheric gases are shown for comparison. Additionally, the scattering by clouds and aerosol is important. The next section aims to provide an introduction to these problems and shows their treatment in the model. The treatment of surface albedo is also discussed.

2.6.1 Incident solar radiation

The radiation incident on the top of the atmosphere is variable on a number of time scales. The number of photons incident on the top of the atmosphere changes with the Earth-Sun distance and with in the output from the Sun itself. The Earth has an elliptical orbit around the sun and so the Earth-Sun distance changes with the time of year, closest in January. The model calculates the Earth-Sun distance from the Julian day.

Variations in solar output are associated with the Sun's 27-day rotation on its axis, and on 11-year magnetic solar cycles associated with sunspots (e.g. Lean, 1991). The variability in the near-ultraviolet, visible and infrared is thought to be a few tenths of a percent, but the changes in the shorter wavelength ultraviolet are much greater.

For this study, a representative solar spectrum is used. The top of the atmosphere fluxes are taken from two different sources. At wavelengths less than 350 nm, high resolution (0.15nm) data are taken from the SUSIM (Solar Ultraviolet Spectral Irradiance Monitor) instrument on board Spacelab 2 (SL2). At longer wavelengths the data is taken from Neckel *et al.*(1984).

2.6.2 Oxygen

Oxygen absorbs high energy ultraviolet ($\lambda < 290$ nm) in the upper atmosphere. The oxygen absorption cross-section is complicated (see Figure 2.3) and contains three main features: the Schumann-Runge continuum, Schumann-Runge bands and the Herzberg continuum.

Higher energy photons produce excitation at shorter wavelengths, which do not penetrate deep into the atmosphere (e.g. Salby, 1996). Thus, the Schumann-Runge continuum absorption ($\lambda < 175$ nm) takes place in the thermosphere (above 85 km). Here absorption at these wavelengths causes oxygen to be dissociated into two-oxygen atoms, one electronically excited. Below this, until about 60 km, the Schumann-Runge bands (175-200nm) dominate. This results in the molecular oxygen becoming vibrationally excited. These excited states are unstable and dissociate to form two ground state oxygen atoms. Each of the vibrational bands in the Schumann-Runge system consists of many rotational lines. This highly structured system has proved difficult to characterise (e.g. Goody and Yung, 1989). Maximum solar energy absorption in the Schumann-Runge system occurs at altitudes of 80-110 km.

The Herzberg continuum (200-242 nm) dominates altitudes below 60 km, since at this altitude all of the shorter wavelength photons have been removed. In this region, the O_2 is dissociated into two ground state oxygen atoms. Although the transitions are weak at these wavelengths, the higher solar intensities mean that these transitions are more atmospherically important than the Schumann-Runge system.

In the model, oxygen absorption cross sections from 116 – 204nm (including Schumann-Runge bands) are from Brasseur and Solomon (1996), whereas for the Herzberg continuum (204-241 nm) the values are from the 1994 JPL recommendations (De More, 1994). The effective oxygen cross-section depends on solar zenith angle, so the effective oxygen absorption in the Schumann-Runge bands is updated in the model at every timestep.

2.6.3 Ozone

Ozone is the only atmospheric constituent that effectively absorbs radiation in the UV-B (λ=280-320 nm), thus protecting the biosphere from exposure to harmful radiation.

The distribution of ozone varies with latitude, season and altitude (see e.g. WMO, 1985 for details). Ozone is usually discussed in terms of tropospheric and stratospheric ozone.

It is estimated that tropospheric ozone (about 10% of total column ozone) in the Northern hemisphere has doubled, from 25 to 50 ppbv, since pre-Industrial times (IPCC, 1994). Ozone concentrations are also highly variable on short timescales.

The absorption cross-section of ozone is complicated because ozone is a tri-atomic molecule. The absorption cross-section of ozone is shown in Figure 2.4. Absorption can be divided into three main regions: the Hartley bands, the Huggins bands and the Chappuis bands. The Hartley bands dominate the absorption of solar radiation by ozone. These have a weak structure imposed on a very strong continuum. At 255.3 nm, the maximum absorption cross-section is 1.15×10^{-17} cm^{-3}. Absorption by these bands is responsible for the 'actinic cut-off' at 290 nm.

The Huggins bands lie on the longwave (300-360 nm) wing of the spectrum. These appear in the low sun spectrum and were first responsible for the identification of ozone in the atmosphere. The Huggins bands are made up of a spectrum of diffuse lines unlike the continuous Chappuis and Hartley bands. At 350-450 nm, ozone is transparent to solar radiation. The Chappuis bands absorb at 450-750 nm. This is important at altitudes below 25 km. This is the spectral region of maximum solar emission, so the amount of radiation absorbed can be significant, leading to rapid photodissociation of ozone in sunlight.

The cross-sections are slightly temperature dependent (< 1%) in the 226-298 K range but the temperature dependence becomes more important above 275 nm. Ozone absorption cross-sections are taken from the 1985 WMO Assessment (174.5 – 847.5 nm) except for the Hartley and Huggins bands (185-300nm) where temperature dependence is calculated based on Molina and Molina (1986).

There are no in-situ balloon measurements available to describe the ozone profile at Mace Head. The profile used is the default profile for the US standard atmosphere (1976). This can be scaled to a required total column ozone. The total column is available from TOMS satellite data (Total Ozone Mapping Spectrometer) on a daily basis.

2.6.4 Nitrogen dioxide

The nitrogen dioxide column increases with latitude and varies with season. In summer, when the column is greatest, at high latitudes it can be three times that at the equator. Due to its variation with latitude, there is evidence that large-scale air motions can alter the [NO_2] by a factor of 2 in a few days. (WMO, 1985). The absorption spectrum of NO_2 is given in Figure 2.5. It should be noted that NO_2 absorbs in the O_3 window between the Huggins and Chappuis bands.

The absorption cross-section used in the model is that used by NCAR (National Center for Atmospheric Research, Colorado). These are the temperature dependent measurements from Davidson *et al.*(1988) from 256.8 to 648.8 nm at approximately 0.5 nm intervals. In the model, the profile of nitrogen dioxide is user defined. An altitude profile of number density can be introduced as required.

2.6.5 Sulphur dioxide and other absorbing gases

There are many other atmospheric gases capable of absorbing radiation in the ultraviolet. Table 2.2 shows their absorption cross-sections, volume mixing ratios and optical depths. It can be seen that other gases are much less abundant than NO_2 or O_3 with smaller optical depths in the spectral region of interest.

The only other gas with a comparable absorption cross-section to NO_2 or O_3 is sulphur dioxide. This, however, is less abundant, especially in unpolluted areas. Due to its potential effect on the ultraviolet flux in regions of high SO_2 emission, the model includes the facility to include a user defined sulphur dioxide profile. This facility was not used in the Mace Head simulation, since Mace Head is considered an unpolluted environment. The sulphur dioxide absorption cross-section is taken from McGee and Burris (1986).

Table 2-2: Absorption cross sections, typical volume mixing ratios and optical depths of various atmospheric gases from Forster (1994), adapted from Wayne (1991)

Gas	VMR	σ_λ (10^{-20} cm^{-2})				optical depth 280 nm	Optical depth 400 nm
		280 nm	300 nm	350 nm	400 nm		
O_3	10^{-6}	500	100	0.0001	0.0	50.0	0.0
NO_2	10^{-8}	5.0	10	40	50	$5x10^{-3}$	$5x10^{-2}$
SO_2	10^{-9}	100	100	0	0	$1x10^{-2}$	0.0
CH_2O	10^{-9}	1.0	1.0	9.0	0.0	$1x10^{-4}$	0.0
N_2O_5	10^{-9}	10	1.0	0.1	0.01	$1x10^{-4}$	$1x10^{-6}$
$ClONO_2$	10^{-10}	20.0	8.0	0.1	0.0	$2x10^{-3}$	0.0
HO_2NO_2	10^{-10}	5.0	1.5	0.0	0.0	$5x10^{-4}$	0.0
$BrONO_2$	10^{-11}	20.0	8.0	8.0	0.0	$2x10^{-4}$	0.0
HOCl	10^{-11}	5.0	5.0	1.0	0.1	$5x10^{-5}$	$1x10^{-6}$

2.6.6 Rayleigh scattering

The surface pressure determines the total Rayleigh scattering in the atmosphere and most of the Rayleigh scattering occurs in the lowest 10km where the density of the air is greatest. At sea level the surface pressure fluctuates by typically 40 mb from a mean pressure of 1013 mb. The variability at Mace Head falls within this range, e.g. the range is between 991 and 1035 mb in 1996.

The US Standard Atmosphere (1976) forms the basis of model atmosphere providing the temperature profile, the air mass profile and the ozone profile (all are given in 1km intervals form 0 to 50 km). Rayleigh cross sections and depths are from WMO (1985). The amount of Rayleigh scattering can be changed by scaling the air mass profile to a different surface pressure.

2.6.7 Surface Albedo

The surface albedo is the ratio of reflected and incident fluxes at the surface level. Measurements show that the albedo in the UV-B is significantly different from that for the total solar radiation (0.3-3.0 μm) (e.g. Blumthaler and Ambach, 1988). In general the albedo is much lower in the UV-B e.g. for grassland the UV-B albedo is 1.3% compared to the total solar albedo of 20.7%. The albedo for snow-free surfaces ranges from 0.01 to 0.15. The model treats the surface as Lambertian i.e. the reflected light is isotropic and independent of direction of incidence. This assumption is true in most cases e.g. radiation reflected from buildings, white rocks. However, radiation form some surfaces (e.g. the sea) at high zenith angles is specular i.e. the angle of incidence is equal to that of reflection. Suitable values for albedo are discussed in chapter 3.

2.6.8 Aerosol

Tropospheric aerosols come from many sources and are distributed through the atmosphere by turbulence and transport of air masses. Aerosols can be of anthropogenic or natural origin (e.g. sea salt, volcanic emissions). Most anthropogenic aerosols have relatively short lifetimes in the troposphere (~ 1 week) (e.g. Harshadvan, 1993). Although this lifetime is small compared to anthropogenic gases, the radiative effect of aerosols in the shortwave is significant (1-2 Wm^{-2}). However, it is important to realise that this forcing is still small compared to the effect of cloud - a change of global cloud cover of only 1-2% would have an effect of a similar magnitude.

In the ultraviolet and the visible spectral regions, the aerosol extinction is dominated by scattering. Typical absorption efficiencies are less than 10% (Krokotov *et al.*, 1998). In polluted areas, where aerosols contain soot or black carbon, their absorption efficiency increases substantially.

Reuder *et al.* (1999) studied the sensitivity of UV radiation to aerosol using models and measurements. Their modelling studies showed that the relevant quantities were aerosol optical depth and single scattering albedo. These are the primary quantities for determining the change in radiation quantities and up to 80% of the calculated change can

be attributed to these two factors. The phase function, spectral extinction and extinction profile were much less important in modifying the radiation field. This is in agreement with previous work (e.g. Ruggaber, 1994).

The relative humidity is also an important factor in considering aerosols since it controls aerosol growth. Observations show that high aerosol optical depth values tend to decrease during the day because the warming effect of the sunlight decreases the relative humidity of the atmosphere (e.g. Finlayson and Finlayson-Pitts, 1986). Gas-to-particle conversion, local advection and air mass changes also affect aerosol concentrations. However, in a simplistic 1-D model it is sufficient to describe the aerosol profile, single scattering albedo and asymmetry parameter.

The aerosol profile used in the model is that of Eltermann (1968). This is commonly used in models (e.g. Shetter *et al.*, 1992). Additionally, the aerosol optical depth is assumed vary inversely with wavelength, so that the largest aerosol optical depths are found at the lowest wavelengths. The aerosol optical depth is assumed to be 0.38 at 340 nm. The values of ω and g are 0.99 and 0.61 respectively.

2.6.9 Cloud

Clouds generally cover about half of the Earth's surface and contribute to approximately half of the global albedo (Salby, 1996). Tables 2.3 and 2.4 give an idea of the breadth of coverage of clouds over the globe and the occurrence of different cloud types. Cloud coverage is greater over the oceans than over land.

Clouds can interact with both longwave and shortwave radiation. There are many different types of cloud, whose properties and coverage are controlled by many different physical processes (e.g. tropical convection, orographic convection, ascent near frontal zones and vertical mixing) (see e.g. Wallace and Hobbs, 1977 for a detailed description) The effect of clouds on the Earth's radiation budget is complicated and depends on the height and type of the cloud (see e.g. IPCC, 1994 for discussion).

Table 2-3: Reports of the Most Common Cloud types over Oceans (from Heymsfield, 1996)

Type of cloud	Frequency of occurrence (%)	Area covered over ocean(%)
Stratus (St) and Stratocumulus (Sc)	45	34
Cumulus (Cu)	33	12
Cumulonimbus (Cb)	10	6
Nimbostratus, Ns	6	6
Altostratus (As) and Altocumulus (Ac)	46	22
Cirrus (Ci), Cirrostratus (Cs) and Cirrocumulus (Cc)	37	13
Global average over oceans		64.8

Table 2-4: Reports of the Most Common Cloud types over land (from Heymsfield, 1996)

Type of cloud	Frequency of occurrence(%)	Area covered over land(%)
Stratus (St) and Stratocumulus (Sc)	27	18
Cumulus (Cu)	14	5
Cumulonimbus (Cb)	7	4
Nimbostratus, Ns	6	5
Altostratus (As) and Altocumulus (Ac)	35	21
Cirrus (Ci), Cirrostratus (Cs) and Cirrocumulus (Cc)	47	23
Global average over land		52.4

Cloud modelling is one of the greatest challenges facing atmospheric physics today. In this study, we are concerned with the effect of cloud in the shortwave. Representation of a cloud in any model necessitates some degree of simplification of its structure. There are two complicating factors: the structure of the cloud itself and the distribution of cloud across the sky.

Observations (e.g. Tessier, 1993) have shown the liquid water distribution can be described as multifractal since it is distributed by coupling with the turbulent wind field. The 3-D cloud morphology is difficult to model (e.g. O'Hirok, 1998) and the further complication of modelling the radiation distribution under broken cloud fields (e.g. Trautmann, 2000) is resource-hungry. In such cases, Monte Carlo models use statistical techniques to simulate the physical processes within the cloudy layer. A large number of photons are tracked through the clouds and an ensemble average picture of the radiation field can be built up. Such techniques can be used to simulate the variable cloud width and a cloud optical depth, which is dependent on cloud cover (e.g. Kite, 1987)

2.6.9.1 Anomalous absorption in a cloudy atmosphere

Further to the problems described above, another problem has been associated with cloud modelling. Initially believed to be a near infrared phenomenon, with increasing numbers of observations, its influence has gradually been extended to increasingly lower wavelength regions. 'Enhanced' or 'anomalous' absorption refers to a difference between modelled and measured irradiances in the presence of cloud. In the solar spectral region, measurements of cloud absorption are consistently higher than expected from model predictions.

This phenomenon has been a topic of heated discussion, particularly over the last 5 years. A summary of the literature (see Table 2.5) shows there is considerable disagreement within the scientific community, not only over a possible mechanism for enhanced absorption, but also over the very existence of anomalous absorption itself. A significant (although unspecified) anomalous absorption in the UV has also been reported although this was in the case for polluted boundary layer clouds (Wendisch, 1999). Solomon *et al.* (1999) attributed extra absorption in the visible to increased concentrations of nitrogen dioxide in deep convective clouds.

There are a number of proposed mechanisms for possible anomalous absorption. These include water vapour absorption, aerosol absorption, cloud inhomogenities and cloud edge effects (see e.g. Stephens *et al.*, 1997 for a comprehensive review). Further suggestions include: black carbon in clouds (Chylek *et al.*, 1996), O_2 continuum absorption not included in models (Mucray *et al.*, 1997), water vapour continuum (Arking *et al.*, 1999) or water vapour clusters in clear and cloudy skies (Chylek and Gelhart, 1997). Some advocates of anomalous absorption propose that a combination of these effects could be responsible (e.g. S. Dobbie, pers. comm., 2000).

However, researchers are still in strong disagreement. Even very recent papers (e.g. Asano, 2000) suggest there is no absorption anomaly in the solar region. Some absorption was found in the near infrared and this could be attributed to water vapour absorption. Wendisch *et al.* (1999) found anomalous absorption in the solar region of 37 Wm^{-2}, in broad agreement with the value found by Cess *et al.*(1995) of 25 Wm^{-2}.

Table 2-5: A summary of some papers on anomalous absorption published since 1995 (from Wendisch, 1999)

Paper	Approach	Enhanced Cloud Absorption	Explanations/ Discussions
Cess *et al.* (1995)	satellite & surface irradiances, GCM	✓	increased water vapour continuum, absorption in cloudy case; aerosol absorption
Ramanathan *et al.* (1995)	measurements of oceanic heat transport	✓	interstitial water vapour absorption
Pilewsie and Valero (1995)	two collocated aircraft	✓	cloud morphology, "water-like problems"
Li *et al.* (1995)	Four year global solar irradiance data (satellite and ground-based)	✓ Tropics ✗ Mid-latitudes and poles	absorbing aerosols produced by seasonal biomass burning; uncertainties in measured /modelled solar irradiances
Hayasaka *et al.*(1995)	collocated aircraft and Monte Carlo simulations	✗	horizontal cloud inhomogenities
Cess *et al.* (1996)	satellite, surface and aircraft measurements	✓	interstitial water vapour
Arking *et al.*(1996)	satellite and surface irradiances, GCM	✗	partial cloud cover problems
Arking (1996)	satellite and surface irradiances, GCM	✗	enhanced clear-sky absorption, mainly due to water vapour, independent of clouds
Taylor *et al.*(1996)	aircraft measurements and radiative transfer calculations	✗	horizontal cloud inhomogenities
Stephens (1996)	analysis of inconsistencies of recent papers	✗	undersampling due to cloud edge effects
Valero *et al* (1997)	collocated aircraft	✓	no enhanced absorption in clear sky
Francis *et al.* (1997)	aircraft measurements	✗	water-vapour absorption in visible and near IR
Zhang *et al.* (1997)	satellite and surface irradiances, GCM	✓	inconsistencies with earlier studies

In this modelling study, clouds are approximated as uniform, horizontally infinite slabs. The cloud is given a specified optical depth, τ, a user specified single scattering albedo and asymmetry parameter. The assumption of horizontal homogeneity is less unreasonable for stratiform clouds than cumuliform clouds, which are detached and dense. Referring back to tables 2.3 and 2.4, it can be seen that cumulus and cumulonimbus clouds are 21% of the recorded clouds over land and 43% over the ocean. In a particular environment, the values will differ from the global average. However, the plane parallel approximation is widely used and currently accepted within the atmospheric community.

In real water clouds, the optical depth of the cloud at a particular wavelength is a function of the liquid water content and the effective radius of the water droplets (2.29). Real water clouds are characterised by their droplet size distribution as well as their liquid water content (Stephens, 1978) .

$$\tau_{cloud} = \frac{3}{2}\frac{lwp}{\rho_l r_{eff}} \qquad (2.29)$$

where ρ_l is the density of liquid water

lwp is the liquid water path, which is the vertically integrated water content

and r_{eff} is the effective radius of the water droplets

Droplets in the range 1-40 μm are believed to be the main contributors to optical thickness. The actual cloud albedo is a function of the cloud optical depth. It is generally assumed that scattering by clouds is independent of wavelength in the UV-A and UV-B (e.g. Frederick *et al.*, 1989)

2.7 Summary

Radiative transfer calculations invoke a number of approximations to describe the atmosphere. In this study a two stream approximation is used in a plane parallel atmosphere, with a pseudo-spherical correction available for high zenith angles. The model solves the radiative transfer equation for 50, 1 km layers which mimic the gas and aerosol concentrations in the atmosphere. Special attention is given to the absorption continua of oxygen, ozone and nitrogen dioxide. Ozone and nitrogen dioxide are especially important, since the photolysis rates of these gases are the focus of this study.

Clouds are represented as plane parallel, horizontally homogeneous and described by their single scattering albedo, asymmetry parameter and optical depth. Sensitivity of the model to different atmospheric and surface conditions will be shown in the next chapter.

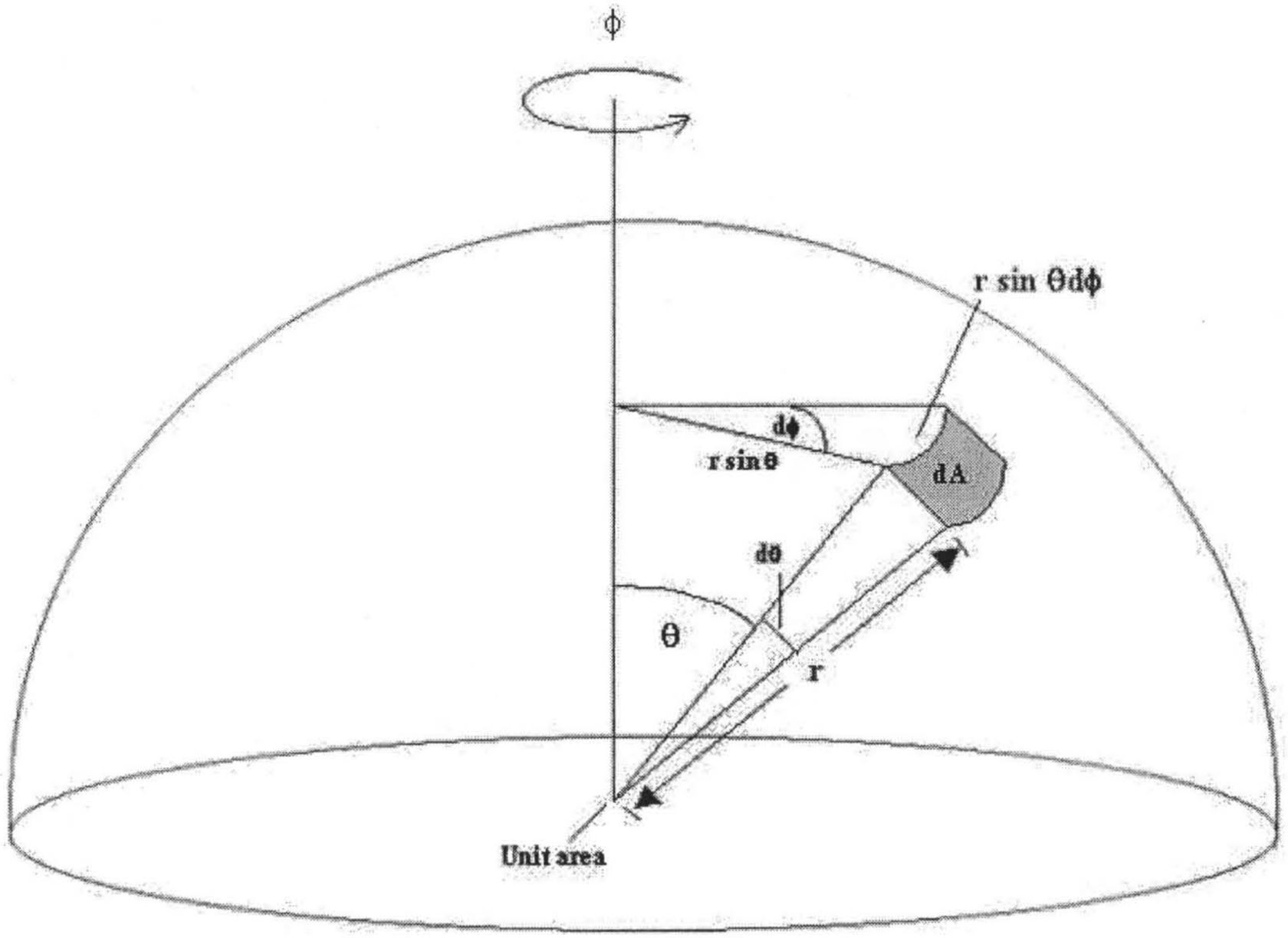


Figure 2.1: A schematic showing spherical co-ordinates used to describe a pencil of radiation.

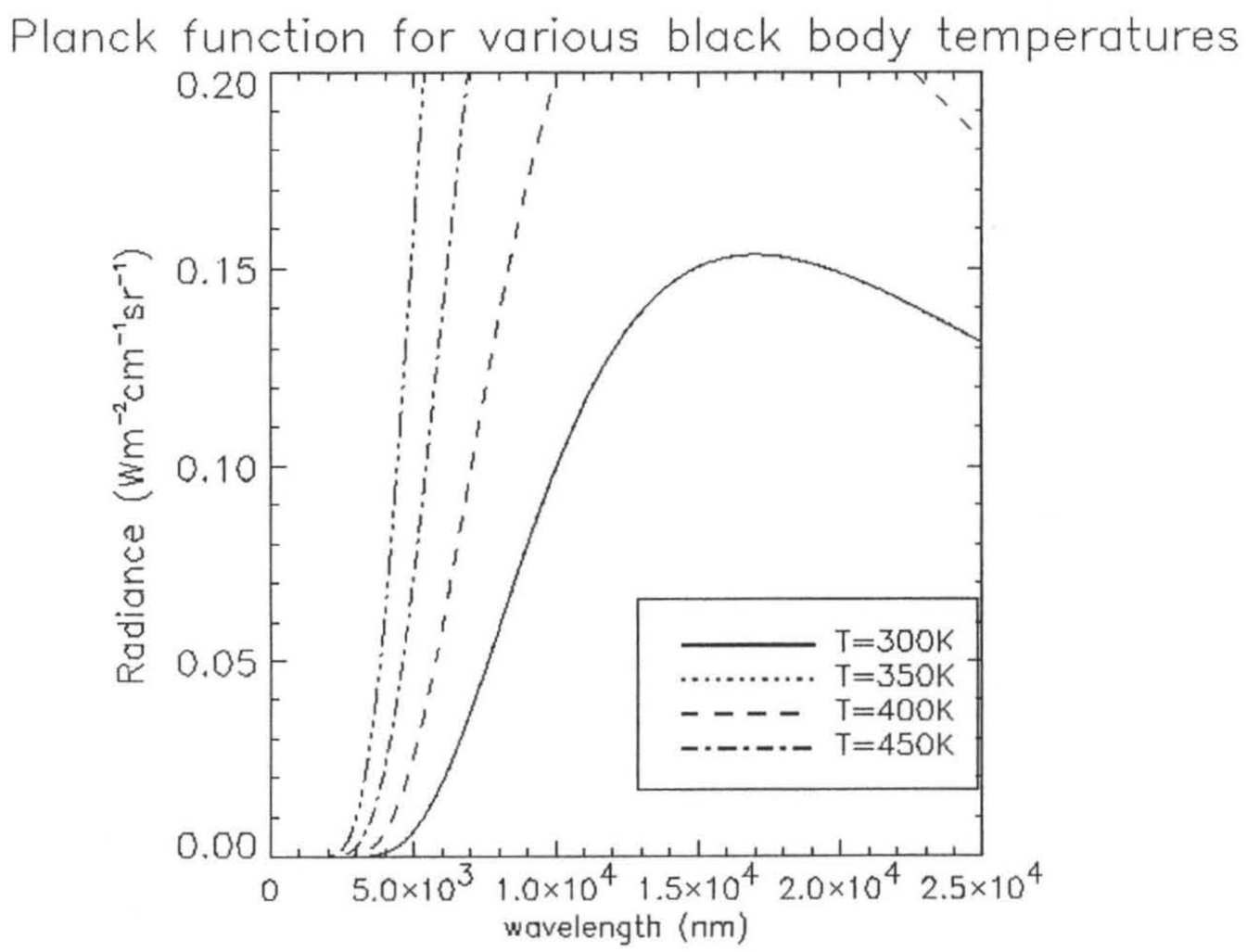


Figure 2.2: The Planck function at atmospheric temperatures and photolysis wavelengths

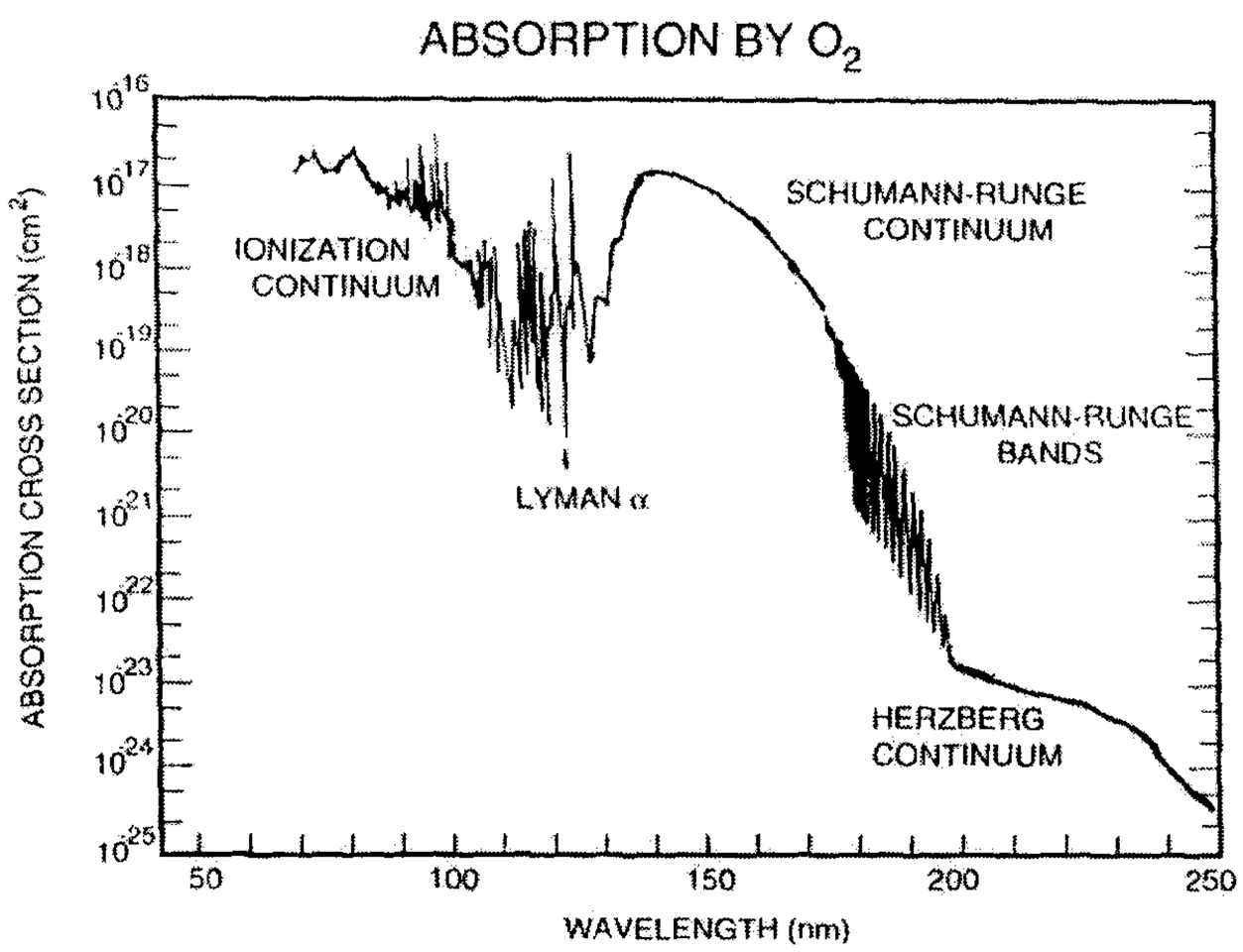


Figure 2.3: Absorption cross section as a function of wavelength for molecular oxygen, from Salby, 1996 (after Brasseur and Soloman, 1986)

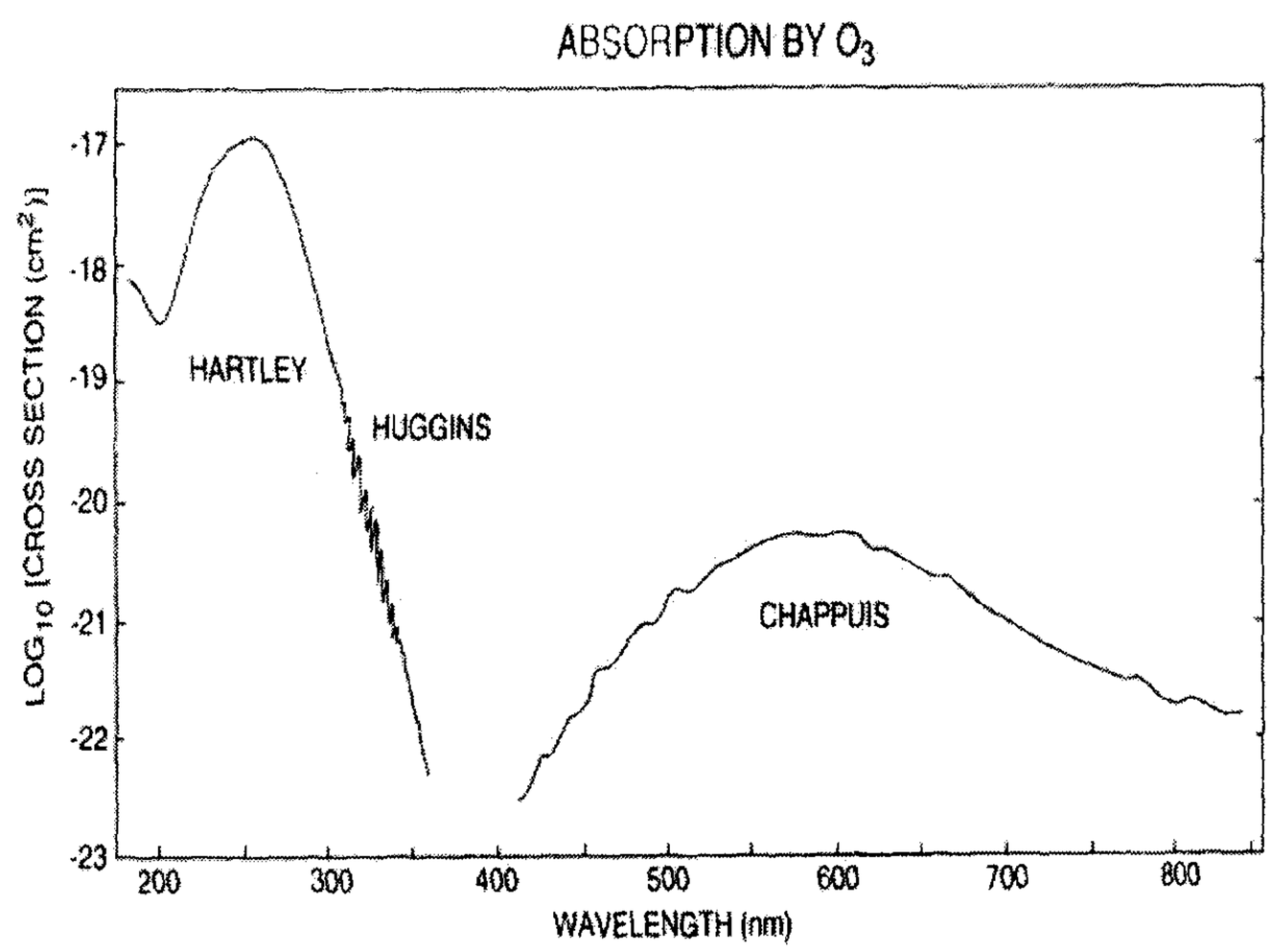


Figure 2.4: Absorption cross section as a function of wavelength for ozone, from Salby 1996 (after Andrews, 1987 and WMO, 1996)

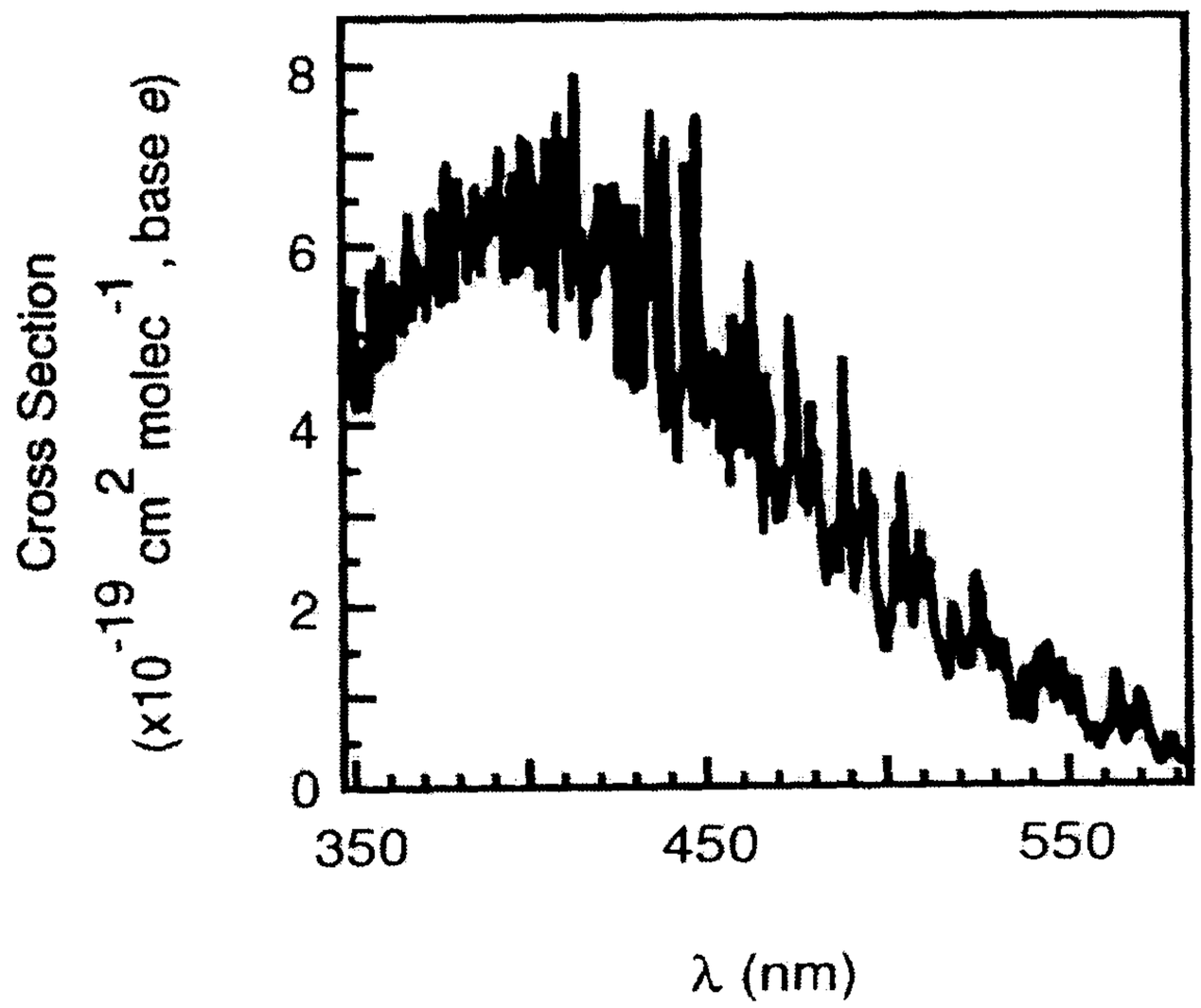


Figure 2.5: Absorption cross section of NO_2 as a function of wavelength (adaped from Harder *et al.*, 1997)

3. Sensitivity of the model and measurements at Mace Head

3.1 Introduction

This chapter investigates the sensitivity of photolysis frequencies, calculated by the radiative transfer model, to different input parameters. The accuracy of the calculated photolysis frequencies depends on the errors introduced by the approximations necessary in their calculation: the radiative transfer method, wavelength resolution and the parameterisations of physical properties of atmospheric gases such as quantum yield and absorption cross-section. In addition to the approximations associated with modelling, the calculated photolysis frequencies are limited by the variables used to describe the atmospheric state such as ozone column and surface albedo. Inaccuracies in the inputs can lead to sizeable deviations between the model results and the measured data. This is particularly relevant when the input parameters of the radiative transfer model are not parameters that are routinely observed in a field campaign (e.g. Zeng *et al.*,1994).

Any quantity that modifies the radiation field, and hence actinic flux, in a spectral region where photolysis occurs will change the photolysis rate coefficient. In the UV, gases, including ozone, nitrogen dioxide and sulphur dioxide, or aerosol can absorb photons. Scattering can be caused by aerosol or cloud. The surface albedo is particularly important at low levels since this determines the amount of upwelling radiation scattered or absorbed at the surface.

There have been many studies on the effect of these variables on photolysis rate and ultraviolet radiation. In this chapter, it will be shown that our model reproduces the broad sensitivities seen in other studies. A detailed sensitivity study is not attempted here, since many similar studies already exist. An outline of relevant previous studies will be given for comparison. Few of the input parameters required for the model are known to any degree of accuracy at Mace Head: the sensitivity studies show that estimation of input

parameters to match modelled to measured values is little more than guesswork and is therefore not the most appropriate use of these data.

This study also shows that cloud optical depth is the factor that within realistic changes has the largest influence on jNO_2 and $jO(^1D)$. This justifies further investigation of the relationship between cloud optical depth and these photolysis frequencies.

3.2 Two stream method

The model contains a choice of two-stream methods (see chapter 2). The use of different two stream methods leads to the calculation of slightly different actinic fluxes, and therefore, photolysis frequencies. Available two-stream methods include: the delta function[1], delta Eddington[2], Hemispheric Mean[3], Practical Improved Flux method (PIFM)[4], quadrature[5], modified quadrature, delta Discrete Ordinate[6], hemispheric constant[3] and hybrid Eddington delta[1].

Figure 3.1 illustrates the sensitivity of jNO_2 and $jO(^1D)$ to the chosen two-stream method. Figure 3.1(a) and (b), the effect on the absolute values of jNO_2 and $jO(^1D)$ show the photolysis frequencies calculated using the delta-Eddington approximation and the delta approximation. The other two stream methods are not shown on this figure because they are indistinguishable from the delta Eddington method on this scale. In all but one case, the deviation from the maximum value is less than 10% at solar noon. The exception to this is the delta function, for which the calculated photolysis frequencies at solar noon differ from the maximum by more than 30%. The delta function was specially developed to characterise strongly forward scattering particles and is usually combined with other two stream methods, so it is misleading to compare it directly with the other methods.

---

[1] Meador and Weaver (1980)

[2] Joseph *et al.*(1976),

[3] Toon *et al.* (1989)

[4] Zdunkovski *et al.*(1980)

[5] Liou (1973, 1974)

[6] Schaller (1979)

Figure 3.1(c) and (d) show the percentage change in photolysis frequency relative to the delta-Eddington approximation. The effect of choosing a different two stream method leads to a fairly constant error for all zenith angles less than 60° for both jNO_2 and $jO(^1D)$.

3.3 Resolution

Madronich and Weller (1990) investigated the effect of degraded spectral resolution on calculated photolysis rates. They concluded that the errors caused by wavelength grid depended on the size of the wavelength interval, the molecule and environmental factors that affect the distribution of the radiation with wavelength e.g. solar zenith angle. The NO_2 photolysis rate is much less sensitive to degraded spectral resolution than the $O(^1D)$ photolysis frequency. For instance, calculation of jNO_2 may be calculated using a 10 nm grid with errors of less than 2%. However, the $jO(^1D)$ requires a grid of 2 nm to achieve the same accuracy. Fluxes were calculated on Isaksen's grid which has a variable wavelength resolution, depending on the spectral region. Below 320 nm the resolution is less than or equal to 2 nm, and similarly a maximum of 5nm below 647 nm. Above 647 nm, the resolution coarsened to 10nm. As can be seen from the work of Madronich and Weller (1990), this should limit errors to less than 2% compared to calculations based on a 0.1 nm grid.

3.4 Ozone quantum yield

The problems encountered in establishing the ozone quantum yield are discussed in chapter 1. Here the sensitivity of the modelled photolysis rates to different quantum yields was tested. Quantum yields both with and without long wavelength tail are tested to see how the presence of the tail affects modelled photolysis rates at Mace Head.

The tails included tested were the Jet Propulsion Laboratory recommendations for 1987 and 1992 (DeMore *et al.*, 1987; De More *et al.*, 1992), the values recommended by Michelsen *et al.*(1994) and Shetter (1996). Figure 3.2 shows that the values of $jO(^1D)$ calculated with the JPL quantum yields are very similar, and this is not surprising since they contain no tail. The quantum yield tail is not expected to have much influence at low

zenith angles at mid-latitudes (e.g. Monks *et al.*, 1998). However, there is a marked difference between the values of $jO(^1D)$ at solar noon calculated using the different quantum yields. The Michelsen *et al.*(1994) tail gave the highest values : this tail is larger (efficiency of 0.2-0.3 from 312-320 nm) than that recommended by Shetter *et al.*(1996). The tail recommended by Shetter *et al.* was the one used in this modelling study. It is the most modern recommendation and is also very similar to that used by Brock and Watson (1980).

3.5 Absorbing gases

The amount of radiation absorbed by a gas depends on the number density of that gas and its absorption cross-section. The resulting impact of gas absorption on a particular photolysis rate coefficient depends on the spectral overlap between the product of absorption cross-section of the absorbing gas, and the quantum yield, with the absorption cross-section of the photolysing species. The attenuation will be greatest when the overlap is greatest.

3.5.1 Column Ozone

On the global scale, total ozone column varies between 150 and 400 DU. At Mace Head, according to TOMS, the range of column is smaller (218-419 DU), but, as calculations will show, still significant. Column ozone is widely accepted to be one of the most important factors influencing the calculation of clear sky $jO(^1D)$. Weihs and Webb (1997) concluded that the main deviations between their modelled UV and clear sky observations resulted from uncertainties in the ozone column optical depth.

Studies suggest that the UV radiation is more sensitive to the total ozone column density than the vertical distribution within that column (Tsay and Stamnes, 1992). Even a 50% increase in tropospheric ozone under a fixed column would only produce a ~ 2-3% change in UV dose rate at 55 degrees and a ~ 1% increase for a solar zenith angle of 75 degrees The efficiency of absorption of an ozone molecule is dependent on the temperature. The altitude profile of the ozone molecules is therefore important because the temperature

affects absorption. A sensitivity study, by definition, imposes artificial constraints on the parameters studied. Manipulation of ozone profile can cause problems since a constant column value is required and arbitrary redistribution of molecules can cause unrealistic ozone and Rayleigh absorption cross-sections.

At Mace Head, we do not have measured ozone profiles and so must use a standard profile. Use of a standard profile will introduce an error, but a much less significant one than incorrect diagnosis of the column depth. Schwander *et al.*(1997) found that the accuracy of using a standard ozone column instead of a real one depended on season as well as zenith angle. In summer, they find that the standard ozone profile overestimates the UV irradiance and underestimates it in winter. For example, Lapeta *et al.*(1999) investigated the influence of ozone profile and temperature on UV irradiance by comparing model results from a psuedo-spherical (Dahlback and Stamnes, 1991) DISORT (Stamnes *et al.*, 1998). They compared fluxes calculated using standard US ozone columns scaled to the total column density with those calculated using actual ozone profiles recorded in Poland. The differences were largest for large solar zenith angles. At 85° the maximum difference in the dose rate was 12.3%. However, by 75° the maximum difference had decreased to 2%. Krzyscin (2000) considered the shape of the ozone profile by splitting it into characteristic layers and investigating the ratio of the ozone in the lower atmosphere to the total column ozone. He found that although extreme redistributions from the low to high atmosphere could cause a change of ~ 5%, the average change of the surface UV dose was only ~ 1%, approximately an order of magnitude less than the change due to the variations in total ozone.

These results show that although the shape of the ozone profile can be significant for low sun situations, it is much less important than the total column amount. At Mace Head the simulation is restricted to zenith angles where these studies show error caused by changes in the ozone profile are very small. The ozone profile is therefore of less interest in calculating absolute values of jNO_2 and $jO(^1D)$ than the total column amount. The random, instantaneous deviations in the ozone column are thought to lead to changes in UV dose of typically < 10% (Krokotov *et al.*1998)

The sensitivity of jNO_2 and $jO(^1D)$ to changes in ozone column is shown in Figure 3.3 (a) and (b) respectively. In this case, the range of ozone column depths over EASE96 and EASE97 is shown. 285 DU is the lowest O_3 column recorded and 419 DU the largest. One percent increases and decreases in total O_3 column are also shown for comparison. As expected from the overlap of cross-sections, $jO(^1D)$ is much more affected by differences in the ozone column than jNO_2. A 1% change in column ozone caused approximately 2% change in the ozone photolysis rate, whilst only an approximately 0.02% percent change in jNO_2 (see Figure 3.3(c) and (d)). The jNO_2 change is therefore two orders of magnitude smaller. This is illustrated by the fact that the curves on the jNO_2 plot for both ends of the range are almost indistinguishable from each other (see Figure 3.3(a)).

Castro *et al.*(1997) found a 10 DU increase in ozone column from 290 to 300 DU decreased the ozone photolysis rate coefficient by almost 7 % . A 110 DU increase to 400 DU decreased the photolysis frequency by 40%. In comparison, the photolysis frequency of nitrogen dioxide only decreased approximately 0.5 % on increasing the ozone column 60 DU from 240 to 300 DU. This is in agreement with our study.

Generally, only the absorption of ozone is considered since the other gases have a smaller effect on the actinic flux and are spatially and temporally extremely variable (Forster *et al.*, 1995). However, the radiative transfer model used in this study also has the facility to include NO_2 and SO_2 columns. The effect of SO_2 has been considered by e.g. Bais (1993), but will not be investigated here since Mace Head is a rural environment. However, NO_2 column will be considered because of its importance to jNO_2.

3.5.2 Nitrogen dioxide

Atmospheric nitrogen dioxide is much less abundant than ozone. A typical column density would be 0.2 DU for the Northern Hemisphere summer (WMO, 1985) compared to 350 DU for ozone. Nitrogen dioxide is spatially and temporally extremely variable.

Figure 3.4(a) -(d) show the effects of various NO_2 column densities on the values of jNO_2 and $jO(^1D)$. The values chosen were: no column, a 'typical' value of $7x10^{15}$ moleculescm^{-2} (WMO, 1985), a 5% change around this assumed value, and a doubling of the column. As can be seen from (a) and (b) the changes from no column to a typical and doubled column are almost indistinguishable. For this reason, the percentage change relative to a 'no column' atmosphere is shown (Figure 3.3 (c) and (d)). It can be seen that column NO_2 has a relatively small effect on jNO_2. This is because of the comparatively small abundance of the species. The difference between no NO_2 column and a NO_2 column double the average is less than one percent at solar noon (θ=33.9°) increasing as the zenith angle and so slant column of the gas increases. The influence of NO_2 on $jO(^1D)$ is still less: the percentage decrease in $jO(^1D)$ on doubling the column NO_2 is approximately one order of magnitude smaller than that on jNO_2 The deviations from the smooth profile that appear in this figure are simply due to the precision involved in calculations using very small numbers.

3.6 Aerosol

Satellite studies have shown that UV absorbing aerosols can cover 10% of the earth's surface with an optical depth of at least 0.1 (Herman *et al.*, 1997). The effect of aerosol on photolysis rates is sensitive to the aerosol optical depth, single scattering albedo and vertical profile, as well as the relative humidity and solar zenith angle.

The attenuation of radiation by aerosols is spectrally dependent. Aerosols attenuate more in the UV than at longer wavelengths (Erlick and Frederick, 1998). Non-absorbing aerosols attenuate UV by 10% for an aerosol optical depth of 1.0 and approximately 5% for an aerosol optical thickness of 0.4. (Krokotov *et al.*, 1998) Absorbing aerosols, e.g. soot mixtures, will further enhance this reduction in photolysis frequency.

Table 3.1 shows optical depths of some different types of aerosol at 300 nm and 400nm, together with the Rayleigh and ozone optical depths of the atmosphere at these

wavelengths. At $jO(^1D)$ wavelengths it can be seen that all the aerosols are much less significant than the ozone optical depth. It can also be seen that aerosol optical depth decreases at higher wavelengths.

Table 3-1 Relative optical depth of aerosol, ozone and Rayleigh molecules at 300 and 400nm respectively (from Liao *et al.*, 1999)

Atmospheric components	Total optical depth	
	λ=300 nm	λ=400nm
Rayleigh molecules[7]	1.22	0.36
Ozone[8]	3.34	0.00
Aerosols		
Pure $(NH_4)_2SO_4$ continental	0.13	0.09
Pure $(NH_4)_2SO_4$ urban	1.34	0.92
Pure soot (continental)	0.03	0.02
Pure soot (urban)	0.26	0.18
Internal mixture (urban)	1.63	1.12
External mixture (urban)	1.60	1.10
Mineral dust	0.11	0.12

These values are consistent with other work, for instance aerosol UV optical depths measured in Poland (Kryzscin, 1998) ranged from 0.1-0.7. It should be noted that stratospheric aerosol and volcanic ash (such as that from the eruption of Mount Pinatubo in the Philippines in 1995) can also have a large effect on tropospheric photolysis rates (e.g. Huang and Massie, 1997).

Reuder *et al.* (1999) used model simulations and measurements to specifically investigate the effects of aerosols on the UV radiation. They found that the short-term variability can change spectrally integrated radiation quantities by the order of 20% to 45%. They list the most significant short term variability at a particular location to be due to changing air

[7] US Standard atmosphere

[8] US standard atmosphere, 319 DU

mass and wash-out of aerosols by rain. Radiative effects of typical aerosol variability were equivalent to ozone changes of 40-90 DU. Extending their work to aerosol effects on actinic flux, they found that high aerosol optical depths were associated with low values of jNO_2 and vice versa. However, for $jO(^1D)$ this association was less clear. The aerosol absorption was also found to be zenith angle dependent

Lu *et al.* (1996) found that the UV-B (280-315 nm) had decrease by 5-18 % in non-urban regions since a result of aerosol formed from SO_2 emissions since the industrial revolution. Kylling *et al.* (1998) found that the presence of aerosol in clear skies can reduce the UV-by between 5 and 35% depending on the single scattering albedo. The effect of aerosol on UV and photolysis largely depends on the composition and characteristics of the aerosol involved. A continental aerosol of optical depth 1.0 placed in the radiation scheme of Forster (1995) produced between 40% and 80% higher surface irradiances than an urban aerosol. In the Arctic, stratospheric aerosols can result in increased UV exposure, whereas tropospheric aerosols (Arctic haze) result in decreased exposure (Tsay and Stamnes, 1992). Castro *et al.*(1997) found that changing their aerosol refractive index from 1.4 (organic) to 1.6 (dust) leads to an increase of almost 20% for jNO_2.

Liao *et al.*(1999) also studied the effect of aerosols on tropospheric photolysis rates. They extended the work of previous authors and specifically examined the effect of aerosols in a cloudy atmosphere. Using a 1-D radiative transfer model, they included sulphate, soot, external and internal mixtures of these and mineral dust to the atmosphere. The photolysis rate profile was of interest to the authors. It was concluded that absorbing soot aerosol reduces the photolysis rates at all altitudes. In contrast, the scattering sulphate aerosol increases the photolysis rates above and at the top of the aerosol layer but decreases it at the bottom of the aerosol layer and at the surface. In both of these cases, this concurs with a decreased photolysis rate at ground level in the presence of aerosol.

Comparison with the aerosol optical depth in Table 3.1 shows that even at very high aerosol optical depths in urban environments the optical depth of aerosol is small

compared to that of cloud. Even in the case of a thin cirrus cloud, the attenuation of radiation by cloud will be more significant than that caused by aerosol. This study, therefore, concentrates on attenuation by cloud. Calculations also show that doubling the aerosol optical depth profile of Eltermann (1968) change jNO_2 by less than 2% at solar noon, compared to 5% for $jO(^1D)$.

3.7 Surface Albedo

The surface albedo is the ratio of reflected and incident fluxes at the surface level. The surface albedo is dependent on surface colour, moisture, surface texture and solar elevation.

Albedo is particularly important where the layers above the ground back-scatter some of the surface-reflected light e.g. a layer of aerosol or cloud. Forster (1995) stated that the albedo for most surfaces in the UV lies between 0.0 and 0.2. If the uncertainty in albedo is taken to be 0.2, then he found the error associated with albedo was less than 10% for clear skies, but it is increased in the presence of low-level cloud (up to a maximum of almost 20% at a cloud optical depth of 50.).

Studies of the UV surface albedo (340-380 nm) from satellite data (TOMS/Nimbus 7) showed low UV estimated Lambertian surface reflectivities over the entire globe. These reflectivities were found to be nearly independent of wavelength and were found to be lower over land, 0.02-0.04 than over the sea, 0.05-0.08 (Herman, 1997). Values were taken at a similar latitude, but for a continental climate, by Eck *et al.*(1987). The hourly average albedo was taken over 280 - 2800nm for 8 years. In snow-free July, the albedo was at a minimum of 0.17±0.04, but covered a range from a minimum of 0.15 for overhead sun, to a maximum of 0.26 in the early morning. They suggest that UV reflectance is about a sixth of average broad-band reflectance for a grass surface, but as much as two thirds for a smooth surface like a car park.

The albedo is also a function of wavelength between the different parts of the UV spectrum. The exact dependence of the albedo on wavelength is unclear. Blumthaler and

Ambach (1988) state 'presumptions are made that the albedo of natural surfaces differs considerably as far as the solar UVB and total solar radiation (300nm - 3μm) are concerned.' However, the wavelength dependence of the albedo can be strong, with the highest albedos generally occurring at the longer wavelengths e.g. the albedo for sand in the UV-A is 0.203 whereas that in the UV-B is 0.152 (Krol and van Weele, 1997).

Recently, further spectral studies of albedo have been undertaken (Webb *et al.*, 2000). These show a general increase in albedo with wavelength, but the magnitude of the increase with wavelength depends on the surface considered e.g. at 300 nm grass has close to zero albedo, whilst at 450nm it is approximately 0.02; light tarmac has an albedo of 0.1 at 300 nm and approximately 0.17 at 450 nm.

In many cases, the composition of the surface near the measurement site is not homogeneous. At Mace Head, the radiometers were situated above grass, rocks, tarmac and a cottage roof. For such case, the overall reflectance of this surface will be characterised by a contribution from each of its components. Weihs and Webb (1997) give a formula relating the overall albedo of an area to the individual albedos of the different surfaces and their relative areas (see equation 3.1).

$$\text{Albedo} = \text{Alb}_a \frac{\text{Sf}_a}{\text{Sf}_a + \text{Sf}_b} + \text{Alb}_b \frac{\text{Sf}_b}{\text{Sf}_a + \text{Sf}_b} \qquad (3.1)$$

Assumption of an average composition of 10% tarmac and 90% grass might give a surface albedo of 0.01 at 305 nm at 0.03 at 380 nm using values based on Webb *et al.*(2000). This compares with published albedos of 0.05 for visible wavelengths for short grassland (Bray *et al.*, 1996). However, in the case of half tarmac and half grass, the albedo at 305 nm would increase further to 0.0775.

Inhomogeneities in albedo have the largest effect where albedo contrast is high. This in agreement with the work of Degunther *et al.* (1998) who concluded that even if the albedo is specified on an area with 40 km radius, in cases of extreme albedo contrast (e.g. snow/grass) the area outwith this can influence the irradiance by up to 3%. When a mere

5 km radius is specified, the error at 330nm was greater than 20%. This was undertaken for a clear sky and the authors stated that the effect of clouds could alter this effect. However, all this research shows that a large amount of potential variability is possible within the albedo measurement, making its estimation tricky.

Since the jNO_2 radiometer at Mace Head had an upward and a downward facing plate, these can be used to give an indication of the ratio of downward to upward actinic fluxes, which has an average value of 0.17. However, it should be noted that this number is not the same as the albedo. Demerjian *et al.*(1980) reported that the actinic flux near the surface could be as much as twice the horizontal irradiance and a change in surface albedo from 0-0.1 could increase the available energy by 10-20%. This value of 0.17 should, therefore, be regarded as an upper limit to the albedo. Examination of the ratio of upward and downward actinic fluxes showed that the ratio was far from constant during the day and this is in agreement with recent work on albedo. Lyapustin (1999) confirms that albedo changes with solar zenith angle and atmospheric optical depth. At low solar zenith angles, the albedo increases as the atmospheric optical depth increases whereas at high solar zenith angles the albedo responds in the opposite sense.

Forster (1994) recommended an albedo of 0.1 as suitable for most surfaces in the UV. Since portable devices exist for measuring the ground albedo in the spectral region of interest, (e.g. Diffey *et al.*, 1996), this would be a simple method of removing the uncertainty associated with estimating the albedo in photochemistry calculations.

Previous work has found $jO(^1D)$ to be more sensitive to albedo than jNO_2. Castro *et al.* (1997) showed that the ozone photolysis rate decreased 12 % when the surface albedo was decreased from 0.10 to 0.05 and increased 11 % when changed by the same amount in the opposite direction from 0.10 to 0.15. The nitrogen dioxide photolysis rate increased 7% on moving from albedo 0.05 to 0.1 and a further 9% on moving from 0.10 to 0.15.

Figure 3.5 shows the effect of different surface albedos on the modelled values of $jO(^1D)$ and jNO_2. The photolysis frequencies increase as the albedo increases (Figure

3.5(a)&(b)). The wavelength dependent albedo used is a function that parameterises the albedo so that it is 0.01 in the UV-B, increasing to a value of 0.03 in the UVA and 0.1 in the visible. However, Figure 3.5(c)&(d) show that the wavelength independent albedos have a very similar effect on $jO(^1D)$ and jNO_2. The percentage change compared to a wavelength independent albedo of 0.05 is shown. The wavelength independent albedo is less than the albedo of 0.05. Increasing the albedo to 0.1 gives an increase of approximately 8% in both photolysis frequencies at solar noon. Entering no albedo into the model decreases the photolysis frequencies by approximately the same amount. The total change from no surface albedo to a surface albedo of 0.1 is approximately 17%.

3.8 Cloud

Cloud generally attenuates UV more than any other atmospheric parameter (Schafer *et al.*, 1996). Clouds are highly variable, both spatially and temporally, so they are often modelled using monthly or seasonally averaged cloud amounts (e.g. Krol and van Weele, 1997). It is far harder to quantify their impact on diurnal and shorter timescales (e.g. Frederick and Snell, 1990). It has been concluded that the variations in UV due to very short timescale cloudiness in some locations is comparable to the UV change from the long term changes observed in total column ozone (Fredrick and Snell, 1990). The effect of cloud on radiation is complicated. Intuitively, a cloud that obscures the sun will decrease the radiation transmitted leading to a decrease in photolysis rates below the cloud and an increase from reflected radiation above it. This is often observed and can be modelled simply (e.g.Vilà-Gureau de Arellano *et al.*, 1994). However, broken cloud fields or cumulus clouds can lead to enhancements of the photolysis rates above their clear-sky values below the clouds. Some very recent studies e.g. Trautmann *et al.* (1999) have investigated the effect of broken cloud fields on actinic fluxes and reproduced these effects using 3-D radiative transfer models.

Clouds can affect the actinic flux differently depending on the location of the detector relative to the cloud and the geometry of the cloud field. Above the cloud, the highly reflecting surface causes actinic fluxes to be increased. Below the cloud, depending on the solar zenith angle and cloud optical depth, the actinic flux can be slightly enhanced (very

high sun and thin cloud), or as is more common, reduced (Madronich, 1987). For instance, Ruggaber (1994) showed that a 1 km thick cloud with its base at 1km and a cloud water path of 300 gm^{-2} doubled the jNO_2 above the cloud and led to the jNO_2 below the cloud reducing to approximately a quarter of its value in a cloudless atmosphere. Most usually, the role of clouds in photodissociation is examined by both measurements and modelling studies.

Studies where in-situ measurements of cloud optical properties are available tend to be quite successful at reproducing vertical profiles of actinic flux. In situ measurements of cloud properties allow precise calculation of the optical properties of particles and droplets: vertical profiles of extinction coefficient and volume scattering coefficient and the phase function and so allow much more accurate inputs into radiative transfer models. Matthijsen *et al.* (1998) were particularly concerned with the effect of multiple cloud layers and the impact of changes in actinic flux on the $jO(^1D)$ and consequently on hydroxyl radical concentrations (see chapter 1 for discussion). They used aircraft UV irradiance data as a proxy for actinic flux, aerosol particle profiles and in situ measurements of cloud liquid water content and effective radius. Frueh (2000) compared observed and modelled profiles of jNO_2 using a four stream radiative transfer model. Again they were able to use in-situ measurements of aerosol and cloud properties. They concluded that although the aerosol is the largest uncertainty in modelling jNO_2 in a clear sky, in a cloudy sky the uncertainty of the observed liquid water content is far more significant.

In this model, we assume the cloud to be infinitely thin given at a base height and its properties are specified in terms of its optical depth, τ, single scattering albedo, ω and asymmetry factor, g. The values are dependent on the cloud type. There is some disagreement about the value of the cloud single scattering albedo in the ultraviolet. Clouds are perfectly scattering, ω=1.00 (e.g. Trautmann *et al.*, 1999) or almost perfectly scattering, ω=0.9999 (e.g. Matthijsen, 1999). The asymmetry factor is set between 0.85 (e.g. Trautmann *et al.*, 1999) and 0.87 (e.g. Dunkerkye and van Weele, 1991). Different asymmetry parameters are used for different cloud types. For instance, g=0.87 would be a

suitable value for a cirrus cloud at 350 nm and a liquid ice path of 100 gm^{-2}, whereas a value of 0.85 might be a suitable for a stratocumulus cloud with the same liquid water at the same wavelength (e.g. Forster, 1995). Decreasing the single scattering albedo will increase the absorption at a scattering event, so fewer photons will be transmitted through the cloud. In contrast, increasing the asymmetry parameter will increase the amount of forward scatter, so there will be more photons beneath the cloud.

3.8.1 cloud optical thickness

Increased cloud optical depth reduces jNO_2 and $jO(^1D)$. This is illustrated in Figure 3.6(a)-(d). Figures 3.6(a) and (b) show the effect of different cloud optical depths on photolysis frequency. The outermost curve is the model calculated clear sky and the diurnal curves calculated for optical depths of 5, 10, 25 and 50 are shown. The smallest reduction, compared to clear sky, occurs at solar noon increasing with increasing zenith angle, until a solar zenith angle of approximately 75°. Beyond this point, a small increase is seen. However, low sun tail of the photolysis frequencies already is small, so the importance of showing a percentage change relative to such a small number is considered negligible. The increased reduction in photolysis frequencies with zenith angle is partially because the optical path of the photons through the cloud increases as the solar zenith angle increases. The effect of solar zenith angle is included in the investigation of cloud optical depth on the relative reduction of jNO_2 and $jO(^1D)$ undertaken in chapter 5, so will not be discussed further here. Here, we are concerned with the fact that that an optical depth of 10 caused a change of more than 25% in each photolysis frequency at solar noon (Figure3.6 (c) and (d)).. This illustrates the importance of cloud optical depth in calculating photolysis frequencies.

3.8.2 cloud base height

The effect of cloud height is shown by investigating the effect of an infinitely thin cloud of optical depth 10 at different atmospheric heights. Figure 3.7 shows that the effect of cloud height is very small for both jNO_2 and $jO(^1D)$. In Figure 3.7(a) and (c) the curves are indistinguishable. If these are shown as the percentage change in jNO_2 (Figure 3-7 (b))

and $jO(^1D)$ (Figure 3-7 (d)) in photolysis frequency, it can be seen that moving the cloud to different heights changes the photolysis frequencies by less than 1%.

3.8.3 asymmetry factor

Figure 3.8 shows the effect of using a different asymmetry factor on a cloud of optical depth of 10. Values of 0.87 and 0.85 are shown to illustrate the effect of an extreme change, although it is doubtful that a cloud with properties analogous to g=0.87 would have such a high optical depth. For example, Matthijsen *et al.*(1999) found that their measured in-cloud properties corresponded to an asymmetry parameter ranging between 0.845 and 0.85. The percentage change shown is that obtained from decreasing g from 0.87 to 0.85. Increasing the asymmetry factor form 0.85 to 0.87 causes an increase of about 6% in both jNO_2 and $jO(^1D)$. In contrast, decreasing the value of asymmetry factor to 0.845 causes a decrease of about 1% in both photolysis frequencies. The magnitude of this change is very slightly zenith angle dependent.

3.8.4 single scattering albedo

The effect of cloud on photolysis frequencies is not much more sensitive to single scattering albedo than to the asymmetry factor (Figure 3.9). A change from almost perfectly scattering cloud droplets (ω=0.9999) to perfectly scattering cloud droplets (ω=1) decreases both photolysis frequencies by less than 1%. The dependence on the value of ω is very weakly zenith angle dependent and very similar for jNO_2 and $jO(^1D)$.

Dunkerkye and van Weele (1993) extended the work of Madronich (1987) and used a simple model to investigate the effect of cloudiness on jNO_2. They found that the cloud optical thickness was the critical factor describing the effect of the cloud on the actinic flux outside of the cloud. The in-cloud properties and cloud height were far less important. These results agree with their findings.

3.9 Summary

This section has shown the sensitivity of photolysis rates to the description of the atmosphere. Calculation of exact photolysis rate profiles for a campaign such as ACSOE is therefore subject to a wide variety of possible errors. These errors can be minimised by sensible guesswork, but with a scarcity of accurate model input parameters a direct comparison of modelled and measurements is not possible.

In addition to this, we have shown that of the model input parameters, within realistic ranges of expected variables, the photolysis frequencies are most sensitive to cloud optical depth. This provides a motivation for further investigation of cloud optical depth and its relationship to jNO_2 and $jO(^1D)$.

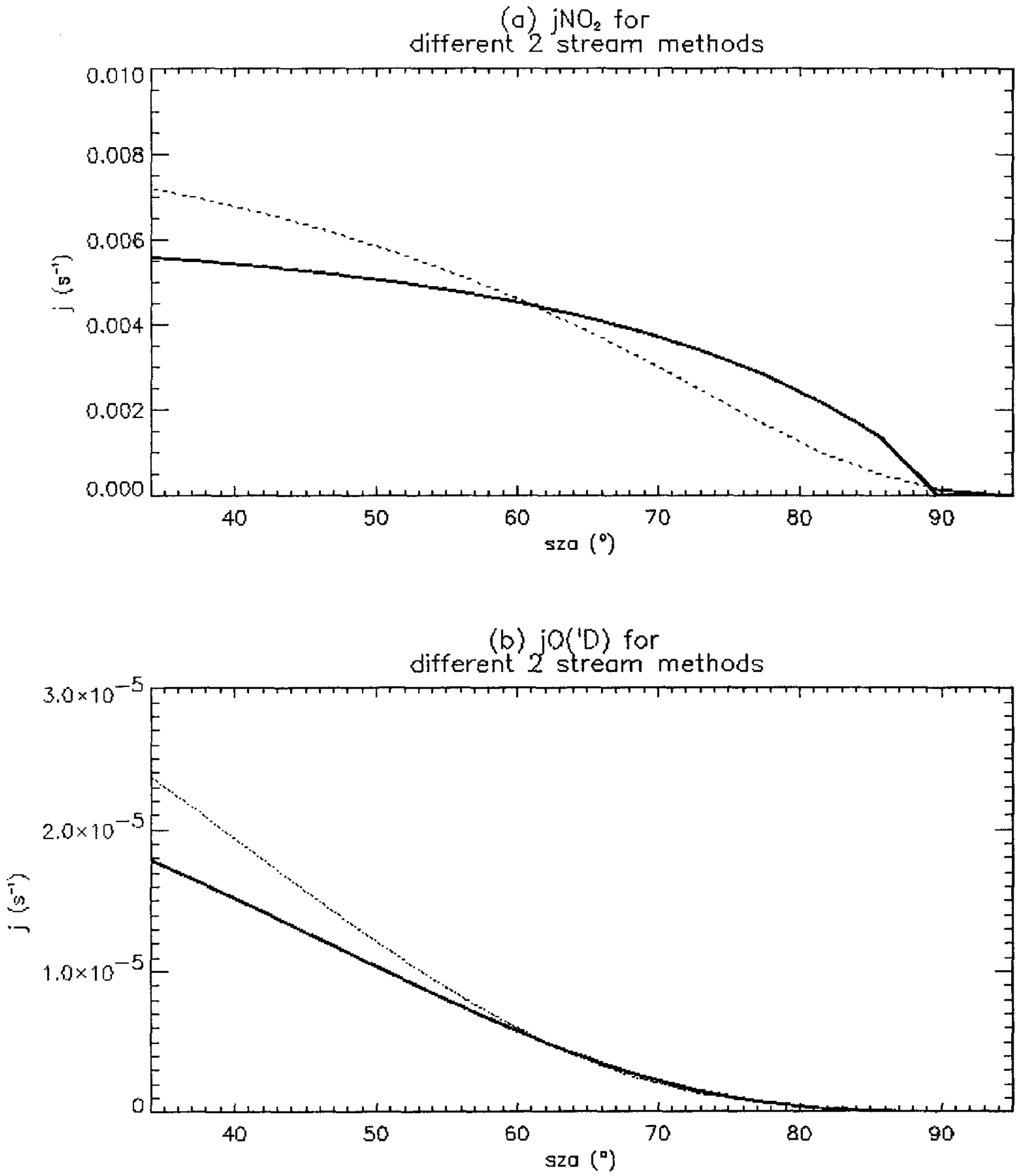
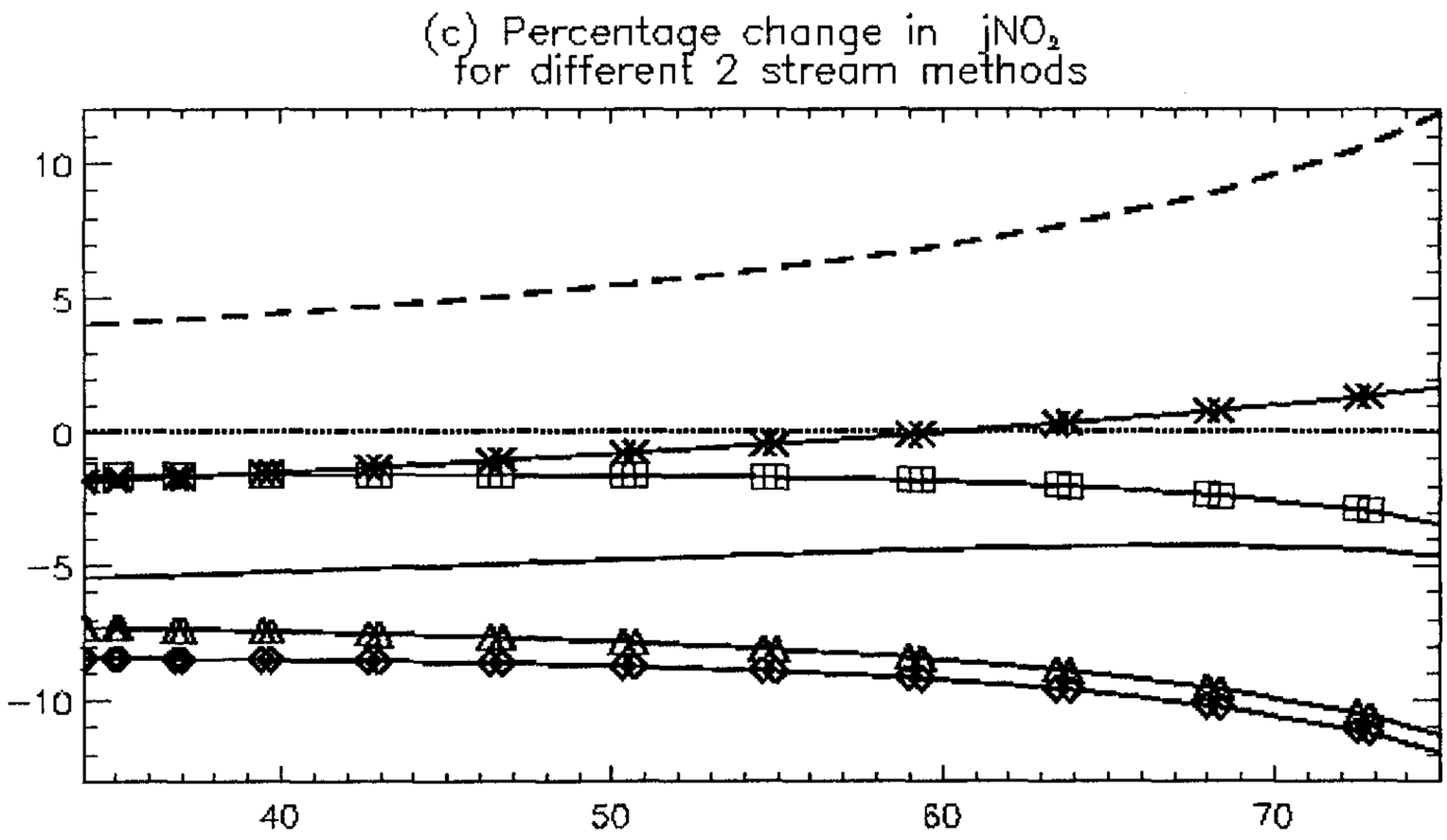
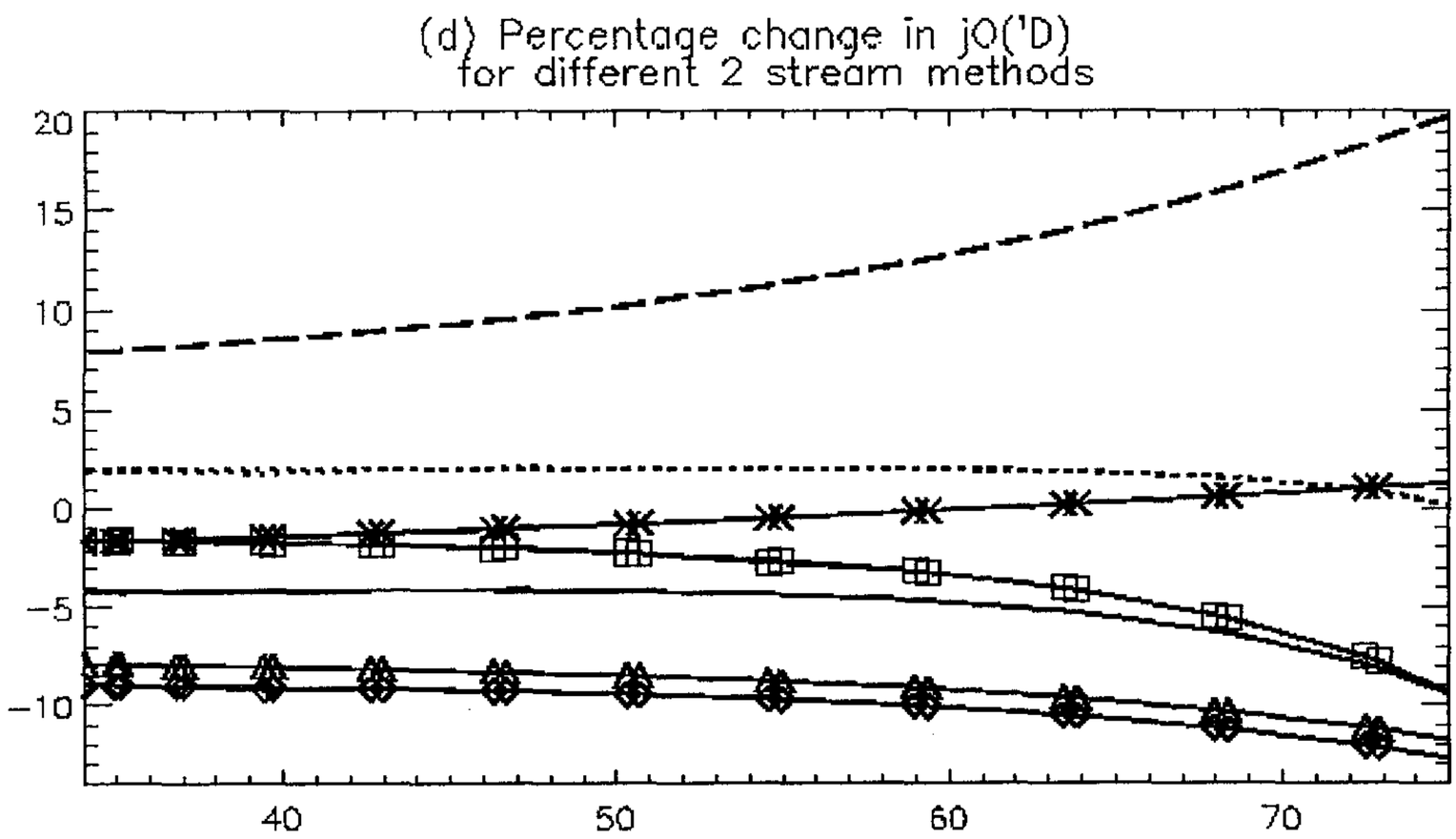


Figure 3.1: Sensitivity of jNO_2 and $jO(^1D)$ to two stream method (a) jNO_2, (b) $jO(^1D)$ Only the Delta Eddington (dotted) and delta (solid) approximations are shown for clarity.





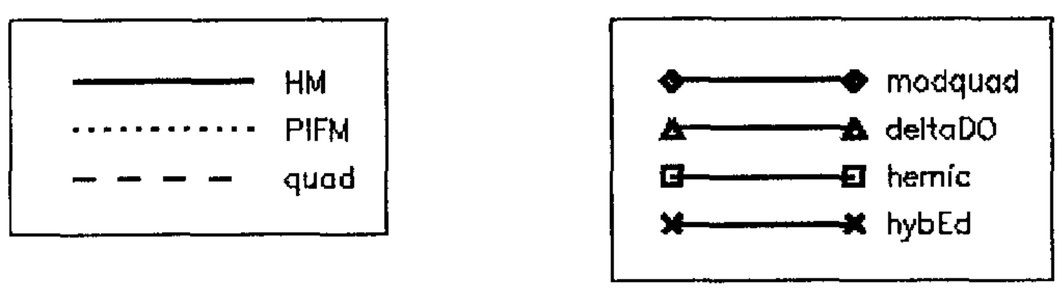


Figure 3.1: Sensitivity of jNO_2 and $jO(^1D)$ to two stream method (c) percentage change in jNO_2 compared to delta-Eddington, (d) percentage change in $jO(^1D)$ compared to delta-Eddington Hemispheric Mean (dotted), PIFM(dashed), quadrature (solid), modified quadrature (diamond), delta Discrete Ordinates (diamond), Hemispheric Constant (square), hybrid Eddington delta (cross)

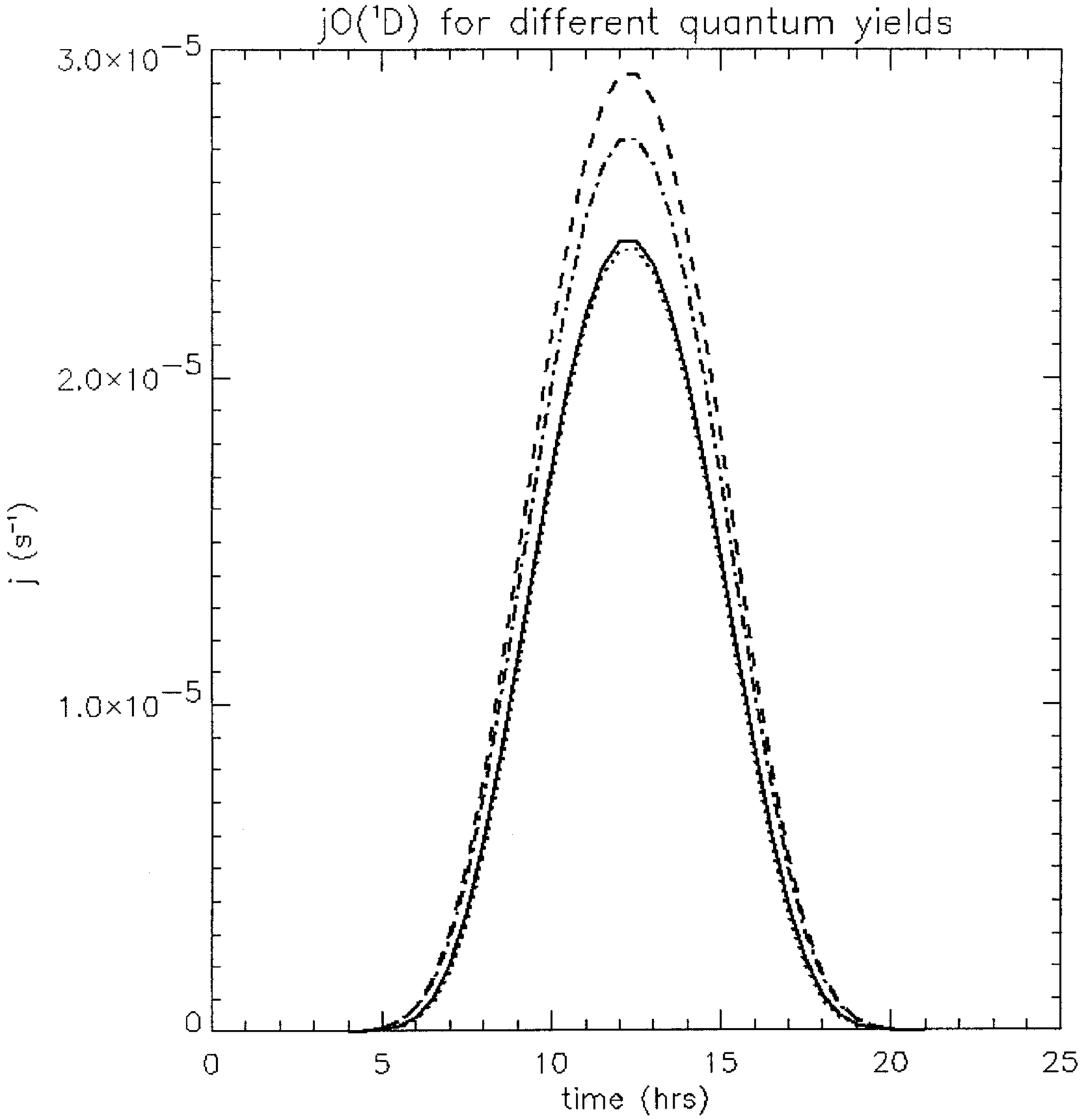


Figure 3.2: Sensitivity of $jO(^1D)$ to O_3 quantum yield

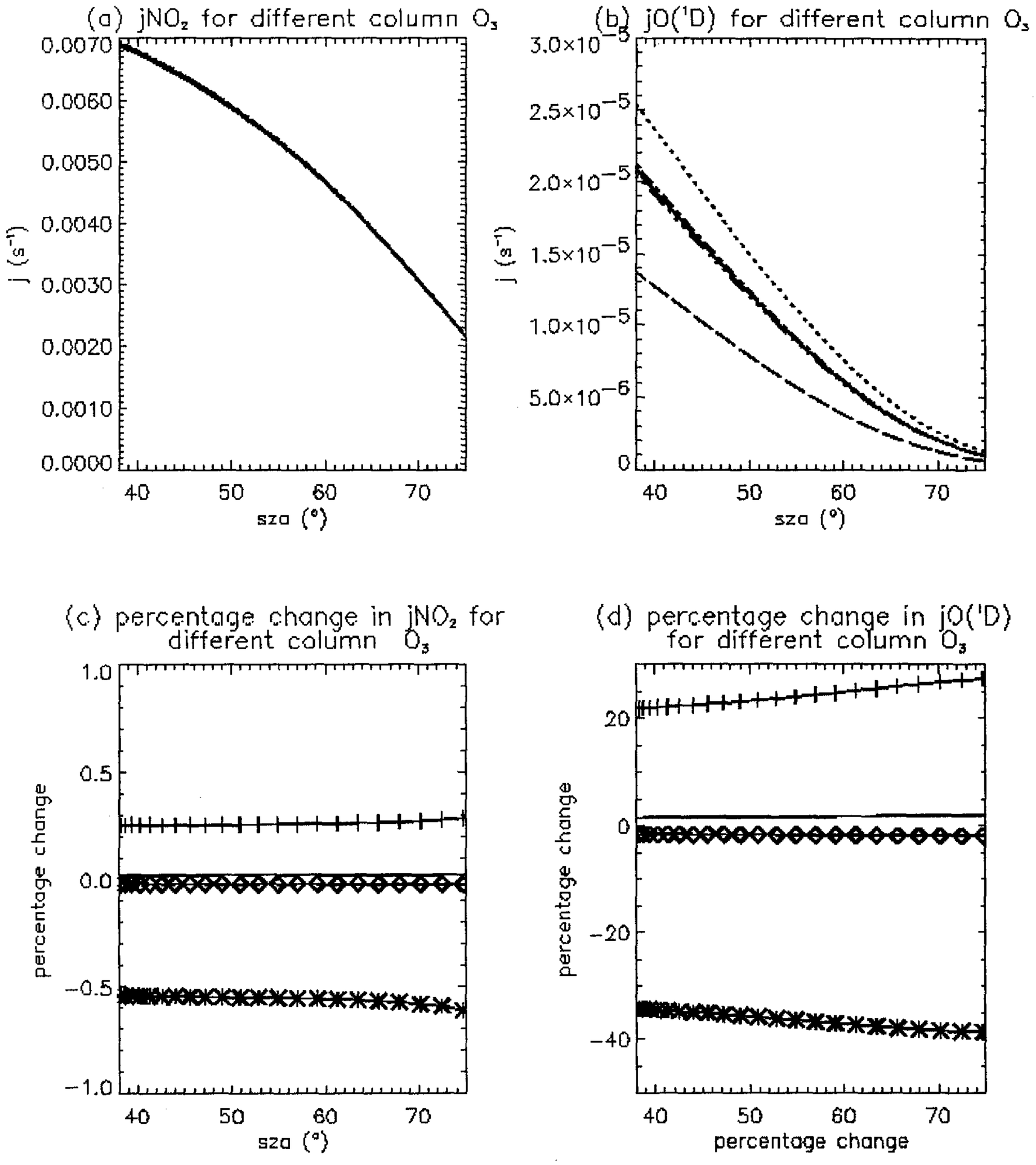


Figure 3.3: Sensitivity of jNO_2 and $jO(^1D)$ to ozone column (a) jNO_2 (b) $jO(^1D)$ 5 different ozone columns are shown: 285 DU (dotted), 321 DU (dot dash), 324 DU (solid), 327 DU (dot dot dot dash) and 419 DU (dashed) (c) percentage change in jNO_2 relative to jNO_2 at 324 DU (d) percentage change in $jO(^1D)$ relative to $jO(^1D)$ at 324 DU: 285 DU (crosses), 321 DU (solid), 327 DU (diamonds), 419 DU (asterisks)

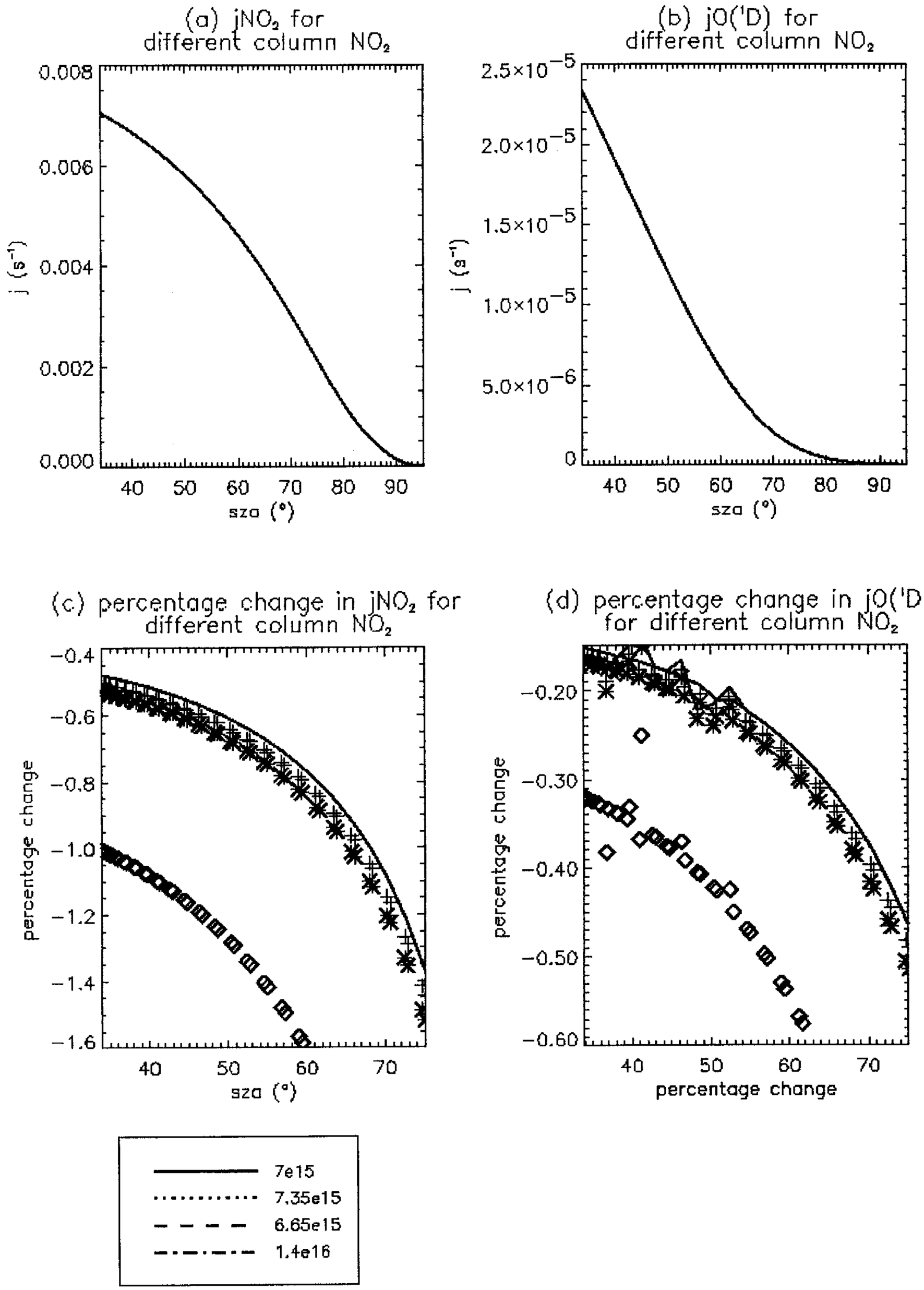


Figure 3.4: Sensitivity of jNO_2 and $jO(^1D)$ to nitrogen dioxide column (a) jNO_2 (b) $jO(^1D)$(c) percentage change in jNO_2 relative to no column (d) percentage change in $jO(^1D)$ compared to no column. column: 7 $x10^{15}$ cm^{-3} (cross), 6.65 $x10^{15}$ cm^{-3} (solid line), 7.35 $x10^{15}$ cm^{-3} (asterisk), 1.4 $x10^{16}$ cm^{-3} (diamond)

Fig

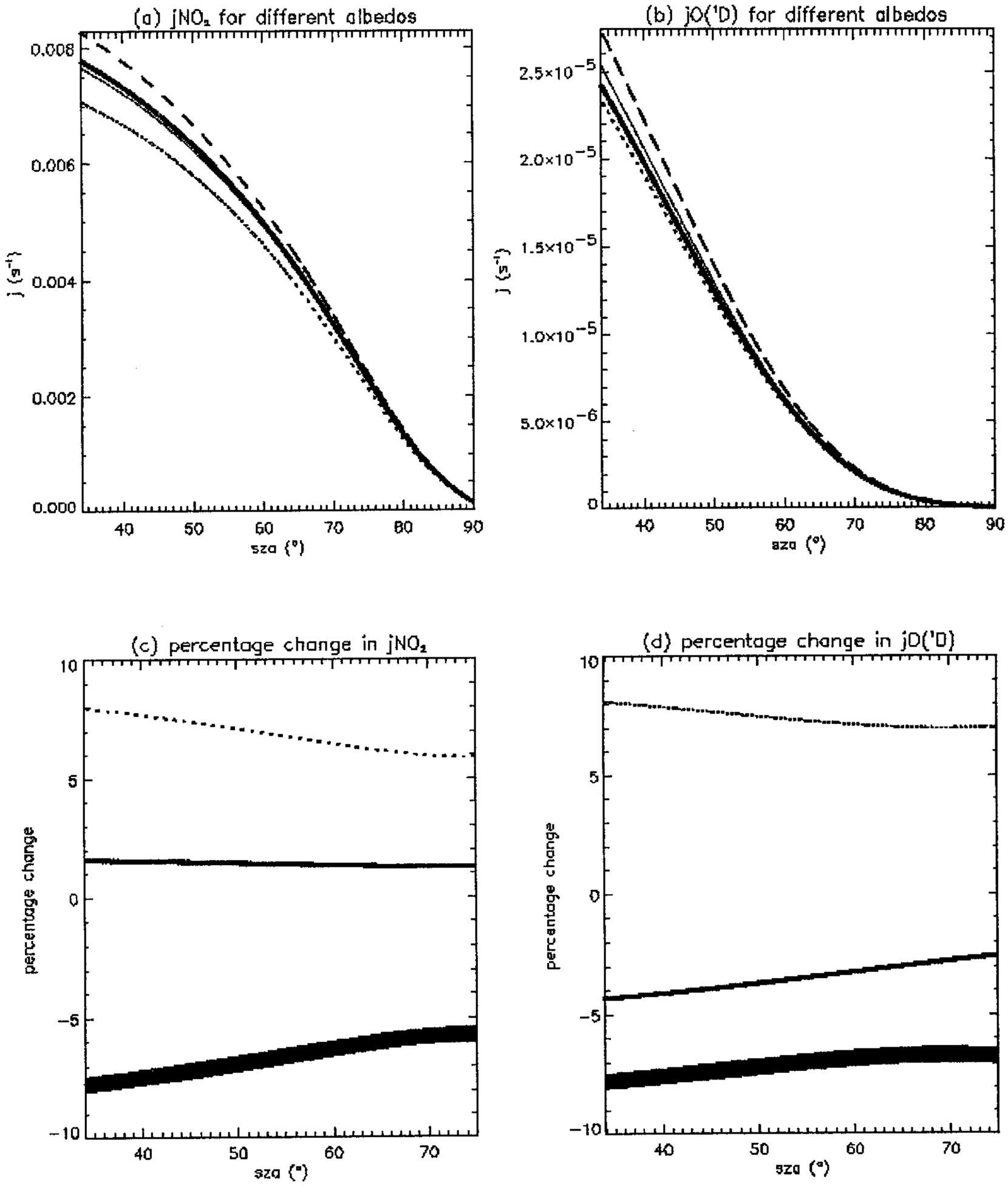
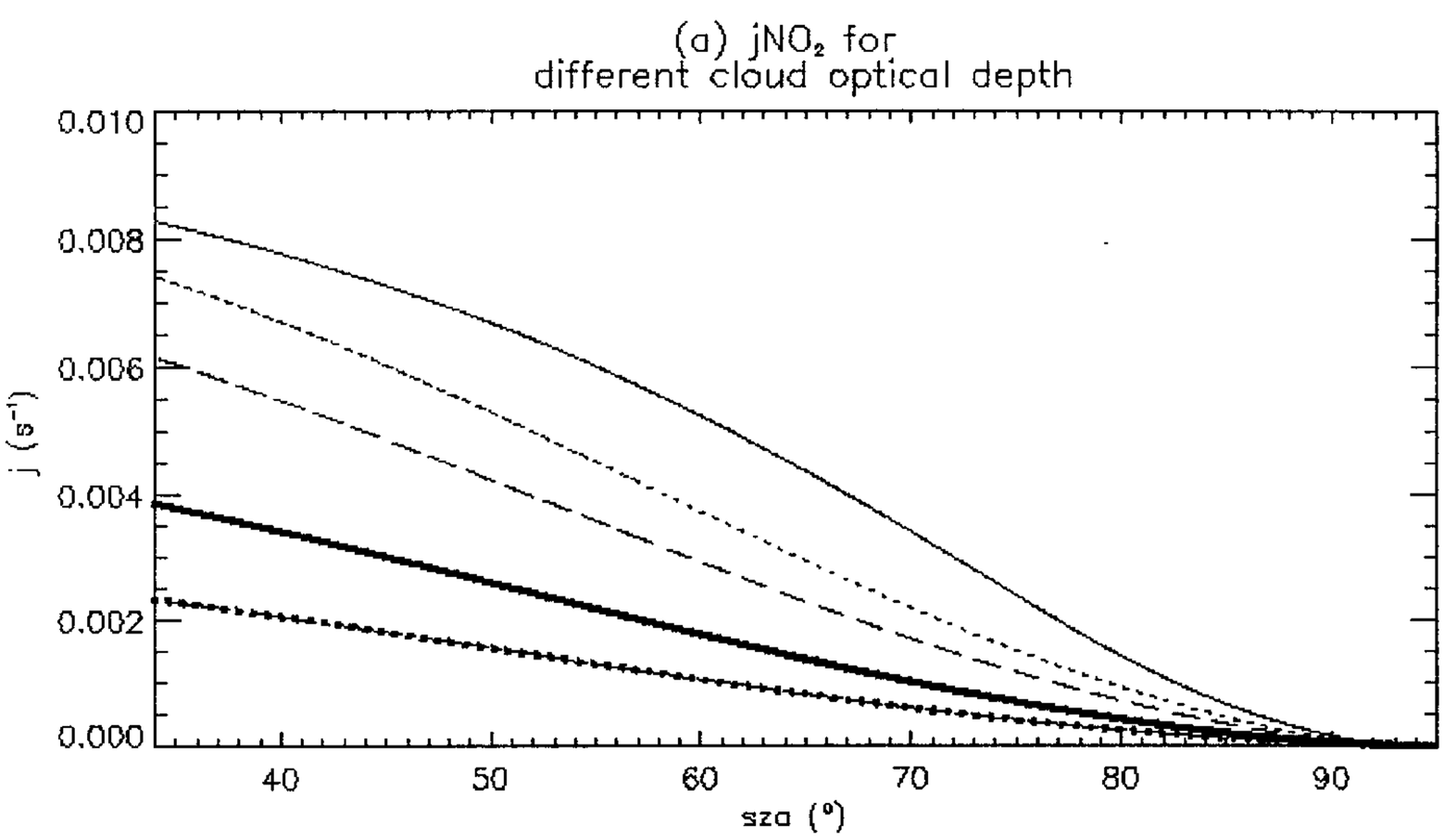


Figure 3.5: Sensitivity of jNO_2 and $jO(^1D)$ to surface albedo (a) jNO_2 (b) $jO(^1D)$ no albedo (dotted line), albedo=0.05 (solid line), albedo=0.1 (dashed line), λ dependent albedo (heavy solid line)

(c) percentage change in jNO_2 relative to a surface albedo of 0.05, (d) percentage change in jo1d relative to a surface albedo of 0.01. 0.05 (solid line), 0.1 heavy solid line, λ dependent albedo (crosses)



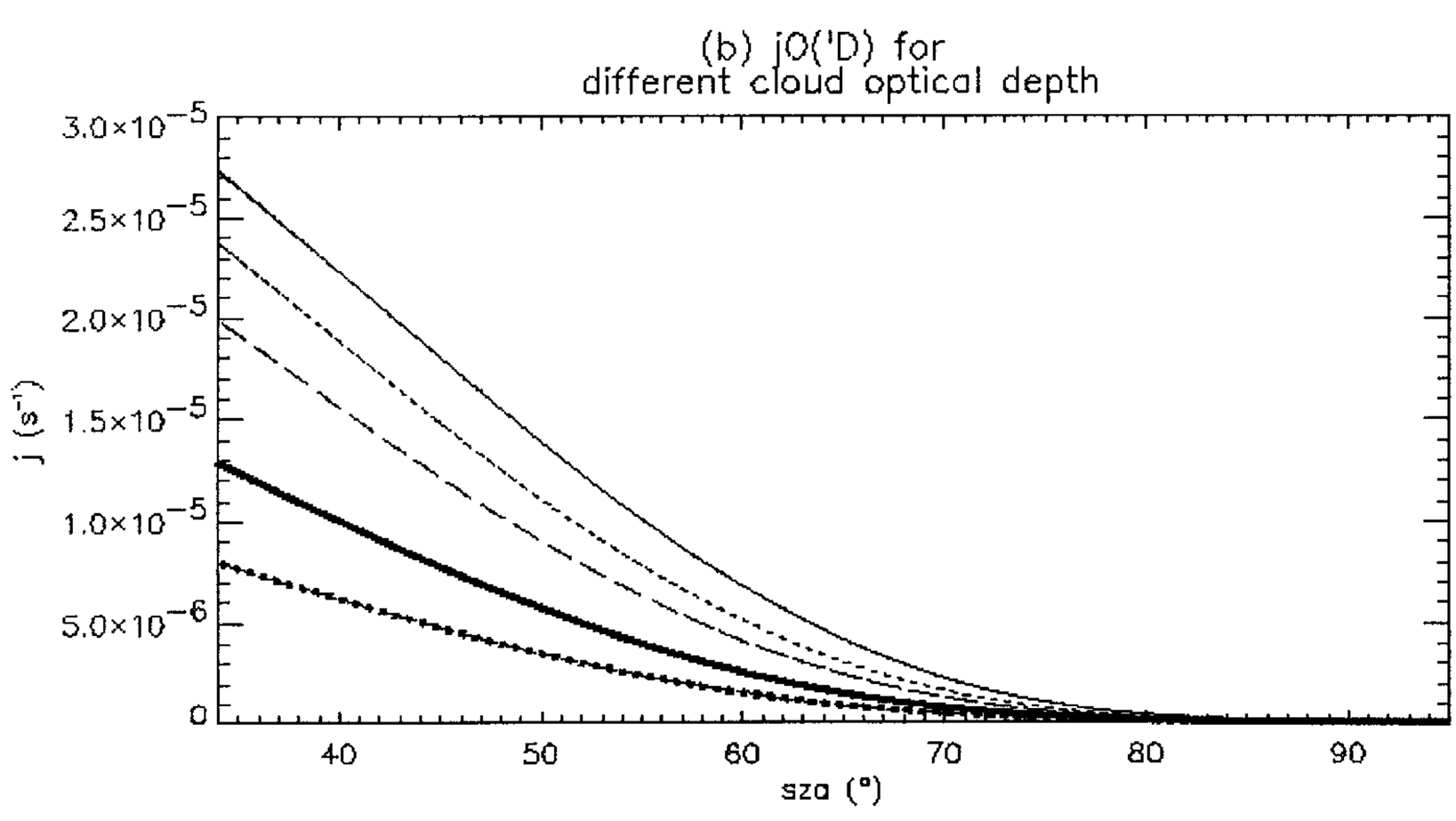
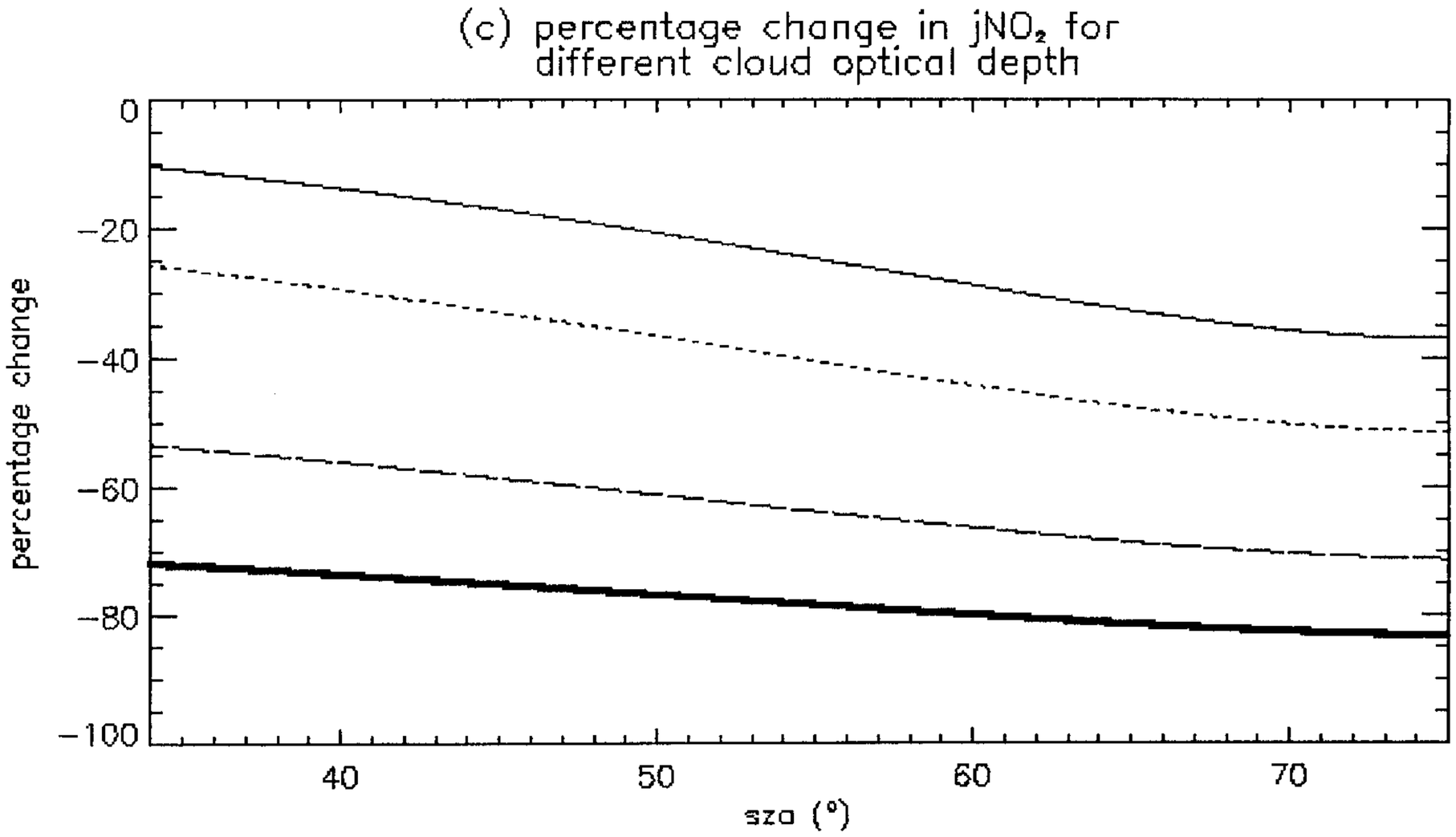


Figure 3.6: Sensitivity of jNO_2 and $jO(^1D)$ to cloud optical thickness (a) jNO_2 (b) $jO(^1D)$ no cloud (solid), τ=5 (dotted), τ=10 (dashed), τ=25 (thick solid), τ=50 (thick dotted)



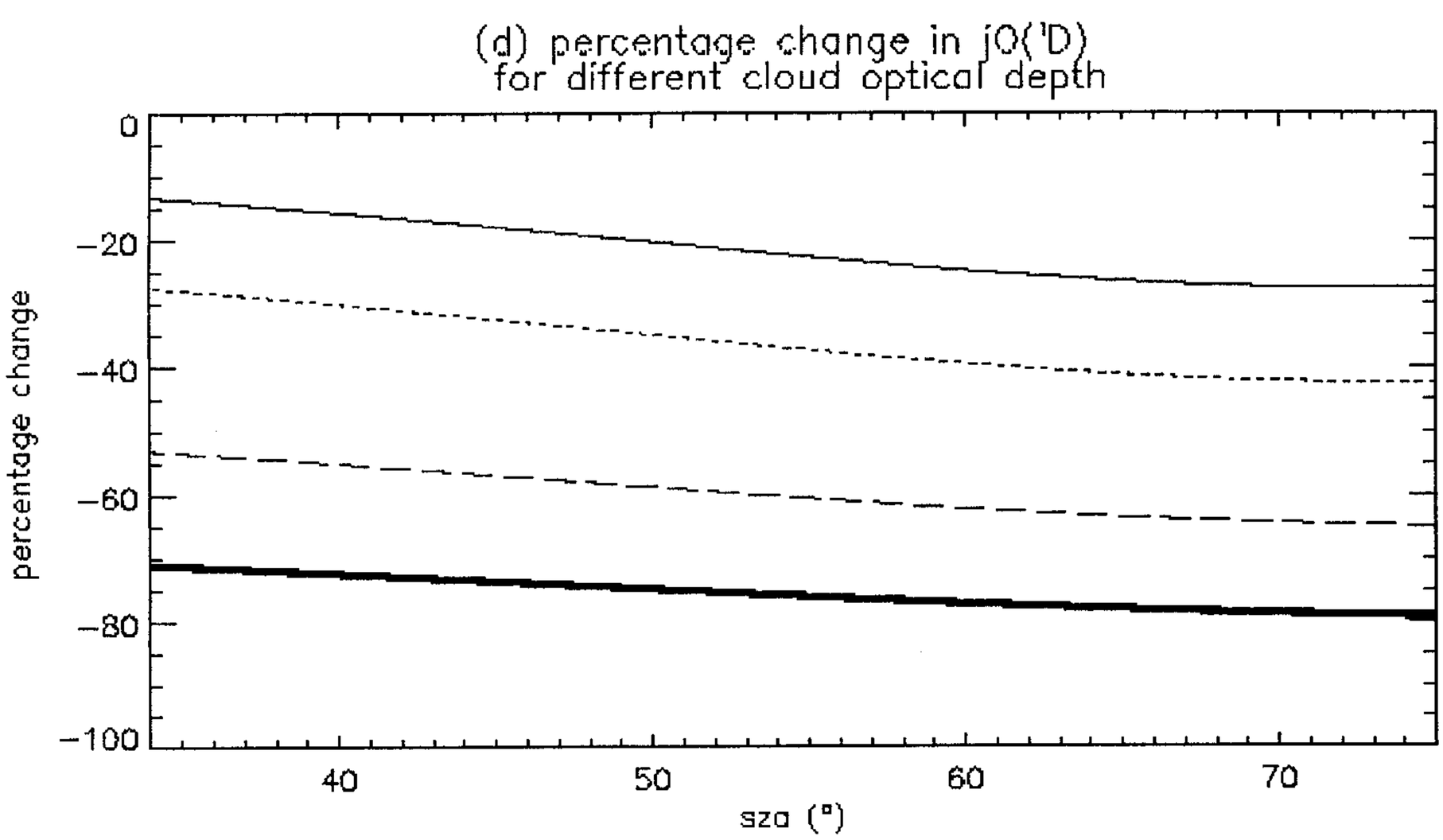


Figure 3.6(ii): (c) jNO_2 relative to clear sky (d) $jO(^1D)$ relative to clear sky τ=5 (solid), τ=10 (dotted), τ=25(dashed), τ=50 (thick solid)

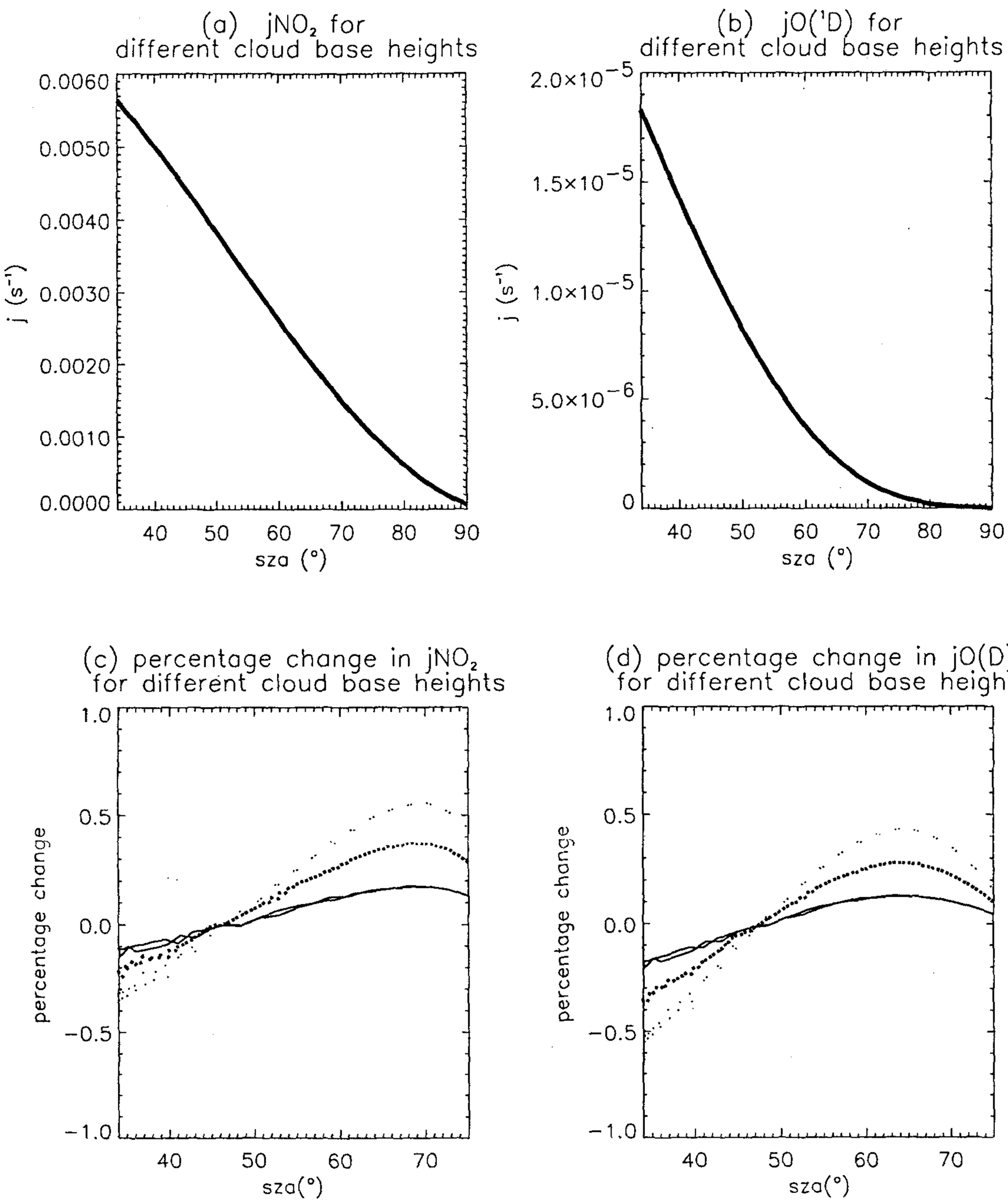


Figure 3.7: Sensitivity of jNO_2 and $jO(^1D)$ to cloud base height (a) jNO_2 (b) $jO(^1D)$ (c) percentage change relative to jNO_2 at 1 km (d) percentage change relative to $jO(^1D)$ at 1km
z=1 km (thick solid line), z=2 km (solid line), z=3 km (thick dotted line), z=4 km (dotted line)

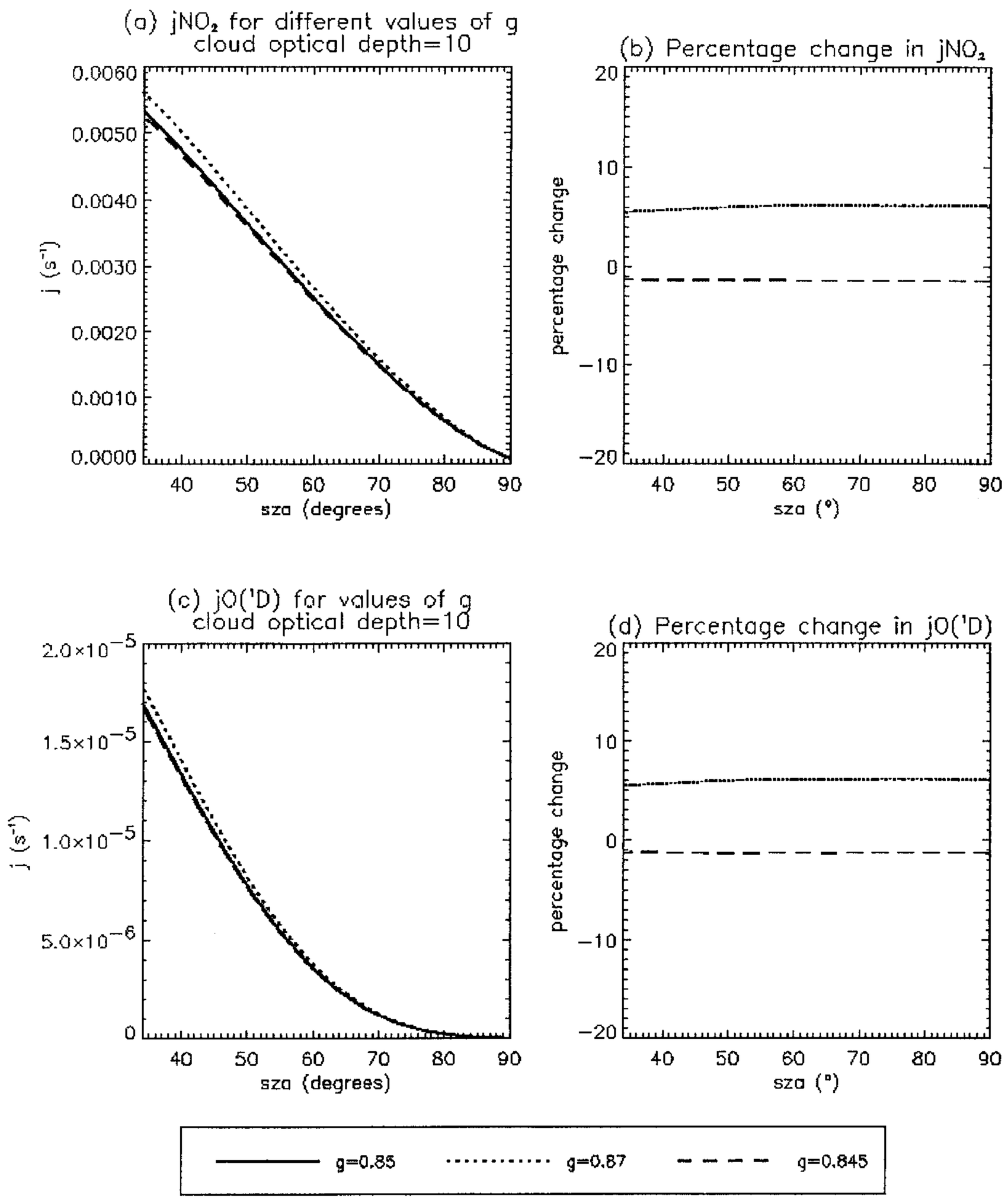


Figure 3.8: Sensitivity of jNO_2 and $jO(^1D)$ to asymmetry factor (a) jNO_2 (b) jNO_2 relative g=0.85 (c) $jO(^1D)$ (d) $jO(^1D)$ relative to g=0.85

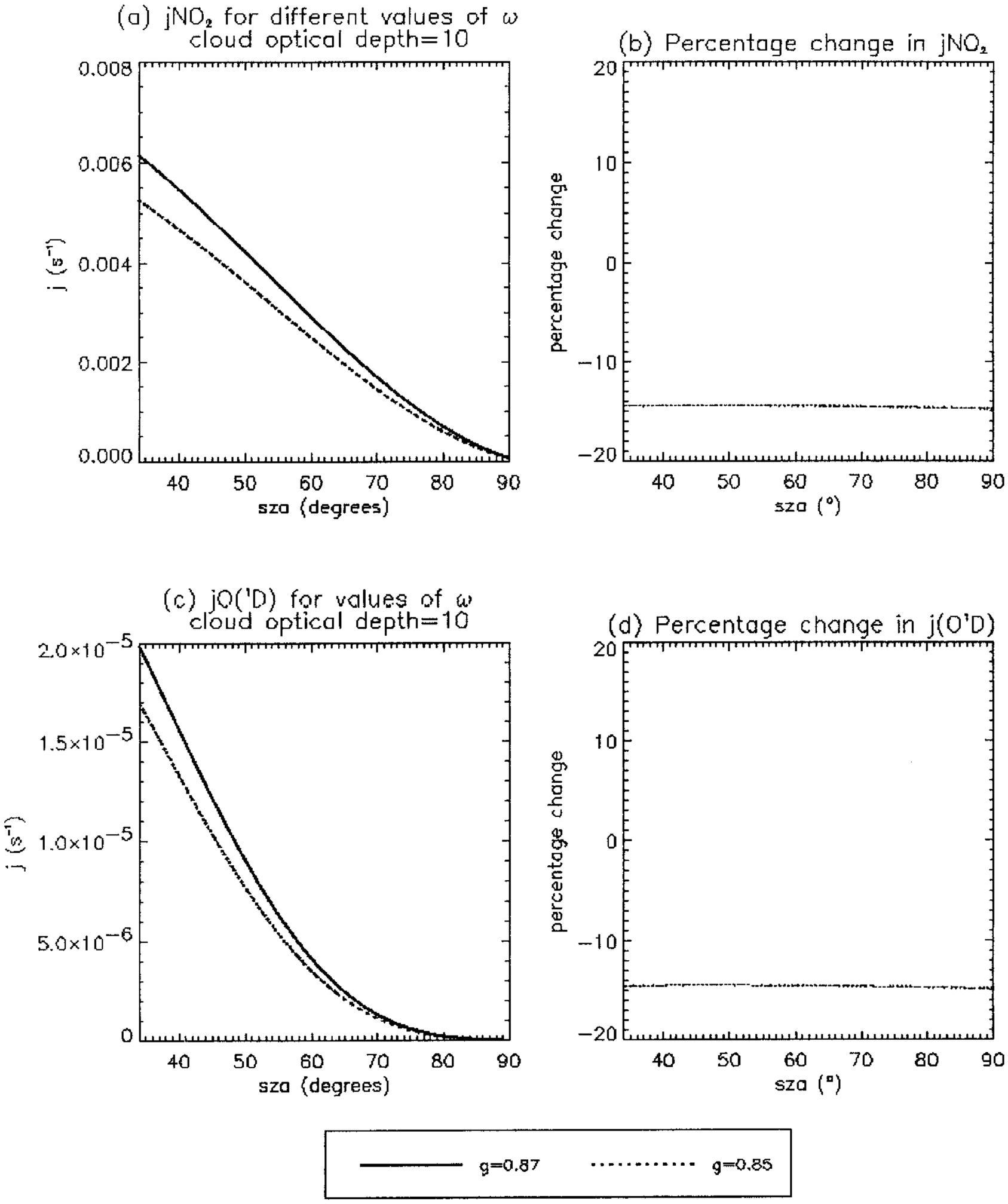


Figure 3.9: Sensitivity of jNO_2 and $jO(^1D)$ to single scattering albedo (a) jNO_2 (b) jNO_2 relative ω=0.9999 (c) $jO(^1D)$ (d) $jO(^1D)$ relative to ω=0.9999

4. Cloud optical depth distribution from photolysis frequency measurements

In this chapter, the nitrogen dioxide photolysis frequency measurements and the model response to increased cloud optical thickness are used in a new way to derive cloud optical depths from the data. These optical depths are used to derive a distribution of cloud optical depth that is shown to be significant for future calculations of photolysis rates and radiative fluxes in larger scale models.

Firstly, jNO_2 measurements are used to derive a clear sky photolysis rate parameterisation for jNO_2 at Mace Head. This is necessary because the altitude ranges specified for previously derived parameterisations make these parameterisations unsuitable for use at Mace Head. It is also desirable since this new parameterisation will take the specific atmospheric and surface conditions at Mace Head into account. This new parameterisation of jNO_2 is compared with those of previous authors.

The radiative transfer model described in chapter 2 is then used to calculate photolysis rate coefficients under clouds of different optical thicknesses. These cloudy sky photolysis frequencies are combined with the clear sky photolysis frequency to describe the effect of increased cloud optical depth on photolysis frequency. This function contains a ratio of the clear and cloudy sky values of jNO_2 in order to minimise the effect of any errors in the input parameters. The resulting parameterisation is used to obtain the ambient cloud optical depth from the measured photolysis rate coefficients.

The diurnal cycle of cloud optical depth at Mace Head is shown. Although this cloud optical depth is a truncated average, it gives an indication of the optical depth diurnal cycle for thick cloud.

Analysis of this optical depth data provides a frequency distribution. A lognormal probability distribution is then fitted and its use in this context justified. Possible implications and applications to the validation of climate models are discussed.

The derived optical depths are compared to those from satellite data and an explanation for the discrepancy between our optical depths and the smaller optical depths retrieved from satellite data is proposed. The derived distribution will be applied in chapter 5.

4.1 Introduction

The amount and thickness of cloud are important variables required to understand the radiation budget of the Earth. Quantifying cloud amount, type and optical depth is a common problem for atmospheric scientists. Ground based meteorological observations traditionally measure the coverage of clouds in eighths (oktas), and describe the height of the cloud (low, medium or high) and its type. Such observations are necessarily subjective, depending on the opinion or experience of the meteorologist. Not only might the meteorologist on the ground be unaware of multiple cloud layers obscured by the low cloud immediately above him, but also he/she can obviously give no information about optical properties such as the cloud optical depth.

Recently, the use of weather satellites has improved methods of cloud observation. Most cloud retrieval techniques give the cloud amount and the cloud top pressure (e.g. Kidder, 1995). There are two major steps in satellite observation: cloud detection and radiative modelling leading to the retrieval of cloud optical properties (e.g. Rossow *et al.*, 1989). There are a number of techniques for cloud detection based on the threshold technique: if a cloud is brighter (in the visible) or colder (in the IR) than a given clear sky threshold then it is counted as covered with cloud. Cloud properties such as optical depth are retrieved by comparing modelled clouds and radiances with radiative transfer models with the observed values. Although much more consistent, and more global, than trained observer methods, these data also have their shortcomings. For example, some clouds, e.g. low stratus, cirrus, or small cumulus can still escape detection (e.g. Kidder, 1995).

Little is known about the statistical nature of cloud optical depth because of its huge variability across space and time. Most of the existing information comes from the International Satellite Cloud Climatology project (ISCCP) (Rossow, 1989; Rossow and Schiffer, 1991). It is important to have an independent validation of the ISSCP data (e.g. Barker *et al.*, 1998) and to validate the retrieval of cloud optical depth from ground based measurements. Ground-based measurements have some advantages over satellite data: contributions from all clouds present will be sensed, and a smaller spatial resolution and higher time resolution can be obtained. However, it must be remembered that ground based measurements are local and so could never give the global picture available from satellite data.

The purpose of this study was to use photolysis frequency measurements in a new way to see if any information about cloud could be obtained from them. The method developed parameterises the modelled reduction of photolysis rate by the cloud as a function of cloud optical depth and solar zenith angle. The measured values of photolysis rate can then be used to infer an 'effective' cloud optical depth. This 'effective' cloud optical depth assumes that attenuation of photolysis rates in the atmosphere will follow the same function as that followed by the model.

Studies to derive cloud optical depth from the ground have been conducted by means of global irradiance measurements taken with Eppley pyranometers (0.3-4 μm). Loeyntiva and Stamnes (1994) presented values of cloud optical thickness derived from hourly mean values of incoming and reflected solar irradiance measured at Barrow, Alaska. They calculated transmittances with a delta-Eddington two stream approximation and compared clear and cloudy sky data to obtain cloud thickness. The cloud optical depth in the model was changed until agreement between calculated and measured irradiances was reached. Monthly probability density functions for these clouds showed that the average optical depth range was between 8 and 20. Similar work was undertaken by Barker *et al.*(1998) who inferred cloud optical depths from measurements of solar irradiance at 21 Canadian stations. A four stream version of DISORT (Stamnes *et. al.*, 1988) was used to generate

look-up tables for a given albedo. These contained values of broadband transmittance as a function of solar zenith angle and cloud optical depth. The optical depth was derived by linear interpolation between the entries. Although the distribution of cloud fraction detected from the ground has been fairly well discussed (e.g. Henderson Sellers, 1991), this study is one of only a handful in which a frequency distribution of cloud optical depth has been derived from these sorts of measurements (e.g. Ricchiazzi *et al.*, 1995; and those above). Here, we extend the frequency distribution to estimate a probability density function.

Much recent work has focussed on the attenuation by clouds of UV(A and B) radiation since this is important from a biological perspective (e.g. Matthijsen, 2000). The attenuation of radiation by clouds in the UV is generally thought to be smaller than in the rest of the shortwave (e.g. McKenzie, 1998). It is difficult to reliably infer UV radiation from broadband shortwave measurements. However, examination of jNO_2 allows us to directly study the effect of cloud on UV in a spectral region little affected by either ozone or water vapour absorption.

There are, of course, more accurate but more complex ways to measure cloud optical depth. Ideally, cloud optical depths would be retrieved using airborne back-scattered LIDAR (e.g. Pelon, 2000) and a microwave radiometer to measure the total liquid water, as well as a measure of extinction. However, such instruments are not always available and are complex to use: time and money simply would not allow their use on a measurement campaign not specifically dedicated to the study of clouds.

At Mace Head, the photolysis frequencies are measured every minute. Previous work in the solar has used hourly averaged values, here ground based observations of the much shorter timescale variability of cloud optical depth are used.

4.2 Method

In this chapter, only NO_2 photolysis frequencies are considered. It is possible to derive a normalisation for $jO(^1D)$ with total ozone by plotting $jO(^1D)$ against total column amount,

e.g. Reuder *et al.* (1999). However, to achieve this a number of clear sky points are required and the column ozone must be known accurately. Since the ozone column is derived once daily from TOMS, there is not enough information to perform this procedure with any degree of accuracy. Additionally, the clear sky days all have very similar ozone column values and extension of this small range to the much larger range seen over the entire campaign could introduce further uncertainty. The use of $jO(^1D)$ at UVB wavelengths would therefore complicate the analysis and lead to unnecessary errors.

4.2.1 Clear sky parameterisation

Two parameterisations for clear sky nitrogen dioxide photolysis frequency in terms of zenith angle have been published. These have both been derived from measurements.

The first parameterisation was proposed by Dickerson *et al.* (1982). They analysed data obtained with a chemical actinometer in Colorado and comparing them to previous work, proposed a parameterisation was suitable for conditions of zero surface albedo and altitudes 0.3 to 3.0 km.

$$jNO_2(\theta) = 0.0167 \exp(-0.575 \sec\theta) \quad (4.1)$$

The second expression, of Parrish (1983), uses measurements also taken from a chemical actinometer in Colorado. This parameterisation is suitable for conditions of low aerosol number density, low background surface albedo and a surface elevation of 3 km. The data were taken from three 'cloud-free' days. The authors further eliminated any noise due to small clouds from their data.

$$jNO_2(\theta)=0.01305\exp(-0.360\sec\theta) \quad (4.2)$$

The altitude dependence of these parameterisations means that neither is suitable for Mace Head data. The station is only 17 m above sea level. Another clear sky parameterisation must, therefore, be found.

The radiative transfer model could be used to obtain a clear sky photolysis frequency at a particular zenith angle and so derive a zenith angle parameterisation. However, this parameterisation would be subject to errors caused by estimating the model inputs - the

albedo, aerosol optical depth etc. (see chapter 3). A more suitable parameterisation can be obtained directly from jNO_2 measured at Mace Head.

The authors who published clear sky photolysis frequency curves did not make it clear how the clear sky data was chosen. It can only be assumed that their 'clear sky' measurement refers to measurements taken at times when no cloud was observed in the sky above their instruments. However, at Mace Head, where the cloud field is highly variable on minute timescales, the frequency of meteorological observations does not allow for this procedure. It is unlikely that any observer would be able to look up at the sky every minute to look for clouds. As discussed in chapter 1, the theoretical clear sky curve is a smooth curve. However, examination of the Mace Head data shows that there are frequent reductions from this clear sky value. If the maximum photolysis frequency occurred under conditions of clear sky, then the clear sky curve could simply be obtained by grouping the whole data set by zenith angle and finding the maximum photolysis frequency in each zenith angle bin. A curve could be fitted through this to correspond to the clear sky situation. However, it is well known that the maximum photolysis rates for a particular zenith angle may be caused by enhancements under broken cloud fields (see chapter 1). Thus, the use of this method would give an artificially high clear sky photolysis rate.

The clear sky photolysis rate was parameterised as a function of zenith angle by examination of photolysis frequency data. Initial examination of the solar irradiance data showed that there were some portions of days that could be considered clear sky: they were smooth with no deviations from a clear sky profile. The jNO_2 data on these days were then examined and portions that contained clear sky data could be seen. Dips and spikes were removed from the data to leave a smooth curve and a curve fitted such that no reading deviates from the curve more than 5%. In some cases, when the data was plotted as a function of solar zenith angle, different clear sky profiles were evident in the morning and afternoon data. This was consistent with a smaller aerosols which would scatter less as the atmosphere warms and dries in the afternoon. Clear sky curves were obtained for each day. The data points used to make these curves were then all used and a curve fitted

to them (see Figure 4.1). The data were also filtered so that only values for solar zenith angles of less than 75° were included. Figure 4.1(a) shows this clear sky data as a polynomial fit of the cosine of the solar zenith angle. There are, in fact, several similar curves. This is due to slightly differing background atmospheric conditions, probably mainly different aerosol loadings, for the days considered. For direct comparison to previous work, the fit is also presented as an exponential fit in terms of the secant of the solar zenith angle (Figure 4.1(b)).

$$jNO_2(\theta)=0.0164\exp(-0.4876\sec\theta) \quad (4.3)$$

The correlation coefficient confirms that this is a reasonable approximation to the data.

Table 4-1: Comparison of parameterisations for clear sky jNO_2

	$jNO_2(s^{-1})$		
sza	This study	Parrish (1983)	Dickerson (1982)
	19m	3 km	0.3-3.0 km
35°	9.30	13.5	8.17
65 °	5.36	5.76	4.28

Tale 4.1 shows a comparison of the values obtained using the new parameterisation with the two existing parameterisations at two different zenith angles. As expected, this parameterisation for clear sky jNO_2 gives lower values than those predicted from the parameterisation developed by Parrish (1982) : photolysis rates generally increase with altitude. The overestimation of clear sky jNO_2 found when their parameterisation is used is in agreement with previous studies (e.g. Wiegand, 2000). Our photolysis frequencies are higher than those calculated by Dickerson *et al.* (1983). However, since his parameterisation holds for conditions of zero surface albedo, this is to be expected. Dickerson claims the parameterisation is accurate to about 10% "for mostly sunny conditions". The disagreement with our derived photolysis frequencies for noon at Mace Head is within this experimental range, but increases towards larger solar zenith angles.

4.3 Cloud optical depth from photolysis frequency

4.3.1 Method: Parameterisation of model response

The modelled response of the nitrogen dioxide photolysis frequency to cloud was parameterised. In this analysis, for simplicity, it is assumed that the cloud present comprises water cloud only. According to Barker *et al.* (1998), this may only lead to slight overestimates of optical depth because: (1) there is very little difference between the asymmetry factor of ice and water clouds at these wavelengths, and (2) the difference in single scattering albedo results in very small differences to the amount of radiation transmitted through the cloud. Clouds are considered as infinitely thin layers, with a single scattering albedo =0.9999 (Hu and Stamnes, 1993) and an asymmetry factor of 0.85. (Matthijsen, 1998).

A US standard model atmosphere was assumed for all calculations. The aerosol profile of Eltermann (1968) was included within this atmosphere. The assumption of an aerosol profile is necessary because the 'real' clear sky atmosphere will also include aerosol of an unspecified amount. The ground albedo was taken as 0.1 and an ozone column of 324 DU was used. The sensitivity chapter shows that jNO_2 is not very sensitive to the magnitude of the ozone column. For a similar reason, a NO_2 column was not included. The model was used to calculate photolysis frequencies for a range of cloud optical depths, from clear sky (τ=0) to cloud optical depth of 200. For every minute of the day, the natural logarithm was then taken of the ratio of the model clear to model cloudy photolysis frequency for every cloud optical depth. The use of the ratio makes this method less sensitive to the absolute clear sky conditions. Figure 4.2 shows the cloud optical depth plotted against natural log of the ratio of the clear and cloudy sky photolysis frequencies. This ratio is non-linear with optical depth- if the Beer Lambert law were obeyed, it would be expected that this function would be linear. However, since scattering and the diffuse flux are also important at jNO_2 wavelengths, a curved function is obtained. As expected, this function is different for different solar zenith angles (see equation 4.4).

$$\ln\frac{j_c}{j_{od}} = f(\tau,\theta) \qquad (4.4)$$

A polynomial fit can be used to describe the dependence of this ratio on optical depth. This polynomial fitting was repeated for a range of solar zenith angles. A series of polynomial fits was obtained, one for each zenith angle. The dependence of the polynomial coefficients (a, b, c) with zenith angle was then described with a further set of polynomial functions. In this way, the dependence of the parameterisation on both zenith angle and cloud optical depth was described.

However, fitting such functions requires approximations that generate errors. In order to minimise the error of the fit to less than 5% at every optical depth, it was necessary to introduce some constraints. The curvature of the function is much greater at low optical depths, that is, the reduction in photolysis frequency with optical depth is much greater at low cloud optical depths. The accuracy of the fit was therefore improved by splitting the function into two regions: one fit for 'low' cloud optical depths (10-40) and one fit for 'high' cloud optical depths (40-200). Two separate polynomials were then employed for each region. A further set of polynomials was introduced to describe the boundary at which the regime from 'low' optical to 'high' optical depth fits ('boundary fits'). In addition to this, the parameterisations with zenith angle were found to be limited to zenith angles less than 60°. Above this threshold, the behaviour can no longer be adequately described by a polynomial.

Figures 4.3(a) and (b) show the accuracy of the fit for different cloud optical depths. The fit for low optical depths (a) is less accurate than the fit for high optical depths (b). The maximum error of <5% occurs at the cloud optical depth of 10. These fits give the ratio of the model clear sky photolysis frequency to cloudy sky photolysis frequency for each optical depth and zenith angle. This parameterises the response of photolysis rates to cloud, in the model and so provides a basis for comparison with the real atmosphere. Further fits were also derived for infinitely thin clouds with their bases at different atmospheric heights (2,3 and 4 km).

For each solar zenith angle less than 60°, at which a measurement for jNO_2 existed, the time of measurement was converted into a zenith angles via the well-known equations

connecting the day, hour angle, and latitude (e.g. Finlayson and Finlayson-Pitts, 2000). For this zenith angle, a clear sky jNO_2 then was calculated from the clear sky parameterisation. These clear and measured data ('cloudy') points were then used to create a ratio, the natural logarithm of which was assumed to follow the same function as derived from the clear and cloudy model responses (equation 4.4). The fits were then used to derive a cloud optical depth corresponding to the ratio. The boundary fits were used to decide whether the data point should be considered a 'low' or 'high' optical depth case, and data was processed accordingly.

4.4 Results

The derived optical depths require careful consideration. These are derived cloud optical depths, assuming that the real atmosphere responds to cloud thickness in the same way as the model. Necessarily, some constraints must be placed on these derived cloud optical depths. Firstly, derived cloud optical depths of less than 10 cannot be considered in any analysis since the fitting equation is not valid for this region of low cloud optical depth. Secondly, the method assumes that the attenuation of photolysis rate is caused by changes in cloud optical thickness. An optical depth of 10 is sufficiently high to be caused by cloud and not a combination of aerosol and/or an absorbing gas and should limit the sensitivity to variations in these other quantities. Even if it were possible to extend the fits to cover the complete range of optical depths, it would be impossible to definitively attribute a small optical depth change to cloud and not some other factor. At a higher optical depth, it is likely that at least most of the change between the clear sky and measured photolysis frequency is due to cloud.

In addition to this difficulty in attributing low optical depth changes to cloud, another problem occurs with optically thin clouds. Under optically thin clouds (τ=4), the conversion of direct to diffuse flux can lead to actinic flux enhancements either when the sun is not obscured by the cloud (see Lantz *et al.*, 1996) or when the sun is obscured and the sun is overhead (see e.g. Madronich, 1987a). It is, therefore, advisable to consider

cloud optical depths where these enhancements will not be seen and the chosen boundary takes account of this.

The derived optical depth was checked against solar zenith angle to ensure no underlying dependence existed. This parameterisation provides a computationally cheap, easy method of determining cloud optical depth using pre-existing instrumentation.

4.4.1 Diurnal cycle of 'thick' cloud

Figure 4.4 and 4.5 (a) show the optical depths (greater than 10) derived for the 1996 and 1997 campaigns as a function of local time (GMT). In these figures, values shown are calculated from the one minute photolysis frequencies. It can be seen that the maximum optical depths, for the same solar zenith range, during EASE97 are much larger than the maximum optical depths for EASE96. However, it is more helpful to consider a 'weighted' optical depth, which is an average only including the values that are greater or equal to 10. This is achieved by summing the values of minute-frequency optical depths with values greater than 10 seen in one hour, then dividing by their number. This weighted, or truncated average, optical depth is shown as a function of time in Figure 4.4 and 4.5(b). The standard errors are also included. A diurnal cycle is evident for both years, with optical depth of thick cloud increasing towards the middle of the day. This is in agreement with Leontieva *et al.* (1994) who, deriving cloud optical depth measurements from 10 years of solar irradiance data, found an increase in cloud optical depths during the middle of the day for Bergen in the summer. Increased temperature during the day would lead to increased cloud thickness e.g. for convective cloud. However, frontal cloud might thin in the afternoon as the dew point temperature drops.

4.4.2 Frequency distributions and derivation of a probability density function

The frequency distribution of the cloud optical depths is shown in Figure 4.6(a)(i)-(d)(i). As can be seen, it is relatively robust in terms of sensitivity to bin size. The distribution is skewed towards higher optical depths and characterised by a long tail. This is in agreement with previous derived cloud frequency distributions (e.g. Leontieva *et al.*, 1994, Ricchiazzi, 1995, Barker *et al.*, 1998). Figure 4.7(a)(i)-(d)(i) shows the data derived for

fits at different cloud base heights. It can be seen that the different heights of the cloud make very little difference to the form of the curve.

A frequency distribution is of limited utility: a better description of data is given by a probability density function. This would allow our optical depths to provide a possible method of validating cloud optical depths generated by General Circulation Models (GCMs). In this work, the frequency distribution is incomplete due to the necessary imposition of a low optical depth boundary, as discussed above. This incompleteness causes problems in terms of defining a probability distribution. The transformation from a frequency distribution to a probability distribution properly requires knowledge of the total number of events, which is simply a constant. However, in this case, the total number of events is not known since there can be no knowledge of the distribution below the cut-off value, 10. It is impossible to say how many of these smaller events are bona fide cloud attenuation events: some could be changes due to gas or aerosol or even flux enhancements due to thin or broken cloud. It is, therefore, difficult to characterise the underlying distribution: neither the mean, nor the variance of an incomplete sample can be calculated. In the case of a complete distribution, a fitting technique such as L-moments (Hosking, 1990) could be used. This procedure would allow easy comparison between the fit of the data to different probability distributions. Since this is not possible with these data, another approach must be attempted.

We must first consider likely probability distributions to fit these data. The skewed shape and long tail preclude a Gaussian distribution.

The long tail of the distribution is reminiscent of a power law. A power law is an equation of the form:

$$f(x) = cx^{\alpha} \tag{4.5}$$

where c and α are constants.

Power laws are self-similar, if x is multiplied by a constant, then f(x) is still proportional to x^{α}, although with a different constant of proportionality. Power laws are believed to

characterise many natural systems and there has been increased interest in the application of power laws as a means of describing natural data in the last few years (e.g. Sornette, 2000). Many natural systems are described as "fractal" or "self-similar".

A common method used to examine frequency distributions is to plot the data on a double logarithmic (log-log) plot. Figure 4.6 (a)(ii)-(d)(ii) shows our frequency distribution plotted in this way for different bin sizes. On this log-log scale, a limited linear regime followed by clear curvature can be seen. This holds for each bin size, but as the size of the bin decreases, the points become more scattered (compare 4.6(d)(ii) with 4.6(c)(ii)).

The data for cloud heights are also plotted in a similar way (Figure 4,7(ii)(a)-(d)).This curvature shows that this distribution is not a power law, since power laws are straight lines on double logarithmic plots.

However, most natural distributions have a curved log-log plot; the curvature means that a thinner tail than predicted by a power law. Although this is usually interpreted as a constraint imposed by the finite size of the system, it could simply be that these 'power laws' are not, in fact, power laws at all (Laherrère *et al.,* 1998). A quadratic can be fitted to these data and this fit is known as a quadratic exponential which has been seen to characterise various systems. However, although a quadratic exponential is recognised, and valid in the case of this data, it has no real physical meaning. For this reason, Laherrère *et al.* (1998) proposed the 'stretched power law' to describe probability density functions where such a curvature is observed on a log-log plot.

$$P(x)dx = c(x^{c-1}/x_0^c)\exp-(x/x_0)^c dx \qquad (4.6)$$

where c is the inverse of the number of generations in a multiplicative process
and x_0 is related to the critical size of the system

The stretched power law is found when the exponent, c, is less than one. The upper limit, c=1, corresponds to the usual exponential distribution. This distribution successfully describes many systems that were previously characterised by power law probability

distributions e.g. biological extinction events, earthquake distributions, and fault displacements (e.g. Laherrère *et al.,* 1998).

The cumulative form of this distribution is written:

$$P_c(x) = \exp\left[-\left(\frac{x}{x_0}\right)^c\right] \tag{4.7}$$

Using the method of Laherrère *et al* (1998), the data is rank-ordered so that the largest value has the lowest rank, i.e.value $Y_1 > Y_2 > Y_3 .. > Y_N$. Following equation 4.7, it can be seen that within a rank ordering plot, where n is the rank, the stretched exponential can be described as a straight line when Y_n^c is plotted as a function of the natural log of n.

$$Y_n^c = -a \ln n + b \tag{4.8}$$

For this method, which emphasises the rare, highest optical depth data points, it is not important that some of the low optical depth data is missing. This method is used precisely to emphasise the tail of the data. The y-axis is the optical depth to the power of the exponent.

As we can only estimate c, the optical depth is plotted as a function of the logarithm of the rank for a number of different values of c between 0 and 1. If the function were a stretched power law, then a straight line would be obtained. Although the correlation coefficient is very high, the data clearly deviate from the stretched exponential (see Figure 4.8). The difference occurs at low rank, so this stretched exponential fit does not adequately describe the tail of the data.

Another skewed, and very commonly used, distribution is the lognormal distribution. This distribution has an even thinner tail than either the power or stretched power laws (e.g. Laherrère *et al.,*1998) and therefore seems more likely to fit our data. The lognormal distribution appears in many different branches of science and is used to describe distributions of variables as diverse as: minerals resources in the Earth's crust, cancer

patient survival times and the population of species. The probability density function of the lognormal distribution is given by:

$$f(x) = \frac{1}{\sqrt{2\pi}\sigma x} \exp - \frac{(\ln(x) - \mu)^2}{2\sigma^2} \qquad (4.9))$$

where μ and σ are parameters associated with the shape of the distribution

To test for the lognormal, the natural log of the frequency was plotted as a function of the bin. In the case of a lognormal distribution, a straight line must be obtained.

$$\ln[f(x)] \alpha \left(\frac{\mu}{\sigma^2} \right) \ln(x) - \frac{\ln(x)^2}{\sigma^2} \qquad (4.10)$$

A μ and σ^2 must be estimated to complete this procedure. An iterative approach was used. The fit of the line was found to be much more sensitive to μ than to σ^2, so this was the first parameter fitted. Taking steps of 0.05, the highest correlating straight line was found with the μ equal to 3. Repeating the procedure with a μ equal to 3, and steps of σ^2 =0.1, the best correlation was found with a σ^2 of 0.7 (see Figure 4.9). This seems a relatively crude method of estimation, especially as it also seems relatively insensitive to the chosen bin size.

This simple procedure can be improved. As previously mentioned, we have no means of knowing how many of the small optical changes are due to cloud, so no value for the total number of events, N. However, with a best-fitting technique, the values of N, μ and σ can be estimated from the data. The value of a point in our bin, n, can be estimate by the product of the total number of points, N, the probability density function, $P(\tau)$ and the bin size ($d\tau$) (pers. comm., G. Pettatino, 2000). A standard curve fitting algorithm which computes a non-linear least squares fit to a user supplied function can be used to estimate N, μ, and σ^2. The results of this fit are shown in Figure 4.10. Figure 4.10(b) shows the results obtained when an average of the distributions obtained from the fits for the four different cloud base heights (1-4 km) is used. There are two limitations associated with this method. The first limitation is that it can only be used for simple analytical functions - the curve-fitting algorithm requires inputs of the partial derivatives of the fitted function

with respect to the required variables. The second limitation is that results of this method are very sensitive to the chosen bin size. The bin size must not be too small because chi-squared fits cannot be used where there are too few points in the bin. However, the bin size must be sufficiently small, so that the resolution adequately captures the shape of the distribution. This sensitivity of the fit to bin size is a common problem when fitting probability distributions.

Table 4-2: Properties of the lognormal distribution, $\Lambda(\mu, \sigma^2)$ (adapted from Aitchison and Brown(1956)) including values obtained from different estimation techniques used in this study

		Method 1	Method 2	Maximum estimate	Minimum estimate
	μ	3.0	2.98±0.02	3.0	2.96
	σ	0.83	0.84±0.02	0.86	0.82
Mean	$\exp(\mu+\sigma^2/2)$	28.5	28.0	29.1	27.0
Mode	$\exp(\mu-\sigma^2)$	10	9.72	9.6	9.85
Median	$\exp(\mu)$	20	19.7	20	19.3

The mean, mode and median from this technique, and the previous one, are presented in Table 4.2. It is interesting to note that the simple linear method results in a distribution with parameters that lie within the bounds of the errors estimated by the more complex curve fitting technique. The mode lies between 9.6 and 9.85 (never sampled because of the cut-off value at τ=10), the median between 19.3 and 20, and the mean between 27 and 29.1.

Barker *et al.*(1998) also presented optical depth distributions for Canada in summer (June, July, and August). The found a gamma distribution fitted their data well. However, gamma distributions and lognormal distributions can appear very similar. The mean values of optical depth were largest for southern continental sites (30-35) and smallest for continental subarctic sites (20-25). These mean optical depths are consistent with those calculated in this study. It is not possible to use a simple curve-fitting algorithm to a gamma distribution - it has no simple analytical expression and so cannot be fitted to these

data for comparison. In any event, we believe a lognormal is the most appropriate distribution to use to describe a distribution of cloud optical depth, as discussed in the following section.

4.4.3 Support for the lognormal distribution

As mentioned before, the lognormal distribution appears across the sciences. In atmospheric science, the size of aerosol is regarded as lognormally distributed (e.g. Jacobson, 1999) and the size spectrum of cloud water droplets is often assumed to be lognormally distributed (e.g. Costa *et al.*, 2000; Miles *et al.*, 2000). Mean rain rate has also been described as lognormally distributed (e.g. Kedem *et al.*, 1997).

Why is the lognormal so popular? A good explanation for the wide-ranging presence of the lognormal distribution can be found by drawing an analogy to the well-understood normal distribution. The normal distribution is a consequence of the central limit theorem. The central limit theorem states in the limit of a large number of distributions, the sum of many independent distributions will tend towards the Gaussian (i.e. normal) distribution. However, the central limit theorem still holds with weakly correlated variables and in distributions with variances of a similar order of magnitude. The lognormal distribution is a special case of the normal distribution where the logarithm of the variate, rather than the variate itself, is normally distributed. The properties of logarithms mean that this is the result of a multiplicative form of the central limit theorem. A lognormal distribution is a 'natural approximate consequence of a random multiplicative process' (Nelkin *et al.*, 1996)

Two complementary explanations for the presence of the lognormal description of cloud optical depth distributions are proposed here. The first follows experimental observations of cloud liquid water and the second is a physical argument.

The distribution of cloud liquid water has been observed to be lognormal, both in the tropics (Westwater *et al.*, 2000) and over North America (Gultepe, 1994). Calahan *et al.* (1994) show a 'lognormal-like' distribution for the liquid water path. Our measurements

are ground based and sample the cloud moving overhead rather than being sampled whilst flying through the cloud. We know that the optical depth of a cloud is related to the liquid water path by the effective radius, r_{eff} (Equation 2.29). If we consider a lognormal distribution of cloud liquid water and consider that the effective radius of a droplet size distribution is approximately constant, or of very small variability, we see that the distribution of the cloud optical depth will be proportional to the distribution of the cloud water, i.e. also lognormal.

It is of interest to note that the variability of cloud liquid water distributions has been analysed and shows a remarkable similarity between the microphysical and macrophysical process that determine cloud structure in the marine boundary layer (e.g. Davis *et al.*, 1999). If the distributions of liquid water content were truly scaling, then our lognormal distribution would be valid on different scales. This could be investigated by repeating the analysis with similar ground based measurements sampled on different timescales.

Clouds are formed by the release of latent heat. A number of conditions need to be met before a cloud can form: in the presence of cloud condensation nuclei, this is dictated by the concentration of water vapour, the temperature and pressure. Examination of a tephigram (e.g. McIlveen, 1992) shows that presence of a cloud layer can be predicted if the vertical profiles of temperature, pressure and humidity are known. Presence of a cloud of particular optical depth will be further dependent on a larger number of factors: the liquid water content, the vertical cloud extent, and the droplet size distribution; suitable pressure gradients, temperature gradients, which will in turn be dependent on further distributions of variables such as wind shear, and ground roughness. The droplet size distribution will in turn be dependent on the number and size of cloud condensation nuclei and the concentration of atmospheric water vapour.

If the probability of a first cloud condition required to form a cloud of a particular optical depth occurs with a probability, $P_1(\tau)$, and the second cloud forming condition with a probability, $P_2(\tau)$, etc., the total probability of a cloud formation, $P_c(\tau)$, will be given by the product of all the probabilities for the processes, $P_1(\tau)$ to $P_n(\tau)$.

$$P_c(\tau)=P_1(\tau).P_2(\tau).P_3(\tau).....P_n(\tau) \quad (4.11)$$

These will be different for different types of cloud. If each of these processes follows a different distribution and these are multiplied together, the resulting distribution will be a lognormal distribution according to the central limit theorem.

4.4.4 Comparison with ISCCP satellite data

The ISCCP (International Satellite Cloud Climatology Project) data set provides 10 years' worth of satellite derived cloud optical depth data over the Mace Head site, from July 1983 until December 1993. The EASE96 took place in July and August 1996, whereas the EASE97 campaign was conducted in April and May 1997.

Table 4-3: Monthly ISCCP derived (D1) data for the Mace Head site

Month	Average τ	σ^2
July, August, April, May	5.36	1.26
April	4.90	1.60
May	4.90	0.986
July	6.10	1.25
August	5.45	0.561

Table 4.3 shows the 3-hour data averaged by month for all of the 10 years of the ISSCP dataset (D1). ISSCP optical thicknesses are for a wavelength of 600 nm. Calculations of the extinction cross-section for water droplets (J.E. Russell, pers. comm., 1999) show that extinction cross-section increases slightly with wavelength and so, these optical depths are expected to be slightly greater than those derived from jNO_2 wavelengths.

It can be seen that the values for the cloud optical depth are considerably smaller than those derived by our method. This is consistent with previous studies. Previous work has found optical depths from ground-based observations have been reported as much larger than those derived from satellite observations. Barker *et al.* (1998) found that for two locations, the values of optical depth obtained from surface measurements were 1.6 times larger than those obtained from satellite measurements, with most in the range of 1.25-

2.25 as large. Min *et al.* (1996) also found that, for high optical depths, the ground-based measurements were higher than those obtained from satellite data by a factor of 2.

Barker *et al.* (1998) proposed that the difference between the two types of measurement might be due to anomalous absorption. We treat this assertion with caution. We propose another reason why the ground-based measurements could be higher than the satellite derived measurements. This is a potential problem associated with partially filled pixels. A pixel may be above the cloud threshold and so diagnosed as cloudy, but still be incompletely filled. The optical depth would be retrieved as if the whole pixel was cloudy and thus this would lead to a lower optical depth over the area of the pixel. There are yet more reasons to explain a difference between these satellite derived data and our ground-based retrievals. Firstly, these ISSCP data were not taken concurrently with EASE96 and EASE97 so cannot be compared exactly to the measurements at Mace Head. Secondly, there is an issue of the validity of comparing an approximately monthly average of 1-minute data with a monthly average of 3-hour data exists. In the next section, we show that there is a discrepancy caused by the analysis (temporal and spatial averaging), which may also contribute to the difference in optical depths retrieved from satellite and ground-based methods.

4.5 Impact of lognormal distribution of cloud optical depths and photolysis rates

The lognormal distribution for the optical depths derived at Mace Head has profound consequences for modelling. This can be illustrated by comparing the photolysis frequencies ($\langle j_{\tau,mean} \rangle$) calculated using the mean optical depth with the mean photolysis frequencies ($\langle j_{\tau,dist} \rangle$) obtained from the whole distribution. In this experiment, the values of μ and σ were taken as 2.98 and 0.84 respectively.

Firstly, the mean optical depth, τ_{mean} ($=\exp(\mu + \sigma^2/2)$), was used to calculate the photolysis frequencies, $\langle j_{\tau,mean} \rangle$. A random series of optical depths conforming to the lognormal cloud probability density function was then generated and the photolysis rates associated with each point calculated. The mean of this photolysis rate series, $\langle j_{\tau,dist} \rangle$ was then calculated for comparison with the photolysis rates calculated from the distribution mean,

$\langle j_{\tau,mean} \rangle$. The results are shown in table 4.4. Photolysis frequencies calculated from the mean of the distribution were much lower than the mean of those calculated from the entire distribution. This implies that the use of an average optical depth in a chemistry model would severely underestimate the photolysis rates obtained in a particular gridbox with potentially huge impacts on the modelled chemistry of the atmosphere (see chapter 1 for a discussion of the importance of photolysis rates).

Table 4-4: Comparison of the mean of the photolysis frequencies obtained from the distribution and the photolysis frequencies obtained using the mean of the distribution.

θ (°)		$\langle j_{\tau,mean} \rangle$ (s^{-1})	$\langle j_{\tau,dist} \rangle$ (s^{-1})
55	jNO_2	1.675×10^{-3}	2.575×10^{-3}
	$jO(^1D)$	3.140×10^{-6}	4.647×10^{-6}
35	jNO_2	2.933×10^{-3}	4.378×10^{-3}
	$jO(^1D)$	9.757×10^{-6}	1.413×10^{-5}

This difference between the photolysis frequencies can be explained by examining the effect of cloud on jNO_2 (Figure 4.11). The reduction of the photolysis frequencies by cloud is non-linear with optical depth. In the case of a linear relationship between photolysis frequency and cloud, the average photolysis frequency from the distribution average, $\langle j_{\tau,mean} \rangle$ would be the same as the distribution averaged photolysis frequency, $\langle j_{\tau,dist} \rangle$. However, the attenuation of photolysis frequency as a function of optical depth is not at all linear. Therefore, at low optical depths where the transmission is largest, this large transmission, even at low probability optical depths, leads to a large contribution to the mean, $\langle j_{\tau,dist} \rangle$. $\langle j_{\tau,dist} \rangle$ is therefore much larger than $\langle j_{\tau,mean} \rangle$. Both the non-linearity of transmission with optical depth and the presence of a probability distribution of optical depths could contribute to the difference between $\langle j_{\tau,dist} \rangle$ and $\langle j_{\tau,mean} \rangle$. However, as the presence of the difference is primarily due to the non-linearity of the transmission function, the difference between $\langle j_{\tau,dist} \rangle$ and $\langle j_{\tau,mean} \rangle$ will be seen for any distribution of optical depths, not just the lognormal used in this study. The mean value of the cloud optical depth is, therefore, not an appropriate value to use to obtain fluxes at a particular

grid-box. Some consideration of the variance, or width, or a parameter that describes the shape of the distribution, must also be considered.

This difference will not just exist for attenuation of flux by clouds. Any atmospheric constituent that causes a non-linear attenuation of flux will cause the same problem (e.g. aerosol, ozone, water vapour).

We have shown that the mean photolysis frequency, $\langle j_{\tau,dist} \rangle$, calculated from the sum of the individual photolysis frequencies corresponding to the individual optical depth of the distribution, is much larger (a factor of 1.6, depending on the photolysis frequency and the solar zenith angle) than the photolysis frequency calculated directly from the mean of the distribution. We will call the optical depth that corresponds to $\langle j_{\tau,dist} \rangle$, the "effective optical depth" of the cloud distribution, $\tau_{eff,\ dist}$. Comparison of $\langle j_{\tau,dist} \rangle$ with $\langle j_{\ \tau,mean} \rangle$ shows that $\tau_{eff,\ dist}$ is lower than τ_{mean}. $\tau_{eff,\ dist}$ varies slightly with solar zenith angle, but is always expected to be less than τ_{mean}. For this distribution, $\tau_{eff,\ dist}$ is around 20, closer to the median of the cloud optical depth distribution. Further investigation is required to establish the exact dependence of $\tau_{eff,\ dist}$ on zenith angle and to see if it is a robust quantity for use in atmospheric models. The use of the mean cloud optical depth is inappropriate to atmospheric modelling and can lead to large errors. It is without doubt that this could have far reaching consequences, but further work is required to establish the details of these.

As an addendum, the difference between $\tau_{eff,\ dist}$ and τ_{mean} could provide the beginning of an explanation for the difference between the cloud optical depth observed by satellite and the cloud optical depth taken from the ground. The time and spatial averaging used in the satellite retrieval implies that the radiances are derived in a manner which may make them more closely associated with $\langle j_{\tau,dist} \rangle$. For similar arguments as before, the non-linearity of the reflectance function with optical depth, means a more appropriate measure to compare with ground-based measurements might exist. The smaller temporal and spatial averaging of ground-based measurements (e.g. jNO_2 is a one minute average of 1Hz measurements)

may have a role to play. For researchers comparing ground-based and satellite measurements there is also the question of how the difference in the shapes of the reflectance and transmittance functions might combine with the probability density functions and if this may also be partly responsible for the differences seen. There are many potential subtleties that could be investigated and further questions to be answered but these are beyond the scope of this study.

4.6 Summary

A clear sky parameterisation for jNO_2 was derived from the measured clear data. This parameterisation compared well with previous parameterisations of jNO_2 (Dickerson *et al.*, 1982; Parrish *et al.*, 1983) and the advantage of correct representation of atmospheric and surface conditions at Mace Head.

This parameterisation was used in a method of determining cloud optical depth, for clouds of an optical depth above 10, from pre-existing measurements. This newly developed use of photolysis frequencies was used successfully to derive cloud optical depths at Mace Head. Cloud optical depths derived for Mace Head data show a marked diurnal cycle, with increased cloud optical depth towards the middle of the day. This is in agreement with previous work (e.g. Loentieva *et al.*, 1994) and theory. A frequency distribution was derived from the optical depths and was heavily skewed towards high optical depths. This is in agreement with previous optical depth frequency distributions of derived cloud optical depth from ground-based measurements in different locations (e.g. Barker *et al.*, 1998; Leontieva *et al.*, 1994).

The frequency distribution was relatively insensitive to cloud height. Further tests of sensitivity to albedo and introduction of a homogeneity constraint could further test the robustness of the frequency and probability distributions.

This frequency distribution is used to infer a probability density function of cloud optical depth. The probability density function of optical depths can be described by a lognormal

distribution. There is some theoretical evidence to explain the existence of the lognormal distribution. The lognormal distribution could be used as a technique to check the cloud formation parameterisations in GCMs.

The use of average optical depths to describe clouds in models could lead to profound errors in calculation of photolysis rates and correspondingly the underlying chemistry of the atmosphere. A more appropriate variable would be the "effective optical depth", described in this work. However, it is found that the effective optical depth is dependent on solar zenith angle and this is in agreement with theory. Further work is required to investigate the variation of optical depth. For this distribution only, the effective optical depth is closer to the median optical depth.

Average optical depths calculated from measurements of transmitted flux were greater than average optical depths calculated from satellite data. This is in agreement with previous work (e.g. Min *et al.*,1996; Barker *et al.*, 1998). It is proposed that this may be because the satellite sees the effective optical depth resulting from the distribution of radiances.

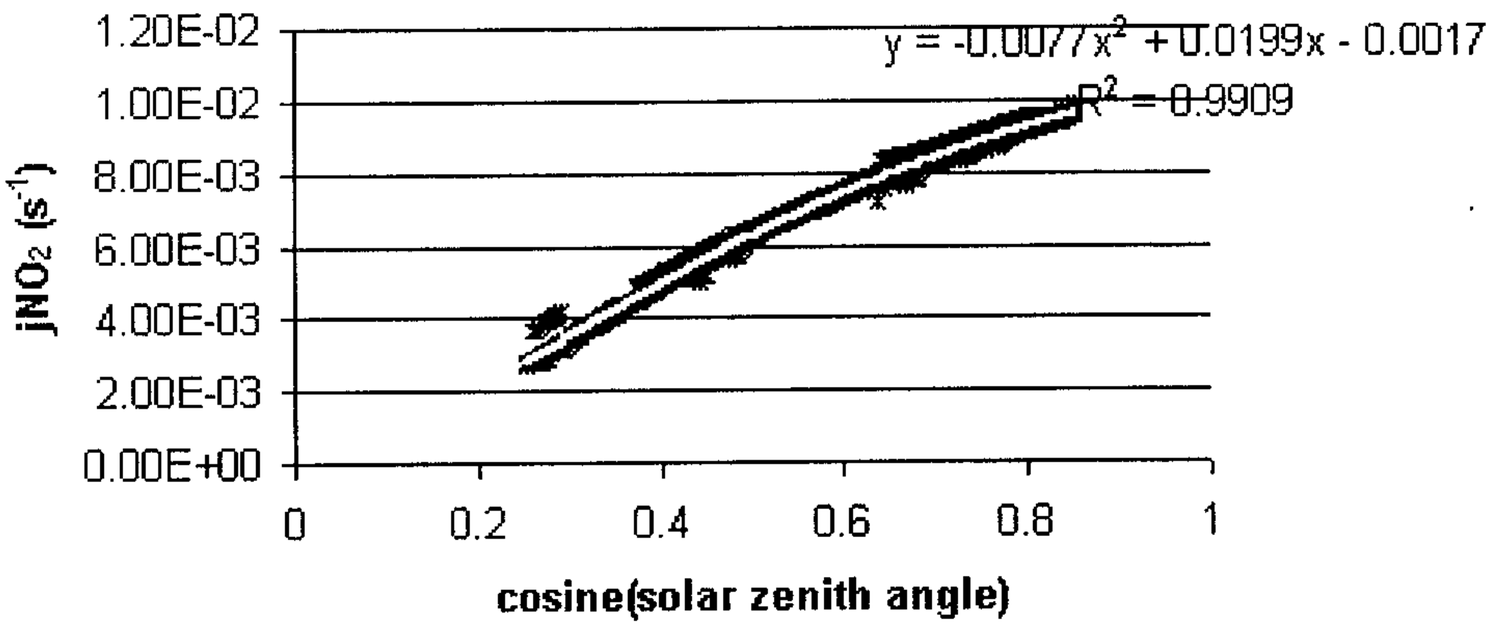
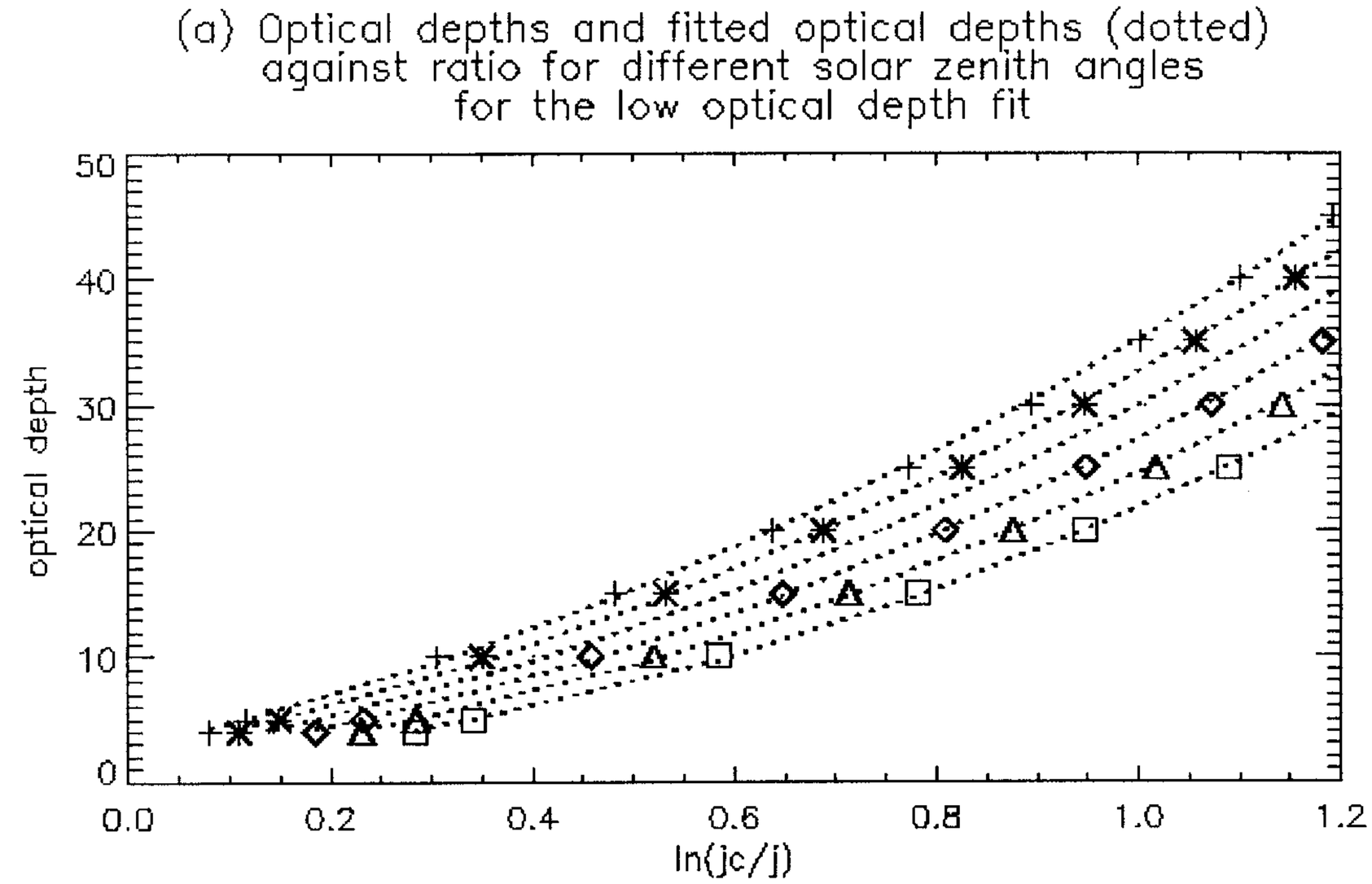
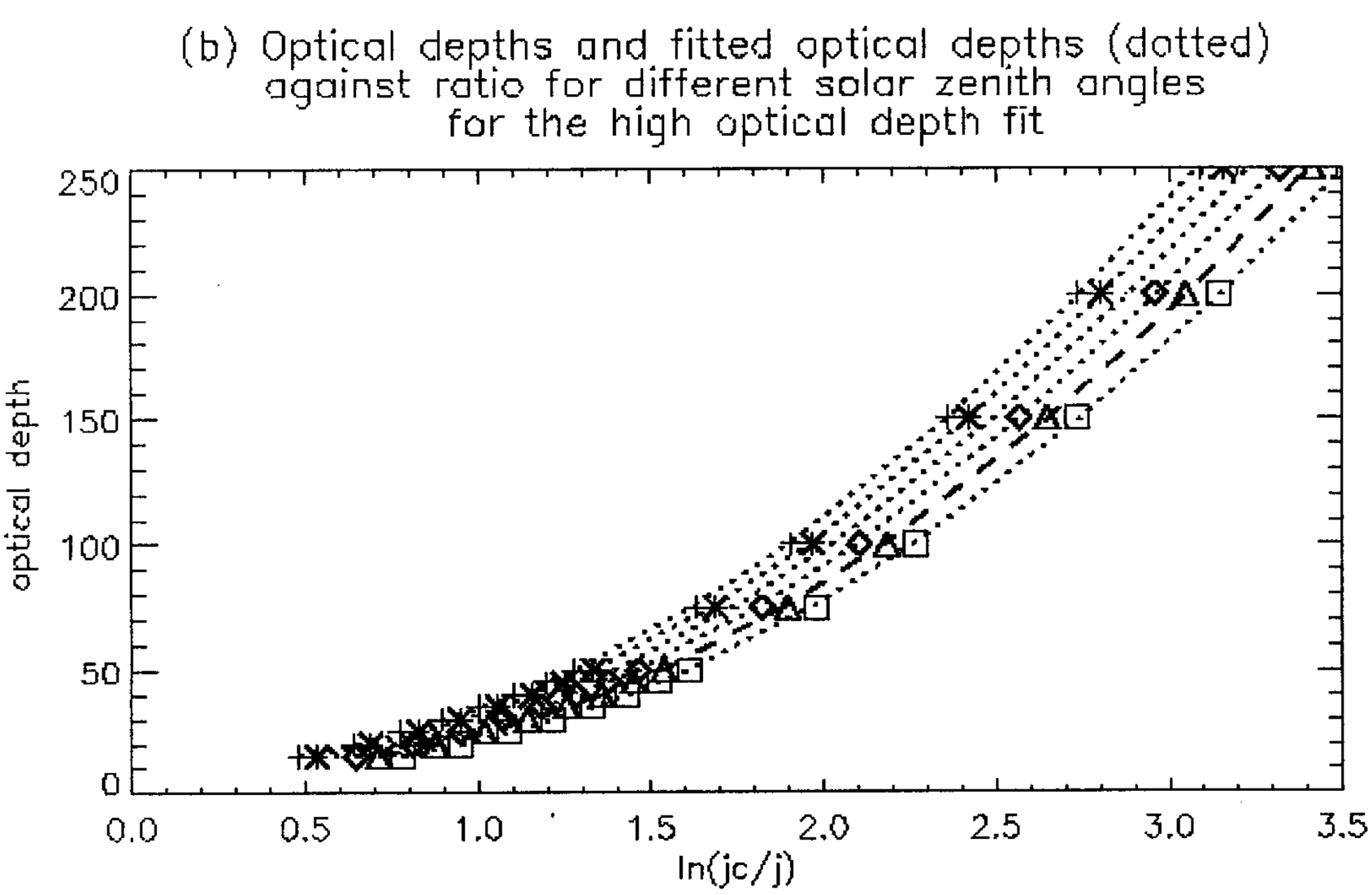


Figure 4.1: Clear sky parameterisation of jNO_2 (a) polynomial in terms of cos(solar zenith angle) (b) exponential in terms of sec(solar zenith angle)





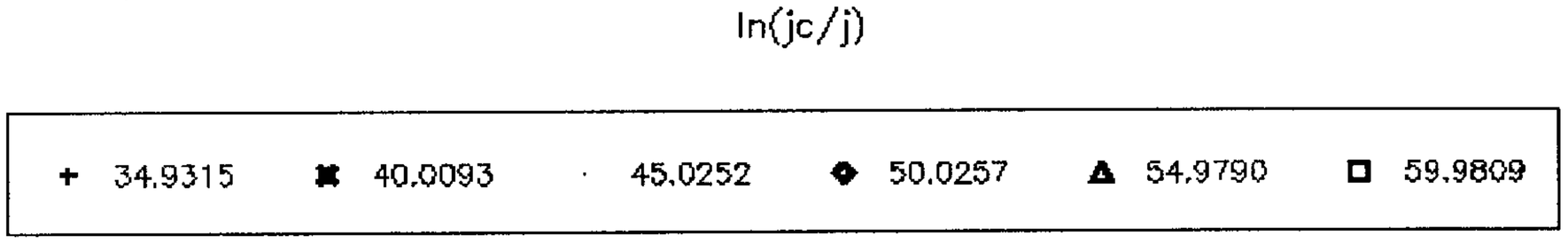


Figure 4.2: Optical depth as a function of $\ln(j_{clear}/j_{cloudy})$ for different zenith angles (a) for low optical depths (b) for high optical depths

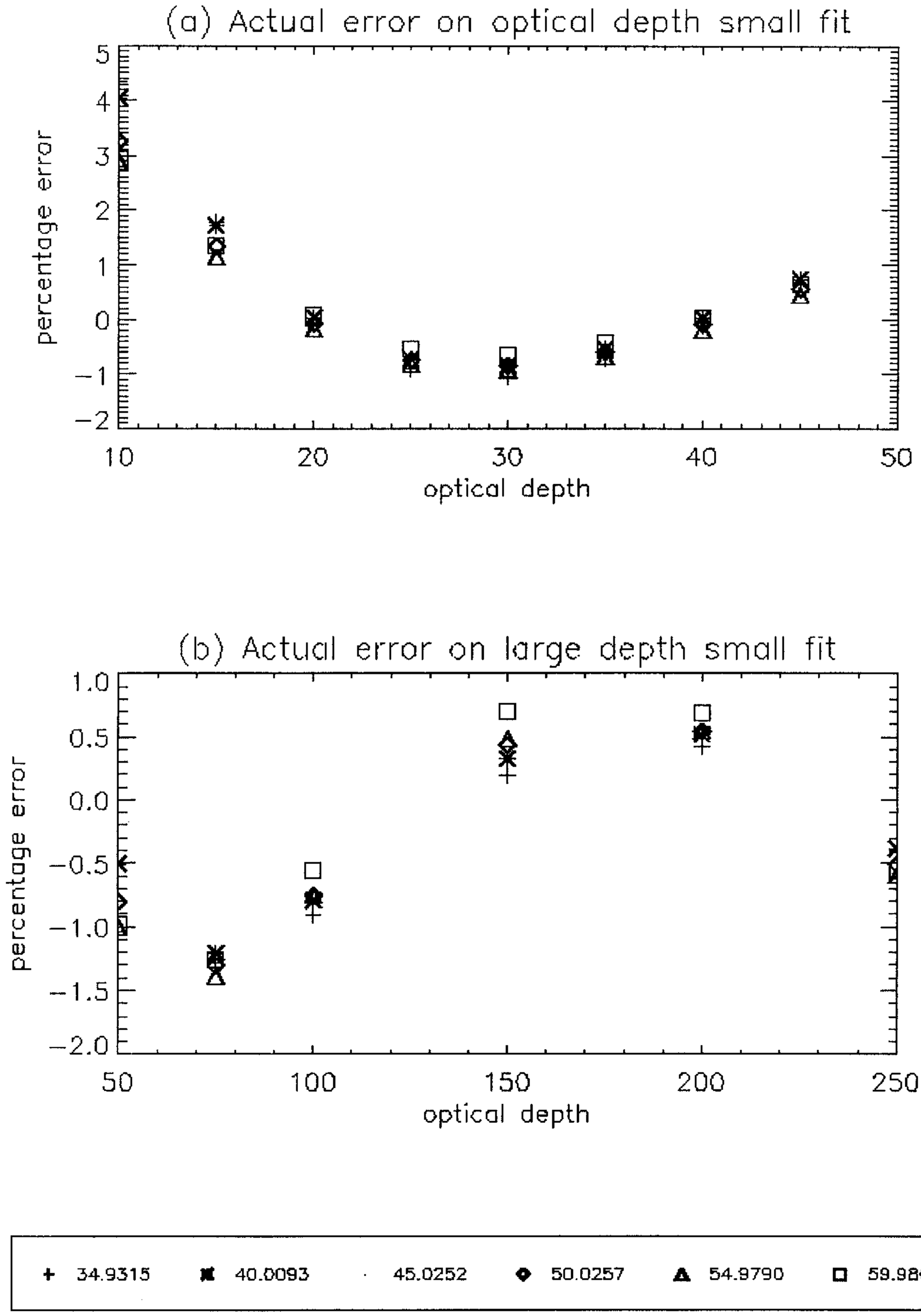


Figure 4.3: Percentage difference between parameterisation and exact values (a) for low optical depth (b) for high optical depth

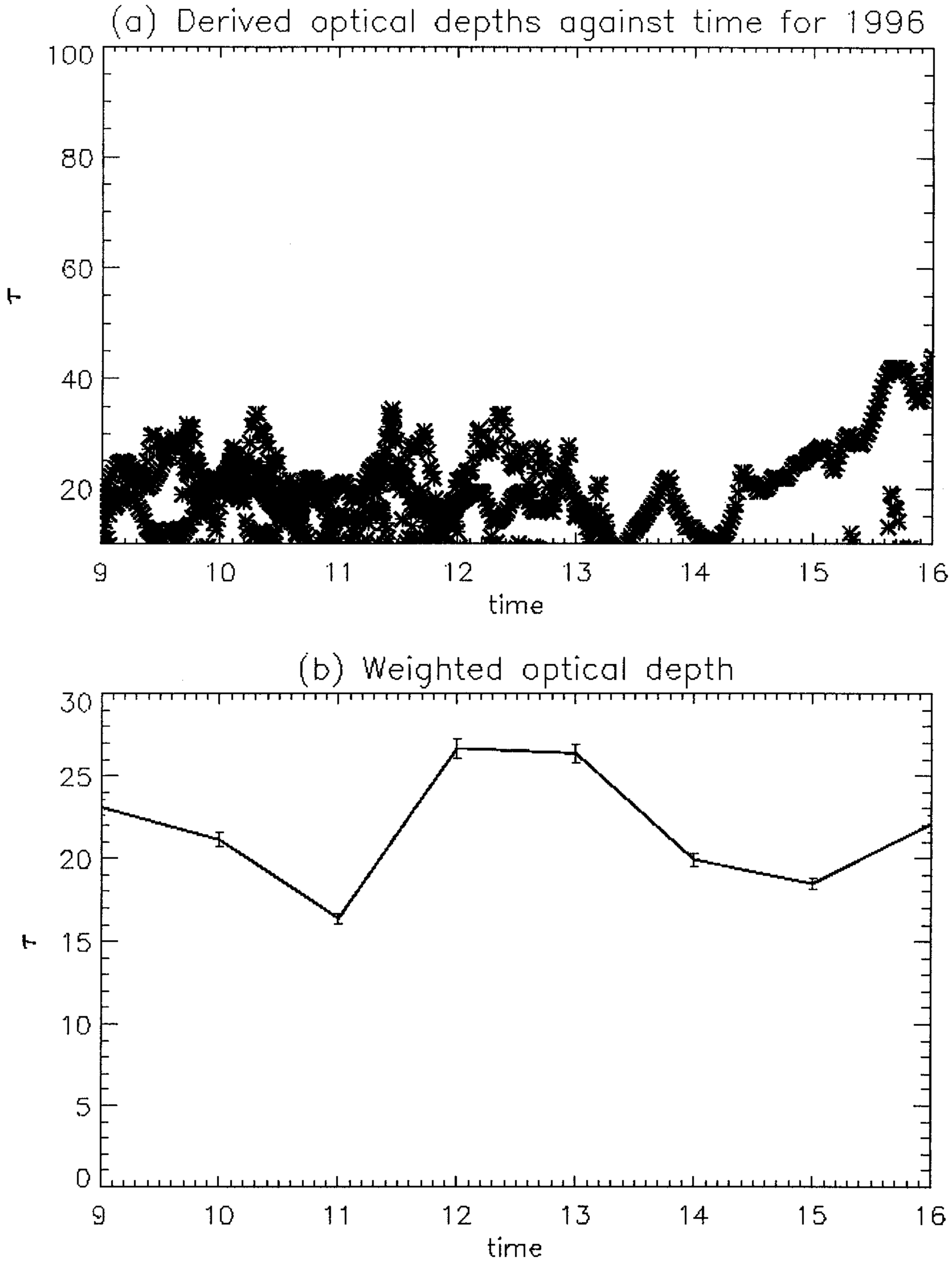


Figure 4.4: Derived cloud optical depths against time (GMT) for 1996 (a) optical depth (b) truncated average optical depth

EASE96 was the summer campaign. Only 13 days are included in this analysis: 25th July - 8th August 1996.

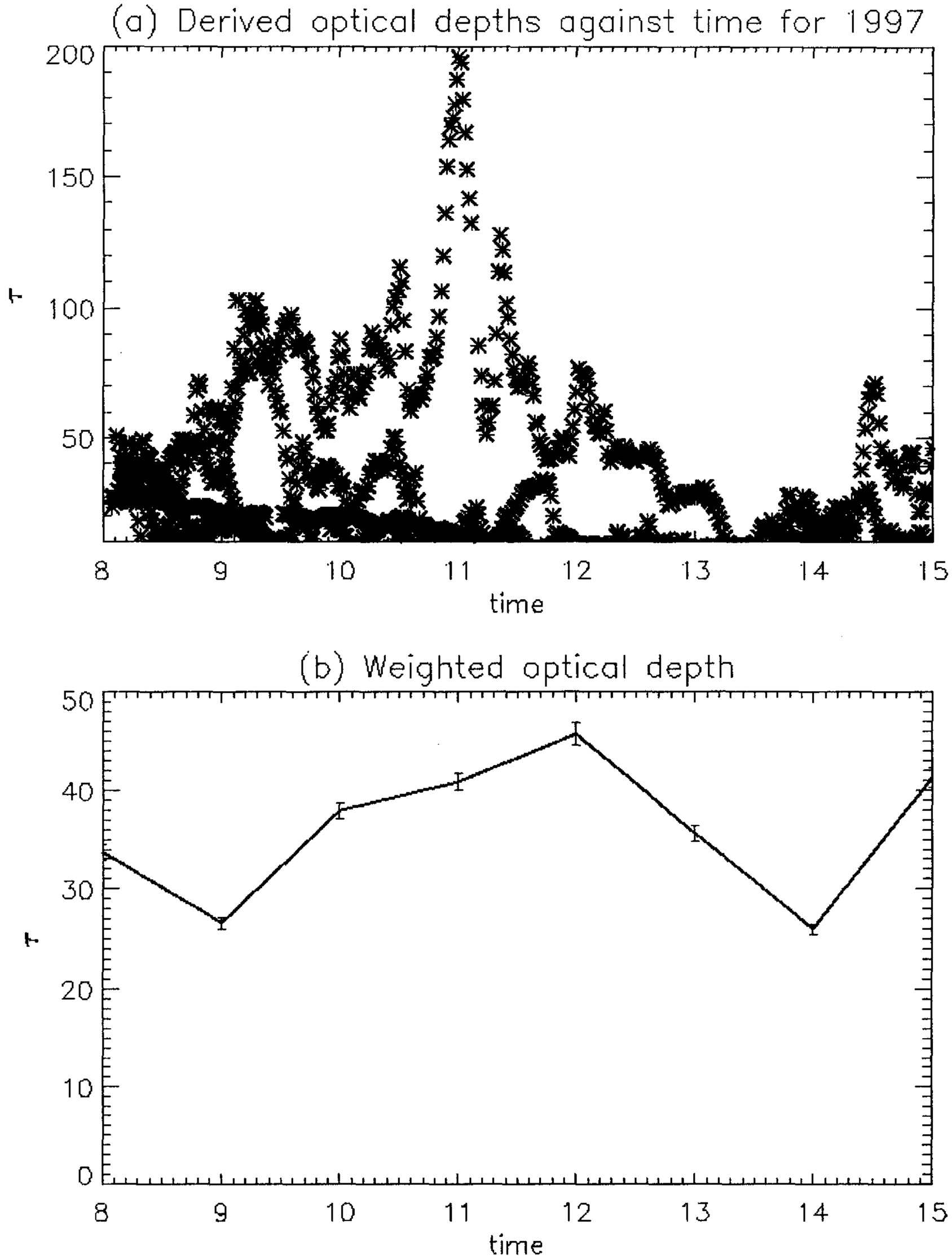


Figure 4.5: Derived cloud optical depths against time (GMT) for 1997 (a) optical depth (b) truncated average optical depth.

EASE97 was the summer campaign. 32 days were included in this analysis - 27th April until 28 May 1997.

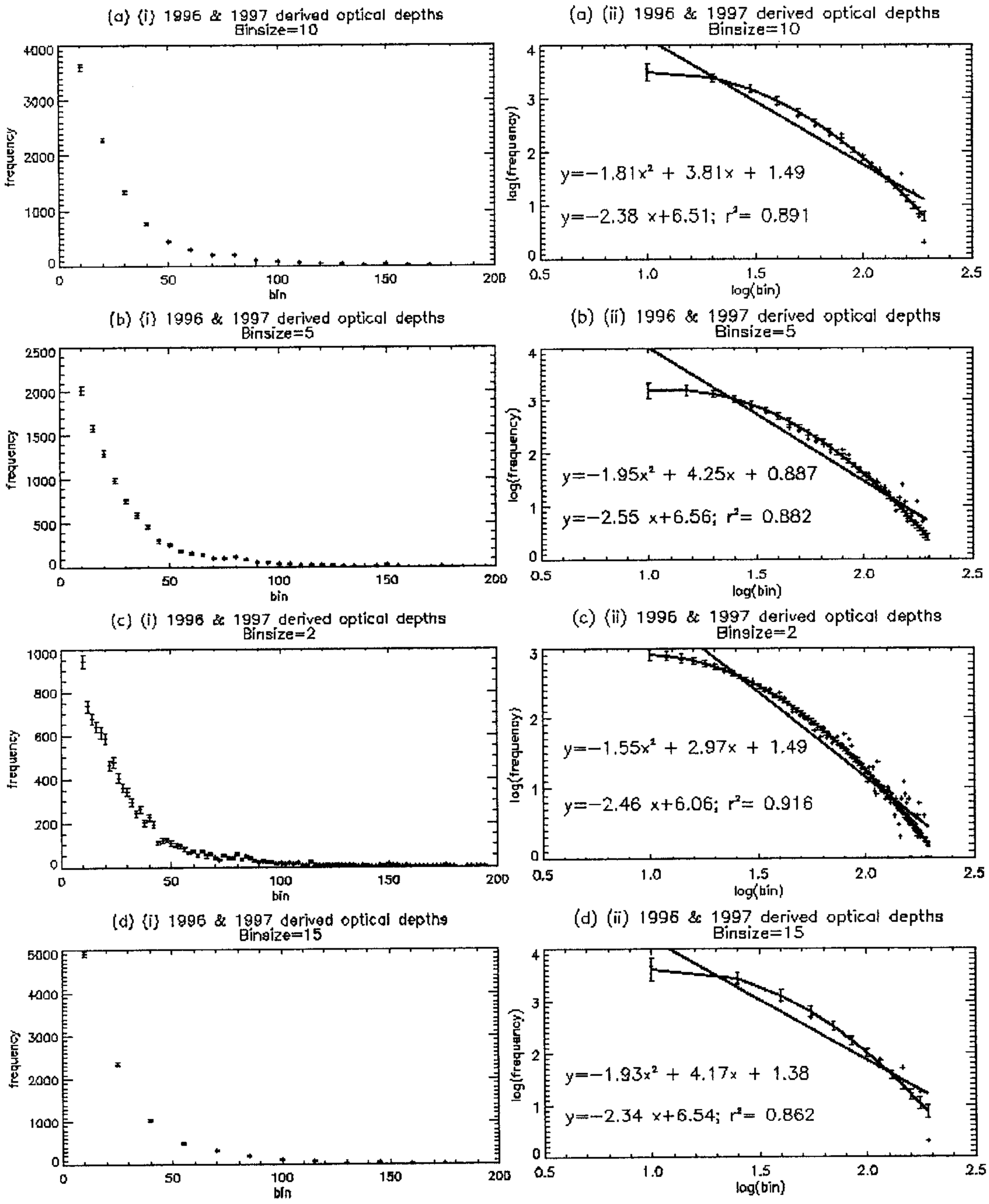


Figure 4.6: Frequency distributions of cloud optical depth for different bin sizes (a) (b) (c) (d) and (ii) on a double logarithmic plot

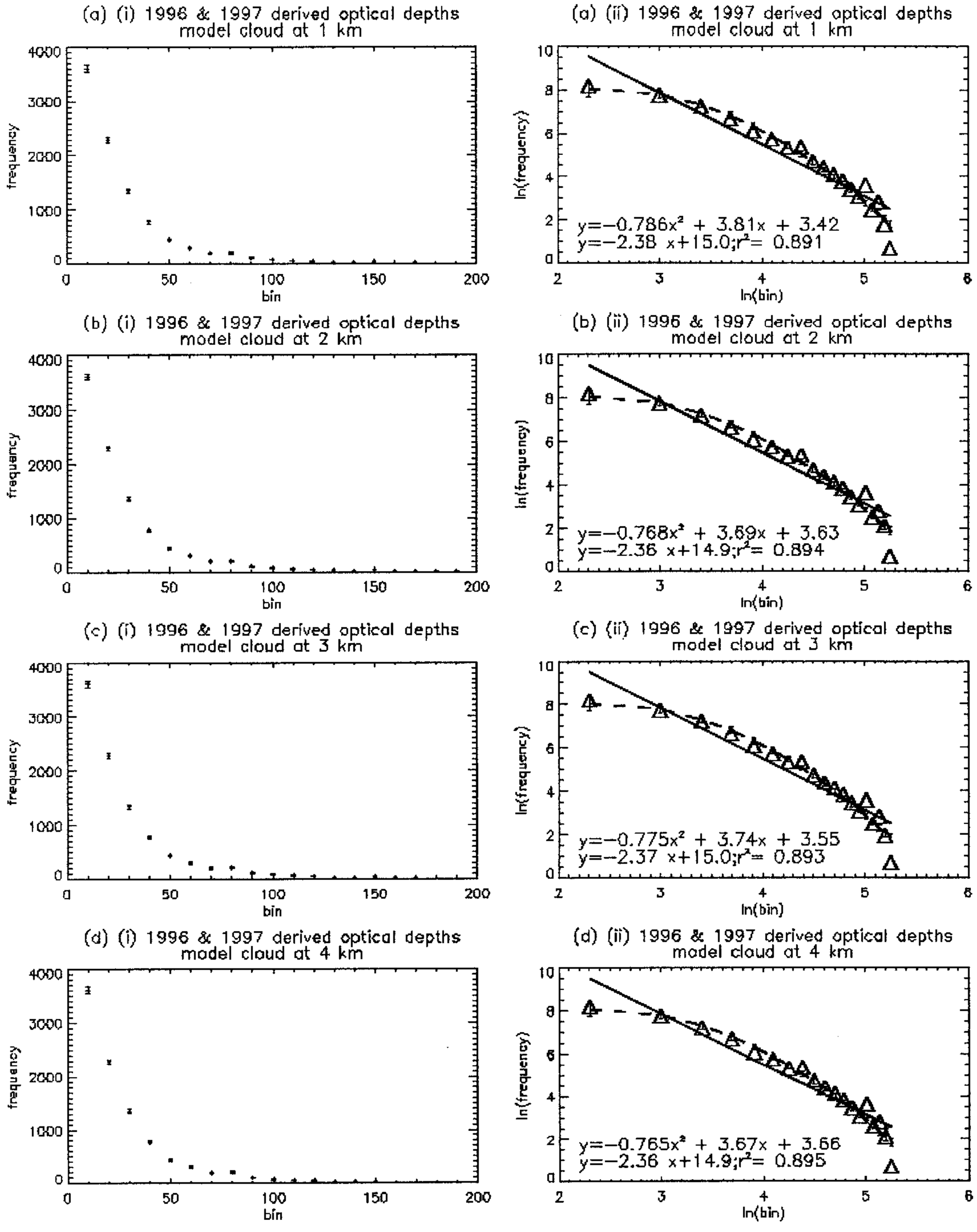


Figure 4.7: Frequency distributions of cloud optical depth for different cloud base heights (i)(a) 1 km (b) 2 km (c) 3 km (d) 4 km (ii) on a double logarithmic plot

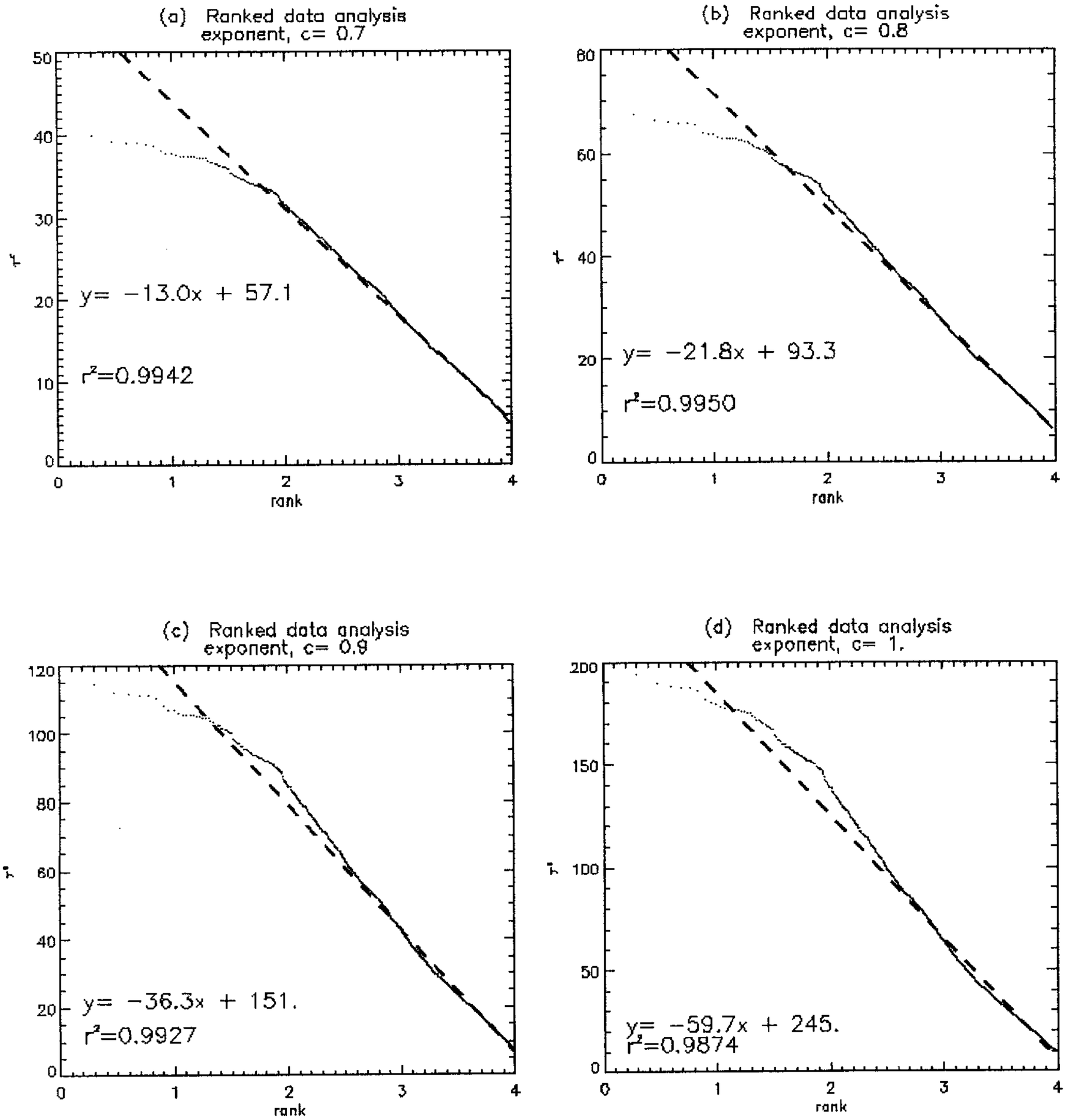


Figure 4.8: Fit of stretched exponential for different values of c

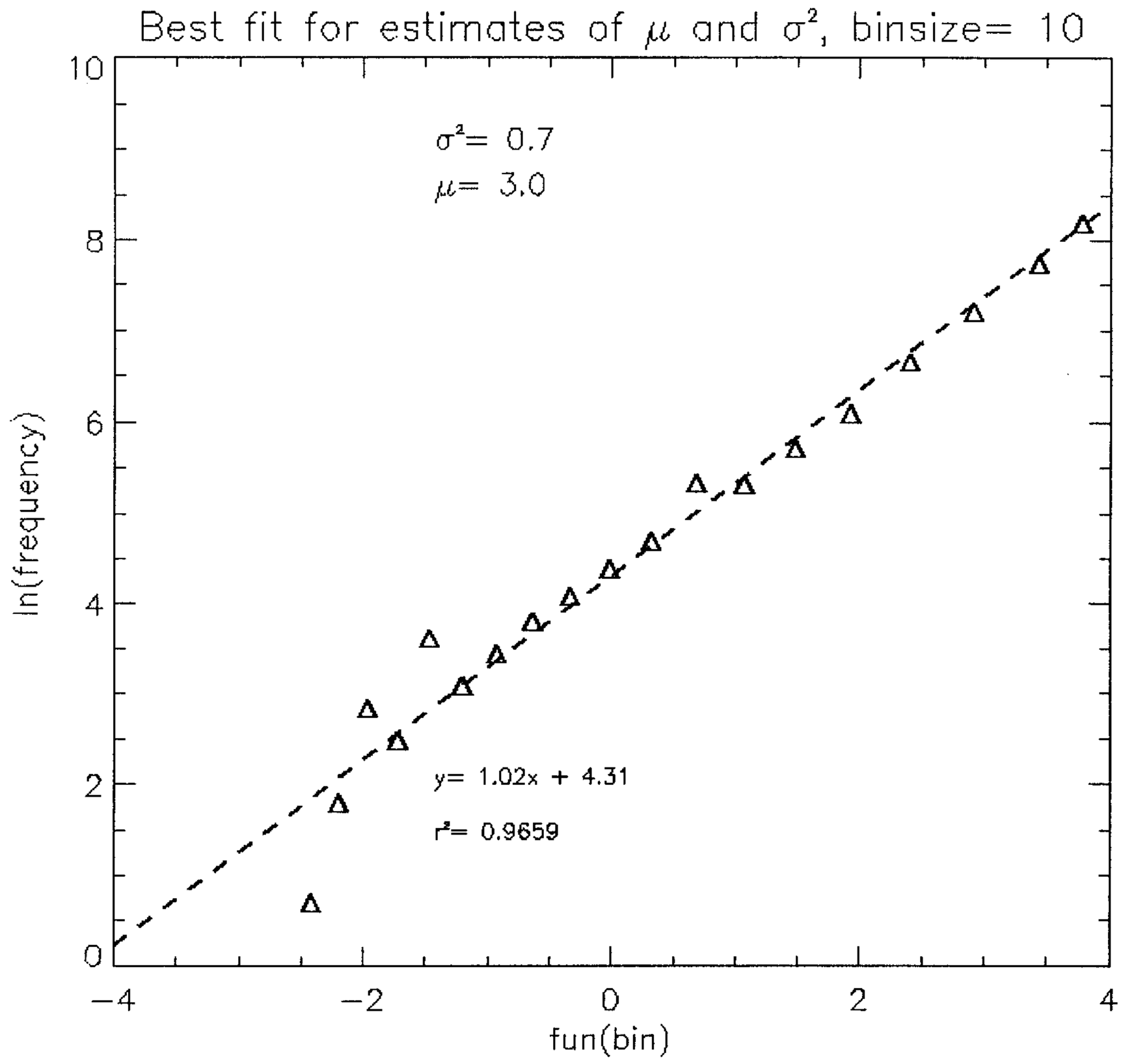


Figure 4.9: Best fit to lognormal using a simple estimation technique

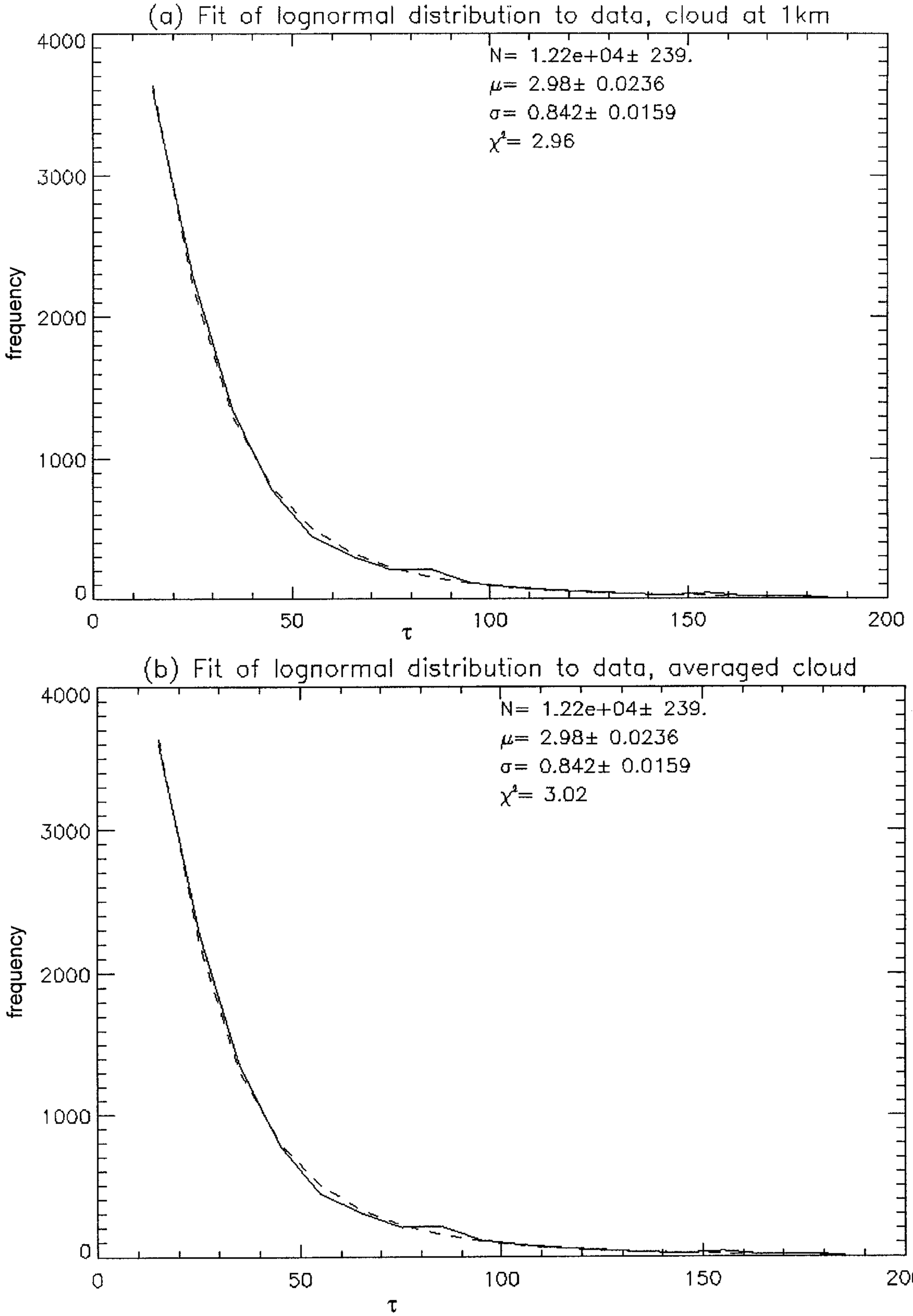


Figure 4.10: Best fit to lognormal using curve fitting technique (a) cloud base of 1km (b) average from data cloud base 1-4 km. Data (solid line), fit (dashed line)

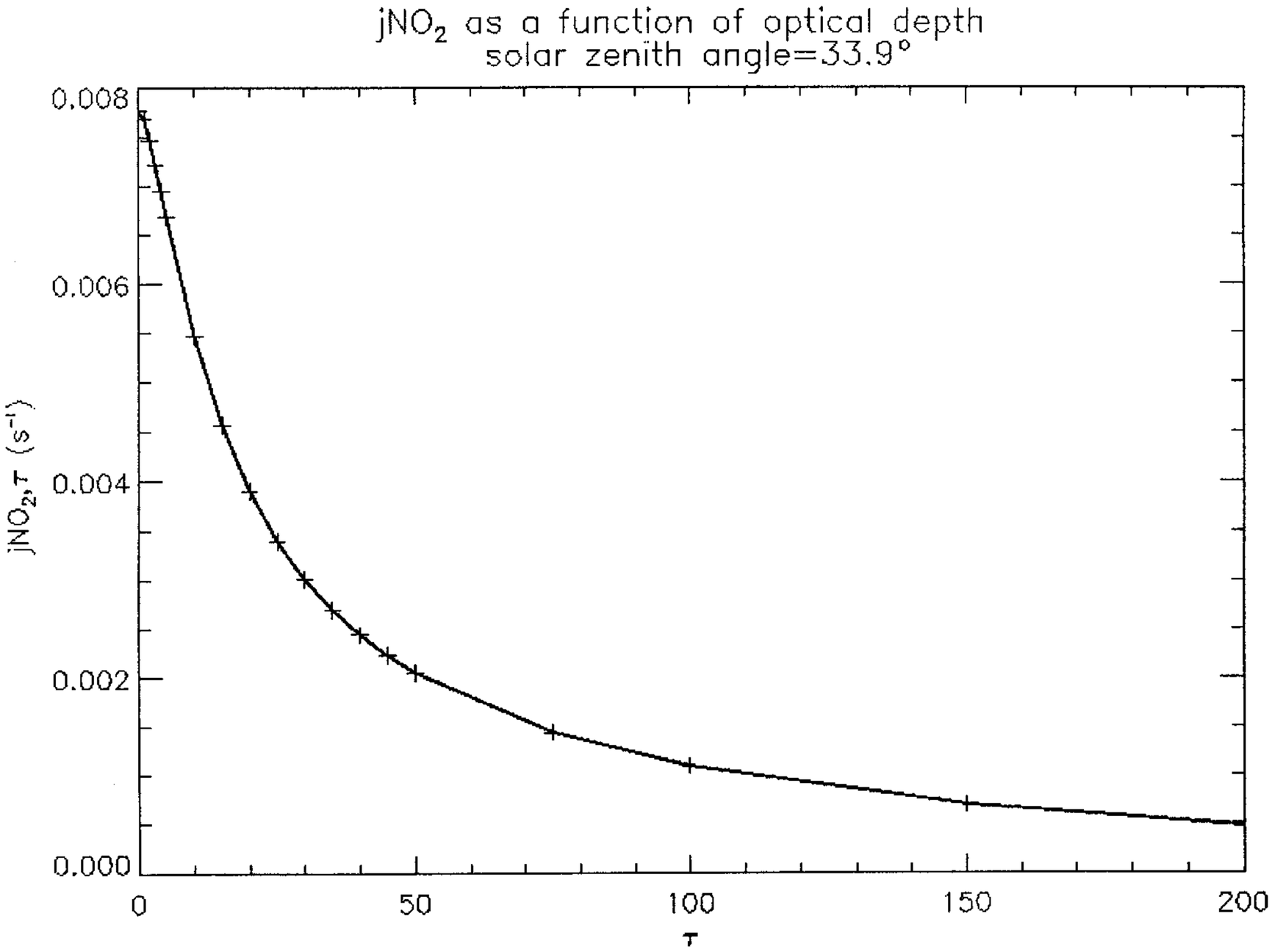


Figure 4.11: jNO_2 as a function of cloud optical depth

5. Response of photolysis rates to cloud

In this chapter, the response of nitrogen dioxide and ozone photolysis rates to cloud is examined using ACSOE data from Mace Head. The analysis is performed using an extension of the method suggested by Crawford *et al.*(1999). Nitrogen dioxide photolysis rates respond more to cloud than ozone photolysis rates, an agreement with the work of Crawford *et al.*(1999). The data from this analysis are further interpreted to glean information about the possibility of gas absorption within clouds.

A theoretical explanation for the differing responses is sought. The results from the campaign data are compared to those obtained using the radiative transfer model described in chapter 2 under different conditions of gas column density and surface albedo. In all these modelled cases, the effect of cloud is to reduce nitrogen dioxide photolysis frequencies more than ozone photolysis frequencies. However, the ratio of the responses, $\Delta jO(^1D)/\Delta jNO_2$ calculated from the model is much greater than that observed, showing that although the model captures the correct sense of the change, it does not reproduce the relative magnitudes. Variation of the inputs that describe the atmosphere and surface cannot bring the sensitivities derived from the model into agreement with those observed in the data. The observed attenuation of jNO_2 relative to $jO(^1D)$ by cloud is always significantly greater than the model predicts.

The discrepancy between model and atmospheric responses is surmised to be a problem with the representation of cloud in the model. Possible causes of a wavelength dependent cloud transmission are suggested: previously observed increased transmission with wavelength (e.g. Seckmeyer *et al.*, 1996) are in agreement with the discrepancy seen here. However, it is proposed that the solution to our problem lies not with the physical description of the cloud and the atmosphere, but rather in the way that the model responses are calculated directly from clear to cloudy sky. To improve the calculation of changes in photolysis rates caused by cloud, the cloud probability density function from the previous chapter is used to simulate the changes in cloud optical depth associated with the cloud

field passing above the radiometers. This method improves the agreement between calculated and observed responses. Two further refinements are suggested. The first approach involves using a wavelength dependent single scattering albedo for the clouds. The second extends the description of the cloud field by including the probability of clear sky. Both of these refinements improve the agreement between the observed and modelled ratios, but the second is believed to have more physical basis.

5.1 Introduction

Investigations of photolysis rates under cloudy conditions were discussed in chapter 3. In summary, there have been a number of analyses, of varying sophistication, of the influence of cloud on nitrogen dioxide and ozone photolysis rates. The majority of recent studies have focussed on modelling the observed vertical profiles of jNO_2 and $jO(^1D)$ (e.g. Mattijsen *et al.*(1998), Crawford *et al.*(1999); Frueh *et al.* (2000)). Despite the breadth and number of these cloud-photolysis rate studies, few focus on simultaneous radiometer measurements of jNO_2 and $jO(^1D)$ (e.g. Pfister *et al.*, 2000). Only one of these studies, Crawford *et al.* (1999) attempts to evaluate the relative responses of $jO(^1D)$ and jNO_2 to cloud, and this analysis is presented as an afterthought to a comparison between measurement techniques.

The relative response of photolysis frequencies to cloud is important, not just as a theoretical question, but also as a practical one. Can photolysis rates be parameterised in terms of one another? How might differing responses affect the chemistry of the atmosphere? Could this be important in terms of HO_x production? As mentioned in chapter 1, a relationship exists between [OH] and $jO(^1D)$, but HO_2 concentrations are dependent on reaction with NO, the product of nitrogen dioxide photodissociation (see Ehhalt, 2000)

The spectral response of actinic flux to cloud is therefore of great interest to experimentalists measuring photolysis coefficients. A parameterisation of these photolysis rates, in terms of filterradiometer measurements would drastically decrease the need for instrumentation. Parameterisations for deriving photolysis frequency from other

measurements already exist. Madronich (1987) derives a semi-empirical formula for estimating the nitrogen dioxide photolysis rate from measurement of ultraviolet obtained with standard ultraviolet (Eppley) radiometers, which allows clear sky jNO_2 to be derived to ±5 % and cloudy sky to ±20%. Extensive testing of this relationship during the experimental campaign MLOPEX (Shetter *et al.*, 1992) provided good agreement with actinometric measurements under clear skies, but under cloudy skies the relationship was much less robust. Inherent in this method is the geometrical problem associated with transformation of irradiance into actinic flux discussed in chapter 3. For measured photolysis rates this can lead to errors of up to 20% even in cloudless skies (e.g. Ruggaber *et al.*, 1993). Under cloudy conditions this error would be larger. The parameterisation of photolysis rates in terms of each other would decrease this geometrical problem and provide a cheap, convenient method for photolysis rate determination from existing measurements.

Cantrell *et al.* (1992) proposed that jNO_2 and $jO(^1D)$ had the same response to cloud. However, Kraus (1998) presented a plot of jNO_2 against $jO(^1D)$ that was very scattered 'due to the differing response to clouds'. Monks *et al.*(1998) also noted differing attenuation of jNO_2 and $jO(^1D)$ by clouds. They noticed that the relative attenuation was dependent on the sun's position in the sky. At low sun (high zenith) angles, the changes in jNO_2 were approximately 15% larger than for $jO(^1D)$. For an overhead sun, the cloud attenuation of the two photolysis rates was similar. Isolated clouds were seen to behave in a more extreme way.

Since nitrogen dioxide and ozone photolysis occur in different spectral regions, it might be expected that they respond differently to cloud. There has been some debate as to whether attenuation of radiation by clouds in the ultraviolet is wavelength dependent. Often attenuation by cloud in the ultraviolet is assumed to be wavelength-independent, as might be expected from the very nearly constant values of the cloud's primary optical properties, i.e. the extinction coefficient, single scattering albedo and asymmetry factor, in this spectral region. However, more than one process has been proposed that could cause wavelength dependence in the ultraviolet. One proposed mechanism is a combination of

scattering from the cloud with other spectrally dependent scattering (e.g. Rayleigh scattering, e.g. Frederick *et al.*, 1997). Another possible cause for spectral dependence is increased absorption of an atmospheric gas inside the cloud which would introduce spectral dependence. These two mechanisms are discussed below.

The attenuation of radiation by cloud is often described in terms of the "transmittance", the ratio of the spectral irradiance below the cloud to that for a cloudless sky. Studies (e.g. Frederick and Lubin, 1998; Wang and Lenoble, 1996) have shown an increase in cloud transmittance at wavelengths longer than 400 nm and a decrease below 320nm. Frederick and Lubin (1988) reported nearly constant values for transmittances between 320 nm and 400nm. Wang and Lenoble (1996) report a cloud transmittance of 0.5 at 300 nm, increasing to 0.57 at 400nm. Seckmeyer *et al.*(1996) derived transmittance from measurements of spectral irradiance taken simultaneously on a mountainside above and below a cloud situated about 1200m. These measurements were normalised by readings from the same stations at cloud-free days to derive a "cloud effect". This cloud effect was wavelength dependent in the ultraviolet, ranging from transmittance of 45% in the UVA through to 60% in the UVB. A theoretical explanation that depends on coupling of cloud scattering with Rayleigh scattering for this phenomenon was proposed by Kylling *et al.* (1996) and this will be discussed later.

However, another quite different explanation exists. Wagner *et al.*(1996) estimated photon path lengths inside clouds from light transmitted to their Differential Optical Absorption Spectroscopy (DOAS) instruments. These photons paths were much larger than expected, possibly due to multiple scattering between patches or layers of cloud: the "ping pong" effect. Extremely long optical paths have been observed by other authors (e.g. Erle *et al.*, 1995) in thick clouds. These very long paths could lead to increased absorption of photons by any gas they encountered along their path e.g. ozone. Pfeilsticker *et al.*(1997a) illustrated this: a thick stratus cloud, with an optical depth of 100 could cause a possible optical path of 96.6 km. Assuming an interstitial ozone concentration of approximately 40 ppb, the increased path due to multiple scattering would lead to absorption equivalent to an ozone column of 430 DU. This increased path

length is called tropospheric path length enhancement (TPLE) and has been proposed as a further possible mechanism for anomalous absorption. The spectral dependence of the transmitted radiation would therefore depend on the spectral dependence of the cross-sections of the absorbing gases present within the cloud, as well as their relative abundances. Examination of jNO_2 and $jO(^1D)$ data could therefore provide some clues to the responsible mechanism and could prove useful in answering both practical and theoretical questions.

Despite a great deal of interest in this problem, there has only been one serious attempt to answer the question of the relative attenuation of nitrogen dioxide and ozone photolysis frequencies under cloudy skies. Crawford *et al.*(1999) examined the responses of jNO_2 and $jO(^1D)$ to cloud during flights in the PEM (Pacific Exploratory Mission) –Tropics campaign in August-October 1996. However, the study merely formed a small part of a radiometer intercomparison and the attempt to explain the relative responses to cloud does not stand up to scrutiny. Further to this, no attempt was made to emulate the observations using modelling studies. This study attempts to fill in the gaps left by that study, provide further data for comparison, use a model to find an explanation and provide a theoretical investigation to see if the spectrally dependent attenuation of cloud in the ultraviolet can be established by examination of jNO_2 and $jO(^1D)$.

5.2 Method

Photolysis rate data contains dips and spikes: deviations from a clear sky profile. Since these dips and spikes are evident in the minute-by-minute data from Mace Head, such variations are caused by a factor influencing the actinic flux over short timescales. In chapter 3, we discussed the main factors affecting photolysis rate data – ozone column (and profile), aerosol and cloud. Photolysis frequencies are acutely sensitive to cloud, which is known to be extremely variable over short timescales (see chapter 4). Ozone column and aerosol concentration fluctuations are more likely to change on longer time scales since they are dependent on air mass, and in the case of aerosol, relative humidity. Therefore, in an initial analysis, it is assumed that fluctuations in photolysis rates over a

small time window are caused primarily by changes in cloud. This is consistent with the assumptions made in the previous chapter. Over a short window, this is a reasonable assumption and as we will show is the best available method for evaluating the sensitivities of jNO_2 and $jO(^1D)$ to cloud.

Since the aim of this chapter is to test the sensitivity of the photolysis rate data to cloud in different wavelength regions, a method must be chosen that accounts for the differing shape and magnitudes of the photolysis frequency curves for jNO_2 and $jO(^1D)$.

The most obvious method of making a comparison would be to use the model to calculate clear-sky photolysis frequencies for each species. This would provide a 'baseline' and, assuming no change in aerosol and gas loadings, any short-term fluctuations from this clear-sky baseline could be attributed to cloud. The sensitivity to cloud in the different wavelength regions could thereby be compared easily. However, since this method depends entirely on an accurate simulation of the clear sky photolysis rate, there are many potential pitfalls, as discussed in chapter 3. As well as the difficulties associated with the modelling, the assumption that the atmospheric parameters are invariant over the time of the baseline model run is also suspect. For instance, TOMS data shows that the average diurnal change in column ozone during the 1997 campaign was approximately 20 DU, and in one case was as much as 80 DU. A 5 DU change ozone column can lead to an error in $jO(^1D)$ of 3% (Crawford *et al.*, 1999). It is likely that whatever ozone column was input to the model, during the course of the real day substantial deviations would occur from it. This could lead to incorrect values for the percentage change in two ways. Firstly, the clear-sky ozone photolysis frequency curve would not reflect the measured frequency and the change due to cloud would be calculated relative to an incorrect clear sky value. The percentage change in ozone photolysis frequency would therefore be inaccurate. Additionally, as the nitrogen dioxide photolysis frequency curve is much less sensitive to the changing ozone column than the ozone photolysis frequency curve, the resulting percentage changes would not accurately reflect the relative sensitivities to cloud in the different wavelength regions. Although a clear sky curve was derived in the previous

chapter, this gives no information about $jO(^1D)$, so this does not provide a satisfactory method either. A different method must therefore be used.

The method used in this chapter, that of Crawford *et al.* (1999), involves calculation of the percentage change in each photolysis rate over a short time interval. This alleviates the need for a clear-sky comparison. Each photolysis frequency measurement becomes a relative value, so determination of absolute clear-sky values is not required. Another advantage of this method is the smaller probability that aerosol, ozone or nitrogen dioxide concentrations will change very significantly over this small time-scale, so the need for the assumption of invariant gas loadings over the length of the model run is removed. Time intervals of three minutes (3 consecutive measurements) were chosen to limit the variation in solar zenith angle to less than a degree and to provide an analysis available for direct comparison with Crawford *et al.*(1999).

5.3 Data Analysis

The percentage change in the photolysis rate, j, over a fixed time interval was calculated using equation 5.1.

$$\Delta j = [(j^{t+\Delta t} - j^t)/j^t] \times 100 \qquad (5.1)$$

where Δj is the percentage change in photolysis frequency

t is the time index

Δt is the chosen time interval

The percentage change can be positive or negative depending on whether the cloud becomes thicker (photolysis rate decreases) or thinner (photolysis rate increases) over the time interval.

To compare the percentage change between two different photolysis rates, simultaneous photolysis rate measurements are required. Any time lag between the radiometers could result in the radiometers 'seeing' different instantaneous cloud fields so changes in photolysis rates might not truly represent the response to cloud. Simultaneous

measurements were available during EASE97, but not during EASE96 where there was a lag of 8.1 seconds between the measurement of jNO_2 and $jO(^1D)$. Since this is about 15% of the data averaged for the minute, this data was necessarily excluded from the analysis. The instrumental set-up is described in chapter 1. It should be reiterated that the jNO_2 radiometer has two plates (upward and downward facing) compared to the single upward-facing plate of the $jO(^1D)$ radiometer. This is because the upward component of the actinic flux for $jO(^1D)$ is considered negligible due to the small albedo in this spectral region. For consistency, only data from the upward facing jNO_2 hemisphere was used for comparison. The jNO_2 diurnal curve is much broader than the $jO(^1D)$ diurnal curve, since the $jO(^1D)$ depends entirely on radiation affected by ozone absorption. This ozone absorption increases at higher zenith angles when the path length is increased. To exclude these 'wing' regions from the calculation, the solar zenith angle range is restricted to zenith angles of less than 75 degrees.

Figure 5.1 (a)-(d) shows the steps used in the analysis and their influence in the result. A least mean squares fit was used. This is a suggested improvement to the method of Crawford *et al.* (1999) who simply calculated the ratio: $\Delta jNO_2/\Delta jO(^1D)$. In this analysis, the calculated gradient is weighted by the distribution of the points. The percentage of total points on either side of the line $|\Delta jO(^1D)| = |\Delta jNO_2|$ is also shown for comparison with Crawford *et al.* (1999). Figure 5.1 (a) shows the raw percentage change data only including data where both radiometer readings are reliable, according to the error flags. The percentage change in ozone photolysis frequency, $\Delta jO(^1D)$, is shown as a function of the percentage change in nitrogen dioxide photolysis frequency, ΔjNO_2. There is a good linear correlation (r^2=0.84) with the majority of points lying close to the best-fit line. The best-fit line gives the weighted average change and the number of times ΔjNO_2 is larger than $\Delta jO(^1D)$ is also shown as a percentage. However, there are a number of points that lie in quadrants two and four of the graph (~ 11.2% of the total). These points, 'anti-correlations' from now on, correspond to a simultaneous increase in one photolysis frequency and decrease in the other. Possible causes for these anti-correlations are discussed, but since it is believed that the points are unlikely to reflect a physical situation

they are removed from the analysis (Figure 5.1(b)). Since the percentage change, Δj, values can be either positive or negative, the response was quantified using absolute values. Figure 5.1 (c) shows $|\Delta j(O^1D)|$ plotted as a function of $|\Delta jNO_2)|$. Further, data points where either percentage change was less than 10% were discarded. These data points were eliminated for two reasons. Firstly, a small change could conceivably be caused by aerosol or gas concentration and a large change in photolysis rate is much more likely to be due to cloud. Secondly, the small changes (<10%) were discarded because they could have been caused by errors of instrument precision. This significantly decreases the number of points available in the analysis, removing ~ 73% of the data. This is similar fraction of the data that was removed when Crawford *et al* (1999) applied the same condition (72%).

Figure 5.1(d) shows the gradient of the resulting data to be 0.75 i.e. over all jNO_2 is attenuated more than $jO(^1D)$. The effect of removing the small fluctuations is shown by the difference between the number of points where $\Delta jNO_2 > \Delta j(O^1D)$ (~ 42% in Figure Figure5.1(c), compared to ~60 % in Figure 5.1(d)) and shows that fluctuations of magnitude smaller than 10% contribute more to $\Delta jO(^1D) > \Delta jNO_2$. This means that when the changes in the absolute response are small, the attenuation dominates the shorter $jO(^1D)$ wavelengths. Now we must consider potential causes for this: we require a mechanism that causes a preferential attenuation of $jO(^1D)$ but only for small changes.

5.3.1 What causes attenuation of $jO(^1D)$ to dominate in the case of small changes?

Short time scale fluctuations in the ozone column would certainly decrease $jO(^1D)$ more than jNO_2. In a clear sky, a 1 % change in O_3 column causes a decrease of 2% in $jO(^1D)$ and a change of only 0.02% in jNO2 (see chapter 3). Under the assumption that any spectral dependence of cloud transmittance is small compared to the effect of ozone absorption, we can use these numbers directly. The ratio of the change in $jO(^1D)$ to that of jNO_2 would then be ~100, a value which is far greater than those we wish to consider. High frequency oscillations in the ozone concentration, for which there is no evidence in the data, are therefore not responsible. If the transmission of the cloud was greater in the

UV-B than UV-A, e.g. Seckmeyer *et al.* (1996), this ratio could be expected to be even higher than the estimated value of 100. Therefore, ozone is believed not to be the culprit.

However, aerosol is known to fluctuate rapidly on short timescales. Table 5.1 shows some values for attenuation of photolysis rates due to aerosol taken from the recent work of Reuder and Schwander (1999). They state that at small zenith angles, the aerosol effect on $jO(^1D)$ is greater than jNO_2, and this is in agreement with the work of Erlick *et al.*(1999) who show that aerosols increase the normalised transmission from 320 nm through to the visible.

Table 5-1: Changes in photolysis rates due to aerosol from Reuder and Schwander (1999)

solar zenith angle, θ (°)	jNO_2	$jO(^1D)$
35	10%	15%
60	30%	30%

At small solar zenith angles, the presence of aerosol causes $jO(^1D)$ to decrease more than jNO_2. Assuming that the values of attenuation are similar in a cloudy sky, the values given correspond to a $\Delta jO(^1D)/\Delta jNO_2$ of 1.5, which is of the appropriate magnitude. It is therefore concluded, that aerosol is the likely cause of the different spectral dependence for small changes. As the aerosol optical depth is not large enough to cause the larger percentage changes, variations in aerosol concentration cannot be used to explain these changes and another explanation must be found.

The intercept of the lines shown in Figure 5.1(a)-(f) is non-zero because of a slight non-linearity for small changes. The extremely high correlation justifies use of this straight line fit. It should also be noted that the asymmetry between the first and third quadrants is a numerical artefact caused by the method of calculation.

5.3.2 Anti-correlations

In general, ΔjNO_2 and $\Delta jO(^1D)$ increase and decrease in the same direction over the time interval. However, there is a significant number of points where one radiometer records an increase in actinic flux over the time interval whilst the other records a decrease. It is important to establish whether these events are due to the small horizontal distance between the radiometers (~ 2m), the small vertical distance (~2m) or some other factor.

There are a number of possible explanations for this unusual behaviour:

(i) horizontal inhomogenities in actinic flux field due to broken cloud fields

(ii) changes in concentrations of absorbing gases over 3 minutes

(iii) incorrect instrument response

(i) Horizontal inhomogenities in actinic flux field due to broken cloud fields

Anti-correlations must be caused by one radiometer experiencing an increased actinic flux over the time interval whilst, at the same time, the other radiometer experiences a decreased actinic flux. Over the 3-minute interval this would mean that a cloud would have to be positioned above only one radiometer at the beginning of the time interval and positioned above the other radiometer at the end of the time interval. Given that the radiometers are only 2m apart, the horizontal extent of even small cumulus clouds (~500m), and the fact that the sun is never directly overhead in Mace Head (so increasing the apparent area of the cloud), this seems extremely unlikely.

However, this idea can be extended further. Under broken cloud fields, the ultraviolet can be more than the clear sky value (e.g. Los, 1996). This is due to scattering from the edges of clouds. However, directly under a cloud the ultraviolet will usually be less than the clear-sky value. If under these broken cloud fields there are regions where the ultraviolet is decreased, as well as regions where it is increased (relative to clear sky), the radiation field is clearly inhomogeneous. Under these circumstances, one radiometer could be subject to an increase in radiation over 3 minutes, whilst the other was subject to a

decrease. However, it seems unlikely that the horizontal actinic flux field should change so rapidly on such a small scale.

Trautmann *et al.* (1999) modelled the actinic flux under a broken two dimensional cloud field. Using a variable liquid water field and two different two-dimensional radiative transfer models they found maxima and minima in calculated photolysis rates at the surface, varying from decreased values under the cloud to increased values near the cloud edges. This effect was greatest for low surface albedo and high sun. As multiple reflections increased, the actinic flux field gradually smoothed out blurring direct distinction between sunlight and shadow regions. The wavelength dependence implies that the $jO(^1D)$ field would be smoother than jNO_2 field. Similar results were found when a simulation of marine stratocumulus was attempted. Although in agreement with the proposed horizontal inhomogenities, the scattering shown on the scale of these simulations (50 and 55m in the horizontal and a minimum of 25m in the vertical) supports the idea that these changes in photolysis frequency are very unlikely to be due to horizontal or vertical inhomogeneities on this small scale.

(ii) Changes in absorbing gases over 3 minutes

The condition of an anti-correlation requires an increase in the concentration of ozone and a decrease in the concentration of NO_2 or vice versa. A decrease in $[NO_2]$ and an increase in $[O_3]$ and increased $[NO_2]$ and decreased $[O_3]$ could be the result of a NOx plume. This would result in reaction of O_3 with NO (S. Baguitte, pers. comm,.1999). However, there is a dearth of any information on the possible frequency of such events at Mace Head. It is suggested that this may be a plausible cause of anticorrelations, but requires investigation on the concentrations required, before a definite conclusion can be drawn.

(iii) incorrect instrument response

Since a large number of anti-correlations still exist when changes of less than 10% are discarded it seems unlikely that these anti-correlations are simply due to instrument response. An analysis of the anti-correlations binned by type and zenith angle does not

reveal anything: there are anti-correlations of a similar magnitude in every zenith angle bin. It is assumed, therefore, that the most likely cause of these events is random fluctuations resulting in incorrect instrument response.

5.3.3 How do the relative responses compare to previous work?

In our analysis, the percentage change in jNO_2 was greater for 60 % of the points. This compares with a value of 59% calculated by Crawford *et al.* (1999) (see Table 5.2). This is remarkably similar given the different locations and different altitude of the measurements. It also should be noted that Crawford *et al.* were flying under a cloud field whereas the measurements used here were taken from a stationary platform above which the clouds moved. These are slightly different methods of sampling the cloud field : the radiometer samples the cloud field at the speed it moves across the sky. The aircraft samples the cloud field at its flight speed across the sky, maybe 90 ms^{-1}. Assuming the upper level wind speed at Mace Head to be equal to a frontal speed of 15 ms^{-1}, then over the same time interval, the two methods are sampling different horizontal cloud resolutions. This hints at a universal ratio of responses under clouds: a fact that could be verified by further work on the subject.

Table 5-2: Response of jNO_2 and $jO(^1D)$ to clouds from Crawford *et al.* (1999)

Altitude range	0-1 km
Number of data points	710
Median solar zenith angle	48
Percent of data with greater response in jNO_2	59 %
Median jNO_2 to $jO(^1D)$ percent change	1.04

Similarly, the transmission under cloudy skies observed by Seckmeyer *et al.*(1996) decreased 60% in the UVB through to 45% in the UVA. In this case, shorter wavelength radiation passing through the cloud is less attenuated by that cloud i.e. in terms of

photolysis frequencies: a smaller Δj for $jO(^1D)$ than for jNO_2. Taking the UV-B as a proxy for $jO(^1D)$ and the UVA as a proxy for jNO_2, this corresponds to attenuation by cloud of 40% for $jO(^1D)$ and 55% for jNO_2, therefore a ratio of $\Delta jO(^1D)/\Delta jNO_2 = 0.72$. Of course, the UV-A and UV-B spectral ranges do not exactly correspond to those used in the calculation of photolysis frequencies and there is no weighting by a quantum yield factor. The irradiance data is different geometrically, unfiltered and taken over two hour scans, as well as just simply representative of the change between a clear and cloudy sky. However, there is qualitative agreement between these results.

Additionally, the small value of the ratio ($\Delta jO(^1D)/\Delta jNO2$) shows that there is no evidence for significant tropospheric path length enhancement in this data. If the photon paths in the cloud were massively enhanced and coupled with extra ozone absorption, far fewer photons would emerge from cloud base at the shorter $jO(^1D)$ wavelengths. In this case, the attenuation due to cloud would be larger for $jO(^1D)$, i.e. $\Delta jO(^1D) > \Delta jNO_2$. This is not observed. The large pathlength enhancements probably do not occur since the clouds are not optically thick enough or do not have a large enough vertical extent. This is consistent with the average optical depth calculated in the previous chapter. Comparison with the ISCCP classification of clouds shows that this optical depth ($\tau=10$) might correspond to a stratus cloud with limited vertical extent. Another possible explanation is that the ozone concentrations within the clouds are not sufficiently high to discern tropospheric path length enhancement i.e. increased absorption by ozone cannot be detected because of the low concentrations of ozone.

We have shown that cloud affects nitrogen dioxide photolysis frequency more than the ozone photolysis frequency, on average and for most of the time. Further analysis of the data in terms of a histogram would allow experimentalists to predict more accurately how often and accurately the photolysis rate data could be parameterised in terms of one another by examination of the distribution of these points. This would provide an interesting extension to the data analysis given. However, here the emphasis lies on trying to simulate our observations with a radiative transfer model and form a theoretical explanation for the observed results.

5.4 Model Analysis

5.4.1 Can the model explain the observed ratio?

The relative response of jNO_2 and $jO(^1D)$ to cloud in the model was determined to provide comparison with the Mace Head observations. A number of scenarios, including different distributions of nitrogen dioxide and ozone, were simulated and the response of each photolysis rate to cloud optical thickness determined. The effect of the cloud on photolysis frequency was expressed as a percentage change in photolysis frequency for each gas, defined relative to a reference cloud optical depth (see equation (5.1)). Considering a clear sky reference, $j_{ref} = j_0$, shows the notional difference between equations 5.1a and 5.1b. Equation 5.1a describes the situation where a clear sky is followed by a cloud (increase in thickness), in contrast to the situation where a cloud is followed by a clear sky (decrease in thickness)

$$\Delta j = [(j_{(od)}{}^{t+\Delta t} - j_{(ref)}{}^{t})/j_{(ref)}{}^{t}] \times 100 \qquad (5.1a)$$

$$\Delta j = [(j_{(ref)}{}^{t+\Delta t} - j_{(od)}{}^{t})/j_{(ref)}{}^{t}] \times 100 \qquad (5.1b)$$

where Δj is the percentage change in photolysis frequency

$j_{(od)}$ is the photolysis frequency at a particular optical depth

$j_{(ref)}$ is the photolysis frequency at a chosen reference optical depth

t refers to the time index

Δt refers to the chosen time interval

This percentage change was calculated over a three minute interval consistent with the one used in the data analysis.

It is important to note that the percentage change in photolysis frequency (Δj) is a relative measure of change and its magnitude depends on the chosen reference optical depth. The biggest change in photolysis rates are at low cloud optical depths (see Figure 5.3). The shape of the curves means that the same Δj can be obtained for different absolute optical depth changes e.g. a small percentage change could be caused by a small change in optical depth with respect to a low reference optical depth or a larger change in optical depth for an optically thicker reference cloud. The Δj values therefore reveal nothing about the

absolute changes in cloud optical depth. It is not possible to determine whether the calculated changes are from thinner to thicker cloud, or from clear sky to thin cloud.
In the absence of any information concerning the cloud field, the reference optical depth is taken to be zero. In this first analysis, it was assumed that all changes occurred relative to clear sky.

Different conditions were chosen to test the model sensitivity and check the results against the data analysis. Absorbing gas columns and wavelength dependent surface albedo were investigated. In all cases, the cloud parameter values (g, ω) were kept constant with wavelength since Mie scattering calculations showed no evidence for significant variation over the wavelengths considered. For consistency with the measurements only data from the upward facing sensor were used for jNO_2.

5.4.1.1 Control run

The model atmosphere in the control runs included an ozone column scaled to 324 DU, but includes no nitrogen dioxide column. The cloud was simulated as a 1km thick layer with its base at 1km. Its optical properties were defined as an asymmetry factor of 0.85 and a single scattering albedo of 0.9999. Different cloud optical depths, τ were chosen ranging from clear sky (0) to a maximum of 250. This maximum was chosen to include the full range of cloud optical depths spanning the distribution derived from the photolysis rates in the previous chapter.

Figure 5.2 shows the best-fit line for the $\Delta jO(^1D)$ versus ΔjNO_2 The gradient, $\Delta jO(^1D)/\Delta jNO_2$, is less than unity, showing $\Delta jO(^1D) < \Delta jNO_2$ i.e. the flux at nitrogen dioxide photolysis wavelengths is more sensitive to cloud that that at $O(^1D)$ production wavelengths. This is in qualitative agreement with the data analysis. However, it can be seen that there is a large discrepancy between the value in the figure and that found from the data analysis (Figure 5.2(a)-(e) compared to Figure 5.1(d)). Perhaps another factor can explain the difference? Perhaps gas absorption or albedo might be the cause? The next sections aim to establish this.

5.4.1.2 NO_2 column

The nitrogen dioxide column can vary significantly at mid-latitudes, but does not contain a high number of molecules (see chapter 3). For this study, a nitrogen dioxide column of 2.668×10^{16} cm^{-3} was chosen (~0.2 DU) as representative of the likely NO_2 column at Mace Head. This value was obtained from those given for the June columns at 52°N in WMO (1985).

Figure 5.2(b) shows the ratio, $\Delta jO(^1D)/\Delta jNO_2$, as given by the gradient after the introduction of the NO_2 column. It is slightly larger than that for the control run (Figure 5.2(a)). In this case, ΔjNO_2, the percentage change in the nitrogen dioxide photolysis frequency is less than in the control run i.e. the sensitivity of the nitrogen dioxide photolysis rate to cloud is decreased when a NO_2 column is introduced.

5.4.1.3 Wavelength dependent albedo

Although the surface albedo in the UV (especially UV-B) is low, it can have a range of values depending on the surface (see chapter 3 for a discussion). We now consider an albedo such as that used in chapter 3. Compared to the wavelength independent albedo used in the control run, this albedo is much lower in the UVB and slightly higher in the UVA. This albedo therefore causes much less reflection at $jO(^1D)$ wavelengths compared to the control run. The ratio, $\Delta jO(^1D)/\Delta jNO_2$, is increased compared to the control run because the sensitivity to cloud at the $jO(^1D)$ wavelengths is increased as there are fewer photons reflected from the ground in this spectral region

5.4.1.4 Ozone

In a clear sky, an increased ozone column decreases the surface actinic flux at ozone photolysis wavelengths by ozone absorption above the ground. This experiment examined how the relative responses to cloud would change when the ozone column was scaled to both the minimum (285 DU) and maximum (419 DU) values for ozone column observed in the campaign. The decreased ozone column decreased the ratio, $\Delta jO(^1D)/\Delta jNO_2$, compared to the control run and the increased ozone column increased the ratio, compared

to the control run. The response of $jO(^1D)$ to cloud was enhanced in the presence of a larger ozone column since the flux beneath the cloud was decreased.

5.4.1.5 Summary

Table 5-3: A summary of the results from varying atmospheric parameters

	control	NO_2	surface albedo	minimum ozone column	maximum ozone column
ozone column	324 DU	324 DU	324 DU	285	419
no2 column	✗	✓ 0.2 DU	✗	✗	✗
Albedo	0.1 λ indpt	0.1 λ indpt	wavelength dependent function	0.1 λ indpt	0.1 λ indpt
$\Delta jO(^1D)/\Delta jNO_2$	0.986	0.996	0.986	0.988	0.987

This analysis shows that the percentage change when taken relative to a clear sky is relatively insensitive to the atmosphere used. The ratios, $\Delta jO(^1D)/\Delta jNO_2$, are always less than unity i.e. jNO_2 is more sensitive than $jO(^1D)$ to cloud. Using a different reference atmosphere or surface albedo can produce changes in the ratio, but the effect is very small. A different background atmosphere or surface albedo cannot, therefore, be the explanation for the difference between the observed and calculated relative sensitivities at Mace Head.

5.5 Model predictions of the effect of increased cloud optical depth on jNO_2 and $jO(^1D)$

The simple model simulation agrees with the experimental finding that the ratio, $\Delta jO(^1D)/jNO_2$, is less than unity, i.e. cloud attenuates jNO_2 more than $jO(^1D)$.

This ratio can be explained by examining jNO_2 and $jO(^1D)$ as a function of cloud optical depth. This is shown in Figure 5.3 which shows jNO_2 and $jO(^1D)$ as a function of optical depth for solar noon (solar zenith angle, θ=33.9°). In Figure 5.3, each photolysis frequency is normalised against its clear sky value so that the shape of the curves can be easily compared. The model flux components shown are those that would be captured by the upward-looking radiometer, i.e. the diffuse downward and the direct component of the fluxes. The two curves have very similar shapes and so are difficult to distinguish on this scale. It can be seen that jNO_2 has larger values at low optical depths and $jO(^1D)$ has larger values at high optical depths. The shape of the curves illustrates two very important points:

(1) The curves are not linear so the magnitude of a change in photolysis frequencies for a given change in optical depth is very sensitive to the starting optical depth. Thus, the same change in optical depth can cause a range of different changes in photolysis rate depending on the initial optical depth.

(2) Similarly, a change in optical depth of the same magnitude, starting from the same point, will increase/decrease the photolysis rate by different amounts depending on whether the cloud is thinning/thickening. For example, a change, of size 10, from τ=20 to τ=30 has a smaller influence on the photolysis rate (22.6% and 21% changes in jNO_2 and $jO(^1D)$ respectively) than the same optical depth change from τ=20 to τ=10 (38.8 and 36.1% respectively).

To compare the relative photolysis rates as a function of optical depth, their ratio, $jO(^1D)/jNO_2$ is shown in Figure 5.4. As well as the curves for solar noon, curves for a range of other solar zenith angles are shown. Each photolysis frequency is again normalised against the clear sky value for that solar zenith angle. The small range on the y-axis highlights the fact that generally relatively small changes are considered. Excepting conditions of low optical depth and low zenith angle, the plot shows that the gradient of $jO(^1D)/jNO_2$ as a function of optical depth is of the same sense for all solar zenith angles.

In general, as the cloud optical depth increases, $jO(^1D)/jNO_2$ increases i.e. $jO(^1D)$ increases relative to jNO_2. Thickening cloud decreases photolysis rates, so this change

corresponds to a greater decrease in jNO_2 compared to $jO(^1D)$. Greater attenuation of jNO_2 means a larger $\Delta jNO2$, so the ratio $\Delta jO(^1D)/\Delta jNO_2$ will be less than unity. This is seen in both the data and model studies. At high optical depths, the decrease for $jO(^1D)$ saturates and cannot drop off any further, the $jO(^1D)/jNO_2$ plateaus.

There are different gradients and different magnitudes of change for different solar zenith angles. Ignoring regions of low optical depth, at high sun, $jO(^1D)/jNO_2$ is approximately or just greater than unity: the responses of $jO(^1D)$ and jNO_2 are comparable. At the low sun extreme, the maximum value is 1.28: the attenuation of jNO_2 is much greater than that of $jO(^1D)$. As the sun tends towards the horizon, the ozone column is increased, there is more ozone absorption and so fewer $jO(^1D)$ photons encounter the cloud and the $jO(^1D)$ response to cloud can no longer change as much as the jNO_2 response. This predicted behaviour shown by the changing absolute values of $jO(^1D)/jNO_2$ can be seen in the data when it is sorted by zenith angle. The ratio, $\Delta jO(^1D)/\Delta jNO_2$ generally decreases with increasing solar zenith angle, (filtered data shows a ratio of 0.75 for $35°<\theta<45°$ compared to 0.70 for $65°<\theta<75°$) as the attenuation of $jO(^1D)$ by cloud decreases.

In contrast, at low optical depths and overhead sun at Mace Head, there is a region where $jO(^1D)$ decreases more than jNO_2 ($jO(^1D)/jNO_2<1$) i.e. $jO(^1D)$ flux is attenuated more than jNO_2 flux so $\Delta jO(^1D)> \Delta jNO_2$. For overhead sun and an optical depth of 5, $jO(^1D)$ reaches its minimum value with respect to jNO_2, ~ 96% of jNO_2. From this minimum, the relative values increase with cloud optical depth and at a cloud optical depth of 20 to 25, the two values become approximately equal again i.e. $\Delta jNO_2 \sim \Delta jO(^1D)$. This reversed response at low optical depths persists in the model simulation until a crossover solar zenith angle of 52° is reached. Above this value, ΔjNO_2 is predicted to always be greater than $\Delta jO(^1D)$.

Figure 5.3 showed that the normalised values of $jO(^1D)$ are less than normalised jNO_2 values at low optical depths. The reason for this can be seen in Figure 5.5, which shows the ratio of the cloudy sky diffuse component to the clear sky diffuse component of the jNO_2 and $jO(^1D)$ actinic fluxes as a function of optical depth. A case of overhead sun

(θ=33.9°) and a case of low sun (θ=70°) are shown. For thin clouds and overhead sun, the diffuse actinic fluxes beneath the cloud are increased relative to their clear sky values. The jNO_2 actinic flux is increased more than the $jO(^1D)$ actinic flux, with the maximum values of ~ 1.45 at 1.15 respectively at τ=5. This increase in the diffuse component with optical depth at low optical depths overlays the overall decrease in total photolysis rates and so there is a smaller attenuation of jNO_2 than $jO(^1D)$ by cloud at low optical depths and zenith angles. This is further discussed in 5.6.2.

5.6 Towards a theoretical explanation for the responses of jNO_2 and $jO(^1D)$ to cloud

5.6.1 $\Delta jNO_2 > \Delta jO(^1D)$

If it is believed that the scattering properties of the cloud itself are not spectrally dependent, what causes the differing attenuation of jNO_2 and $jO(^1D)$ by cloud?

Crawford *et al.*(1999) state that response of jNO_2 to cloud is greater than $jO(^1D)$ because of the differing clear sky direct to diffuse ratios for the actinic flux in the UVB and UVA spectral regions. "That jNO_2 has a larger fraction of direct radiation leads to the expectation that it might experience larger fluctuations due to clouds". It is true that the direct contribution to the jNO_2 flux is larger, since at the longer wavelengths this radiation experiences less Rayleigh scattering in the atmosphere. Calculations show that at 2 km in a cloudless sky the ratio of the direct flux to the diffuse flux for jNO_2 is 1.27 compared to just 0.59 for $jO(^1D)$ for a solar zenith angle of 0°. These portion decrease as the solar zenith angle increases: the direct to diffuse portions are 1.22 and 0.54 for jNO_2 and $jO(^1D)$ at 35 degrees and further to 0.698 and 0.118 for 75 degrees respectively. However, since the transmitted direct actinic flux drops to zero at low cloud optical depths (see Figure 5.6) (and is not always dominant), the attenuation of direct flux alone is too simplistic to explain the relative responses under the large range of cloud optical depths encountered at Mace Head. The reason cannot simply be that there is more direct flux and therefore greater attenuation by clouds because attenuation of UV by clouds is more complex than this: both the diffuse and direct fluxes are important, with the diffuse flux becoming more so at higher cloud optical depths. However, a key point is made here: scattering of

photons by the atmosphere is wavelength dependent and this fact underpins any further explanation.

Kylling *et al.*(1997) explained the increased transmission in the UV-B compared to the UV-A shown by Seckmeyer *et al.*(1996) as caused by photons that are reflected upwards from the cloud top, scattered by the overlying atmosphere and transmitted back down through the cloud. The wavelength dependence is therefore not due to differing opacity of the cloud itself, but comes from the wavelength dependent Rayleigh scattering ($\sim 1/\lambda^4$) of the photons above the cloud top, which then travel back through the cloud. They support their argument by showing an increase in the global radiation at cloud top. The longer wavelength UVA photons are less Rayleigh scattered and therefore less likely to be transmitted back through the cloud, resulting in a larger ΔjNO_2.

As well as the atmosphere above the cloud, the scattering properties of the underlying atmosphere determine what is sensed at the ground. At these lower altitudes, the increased density of the atmosphere means an encounter between the photon and a molecule is much more probable than at the cloud top. We propose another similar mechanism to that of Kylling *et al.* (1997) involving Rayleigh and cloud scattering, which has also been suggested by Frederick *et al.*(1997). This time however, reflection is from the cloud base rather than the cloud top. Underneath the cloud, radiation will be backscattered by the molecules of the atmosphere. A greater portion of the shorter wavelength $jO(^1D)$ radiation will be Rayleigh scattered and in cloudy conditions that Rayleigh scattered radiation will travel upwards to encounter the cloud base. From the cloud base, the radiation is reflected to increase the downward flux measured at the ground compared to clear sky conditions.

However, both of these mechanisms have a potential flaw when considering photons at $jO(^1D)$ wavelengths. The Rayleigh-cloud scattering coupling will increase the photon path length and so photons are more likely to suffer absorption by ozone molecules. This would increase absorption at shorter wavelengths, opposing the increase in transmittance with wavelength and resulting in a larger $\Delta jO(^1D)$. However, calculation of the Rayleigh

scattering and ozone absorption optical depths at an effective wavelength of 310 nm shows that even with an ozone abundance of 40ppb, the Rayleigh scattering will dominate by at least an order of magnitude.

Another consideration is what happens under thicker cloud. As the cloud becomes thicker and thicker, the cloud will reflect more incident radiation from its base and top. Although less flux would be expected to emerge from the cloud, the transmittance would still be larger at shorter UVB wavelengths than at the longer UVA wavelengths. As the cloud albedo increases, it is expected that this would lead to more multiple reflections between the cloud reflective surface and the atmosphere and so a steeper dependence of the transmission on wavelength. However, as the path length increases absorption by ozone would temper this effect until eventually ozone absorption would be expected to dominate.

5.6.2 $\Delta jO(^1D) > \Delta jNO_2$

At small optical depths and low zenith angles, a reversal of the responses is seen. This can be explained by considering the scattering processes in the cloud. Single scattering causes the direct component to be converted to the diffuse component. However, with increasing orders of scattering, this is opposed: more and more of the diffuse component is backscattered and this leads to less transmittance for higher cloud optical depths.

Longer wavelength jNO_2 flux has a larger direct portion of direct flux, so this direct to diffuse conversion (single scattering) is relatively more important at these longer wavelengths. This is illustrated in Figure 5.5(a), which shows the increase of the diffuse flux at the ground relative to the clear sky. In our model, this effect peaks at an optical depth of 4 for high sun and this is consistent with the work of Madronich (1987). This means that, for thin cloud, the larger direct component allows a increase in the diffuse component (single scattering dominates over multiple scattering) and means that more jNO_2 wavelength photons are seen beneath the cloud, so ΔjNO_2 is less than $\Delta jO(^1D)$. As the optical depth of the cloud increases, this enhancement of the diffuse flux below the cloud disappears as the backscattering dominates. Similarly, this conversion is only

significant at small solar zenith angles when the sun is overhead (see Figure 5.5 (b)): at larger zenith angles there is much less direct flux at cloud top.

Our analysis shows that in our filtered data (Figure5.1(c)), $\Delta jNO_2 > \Delta jO(^1D)$ approximately 60% of the time. This means that this direct to diffuse conversion effect occurs in the 40% of remaining points. About 50% of the time $\theta < 52°$ so the direct component is more significant and the reduction in $jO(^1D)$ is greater, but the probability of low cloud optical depths is generally quite small. This means that $\Delta jO(^1D) > \Delta jNO_2$ occurs more frequently than we might expect from the model, and that is in qualitative agreement with the discrepancy between the observed (~0.75) and modelled (~0.99) ratios.

We have seen (Figure 5.4) that optical depth is the critical parameter for the response of the two photolysis rates to cloud. However, because of the importance of the direct beam relative to the diffuse component, solar zenith angle can also be important. This agrees with Monks *et al.*(1988) who observed that the responses in jNO_2 and $jO(^1D)$ were more similar for overhead sun, although we now know that that is only a fragment of the story.

5.7 Mechanisms for obtaining a more realistic ratio

The observed value of the ratio of the photolysis rate fluctuations caused by cloud, $\Delta jO(^1D)/\Delta jNO_2$, is much smaller than expected from the model. From the model, we have developed a theoretical explanation for the wavelength dependence of cloud transmission, (the ratio of cloudy to clear sky fluxes) but this wavelength dependence is not enough to explain our observed ratio. Some atmospheric process that is not correctly described, or accounted for by the model must be responsible.

In the atmosphere, there are two obvious possibilities. Either $\Delta jO(^1D)$ is smaller than expected : more photons are transmitted at shorter (UVB) wavelengths or ΔjNO_2 is larger than expected: fewer photons are transmitted at longer wavelengths, or both. Since Δjs are calculated for a cloudy sky, we are looking for a process that causes a perceived wavelength dependence in the presence of clouds. Subsequent to the earlier discussion of ozone, it is believed that changing concentrations of atmospheric gases over the short

timescales required are not the culprits. Other differences between our model atmosphere and the real atmosphere that might influence cloud must therefore be considered.

The first and most obvious difference between the model and the real atmosphere is the representation of cloud. Perhaps the unrealistic representation of a horizontally infinite uniform slab of cloud could be artificially increasing the ratio? In the case of broken cloud fields, enhancements of photolysis rates are observed. Following the work of Laird and Harshadvan (1997) and others, it is seen that these enhancements are smaller in the UV than in the visible. Thus, it would be expected that the longer wavelength jNO_2 flux would be enhanced more than $jO(^1D)$. Under broken clouds, then, this enhancement would lead to a smaller decrease in jNO_2 than is observed. The ratio $\Delta jO(^1D)/\Delta jNO_2$ would therefore actually increase compared to the values of ~ 0.9 predicted by the model.

Apart from the considerations of cloud geometry, other factors could influence the spectral transmittance of clouds in the ultraviolet. The asymmetry factor, g, is used in models to represent the amount of forward scattering from particles like cloud particles (see chapter 2). Mie scattering calculations for particles with an effective radius of 10μm (pers. comm., J.E. Russell, 2000) show that the asymmetry factor has a slight spectral dependence in the UV/visible region, increasing by about 0.0141% from 250 to 600nm. similar increases are seen for other particle sizes with effective radius 5-20μm. This spectral increase in asymmetry factor would lead to more forward scattering and so a larger downward flux at longer wavelengths. This increased flux at longer wavelengths would lead to a smaller decrease in flux under clouds at longer wavelengths. This would result in a smaller ΔjNO_2 and, therefore, again a larger value of $\Delta jO(^1D)/\Delta jNO_2$. According to the same Mie scattering calculations, the single scattering albedo, ω, is constant in this region, so should have no influence on the spectral dependence of transmission.

In the absence of a factor influencing the transmission in the two spectral regions, another possibility lies with the calculation of the ratio itself. Our ratio is simply calculated for clear to cloudy skies. However, Figure 5.3 showed us that the magnitude of the change in

photolysis frequency for a particular change in optical depth is highly dependent on the starting optical depth. The changes in the photolysis frequencies are also different at different optical depths because $jO(^1D)$ saturates more quickly. Changes between cloud of different optical thicknesses could therefore lead to a different average response, $\Delta jO(^1D)/\Delta jNO_2$. The next section replaces the simple cloud to clear sky changes with a realistic cloud field to see if this could be the cause of the difference between the modelled and the observed ratios.

5.7.1 Introducing a realistic cloud field into the model

In the previous section, the changes are calculated relative to a clear sky. As already discussed, the plots of photolysis frequency as a function of cloud optical depth show that the starting point of a given optical depth change will hugely influence the magnitude of its effect on the photolysis frequency, since the response to optical depth is non-linear. Some knowledge of the optical depths at which the changes occur would, therefore, be instructive.

In the previous chapter, a lognormal distribution was derived to describe the cloud optical depths at Mace Head. A random series of optical depths based on a lognormal distribution was generated and used as input to the model. This series had to be large to capture the shape of the lognormal distribution, so ten thousand points were used. Obviously with such a large number of steps, this calculation could not be repeated for every zenith angle during the day. Two solar zenith angles were chosen to ensure that the different regimes shown in Figure 5.5 were both represented. The changes in photolysis rates were calculated from one step to the next and to emulate the real changing cloud situation at Mace Head. Again, only direct and diffuse components were considered. Figure 5.7(i) and (ii) show the results of these calculations. It can be seen that using this method of simulation decreases the overall gradient to 0.91 at $\theta=35°$ and 0.90 at $\theta=55°$. Plots of the values of $\Delta jO(^1D)$ against ΔjNO_2 calculated from the measurements are shown for comparison with the simulated values at these two zenith angles. The measured values are

from solar zenith angle ranges with bins centred at 35°(Figure 5.8) and 55°(Figure 5.9) respectively.

At, θ=35°, we compare Figure 5.8 with 5.7(i). The same data filtering process as in Figure 5.2 is shown for comparison, but the most important result is the comparison between Figure 5.7(d) and Figure5.7(i)(c). The gradient in the data is 0.78 compared to that from the model simulation of 0.91. Similarly, at θ=55° the observed gradient is 0.82 and the simulated gradient is 0.90. The range of points in the simulation (Figure 5.7(i)&(ii)(c)) is much greater than seen in the data (Figure 5.8(d) & Figure 5.9(d)). This can be understood by considering the fact that changes between the optical depths used in the model are of a random size, although constrained to the lognormal distribution. In the atmosphere, we would probably not expect to suddenly go from a condition of very low to very high optical depth (or vice versa). We might expect to see smaller variations around an overall gradually thickening cloud optical depth (say, as a front approaches) or gradually thinning cloud optical depth. This is a problem of time constraint. However, the probability distribution means that extremely large changes (e.g. from very thin cloud to a τ of say 190) should not happen very often. The simulation gradients increase with zenith angle, as do the ones seen in the data.

Another problem with the simulation appears with the differences between thickening and thinning cloud. Quadrant 1 (Q1) shows positive changes in photolysis frequency, which correspond to clouds decreasing in optical depth. Quadrant 3 (Q3) corresponds to negative changes in photolysis rate: increases in optical depth. In the data (Figure 5.1), the gradients appear relatively similar in Q1 & Q3 at θ=35 and θ=55° (although more similar for θ=35° than at θ=55°). However, in the model simulation, this is not the case. The Q3 gradient values in the model simulation are much higher than observed in the data simulation. The plots of jNO_2 and $jO(^1D)$ as a function of optical depth calculated by the model (Figure 5.3) illustrate the reason for this. From the cloud probability density function, we know that the most probable value for optical depth in this simulation is

around 10 (see Table 4.2). If we choose an optical depth around the most probable, and want to move to a thicker cloud (moving right along the x-axis) we can see that the changes in photolysis rate are fairly similar in this case, $\Delta jNO_2 \sim \Delta jO(^1D)$, so the gradient is close to 1. This is not observed in the data, which shows approximately equal gradients for Q1 and Q3. Figure 5.4 shows that the slope of $jO(^1D)/jNO_2$ calculated by the model at high optical depths is almost flat. The response of $jO(^1D)$ has saturated. However, from the discussion in 5.5.2, we see that in a real atmosphere we would expect a further spectral differentiation of the flux even at high optical depths due to the multiple reflections between the cloud and the atmosphere. This would mean that $\Delta jO(^1D)$ would not have saturated, leading to a steeper gradient is seen in Figure 5.4 and so a larger difference between $\Delta jNO2$ and $jO(^1D)$. This is not shown by the model, probably because it is only a 2 stream model and is unable to represent the directionality of the multiple scattering accurately enough.

However, in Q1 we consider thinning cloud. Examination of the Figure 5.3 shows that decreases in cloud optical depth are likely to have a larger change in jNO_2 than $jO(^1D)$. This explains the much lower gradient (compare Figure 5.7(i) &(ii)(d) and (e) to Figure 5.8 & 5.9(e) and (f).

The model simulation shows small a range of values for points in Q3, since the decrease in transmission becomes smaller with increasing optical depth. This small range is also evident in the data. In the model, the Q1 range is much larger than in Q3. This extended range is noticeable in the measurements, but is greater in the simulation probably due to the lack of time constraint, as mentioned earlier.

From all the data, Figure 5.1(e)&(f), there is a tendency for the gradient to increase in Q3 with respect to Q1, so the in this the simulation agrees with the measurements.

Apart from the problem of thickening cloud, the overall agreement between the gradient representing the change $\Delta jO(^1D)/\Delta jNO_2$ in this model simulation is much better than that just using the clear to cloudy assumption. In general, $\Delta jO(^1D)/\Delta jNO_2$ decreases as we move towards higher reference optical depths. In this simulation, a lognormal probability distribution is used which is skewed i.e. the mean is greater than the mode. For this reason, most of the changes will be based around a higher reference optical depth and so the relative change in $\Delta jO(^1D)$ will be less than ΔjNO_2. This curvature will therefore lead to a decreased ratio (see Figure 5.3/5.4) as is observed in this simulation.

5.7.1.1 Possible evidence for anomalous absorption?

As discussed in previous chapters, anomalous absorption has been proposed and is also frequently invoked as a possible explanation when researchers have results that they cannot explain (e.g. Barker *et al.*, 1998). Increased absorption has been observed by NO_2 in deep convective thunderclouds (Solomon *et al.*, 1999) and the ultraviolet anomalous absorption noted by Wendisch *et al.*(1999) was in polluted boundary layer clouds. Neither of these conditions is thought to be particularly appropriate to Mace Head, so although a precedent for introducing anomalous absorption may exist, it is not very strong.

Mie scattering calculations show that the single scattering albedo is constant across the spectral region considered in this study. However, Kylling *et al.*(1996) use a wavelength dependent single scattering albedo when forming an explanation for spectrally dependent cloud transmittance observed by Seckmeyer *et al.*(1996). Their values range from ω=1 at 300nm to ω=0.9998 at 400nm, a rather steep change if Mie scattering calculations are to be believed. However, single scattering albedos ranging between 1 at 300nm and 0.9999 at 550 nm are sometimes used, depending on the precise details of the cloud (P. Forster, pers. comm., 1999). A wavelength dependent asymmetry factor was also included in their calculations.

Inclusion of a wavelength dependent asymmetry factor decreasing from 0.9999 at 310nm to 0.9994 at 550 nm with a gradient of 0.05% is included in our simulation, the gradient of the photolysis responses simulation is very similar to that of the data. A wavelength

dependent albedo is also introduced in this case. Only one zenith angle (θ=55°) is used since the previous calculations showed that the overall form of the results was very similar at the two zenith angles (compare 5.7(i)&(ii)). The results are shown in Figure 5.10(a)-(e). Although the gradient is in much better agreement with the data, ($\Delta jO(^1D)/\Delta jNO_2$=0.78 c.f. 0.82 in Figure 5.9(d)) the problem of the gradient in Q3 persists, substantiating the assumption that this problem is caused by the model not being able to represent the multiple scattering well. It should be noted that the justifiable inclusion of a wavelength dependent asymmetry factor would slightly oppose this dependence requiring a slightly larger decrease in single scattering albedo. However, this is just a question of exact magnitude and brings no more to the discussion.

In conclusion, anomalous absorption at longer wavelengths brings the overall model simulation (Figure5.10(c)) into good agreement with the data (Figure 5.9).

5.7.1.2 Clear sky and cloud optical depth distributions

In the previous section, the cloud field at Mace Head was modelled using the cloud optical depth distribution derived in the previous chapter. This improved the agreement between the modelled ratio and the observed ratio. The agreement could be improved further by the use of a spectrally dependent single scattering albedo equivalent to anomalous absorption at longer wavelengths. This anomalous absorption is sometimes used by researchers to gloss over differences in values calculated by models and measurements. However, there is another solution. Considering the lognormal form of the cloud optical depth probability density function, we can see that there is a very low probability of thin clouds occurring. The greatest change in photolysis frequencies for a given optical depth is at low optical depth, and it is here that ΔjNO_2 is generally much bigger than $\Delta jO(^1D)$ (see Figure 5.4). In this distribution, we have not included the probability of a cloudless sky. Obviously, although a good description of the probability of encountering a particular cloud optical depth, this does not describe the situation the radiometers are likely to encounter at Mace Head. The previous two distributions are therefore missing a process that would further decrease our ratio.

The probability distribution function required is therefore the sum of two probabilities (the sky is either cloudy or cloudless), the first is simply probability of clear or cloudy sky and the second a probability of cloudy optical depth and this must conform to the lognormal probability density function. This probability of clear sky events is not known and must be estimated from the ratio of the number of points calculated in the previous chapter to the total number of points recorded. The clear sky probability, is the ratio of difference between unity and the cloudy sky probability and the total number of events considered over the period.

Taking the probability of clear sky as 0.538, that fraction of clear sky points were randomly inserted into a ten thousand-point grid. The rest of the grid was then filled with the cloudy optical depth distribution of the remaining number of points. Since the probability of clear sky is estimated as greater than 50%, 'patches' of clear sky randomly appear where two or more clear events follow each other. This is not unrealistic. The cloudy sky is constrained in terms of the number of occurrences by the probability distribution, but as before, these are not necessarily constrained as real time changes might be. In the model simulation, there is chance that a change from clear sky to a very high optical depth might occur, something that might not be expected in real life. This change however would have a very small probability in the model. However, despite its limitations this simulation is reasonably realistic and performed reasonably well. Figure 5.11(a)-(e) shows the results of this simulation plotted in the same way as before. It can be seen that the total number of changes is reduced, because of these clear sky patches.
The overall agreement between the data (Figure 5.9(d)) and the simulation is good (Figure 5.11(c)) at this solar zenith angle. In fact, the $\Delta jO(^1D)/\Delta jNO_2$ is less (0.75) than that observed (0.82), perhaps due to an overestimate of the number of clear sky points. Another feature of this simulation is that very large values of the intercept appear. This indicates a non-linearity in the data. It is believed that this is the result of the unrealistic time series combined with the clear sky optical depths: this can lead to much larger changes than would be expected and creates a large value of the intercept in Q1. The

gradient shows that there is not need to include a wavelength dependent single scattering albedo.

In summary, the introduction of a realistic cloud field improves calculation of the responses of photolysis rates to cloud. The overall agreement between the values is much better than that obtained with simple clear to cloudy (and vice versa) changes in cloud. The agreement with the data analysis can be improved either by including a wavelength-dependent single scattering albedo, or by introducing a clear sky probability. Introduction of the clear sky probability is favoured, as it has a very sound physical basis. In terms of the gradient, the model is good at describing the changes when cloud gets thinner. However, the range of the changes is too large because of the unrealistic time series caused by generation of a random series of fluctuations of cloud optical depth around a lognormal distribution. There are also problems using this model to describe very thick clouds since this requires calculation of clouds and high optical depths and the two streams are not able to calculate the diffuse flux accurately enough. However, despite these drawbacks, this analysis has shown the importance of using a realistic cloud field to emulate the relative sensitivities of photolysis frequencies to cloud. The new distribution of cloud was applied and proved successful, within the limitations of the model. The importance of considering the cloud optical depth and changes in cloud optical depth when attempting to model atmospheric transmittance has been shown.

It should also be noted that since introduction of a clear sky into the realistic cloud field makes a large contribution in moving the ratio towards the expected value, the reduction of the direct flux (as suggested by Crawford *et al* (1999)) must play a significant role at lower optical depths where this component of the flux is not negligible.

5.8 Summary

In general, clouds are found to reduce the nitrogen dioxide photolysis rate less than $jO(^1D)$. For solar zenith angles less than 75 degrees, the overall ratio was calculated as $\Delta jO(^1D)/\Delta jNO_2=0.75$. Aerosol reverses this general trend, attenuating $jO(^1D)$ more than jNO_2 and its effect contributes to many of the small changes in photolysis frequency that

were removed from the data. There are a significant number of anti-correlations i.e. increases in one photolysis rate over the time interval whilst the other decreases. No adequate physical explanation has been found for these anti-correlations; they are attributed to random error.

The proportion of points $\Delta jNO_2 > \Delta jO(^1D)$ is almost identical to that found by Crawford *et al.*(1999) (60 and 59% respectively) despite the differences in measurement method and location. The increase in cloud transmittance with wavelength found in the study qualitatively agrees with the UVA and UVB transmittances measured by Seckmeyer *et al.* (1996). There is no evidence for consistent tropospheric path length enhancement in the data (e.g. Pfeilsticker, 1998a). This may be due to low ozone concentrations or insufficiently thick clouds.

Using constant cloud optical properties, clear sky to cloudy sky changes can never explain the size of the observed ratio. Simulations with different concentrations of nitrogen dioxide, ozone, and a different surface albedo were used. For all of these, the nitrogen dioxide photolysis rate responded more to cloud than the ozone photolysis rate, showing the correct sense but not the magnitude

The theoretical explanation for greater response of jNO_2 compared to $jO(^1D)$ given by Crawford *et al.*(1999) is shown to be inadequate over a large range of optical depths. Two further mechanisms involving coupling of cloud scattering with Rayleigh scattering are proposed for this response. The explanation is believed to stem from a combination of these two mechanisms. The two stream model at high optical depth does not capture these mechanisms adequately. At low zenith angles and low optical depth, the ratio is predicted to reverse with $jO(^1D)$ showing increased sensitivity to cloud. A theoretical explanation is proposed and this is consistent with earlier work by Madronich (1987). Model predictions show that the ratio should show some zenith angle dependence. There is some evidence to

support this in the data. The most important parameter for determining the size of the change in photolysis frequency is the starting optical depth of the change.

Introduction of the cloud optical depth distribution derived in the previous chapter to describe the changing optical depth of the cloud field improves the agreement between the observed and modelled ratios. Using the cloud optical depth probability distribution alone cannot explain the magnitude of the observed ratio. The agreement between the observed and modelled ratios can be further improved by introducing a wavelength dependent single scattering albedo, analogous to anomalous absorption at longer UV wavelengths. Although, anomalous absorption successfully describes the agreement between model and observed ratio, a further, more physically based explanation can be found. Inclusion of an estimated clear sky probability also improves the agreement between model and observed ratios.

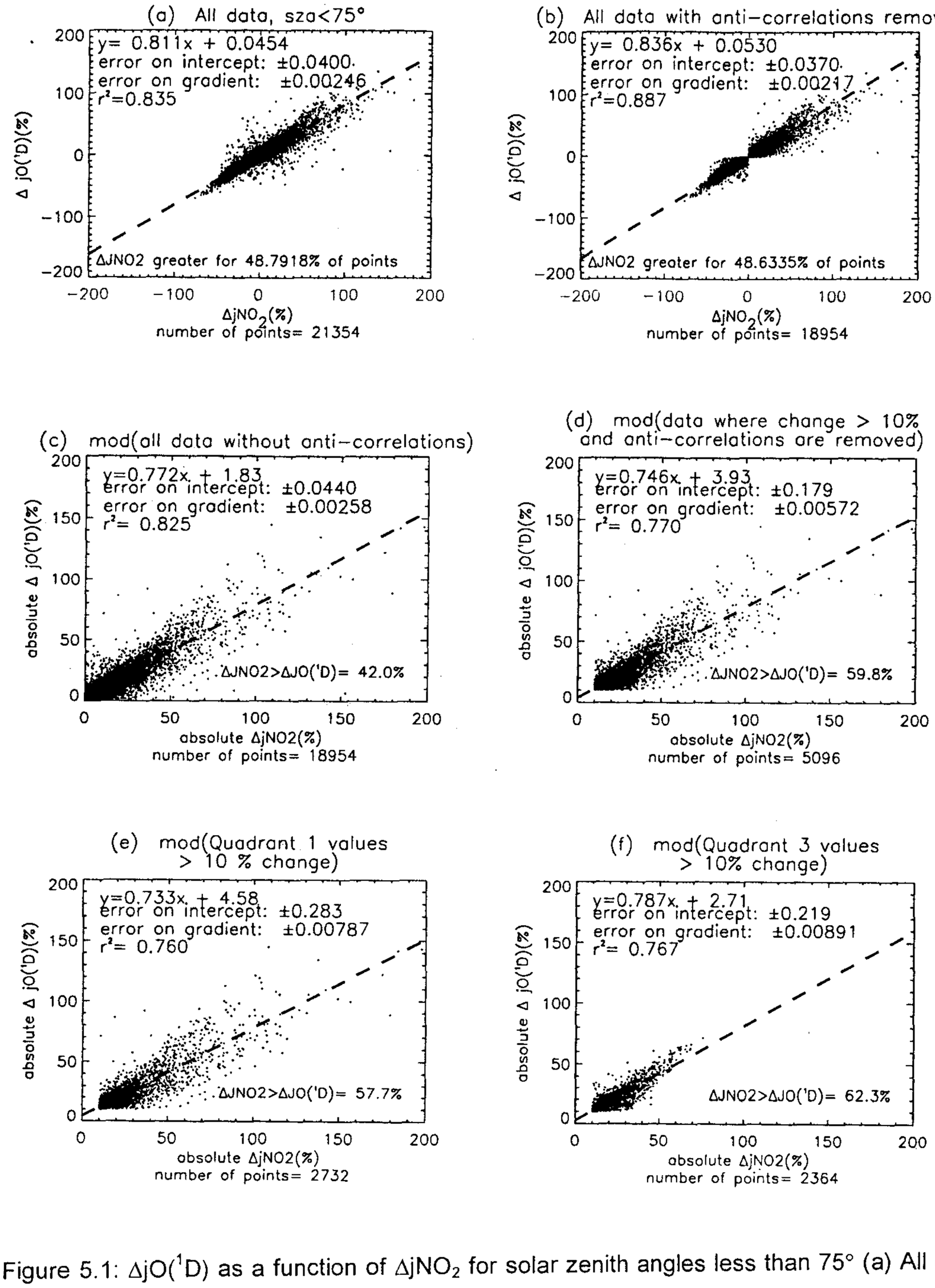


Figure 5.1: $\Delta jO(^1D)$ as a function of ΔjNO_2 for solar zenith angles less than 75° (a) All data (b) All data without anti-correlations (c) Absolute values of all data without anticorrelations (d) As (c) but only including values >10% (e) Positive-positive changes only (f) Negative-negative changes only

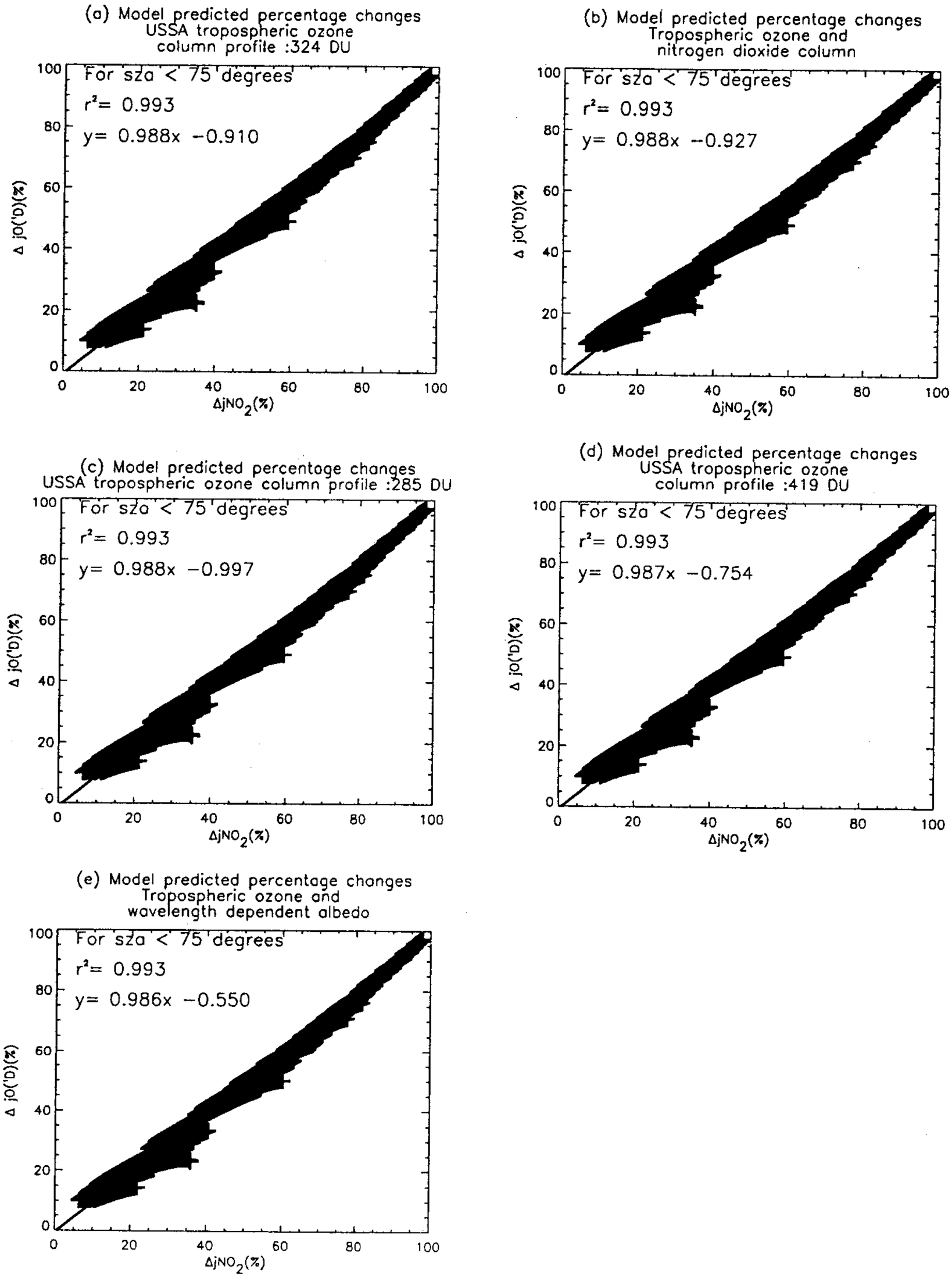


Figure 5.2: Model predicted clear to cloudy changes (a) control run (b) Including NO_2 column (c) Decreased O_3 column (d) Increased O_3 column (e) Wavelength dependent albedo

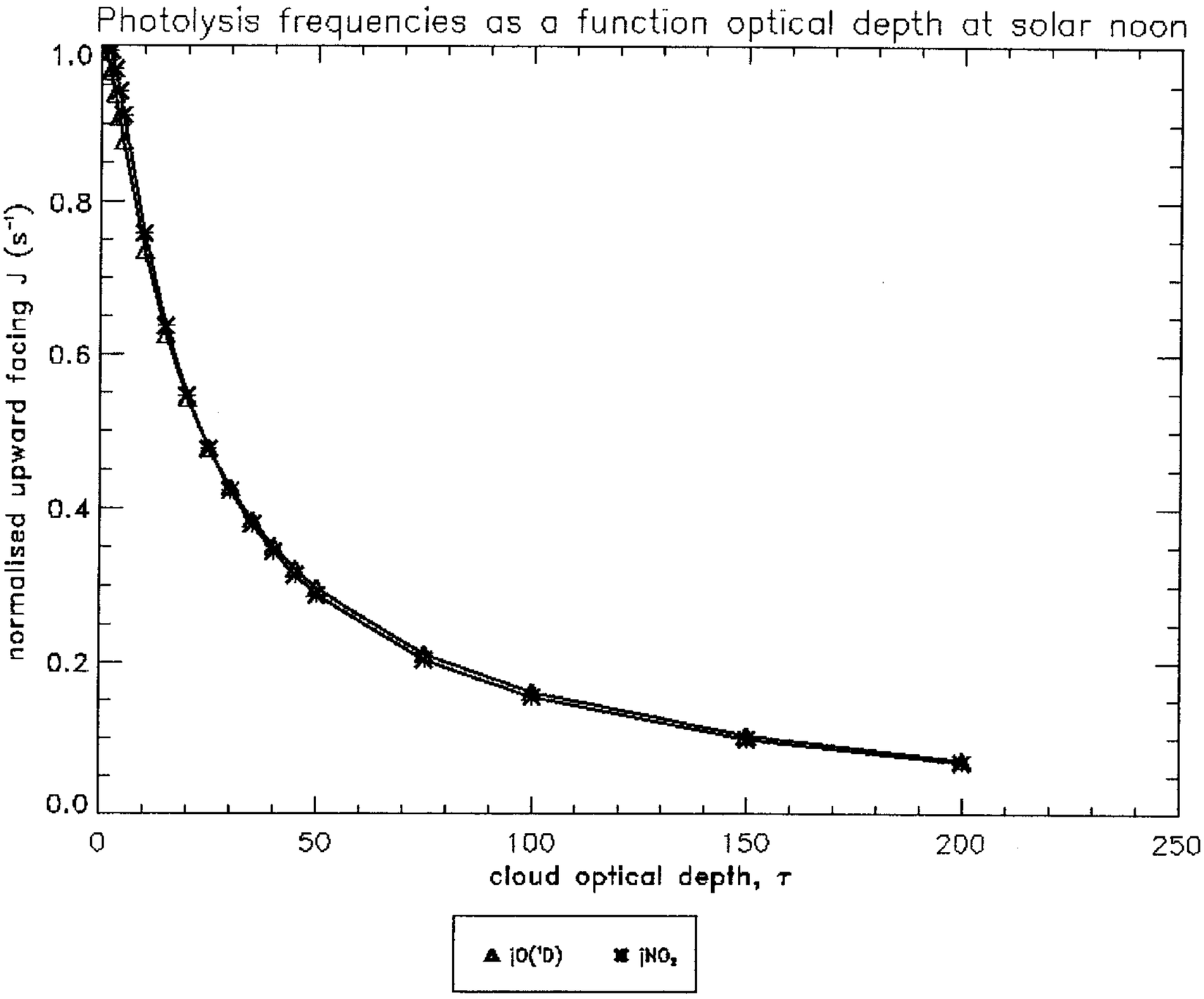


Figure 5.3: $jO(^1D)$ and jNO_2 normalised to their clear sky values as a function of cloud optical depth

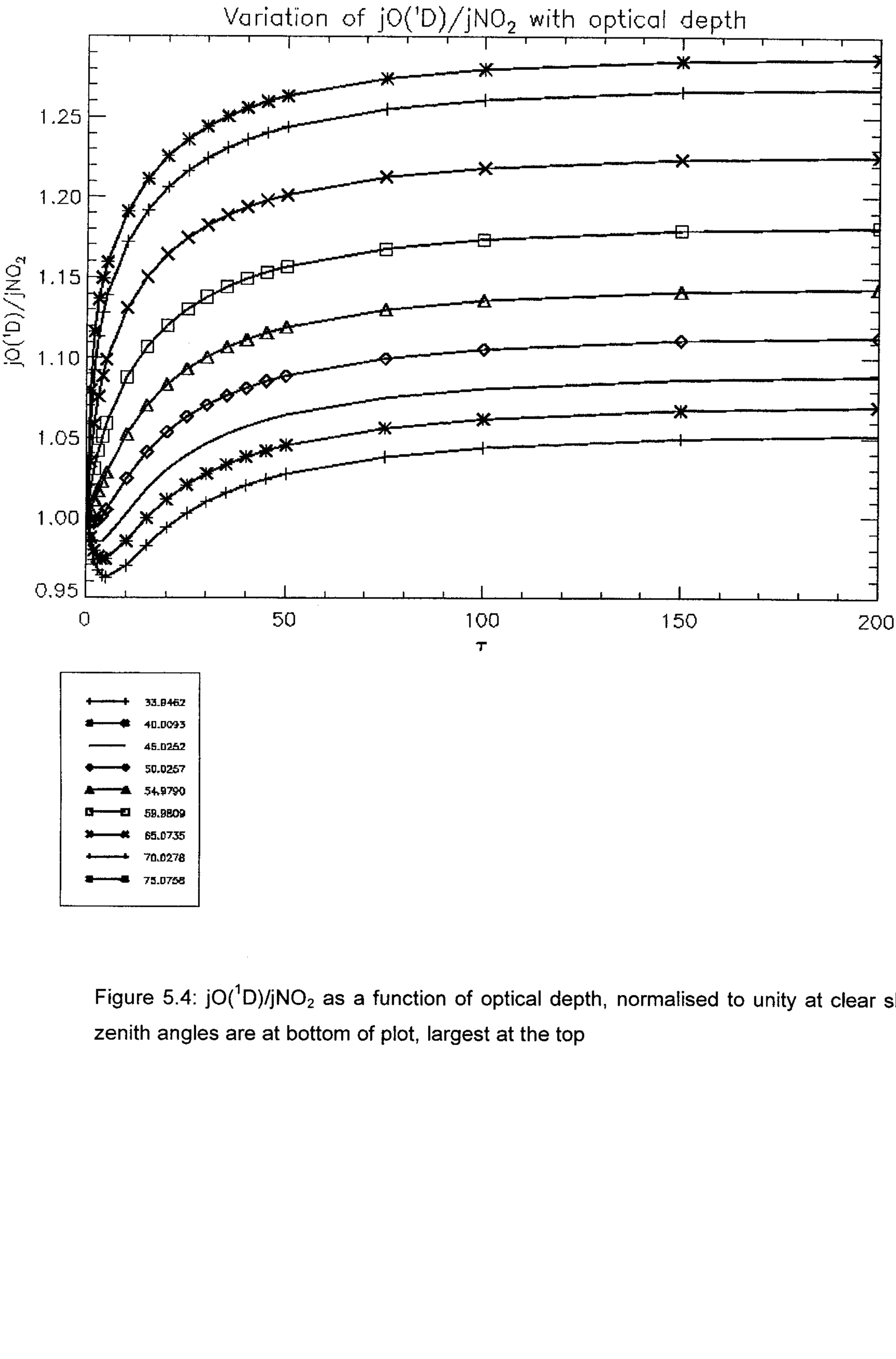


Figure 5.4: $jO(^1D)/jNO_2$ as a function of optical depth, normalised to unity at clear sky. Smallest zenith angles are at bottom of plot, largest at the top

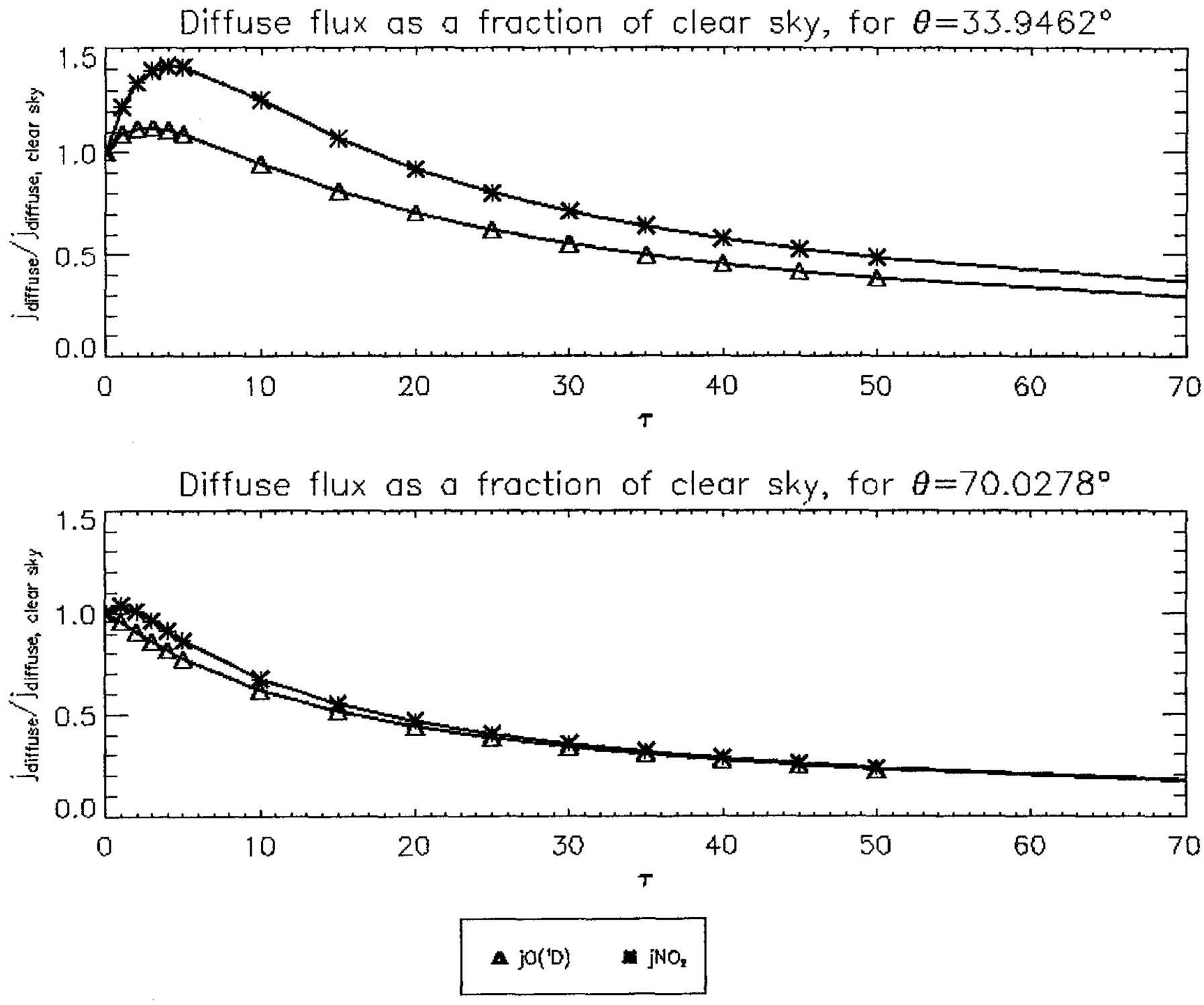


Figure 5.5: Diffuse fraction of $jO(^1D)$ and jNO_2 as a fraction of their clear sky values for (a) 33.9° and (b) 70°

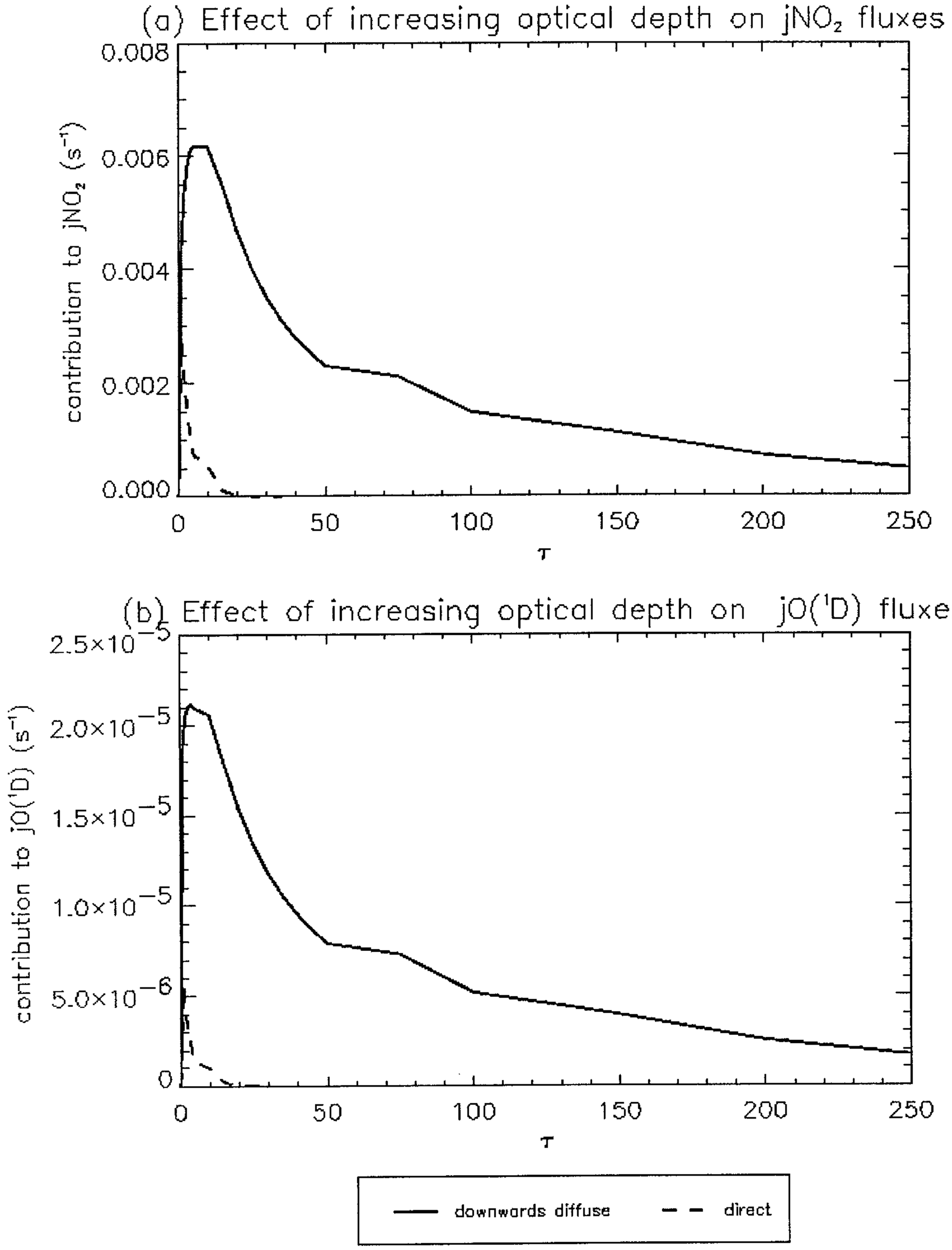


Figure 5.6: Direct and diffuse downwards portions of photolysis frequency flux, each normalised to unity at clear sky (a)jNO_2 (b)$jO(^1D)$

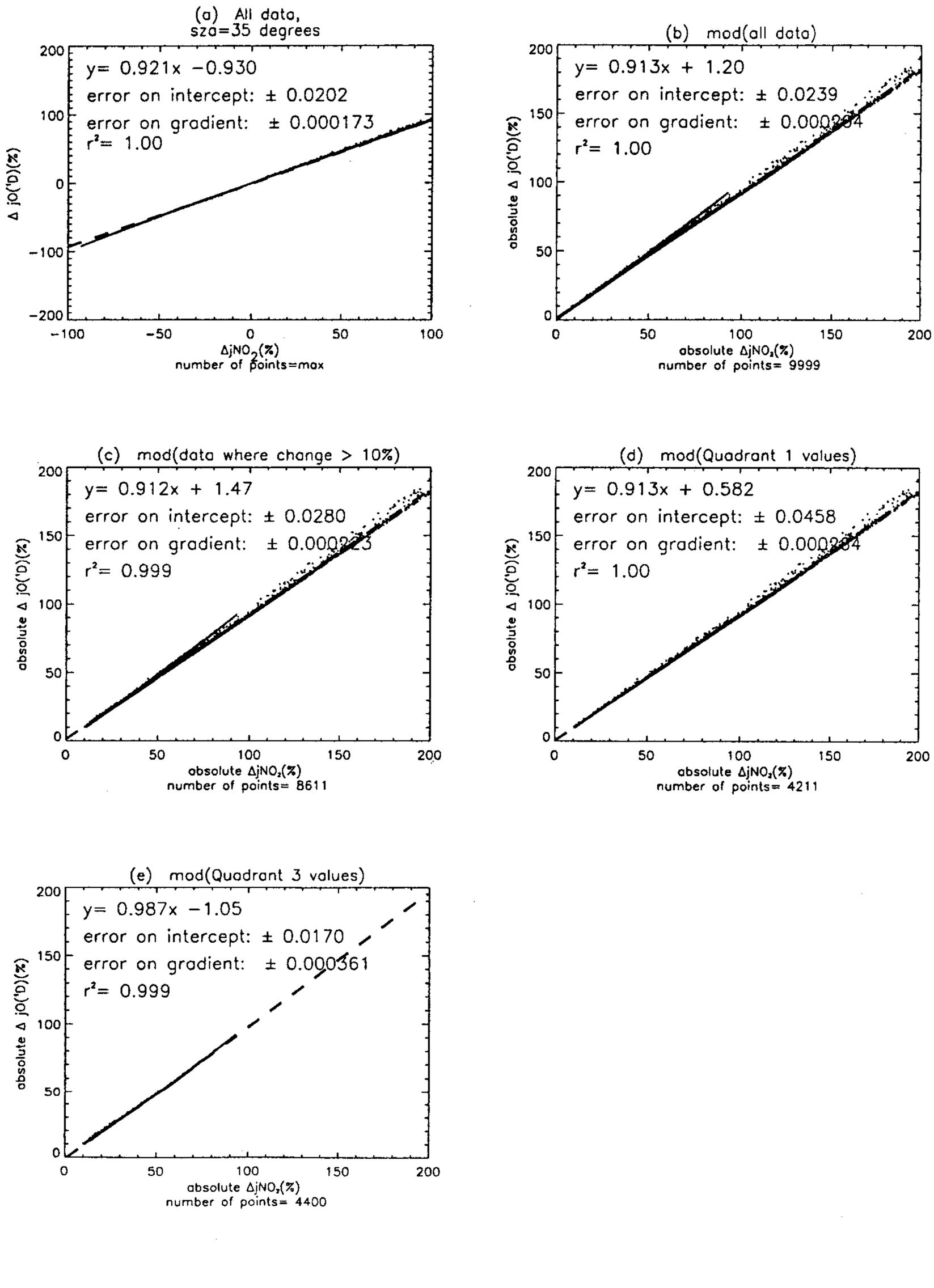


Figure 5.7(i): Simulation including cloud probability density function for zenith angle of 35° a) All data (b) Absolute values of all data without anticorrelations (c) As (b) but only including values >10% (d) Positive-positive changes only (e) Negative-negative changes only

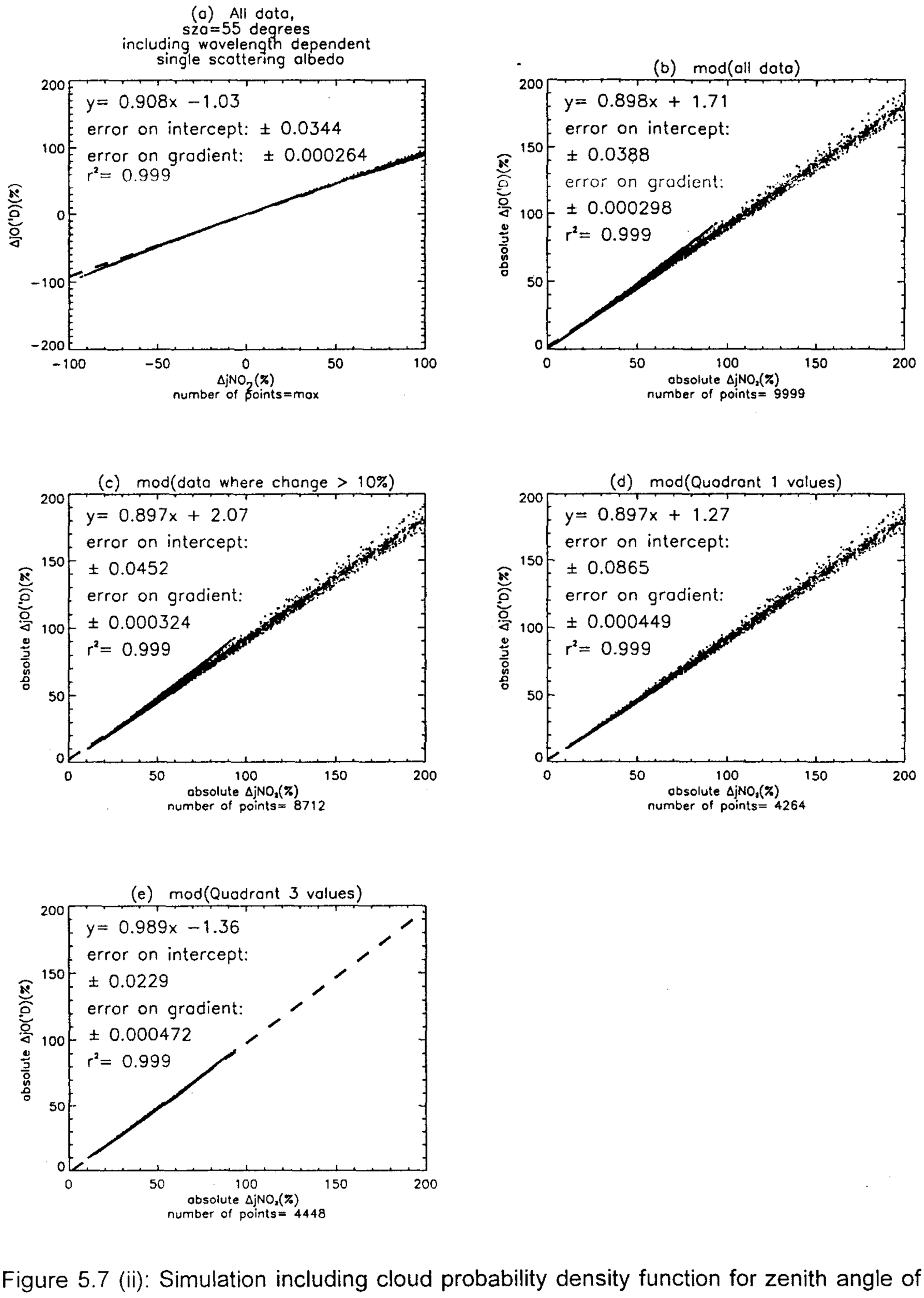


Figure 5.7 (ii): Simulation including cloud probability density function for zenith angle of 55° a) All data (b) Absolute values of all data without anticorrelations (c) As (b) but only including values >10% (d) Positive-positive changes only (e) Negative-negative changes only

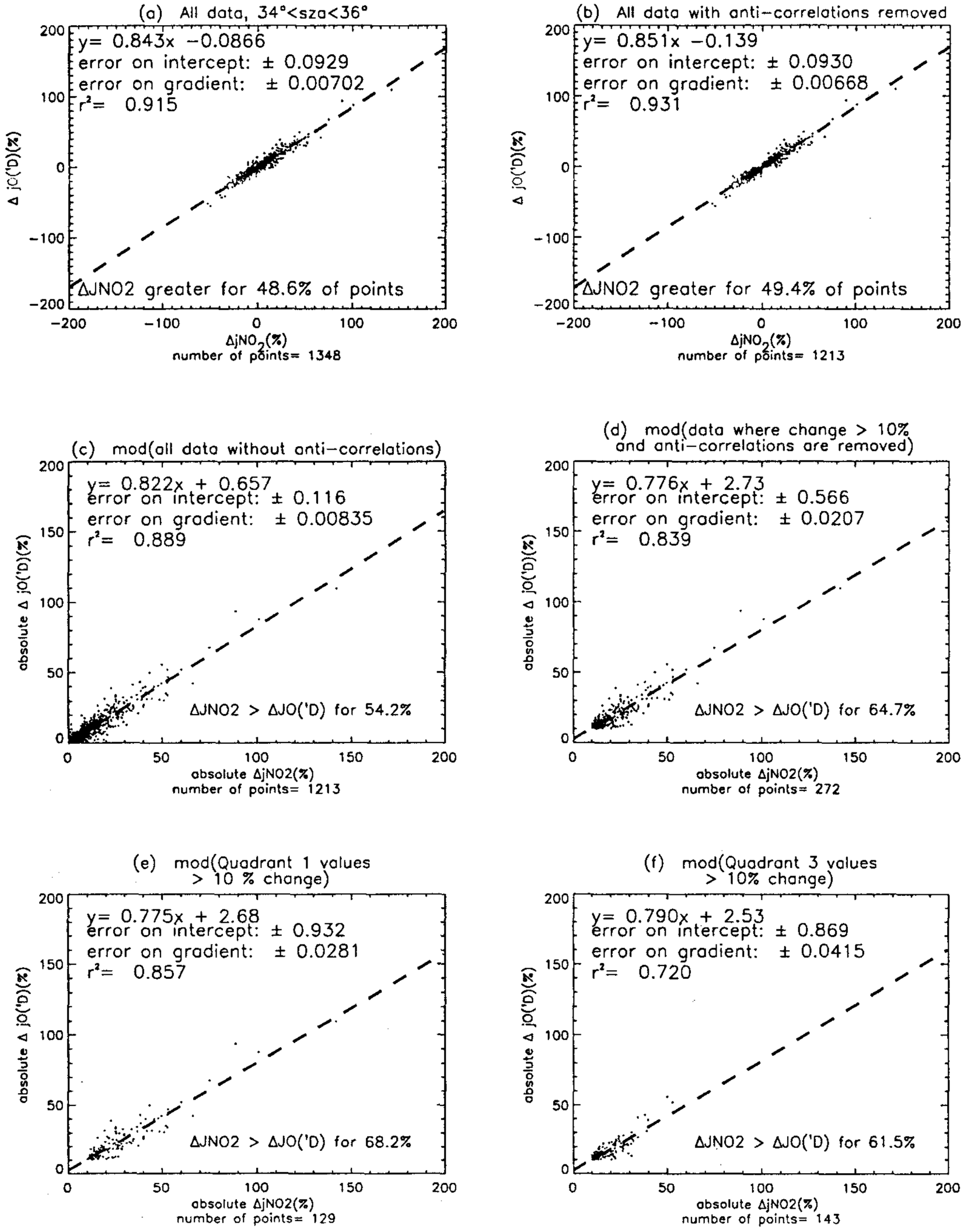


Figure 5.8: Data for solar zenith angle bin centred on 35° (a) All data (b) All data without anti-correlations (c) Absolute values of all data without anticorrelations (d) As (c) but only including values >10% (e) Positive-positive changes only (f) Negative-negative changes only

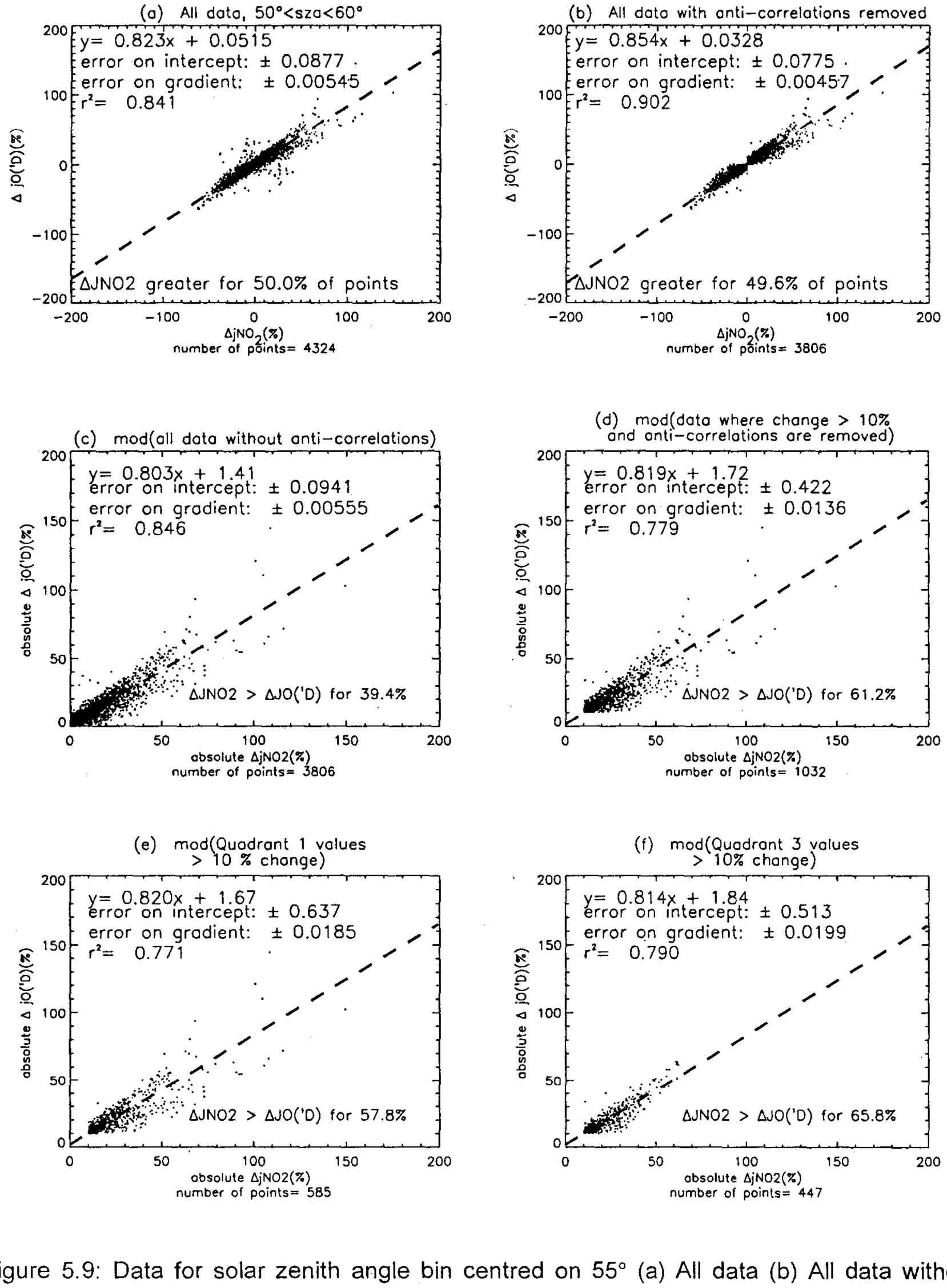
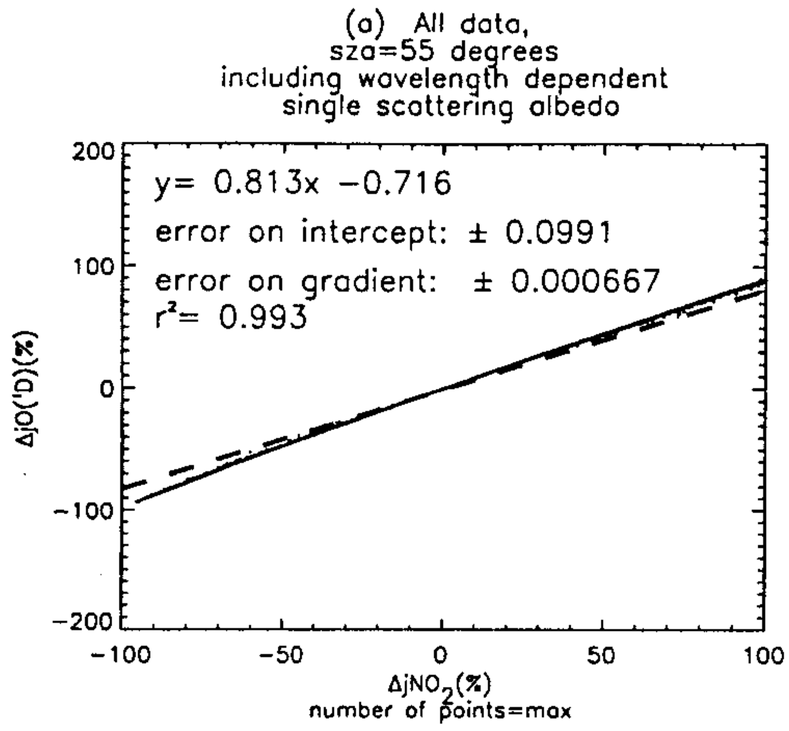
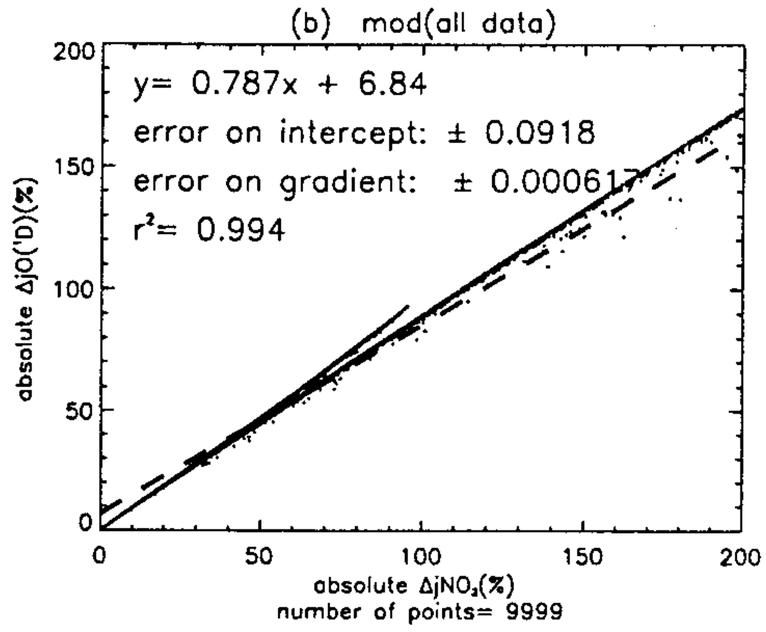
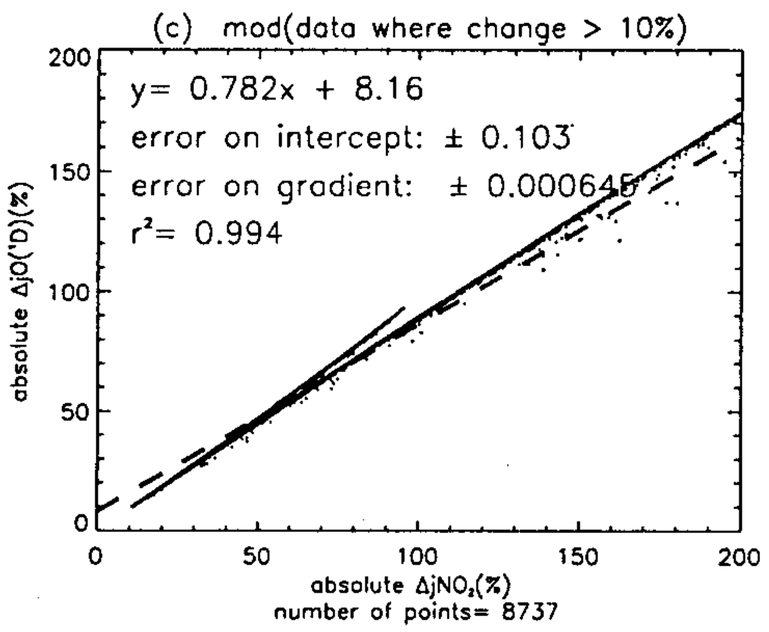
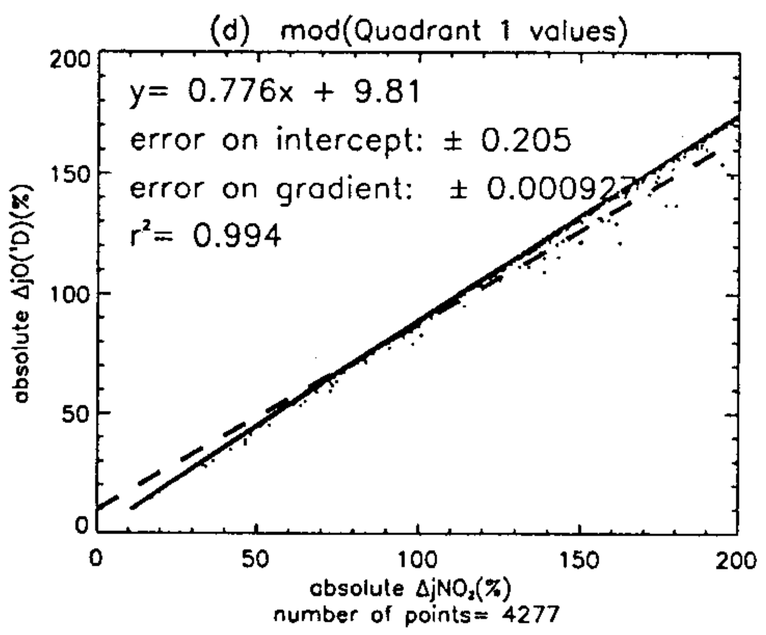


Figure 5.9: Data for solar zenith angle bin centred on 55° (a) All data (b) All data without anti-correlations (c) Absolute values of all data without anticorrelations (d) As (c) but only including values >10% (e) Positive-positive changes only (f) Negative-negative changes only









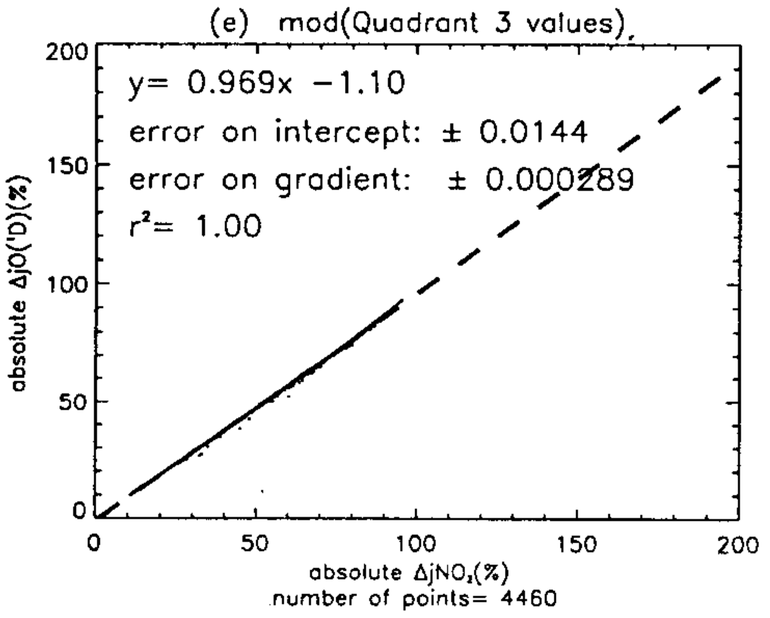


Figure 5.10: Results of model simulation including wavelength dependent single scattering albedo a) All data (b) Absolute values of all data without anticorrelations (c) As (b) but only including values >10% (d) Positive-positive changes only (e) Negative-negative changes only

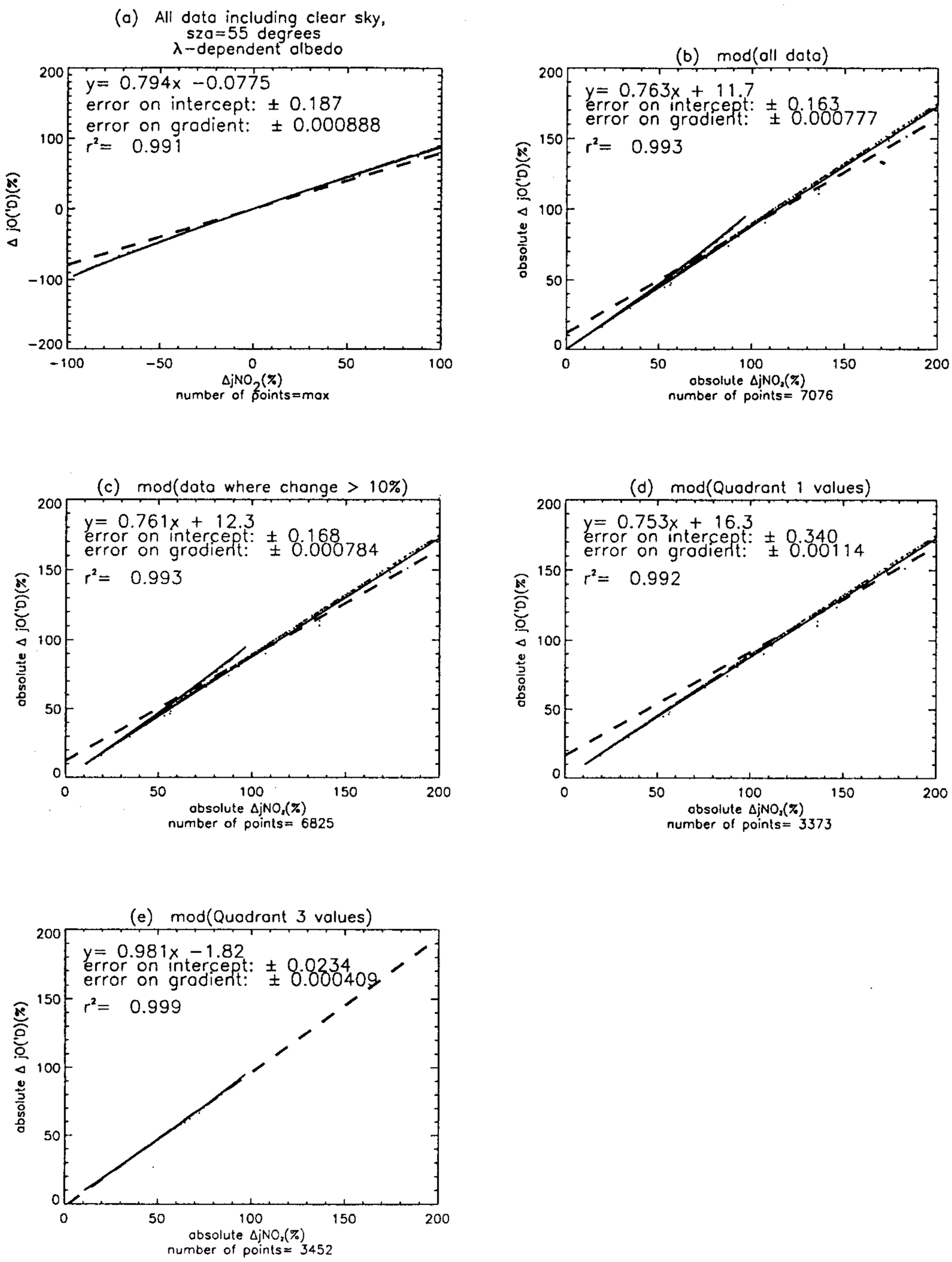


Figure 5.11: Results of model simulation including clear sky probability, solar zenith angle=55° a) All data (b) Absolute values of all data without anticorrelations (c) As (b) but only including values >10% (d) Positive-positive changes only (e) Negative-negative changes only

(e.g. Min *et al.*,1996; Barker *et al.*, 1998). Further investigation of the significance of the cloud optical depth distribution shows that the photolysis frequencies calculated from the mean of the optical depth distribution are less than the average computed from the model photolysis frequencies using the optical depth defined by the probability distribution.. This is a result of the combination of the non-linear dependence of photolysis frequency on cloud optical depth and the presence of this distribution. The difference between the values of j shows that use of an average optical depth, in the presence of a distribution, results in the underestimation of the photolysis frequency. A measure of the variance, or an alternative parameter, the 'effective optical depth' are suggested as potential solutions to this problem.

The relative response of jNO_2 and $jO(^1D)$ to cloud is an important theoretical and experimental problem. The spectral dependence of cloud transmittance is of interest to researchers and the work here has some interesting conclusions. Analysis shows, that on average, jNO_2 responded more to cloud than $jO(^1D)$ i.e. the transmittance decreases with wavelength. This is in agreement with previous observations (e.g. Seckmeyer *et al.*, 1996) and analysis (Crawford *et al.*, 1999). The data also showed no significant evidence for anomalous absorption by tropospheric path length enhancement as suggested by Pfeilsticker *et al.* (1997). It is proposed that, at optical depths when the transmitted direct flux is unimportant, the observed wavelength dependence of the response arises from coupling between Rayleigh scattering and reflection from the cloud, at either the cloud top (e.g. Kylling *et al.*,1997) or cloud base (e.g. Fredrick *et al.*, 1997). For thin clouds and overhead sun, the model predicts that this response will reverse so that the response of $jO(^1D)$ to cloud is greater than jNO_2. This is in agreement with the work of Madronich (1987) and there is some evidence to support this prediction in the data. This is in qualitative agreement with the observation of Monks *et al.*(1988) that the responses of $jO(^1D)$ and jNO_2 to cloud were more similar when the sun was overhead.

The radiative transfer model is used to try to simulate the responses seen in the data. It is found that clear to cloudy sky changes cannot reproduce the magnitude of responses seen,

Byrne, R.N., R.C.J. Somervillle and B. Subasilar, Broken cloud enhancement of solar radiation absorption, *J. Atmos. Sci.*, **53**(6), 878-886, 1996

Cahalan, R.F., W. Ridgeway, W.J. Wiscombe and T. L. Bell. The albedo of fractal stratocumulus clouds, *J. Atmos. Sci.,* **51**(16), 2434-2455, 1994

Carslaw, N., D.J. Creasey, D.E. Heard, A.C. Lewsis, J.B. McQuaid, M.J. Pilling and P.S. Monks. Modelling OH, HO_2, and RO_2 radicals in the marine boundary layer. 1. Model construction and comparison with field measurements. *J. Geophys. Res.*, **104**(D23), 30,241-30, 255, 1999

Castro, T.,L. G. Riuz-Suàrez, J. C. Riuz-Suàrez, M.J. Molina and M. Montero. Sensitivity analysis of a UV radiation transfer model and experimental photolysis rates of NO_2 in the atmosphere of Mexico City, *Atmos. Env.,* **31**(4), 609-620, 1997

Cess RD, M.H. Zhang, Y. Zhou , X. Jing and V. Dvortsov. Absorption of solar radiation by clouds: Interpretations of satellite, surface, and aircraft measurements, *J. Geophys. Res.,* **10** (D18),23,299-23,309,1996

Cess, R.D., MH Zhang, P. Minnis, L Corsetti, E.G. Dutton, BW Forgan, DP Garber, WL gates, J.H. Hack, E.F. Harrison , X. Jing , J.T. Kiehl, C.N. Long, JJ Morcrette, GL Potter, V. Ramanathan, B. Subasilar, C.H.Whitlock, D.F. Young and Y. Zhou. Absorption of solar radiation by clouds - Observations versus models, *Science*, **267**,496-499,1995

Chylek, P. and D.J.W. Gledart. Water vapour dimers and atmosspheric absorption of atmsopheric radiation. *Geophys. Res. Lett.,* **24**, 2015-2018, 1997

Chylek, P., G.B. Lesins, G. Vidden, G.D.Wong, R.G. Pinnick, D. Ngo and J.D. Klett. Black carbon and absorption of solar radiation by clouds, *J. Geophys. Res.,***101**(D11), 23,365-33,371, 1996

Costa A.A, C.J. de Oliveira, J.C.P de Oliveira and AJD Sampaio. Microphysical observations of warm cumulus clouds in Ceara, Brazil, *Atmos. Res,* **54** (2-3) 167-199, 2000

Cotte, H., C. Devaux and P. Carlier. Transformation of irradiance measurements into spectral actinic flux for photolysis rates determination, *J. Atmos. Chem.*, **26**, 1-28, 1997

Crawford, J., D. Davis, G. Chen, R. Shetter, M. Mueller, J. Barrick and J. Olson, An assessment of cloud effects on photolysis rate coefficients: Comparison of experimental and theoretical values, *J. Geophys Res.*, **104**, D5, 5725-5736, 1999

Crutzen, P. J., M. G. Lawrence and U. Poeschl. On the background photochemistry of troposheric ozone, *Tellus*, **55A-B**, 123-146, 1999

Dahlback, A. and K.Stamnes. A new spherical model for computing the spherical radiation field available for photolysis and heating at twilight, *Plan. Sp. Sci.*, **39**, 671-683, 1991

Davidson, J.A., C.A. Cantrell, A.H. McDaniel, R.E. Shetter, R.E. Shetter and S. Madronich. Visible-ultraviolet absorption cross-sections as a function of temperature. *J. Geophys. Res.*, **98**, 23,501-23,503, 1993

Davidson, J.A., C.A. Cantrell, A.H. McDaniel, R.E. Shetter, S. Madronich and J.G. Calvert. Visible-Ultraviolet cross-sections for NO_2 as a function of temperature, *J. Geophys. Res.*, **93** (D6) 7105-7112, 1988

Davis, A.B., A. Marshak, H. Gerber and W.J. Wiscombe. Horizontal structure of marine boundary layers from centimeter to kilometer scales. *J. Geophys. Res.*, **104**(D6), 6123-6144, 1999

Degunther M, R. Meerkotter , A. Albold and G. Seckmeyer G Case study on the influence of inhomogeneous surface albedo on UV irradiance, *Geophys. Res. Lett.*, **25**(19), 3587-3590, 1998

Demerjian, K.L., K.L Schere and J.T. Peterson. Theoretical estimates of actinic (spherically integrated) flux and phtolytic rate constants of atmospheric species in the lower troposphere, *Adv. Environ. Sci. Tech.*, **10**, 368-459, 1980

DeMore, W.B, M.J. Molina, S.P. Sander, D.M. Golden, C.E. Kolb, R.F. Hampson, M.J. Kurylo, C.J. Howard, A.R. Ravishankara, and. Chemical Kinetics and photochemical data for use in stratospheric modeling, Evaluation no. 11, JPL publication, 94-26, 1994

DeMore, W.B, S.P. Sander, D.M. Golden, R.F. Hampson, M.J. Kurylo, C.J. Howard, A.R. Ravishankara, C.E. Kolb and M.J. Molina. Chemical Kinetics and photochemical data for use in stratospheric modeling, Evaluation no. 10., JPL publication 92-20, 1992

DeMore, W.B., S.P. Sander, D.M. Golden, M.J. Molina, R.F. Hampson, M.J. Kurylo, C.J. Howard, A.R. Ravishankara, Chemical Kinetics and Photochemical Data for use in Stratospheric Modeling, Evaluation no. 8., JPL NASA Jet Propulsion Laboratory, 87-41, 1987

Dickerson, R.R, D.H. Stedman, W.L Chameides, P.J. Crutzen and J. Fishman. Measurements and theoretical calculations of $j(O_3)$, the rate of photolysis of ozone to $O(^1D)$, *Geophys. Res. Lett.*. **6**, 833-836, 1979

Dickerson, R.R., D.H. Stedman and A.H. Delany, Direct measurement of ozone and nitrogen dioxide photolysis rates in the troposphere, *J. Geophys. Res.*, **87**, 4933-4946, 1982

Diffey, B.L., A.T. Green, M.J. Loftus, G.J. Johnson and P.S. Lee. A portable instrument for measuring ground reflectance in the ultraviolet, *Photochem. Photobiol.*, **61**(1), 68-70, 1995

Dunkerkeye, P.G. and Van Weele,M. Actinic fluxes: the role of clouds in photodissociation, *Bound. Lay. Meteorol.*, **62**, 417-432, 1993

Eck, T.F., P.K. Bhartia, P.H. Hwang and L.L. Stowe. Reflectivity of Earth's surface and clouds in ultraviolet from satellite observations, *J. Geophys. Res.*, **92**(D4), 4287-4296, 1987

Ehhalt, D.H. and F. Rohrer. Dependence of the OH concentration on solar UV, *J. Geophys. Res.*, **105**(d3), 3565-3571, 2000

Eltermann, L. UV, visible and IR attenuation for altitudes up to 50 km, Rep AFCRL-68-0153 ERP 285, Air Force Cambridge Research Laboratories, Cambrdige, Mass., USA,1968

Erle, F., K. Pfeilsticker and U. Platt. On the influence of tropospheric clouds on zenith-scattered-light measurements of stratospheric species. *Geophys. Res. Lett.,* **22**(20), 2725-2718, 1995

Erlick, C. and J.E. Fredrick, Effect of aerosols on the wavelength dependence of atmospheric transmission in the ultraviolet and visible 2.Continental and urban aerosols in clear skies, *J. Geophys. Res.,* **103** , 23,275-23,285, 1998

Erlick, C., J.E. Frederick, V.K. Saxena, B.N. Wenny. Atmospheric transmission in the ultraviolet and visible: Aerosols in cloudy atmospheres. *J. Geophys. Res* ,**103**(D24), 31,541-31,555 ,1998

Estupiñán, S. Raman, G. H. Crescenti, J. J. Streicher and W. F. Barnard. Effects of Clouds and haze on UV-B radiation. *J. Geophys. Res.*, **101**, 16 807-16 816, 1996

Finlayson, J.N. and B.J. Finlayson-Pitts. Atmospheric chemistry: Fundamental and Experimental Techniques, John Wiley and Sons, New York, 1098pp. 1986

Finlayson-Pitts, B.J. and J.N. Finlayson Chemistry of the upper and lower atmosphere, Academic Press, San Diego, 969pp, 2000

Forster, P. M. de. F. Measuring and Modelling UV radiation, PhD thesis, University of Reading, 1994

Forster, P. M. de. F., Modelling Ultraviolet Radiation at the Earth's surface. Part I: The sensitivity of Ultraviolet irradiances to Atmospheric Changes, *J. Appl. Meteorol.I,* **34**, 2412-2425, 1995

Francis, P.N., J.P. Taylor, P. Hignett and A. Slingo. On the question of enhanced absorption of solar radiation by clouds, *Q. J. Roy. Met. Soc.*, **123**, 419-434, 1997

Frederick, J. E. and H. E. Snell. Tropospheric influence on solar ultraviolet radiation : the role of clouds, *J. Climate*, **3**, 373-381, 1990

Frederick, J.E. and D. Lubin. The budget of biologically active ultraviolet radiation in the Earth-atmosphere system, *J. Geophys. Res.*, **93**(D4), 3825-3823, 1988

Frederick, J.E., H.E. Snell and E.K. Haywood. Solar Ultraviolet radiation at the Earth's surface. *Photochem. Photobiol.*, **50(8)**, 443-450, 1989

Frederick,J.E. and C. Erlick. The attenuation of sunlight by high-latitude clouds: Spectral dependence and its physical .mechanisms. *J. Atmos. Sci.,* 54:(24) 2813-2819,1997

Frueh, B, T. Trautmann, M. Wendisch and A. Keil Comparison of observed and simulated NO2 photodissociation frequencies in a cloudless atmosphere and in continental boundary layer clouds, *J. Geophys. Res,* **105**(D8), 9843-9857, 2000

Gardener, E.P., D. Sperry and J.G. Calvert. Primary quantum yields of NO_2 photodissociation, *J. Geophys. Res.*, **92**, 6642-6652, 1987

Goody, R.M. and Y.L.Yung. Atmospheric radiation: a theoretical basis, Oxford University press, New York, 1989

Gultepe, I. nd G.A. Isaac. Liquid water content and temperature relationship from aircraft observations and its applicability to GCMs, *J. Clim.* , **10**(3) 446-452,1997

Harder JW, J.W. Brault, P.V. Johnston and G.H. Mount. Temperature dependent NO_2 cross sections at high spectral resolution, *J. Geophys. Res.,* **102**(D3), 3861-3879, 1997

Harshadvan. Aerosol- climate Interactions, Aerosol-Climate Interactions, p76-93, edited by P. V. Hobbs, Academic Press, Inc., San Diego, 1993

Hayasaka, T., N. Kikuchi and M. Tanaka, Absorption of solar radiation by stratocumulus clouds- aircraft measurements and theoretical calculations, *J. Appl. Met.,* **34**(5), 1047-1055, 1995

Henderson Sellers, A. and K.. McGuffie. An investigation of the Burger distribution to characterise cloudiness, *J. Clim.*, **4**(12), 1181-1209, 1991

Herman, J.R. and E.A. Celarier. Earth surface reflectivity climatology at 340-380 nm from TOMS data, *J. Geophys. Res.*, **102** (D23), 38, 003-28, 011, 1997

Heymsfield, A. J. Microphysical structures of stratiform and cirrus clouds, Aerosol-Cloud-Climate Interactions, p97-119, edited by P. V. Hobbs, Academic Press, Inc., San Diego, 1993

Hofzumahaus A., A. Kraus and M. Mueller. Solar actinic flux spectroradiometry: a technique for measuring photolysis frequencies in the atmosphere, *Appl. Opt.*, **38(21)**, 1999

Hofzumahaus, A., T. Brauers, U. Platt and J. Callies. Latitudinal variation of measured O_3 photolysis frequencies $J(O^1D)$ and primary OH production rates over the Atlantic between 50° N and 30° S, *J. Atmos. Chem.*, **15**, 283-198, 1992

Hofzumahaus, U. Aschmutat, M. Hessling, F. Holland and D.H. Enhalt. The measurement of tropospheric OH radicals by Laser Induced Fluorescence spectroscopy during the POPCORN field campaign, *Geophys. Res. Lett.*, **23**, 2541-2544, 1996

Hosking, J.R.M. Analysis and estimation of distributions using linear combinations of order statistics, *J. Roy. Stat. Soc. B,* **52**(1), 105-124, 1990

Hu, Y.X. and K. Stamnes. An accurate parameterisation of the radiative properties of water clouds for use in climate models, *J. Clim.*,**6**, 728-742, 1993

Huang, T.Y.W. and S. T. Massie. Effect of volcanic particles on the O_2 and O_3 photolysis rates and their impact on ozone in the tropical stratosphere. *J. Geophys. Res.*, **102**(D1), 1239-1249, 1997

Intergovernmental Panel on Climate Change, Climate Change 1994, Cambridge Univesity Press, 1994

Jacobson, M. Z. Fundamentals of atmospheric modelling, Cambridge University Press, Cambridge, 1999

Joseph, J.H., W.J. Wiscombe and J.A. Weiman. The Delta-Eddington approximation for radiative flux transfer, *J. Atmos. Sci.,* **33**, 2452-2459, 1976

Junkermann, W. Measurements of the J(O(1)D) actinic flux within and above atraiform clouds and above snow, *Gephys. Res. Lett.*, **21**(9), 793-796,1994

Junkermann, W., U. Platt and A. Volz-Thomas, A photoelectric detector for the measurement of photolysis frequencies of ozone and other atmospheric molecules, *J. Atmos. Chem.*, **8**, 203-337, 1989

Kedem, B, and R. Pfeiffer and D.A. Short. Variability of space-time mean rain rate *Jour. Appl. Met.*, **36**(5), 443-451, 1997

Kelley, P., R. R. Dickerson W.T. Luke and G.L. Kok, Rate of NO_2 photolysis from the surface to 7.6km altitude in clear sky and clouds, *Geophys. Res Lett.,* **22**, 2621-26332, 1995

Kidder, S.Q. and T.H. Vonder Vaar. Satellite Meteorology- An Introduction, Academic Press, London, 1995, 466pp

Kite, A. The albedo of broken cloud fields, *Q. J. Roy. Met. Soc.*, **113**, 517-531, 1997

Kraus, A. and A. Hofzumahaus. Field measurements of atmospheric photolysis frequencies for O_3, NO_2, CH_3CHO, H_2O_2 and HONO by UV spectroradiometry. *J. Atmos. Chem.*, **31**, 161-180, 1998

Kraus, A., F. Rohrer and A. Hofzumahaus. Intercomparison of NO_2 photolysis frequency measurements by actinic flux spectroradiometery and chemical actonimetry during JCOM97,*Geophys. Res. Lett.,***27(8)**, 1115-1118, 2000

Krokotov, N. A., P.K. Bhartia, J. Herman, V. Fieltov and J. Kerr, Satellite estimation of spectral surface UV irradiance in the presence of tropospheric aerosols. 1. Cloud free case, *J. Geophys. Res.*, **103**, 8779-8794, 1998

Krol, M. C. and M. van Weele. Implications of variations in photodissociation rates for global tropospheric chemistry, *Atmos. Env.*, **31**(9), 1257-1273, 1997

Krol, M.; P.J Van Leeuwen.; J. Lelieveld. Global OH trend inferred from methylchloroform measurements, *J. Geophys. Res.*, **103**(D9), 8, 10,697-10,711 , 1998

Krzyscin, J. W., Impact of the ozone profile on the surface UV radiation: Analyses of the Umkehr and UV measurements at Belsk (52 °N, 21° E), Poland, *J. Geophys. Res.*, **105**(D4), 5009-5015, 2000

Krzyscin, J.W. and S. Puchalski. Aerosol impact on the surface UV radiation from the ground-based measurements taken at Belsk, Poland, 1980-1996, *J. Geophys. Res,* **103**(D13), 16,175-16,181,1998

Kylling A, AF Bais, M Blumthaler, J Schreder, CS Zerefos, E Kosmidis. Effect of aerosols on solar UV irradiances during the photochemical activity and solar ultraviolet radiation campaign, *J. Geophys. Res*, **103**(D20),26,051-26,060 , 1998

Kylling, A., A. Abold and G. Seckmeyer. Transmittance of a cloud is wavelength-dependent in the UV-range: Physical interpretation, *Geophys. Res. Lett.,* **24**(4), 397-400, 1997

Laherrère, J. and D. Sornette. Stretched exponential distributions in nature and economy: "fat tails" with characteristic scales, *Eur. Phys. Jour. B*, **2**, 525-539, 1998

Laird, J.L.and Harshvardhan. Analysis of cumulus solar irradiance reflectance (CSIR) events, *Atmos. Res.*, **44**(3-4), 317-332, 1997

Lantz, K.O., R. E. Shetter, C.A. Cantrell, S.J. Flocke, J.G. Calvert and S. Madronich. Theoretical, actinometric, and radiometric determinations of the photolysis rate coefficient

of NO_2 during the Mauna Loa Observatory Photochemistry Experiment 2, *J. Geophys. Res.*, **101**(D9), 14613-14629, 1996

Lapeta, B., Engelesen, O., Litynksa, Z., Kois, B. and A. Kylling, Sensitivity of surface UV radiation and ozone column retrieval to ozone column and temperature profiles, *J. Geophys. Res.*, **105**(D4), 5001-5007, 2000

Lean, J. Variations in the Sun's radiative output, *Rev. Geophys.*, **29**(4) 505-535 1991

Leontieva and K. Stamnes. Remote sensing of cloud optical properties from ground-based measurements of transmittance : a feasibility study, *J. Appl. Met.*, **35**, 2011-2023, 1996

Leontieva, E. Stamnes, K. and J.E. Olsteth. Cloud optical properties at Bergen (Norway) based on the analysis of long term solar irradiance methods. *Theor. Appl. Climatol.*, **50**, 73-82, 1994

Leontyeva, E. and K. Stamnes. Estimations of cloud optical thickness from ground based measurements of incoming solar radiation in the Arctic, *J. Clim.*, **7**, 566-579, 1994

Li, Z.Q., H.W. Barker and L. Moreau. The variable effect of clouds on atmospheric absorption of solar radiation, *Nature*, **376**, 486-490, 1995

Liao, H, Yung, YL, and J.H. Seinfeld . Effects of aerosols on tropospheric photolysis rates in clear and cloudy atmospheres , *J. Geophys. Res.*, **104**(D19), 23,697-23,707,1999

Limpert, E. and W.A. Sthael, Life is lognormal: science and art, life and statistics, published on http://www.inf.ethz.ch/~gut/lognormal/brochure.html

Liou, K.N. Radiation and cloud processes in the atmosphere, O.U.P., 487pp, 1992

Liou, K.N., A numerical experiment on Chandrasekhar's Discrete-Ordinate Method for Radiative Transfer: Applications to Cloudy and Hazy Atmospheres, *J. Atmos. Sci.*, 30, 1303-1325, 1973.

Liou, K.N., Analytic Two-Stream and Four-Stream Solutions for Radiative Transfer, *J. Atmos. Sci.*, 31, 1473-1475, 1974.

Los, A, M. van Weele and P.G. Dunykerke. Actinic fluxes in broken cloud fields, *J. Geophys. Res.*, **102**(D4), 4,257-4,266, 1997

Lu, Y and M.A.K. Khalil. The distribution of solar radiation in the Earth's atmosphere: the effects of ozone, aerosol and clouds, *Chemosphere*, **32**(4), 739-758, 1994

Lyapustin, A.I. Atmospheric and geometrical effects on land surface albedo, *J. Geophys. Res.*, **104**(D9), 4127-4143, 1999

Madronich S., D.R. Hastie, B.A. Ridley and H.I. Schiff, Measurement of the photodissociation coefficient of NO_2 in the atmosphere, I. Method and surface measurements, *J. Atmos. Chem.*, **1**, 3-25, 1983

Madronich, S. Intercomparison of NO_2 photodissociation and U.V. radiometer measurements, *Atmos. Env.*, **21**(3), 569-578, 1987

Madronich, S. Photodissiciation in the Atmosphere 1. Actinic Flux and the effects of Ground refelections and Clouds, *J. Geophys. Res.*, **92**(98), 9740-9752, 1987

Madronich, S. and G. Weller. Numerical integration errors in calculated tropospheric photodissociation rate coefficients, *J. Atmos. Chem.*, **10**(3), 289-300, 1990

Martin, D., J. Girman and H.S. Johnston, 167th ACS National Meeting, 1974

Matthijsen, J, H. Slaper, H.A.J.M. Reinen and J.G.M Velders. Reduction of solar UV by clouds: A comparison between satellite-derived cloud effects and ground-based radiation measurements. *J. Geophys. Res,* **105**(D4), 5069-5080, 2000

Matthijsen, J., K. Suhre, R. Rosset, F.L. Eisele, R.L. Mauldin III and D.J. Tanner. Photodissociation and UV radiative transfer in a cloudy atmosphere : modeling and measurements. *J. Geophys. Res,* **103(D13)**, 16665-16676, 1998

Mauldin, R.L. II, G.J. Frost, G. Chen, D.J. Tanner, A.S.H. Prevot, D.D. Davis and F.L. Eisele. OH measurements during the First Aerosol Characterisation Experiment (ACE 1): Observations and model comparisons. *J. Geophys. Res.*, **103** (D13), 16,713-16729, 1998

Mayer, B., A. Kylling, S. Madronich and G Seckmeyer. Enhanced absorption of UV radiation due to multiple scattering in clouds: Experimental evidence and theoretical explanation, *J. Geophys. Res.*, **103**(D23), 31241-31254, 1998

McGee, T.J. and J. Burris. SO_2 absorption cross-sections in the near UV, *J. Quant. Spec. Rad. Trans.*,**37** (2), 165-182, 1987

McIlveen, R. Fundamentals of weather and climate, 2nd edition, Nelson Thomas, 498pp, 1992

McKenzie RL, K.J.Paulin, G.E. Bodeker, J.B. Liley and A.P.Sturman. Cloud cover measured by satellite and from the ground: relationship to UV radiation at the surface, *Int. Jour. Remote Sens*, **19**(15) 2969-2985,1998

Meador, W.E. and W.R. Weaver. Two stream approximations to radiative transfer in planetary atmospheres: a unified description of existing methods and a new improvement, *J. Atmos. Sci.*, **37**, 630-643, 1980

Meier, R. R., G. P. Anderson, C.A. Cantrell, L.A. Hall, J. Lean, K. Minschwaner, R.E. Shetter, E.P. Shettle and K. Stamnes. Actinic radiation in the terrrestrial atmosphere, *J. Atmos. Sol. Terr. Phys.*, **59(17)**, 2111-2157, 1997

Michelsen, H.A., R.J. Salawitch, P.O. Wennberg and J.G. Andersen. Production of $O(^1D)$ from photolysis of O_3, *Geophys. Res. Lett.*, **21**(20),2227-2230,1994

Miles, N.L., J. Verlinde and E.E. Clothiaux, Cloud droplet size distributions in low-level stratiform clouds, *J. Atmos. Sci.*,**57**(2), 295-311, 2000-12-16

Min, Q. and L.C. Harrison. Cloud optical properties derived from surface MFRSR measurements and comparison with GOES measurements at the ARM SGP site, *Geophys. Res. Lett.*, **23**, 1641-1644, 1996

Molina, L.T. and M.J. Molina. Absolute absorption cross-sections of ozone in the 185-350 nm wavelength range, *J. Geophys. Res.*, **91**, 14.501-14, 508, 1996

Monks, P.S. ,G. Salisbury, G. Holland , S.A. Penkett and G.P. Ayers, A seasonal comparison of ozone photochemistry in the remote marine boundary layer, *Atmos. Env.*, 34(16), 2547-2561,2000

Monks, P.S., L.J.Carpenter, S.A. Penkett, G.P. Ayers, R.W. Gillett, I.E. Galbally and C.P. Fundamental ozone photochemistry in the remote marine boundary layer: The SOAPEX experiment, measurement and theory, *Atmos. Env.*, **32**(21), 3647-3664,1998

Mueller, M., A. Kraus., A. Hofzumahaus, O_3-> $O(^1D)$ photolysis frequencies determined from spectroradiometric measurements of solar actinic UV-radiation : Comparison with chemical actinometer measurements, *Geophys. Res. Lett.*, **22**(6), 679-682, 1995

Mueller, R. and U. Schurath Entwicklung eines Geraetes zur kontinuerlichen Messung Photodissoziations-Geschwindigkeit von Aldehyden in der Atmosphaere durch Nacherzeugten CO, Gesellschaft fur Strahlen-und Umwelt Forschung mbH, Muenchen, Abschlag Vorhaben KBF 53, 1986

Murcray, F.J., A. Goldman, J.C. Landry and T.M. Stephen, O_2 continuum: A possible mechanism for the discrepancies between modelled and measured shortwave surface irradiances, *Geophys. Res. Lett.*, **24**, 2315-2217, 1997

Neckel, H. and D. Labs. The solar irradiance between 3300 and 1250 Å, *Solar Phys.*, **90**, 205-258, 1984

Nelkin, M. and G. Stolovitzky. Limitations of random multipliers in describing turbulent energy dissipation, *Phys. Rev*. E, **54**(5), 1996

O'Hirok, W. and C. Gaultier. A three-dimensional radiative transfer model to investigate the solar radiation within a cloudy atmosphere. Part II: Spectral effects, *J. Atmos. Sci.*, **55**, 3065-3077, 1998

Olson, J. and M. Prather, T. Berntsen,G. Carmichael, R. Chatfield, P. Connel, R Derwent, L. Horowitz, S. Jin, M. Kanakidou, P. Kasibhatala, R. Kotamarthi, M. Kuhn, K. Law, J. Penner, L. Perliski, S. Sillman, F. Stordal, A. Thompson and O. Wild. Results from the

Intergovernmental Panel on Climatic Change Photochemical Model Comparison (PhotoComp), *J. Geophys. Res.*, **102**(D5), 5979-5991, 1997

Parrish, D.D., P.C. Murphy, D.L. Albritton and F.C. Fehsenfeld, The measurement of the photodissociation rate of NO_2 in the atmosphere, *Atmos. Env.*, **17**, 1365-1379, 1983

Pelon, J., C. Flamant, V. Trouillet and P.H. Flamant. Optical and microphysical parameters of dense stratocumulus clouds during mission 206 of EUCREX '94 as retrieved from measurements made with the airborne lidar LEANDRE 1, *Atmos. Res.* **55**(1), 47-64, 2000

Penkett, S.A., P.S. Monks, L.J. Carpenter, K.C. Clemitshaw, G.P. Ayers, R.W. Gillett, I.E. Galbally, C.P. Meyer. Relationships between ozone photolysis rates and peroxy radical concentrations in clean marine air over the Southern Ocean, *J Geophys. Res.*, **102**(D11), 12,805-12,817, 1997

Pfeilsticker, K., F. Erle, O. Funk, H. Veitel and U. Platt. First optical pathlength distribution measurement of the skylight using the oxygen A-band absorption technique. 1. Measurement technique, atmospheric observations, and model calculations, *J. Geophys. Res,* **103** (D10) 11,483-11,504,1998

Pfeilsticker, K., F. Erle., O. Funk, L. Maquard, T. Wagner and U. Platt. Optical Path modification due to tropospheric clouds: Implications for zenith sky measurements of stratospheric gases, *J. Geophys. Res.,* **103**(D19) 25323-25335,1998

Pfister G, D. Baumgartner , R. Maderbacher and E Putz. Aircraft measurements of photolysis rate coefficients for ozone and nitrogen dioxide under cloudy conditions, *Atmos. Env.,* **34**(23), 4019-4029, 2000

Pilewskie, P. and F.P.J. Valero. Direct observations of excess solar absorption by clouds, *Science*, **267,**1626-1629, 1995

Ramathan, V., B. Subusilar, G.J. Zhang, W. Conant, R.D. Cess, J.T. Kiehl, H. Grassl and L. Shi. Warm pool heat budget and shortwave cloud forcing: a missing physics, *Science*, **267**, 499-503 ,1995

Reuder, J. and H. Schwander, Aerosol effects on UV radiation in non-urban regions, *J. Geophys. Res.*, **104**, 4065-4077,1999

Ricchazzi, P., C. Gautier and D. Lubin. Cloud scattering optical depth and local surface albedo in the Antarctic : simultaneous retrieval using ground based, *J. Geophys. Res,* **100**(D10), 21,091-21,104, 1995

Rossow, W.B and R.A. Schiffer. ISCCP cloud products. *Bull. Am. Met. Soc.*, **72**, 2-20, 1991

Rossow, W.B., Measuring cloud properties form space: a review. *J. Clim.*, **2**, 201-213, 1989

Ruggaber A., R. Forkel and R. Dlugi. Spectral actinic flux and its ratio to spectral irradiance by radiative transfer calculations, *J. Geophys. Res.*, **97**, 1151-1162, 1992

Ruggaber, A. R. Dlugi and T. Nakajima. Modelling radiation quantatites and phtolysis frequencies in the troposphere, *J. Atmos. Chem.*, **18**(2), 171-210, 1994

Salby, M.L. Fundamentals of Atmospheric Physics, Academic Press, 627pp,1 996

Schafer, J.S., V.K. Saxena, B.N. Wenny, W. Barnard and J.J. De Luisi. Observed influence of clouds on UV-B radiation. *J. Geophys. Res.*, **23**(12), 2625-2628, 1996

Schaller, E., A Delta Two Stream approximation in radiative flux calxulations, *Contrib. Atmos. Phys.*, **52**, 17-26, 1979

Schwander, H., P. Kopke and A. Ruggaber. Uncertainties in modeled UV irradiances due to limited accuracy and availability of input data, *J. Geophys. Res.*, **102**(D8), 9419-9429, 1997

Shetter, R.E. and M. Mueller. Photolysis frequency measurements using actinic flux spectroradiometry during the PEM-Tropics mission: Instrumentation description and some results, *J. Geophys. Res.*, **104**(D9), 5647-5661, 1999

Shetter, R.E., A.H. McDaniel, C.A. Cantrell, S.Madronich and J.G. Calvert. Actinometer and Eppley Radiometer measurements of the NO_2 Photolysis Rate Coefficient During the Mauna Loa Observatory Photochemistry Experiment, *J. Geophys. Res.*, **97**(D10), 10349-10359, 1992

Shetter, R.E., C.A. Cantrell, K.O. Lantz, S.J. Flocke, J.J. Orlando, G.S. Tyndall, T.M. Gilpin, C.A. Fischer, S. Madronich and J.G. Calvert, Acinometric and radiometric measurement and modeling of the photolysis rate coefficient of ozone to $O(^1D)$ during the Mauna Loa Observatory Photochemistry Experiment 2, *J. Geophys. Res.*, **101** (D9), 14631-14641, 1996

Silvente, E., R.C. Richter, M. Zheng, E.S. Saltzman and A.J. Hynes. Relative quantum yields for O^1D production in the photolysis of ozone between 301-336 nm: evidence for the participation of a spin-forbidden channel, *Chem. Phys. Lett.*, **264,** 309-315, 1997

Solomon, S., R.W. Portmann, R.W. Sanders, J.S. Daniel, W. Madsen, B. Bartram and E.G. Dutton. On the role of nitrogen dioxide in the absorption of solar radiation, , *J. Geophys. Res.*, **104**(D10)12.047-12,058,1999

Sornette, D. Critical Phenomena in Natural Sciences, Springer Verlag, Berlin, 434pp, 2000

Stamnes, K., S.-C. Tsay, W. Wiscombe and K. Jayaweerea. Numerically stable algorihm for discrete-ordinate method radiative transfer in multiple scattering and emitting layered media. *Appl. Optics,* **27**(12), 1988

Stephens, G.L. Radiation profiles in extended water clouds, II parameterisation schemes, *J. Atmos. Sci.,* **35**, 2123-2132, 1978

Stephens, G.L. and S.-C. Tsay. On the cloud absorption anomaly. *Quart. J. Roy. Met. Soc.*, **116**, 671-704

Stephens, G.L. and S.-C. Tsay. On the cloud absorption anomaly. *Quart. J. Roy. Met. Soc.*, **116**, 671-704

Stephens, G.L. How much solar radiation do clouds absorb? *Science*, **271**,1131-1133, 1996

Swartz, W.H., S.A. Lloyd, T.L. Kusterer, D.E. Anderson, C. T. McElroy and C. Midwinter. A sensitivity study of photolysis rate coeffcients during POLARIS. *J. Geophys. Res.*, **104**(D21), 26,725-26, 735, 1999

Takahashi K., N. Taniguchi, Y. Matsumi, M. Kawasaki and M.N.R Ashfold. Wavelength and temperature dependence of the absolute O(^{1}D) production yield from the 305-329 nm photodissociation of ozone, *J. Chem. Phys.*, **108**, 7161-7172, 1998

Talkudar, R.J., M.K. Gilles, F. Battin-Leclerc, A.R. Ravishankara, J.-M. Fracheboud, J.J. Orlando and G.S. Tyndall. Photolysis of ozone at 308 and 248 nm: Quantum yield of O(^{1}D) as a function of temperature. *Geophys. Res. Lett.*, **24**(9), 1091-1094, 1997

Taylor, J.P, J.M. Edwards, M.D. Glew, P. Hignett and A. Slingo. Studies with a flexible new radiation code .2. Comparisons with aircraft short-wave observations, *Q. J. Roy. Met. Soc.*, **122**,839-861, 1996

Tessier, Y, S. Lovejoy, and D. Schertzer. Universal multifractals: Theory and Observations for Rain and Clouds, *J. Appl. Met.*, **32**(2), 1993

Thompson, A.M. and R.W. Stewart. Effect of chemical kinetics uncertainties on calculated constituents in a tropospheric photochemical model. *J. Geophys. Res.*, **96**, 13, 809 -13, 108, 1991

Titov, G.A. Radiative horizontal transport and absorption in stratocumulus clouds, *J. Atmos. Sci.*, **55**, 2549-2560, 1998

Toon, O. B., C. P. McKay, T.P. Ackerman and K. Santhanam. Rapid calculation of Radiative Heating Rates in Inhomogeneous Multiple Scattering Atmospheres, *J. Geophys. Res.*, **94**(D13), 16287-16301, 1989

Trautmann, T., I. Podgorny, J. Landgraf and P.J. Crutzen. Actinic fluxes and photodissociation coefficients in cloud fields embedded in realistic atmospheres, *J. Geophys. Res.*, **104**(D23), 30,173-30,192,1999

Tsay, S.-C. and K. Stamnes. Ultraviolet Radiation in the Artic : The impact of potential ozone depletions and cloud effects, *J. Geophys. Res.*, **97**(D8), 7829-7840, 1992

Valero, F.P.J., R.D. Cess, M.H. Zhang, S.K. Pope, A. Bucholtz, B. Bush and V. Vitko Absorption of solar radiation by the cloudy atmosphere: Interpretations of collocated aircraft measurements, *J. Geophys. Res.*, **102**(D25), 29,917-29,927, 1997

Vilà-Guerau de Arellano, G., P. G. Duykerke and M. van Weele. Tethered-balloon measurements of actinic flux in a cloud-capped marine boundary layer, *J. Geophys. Res.*, **99**(D2), 3699-3705, 1994

Volz-Thomas, A. Lerner, H.-W. Pätz, M. Schulz, D.S. McKenna, R. Schmitt, S. Madronich and E.P. Röth. Airborne measurements of the photolysis frequency of NO_2, *J. Geophys. Res.*, **101**(D13), 18613-18627, 1996

Wagner ,T., F. Erle, L. Marquard, C. Otten, K. Pfeilsticker, T. Senne, J. Stutz and U. Platt. Cloudy sky optical paths as derived from differential optical absorption spectroscopy observations, *J. Geophys. Res* , **103**(D19) 25,307-25,321, 1998

Wallace, J.M and P.V. Hobbs. Atmospheric Science : An Introductory Survey, Academic Press, Inc., London, 467pp

Wang. P. and J. Lenoble. Influence of clouds in UV irradiance at ground level at backscattered exittance, *Adv. Atmos. Sci.*, **13**, 217-228, 1996

Wayne, C.E. and R.P.Wayne, Photochemistry, Oxford University Press, Oxford, 2nd edition, 1999

Wayne, R. P. Chemistry of atmospheres, Clarendon Press, Oxford, Second edition, 1991

Webb, A.R, I.M Stromberg, H. Li and L.M. Bartlett. Airborne spectral measuremnts of surface reflectivity at ultraviolet and visible wavelengths, *J. Geophys. Res.*,**105**(D4), 4945-4948, 2000

Weihs, P. and A.R. Webb. Accuracy of spectral UV model calculations 2. Comparison of UV calculations with measurements. *J. Geophys. Res.*, **102,** 1551-1560, 1997

Weihs, P., A.R Webb, S.J. Hutchinson and G.W. Middleton. Measurements of the diffuse UV sky radiance during broken cloud conditions, *J. Geophys. Res.*, **105**(D4), 4937-4944, 2000

Wendisch M. and A. Keil. Discrepancies between measured and modeled solar and UV radiation within polluted boundary layer clouds, *J. Geophys. Res.*,**104**(D22), 27,373-27,385, 1999

Westwater, E.R., Y. Han, J.B. Snider, J.H. Churnside, J.A, Shaw, M.J. Falls, C.N. Long, T.P. Ackerman, K.S.Gage, W. Ecklund, A. Riddle Ground-based remote sensor observations during PROBE in the tropical western, *Bull. Amer. Met. Soc.*, **80**(2) 257-270,1999

Wiegand A.N. and M.D. Bofinger, Review of empirical methods for the calculation of the diurnal NO2 photolysis rate coefficient, *Atmos. Env.*, **34**(1), 99-108, 2000

World Meteorological Organisation. Global ozone research and monitoring project -report no. 16, Atmospheric ozone, 1985.

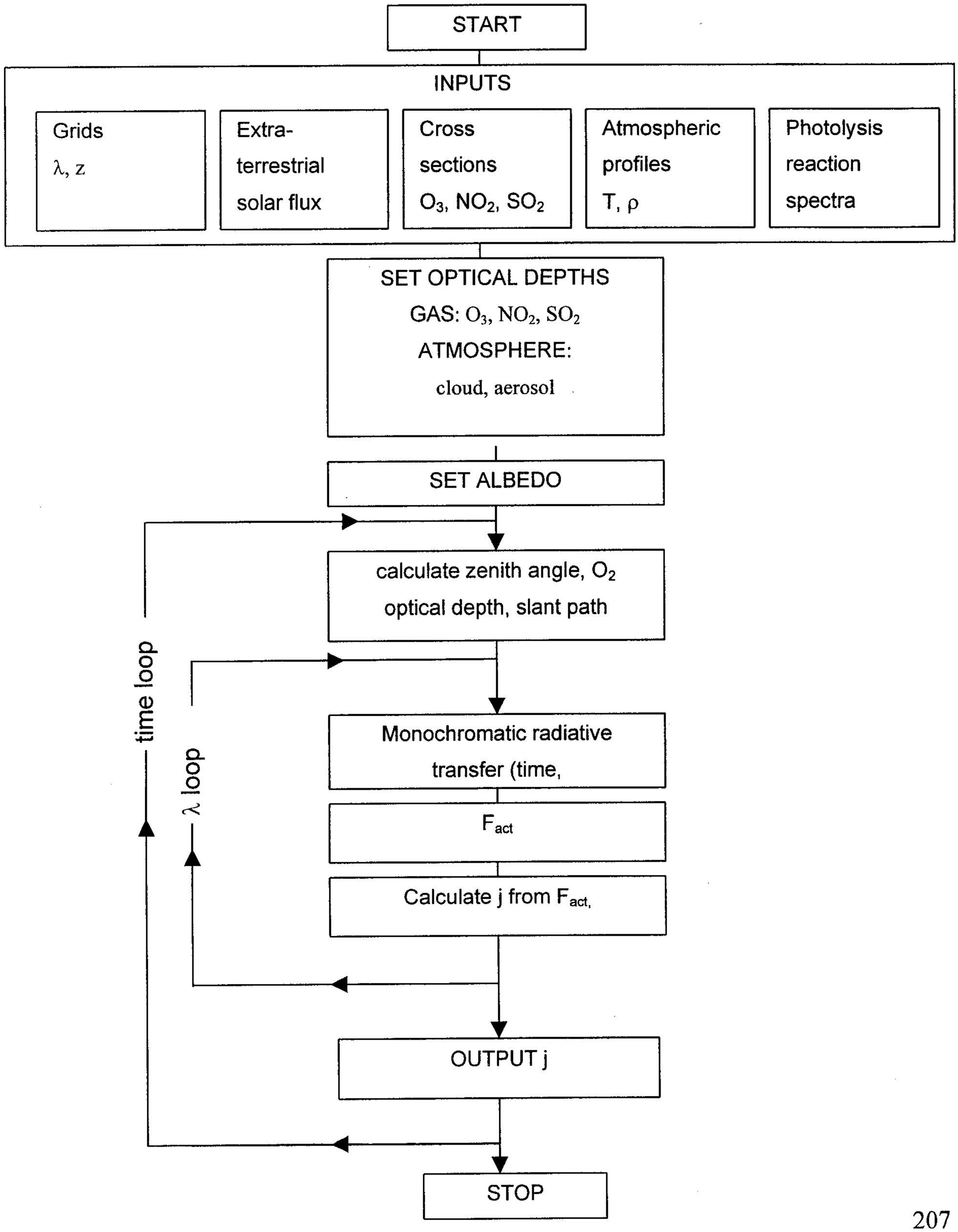
Zdunkovski, W, R. M. Welch and G Korb., An investigation of the structure of typical two stream methods for the calculation of solar fluxes and heating rates in clouds, Contrib. Atmos. Phys., 53, 147-166, 1980

Zeng, J., S. Madronich and K. Stamnes. A note on the use of the two-stream delta-scaling approximation for calculating atmospheric photolysis rate coefficients. *J Geophys. Res.*, **101**(D9), 14, 525-14, 530, 1996

Zhang, MH. R.D. Cess and X.D Jing. Concerning the interpretation of enhanced cloud shortwave absorption using monthly-mean earth radiation budget experiment/global energy balance archive measurements, *J. Geophys. Res.*,**102**(D22), 25,899-25,905, 1997

Appendix A

Block diagram of TUV3.9



The block diagram shows the structure of TUV3.9.

Before the program can start, input data must be read in from the files. This data includes: the grids on which the calculation will be performed (wavelength and altitude), the extraterrestrial solar flux used at the top of the atmosphere, absorption cross-sections for ozone, nitrogen dioxide and sulphur dioxide, atmospheric profiles of temperature and pressure and photolysis reaction spectra (the product of absorption cross section and quantum yield). The optical depths are then set. These include optical depths of gases that absorb significantly in the UV/visible (O_3, NO_2, and SO_2) as well as the cloud and aerosol optical depths. (The Rayleigh optical depth is calculated from the air profile). The ground albedo is then chosen.

The program now has all the information required to perform the calculations. An initial time is set and a loop over time begins. Within this loop, the zenith angle is calculated. This zenith angle is used to calculate the zenith angle dependent oxygen optical depth and slant path. A loop over wavelength then begins. The monochromatic radiative transfer calculations are performed within this loop, outputting the actinic flux (F_{act}). The actinic flux is transformed into photolysis frequencies for each wavelength interval by multiplication by the photolysis rate spectra. Once the loop over wavelength is complete, the wavelength integrated photolysis frequency for each species (j) is output at each time step.

BRL
LOYOLA
UNIV.